AFRL-AFOSR-VA-TR-2024-0161

Unsteady Flow, Shock and Combustion Physics in High Reynolds Number Systems

Lieuwen, Timothy
GEORGIA TECH RESEARCH CORPORATION
926 DALNEY ST NW
ATLANTA, GA, 30332
USA

02/16/2024
Final Technical Report

DISTRIBUTION A: Distribution approved for public release.

Air Force Research Laboratory
Air Force Office of Scientific Research
Arlington, Virginia 22203
Air Force Materiel Command

REPORT DOCUMENTATION PAGE

PLEASE DO NOT RETURN YOUR FORM TO THE ABOVE ORGANIZATION.

1. REPORT DATE	2. REPORT TYPE	3. DATES COVERED	
20240216	Final	START DATE 20200801	END DATE 20231031

4. TITLE AND SUBTITLE
Unsteady Flow, Shock and Combustion Physics in High Reynolds Number Systems

5a. CONTRACT NUMBER	5b. GRANT NUMBER	5c. PROGRAM ELEMENT NUMBER
	FA9550-20-1-0215	61102F
5d. PROJECT NUMBER	**5e. TASK NUMBER**	**5f. WORK UNIT NUMBER**

6. AUTHOR(S)
Timothy Lieuwen

7. PERFORMING ORGANIZATION NAME(S) AND ADDRESS(ES)
GEORGIA TECH RESEARCH CORPORATION
926 DALNEY ST NW
ATLANTA, GA 30332
USA

8. PERFORMING ORGANIZATION REPORT NUMBER

9. SPONSORING/MONITORING AGENCY NAME(S) AND ADDRESS(ES)	10. SPONSOR/MONITOR'S ACRONYM(S)	11. SPONSOR/MONITOR'S REPORT NUMBER(S)
Air Force Office of Scientific Research 875 N. Randolph St. Room 3112 Arlington, VA 22203	AFRL/AFOSR RTA1	AFRL-AFOSR-VA-TR-2024-0161

12. DISTRIBUTION/AVAILABILITY STATEMENT
A Distribution Unlimited: PB Public Release

13. SUPPLEMENTARY NOTES

14. ABSTRACT
Rotating detonation engines (RDEs) utilize pressure gain combustion, granting them significantly improved theoretical efficiency over traditional combustion engines. However, several fundamental knowledge gaps must be addressed before such improvements can be realized. Many of these relate to three key areas: detonation wave dynamics in annular geometries, injector response, and general transient combustion/fluid mechanic interactions. Concerning the first point, the circumstances dictating the strength, number, and direction of detonations is an area of particular concern. The strength of detonations likely relates to the mechanisms by which detonations gain and lose energy, which remain largely unknown. The number and direction of detonations may be dictated in part by periodic wave reflections from injector elements, which can potentially dominate the primary wave direction. Concerning the second point, the injection system is known to play several governing roles in RDEs: these include providing well-conditioned reactants in a timely manner, a process influenced by shock feedback into the injection system and influencing detonation behavior through the aforementioned reflections. Concerning the final point,

15. SUBJECT TERMS

16. SECURITY CLASSIFICATION OF:			17. LIMITATION OF ABSTRACT	18. NUMBER OF PAGES
a. REPORT U	b. ABSTRACT U	c. THIS PAGE U	UU	167

19a. NAME OF RESPONSIBLE PERSON	19b. PHONE NUMBER *(Include area code)*
CHIPING LI	426-8574

Standard Form 298 (Rev.5/2020)
Prescribed by ANSI Std. Z39.18

DISTRIBUTION A: Distribution approved for public release.

Final performance report presented to the Air Force Office of Scientific Research

Unsteady Flow, Shock, and Combustion Physics in High Reynolds Number Systems

Tim Lieuwen
Professor and David S. Lewis Jr., Chair
School of Aerospace Engineering, Georgia Institute of Technology

January 31, 2024

Dr. Chiping Li, Program Monitor

DISTRIBUTION A: Distribution approved for public release.

Accomplishments

Background

Detonation Wave Dynamics in Annular Passages

The defining feature of RDCs is a traveling, large amplitude pressure wave or waves. There exists a large literature in the rocket community on large amplitude combustion instabilities with shock waves axially propagating back and forth (analogous to a pulse detonation engine), or rotating around (analogous to a RDC) [1, 2].

The RDC problem itself consists of a shock wave travelling in a round or annular passage. There has been a significant amount of work on combustion driven pressure wave propagation in annular passages in the last decade, motivated by the problem of combustion instabilities in annular combustion chambers [3, 4]. We briefly review what is known about these types of wave dynamics in annular combustion systems next. In these cases, the key nonlinearities arise from the combustion process, while gas dynamic processes are linear. Clearly, the RDC system has significant nonlinearities associated with both combustion and gas dynamics.

For low amplitude pressure oscillations, the nature of the wave solution is indeterminate, and three potential solutions exist in some combination (1) a single traveling wave that rotates in the clockwise (CW) direction, or (2) counterclockwise (CCW) direction, or (3) a standing wave, composed of two equal amplitude travelling waves, one propagating in the CW direction and the other in the CCW direction. A convenient way to characterize the degree to which the waves are traveling, or standing is to define the spin ratio, where $S = 0$ corresponds to a standing wave and $|S| = 1$ to a traveling wave, with $S = -1$ and $S = +1$ values corresponding to CW and CCW travelling waves, respectively. Because of the turbulent, stochastic environment of combustion systems, experimental observations often show that, in the case of standing waves, that pressure nodes and anti-nodes do not remain at a fixed location, but wander around erratically. Similarly, other experiments show erratic switching in direction of traveling waves and solutions jumping between standing and traveling waves [5]. In RDC's, related observations have been made on erratic switching of wave directions, and presence of counterpropagating waves (e.g., see Bennewitz *et al.* [6]).

As pressure amplitudes rise and nonlinear effects dominate, additional constraints arise on the nature of solutions which, as noted above, are experimentally observed to exhibit a wide variety of behaviors. For example, models generally show that all three solutions exist at low amplitudes, while only a CW or CCW solution exists at large amplitudes [4]. To use dynamical systems language, while both CW and CCW waves are theoretically possible, one of the wave "entrains" the other, so that during a limit cycle only a single traveling wave exists with $S = +1$ or $S = -1$.

Turning to the RDC, as noted above, the name itself suggests traveling wave behavior. Indeed, observations show that the number, n, of rotating shocks can vary with operating conditions

DISTRIBUTION A: Distribution approved for public release.

and can jump chaotically between multiple values, as shown in Figure 1. One hypothesis for scaling the approximate value of n suggests that it is a function of injector velocity and RDC frequency [7]. The blue line in the figure shows this theoretical value from Wolanski [8] – in this case it is a non-integer value, suggesting that the $n = 2$ and $n = 3$ solutions nonlinearly compete with each other, leading to the intermittent mode switching evident in the data. This effect is not just fundamentally interesting, but also has important influences on overall engine performance, as results show that shock strength and engine performance deteriorates as n increases [9]. For example, Lin *et al.* [10] measured a factor of two difference in peak pressure between $n = 2$ and $n = 1$ operation. Similarly, measurements show a reduction in wave velocity with increase in number of waves [11].

It is worth noting that there are significant problems in interpreting existing data on this topic for the many studies where wave speeds are deduced from discrete pressure measurements; in such situations, there is ambiguity in the product of the wave speed and number of waves. *It is likely that several studies report incorrectly high wave velocities for these reasons*. In contrast, the imaging approach of, for example, Bennewitz *et al.* [9] necessarily captures n and the wave speed correctly.

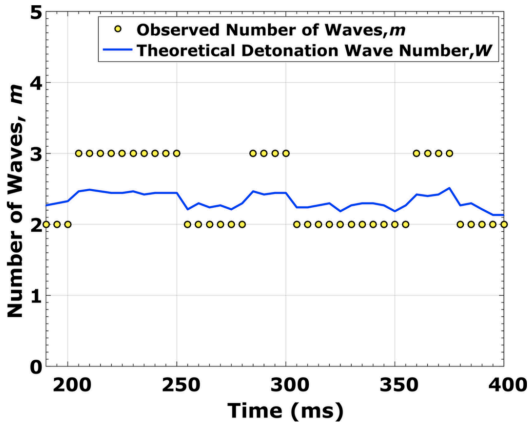

Figure 1 – Time dependence of number of waves during a rocket RDE test, reproduced from Bennewitz et al. [6].

Moreover, other data, such as from Bennewitz *et al.* [6], shows that counterpropagating waves can exist in RDC. For example, Figure 2 shows measurements from Gamba and co-workers [12]. Here, in addition to the primary rotating shock wave (A), there is a weaker pressure disturbance that rotates in the same direction and an additional counter-rotating pressure disturbance (C). Again, measurements show that the presence of counterpropagating waves generally degrades engine performance.

DISTRIBUTION A: Distribution approved for public release.

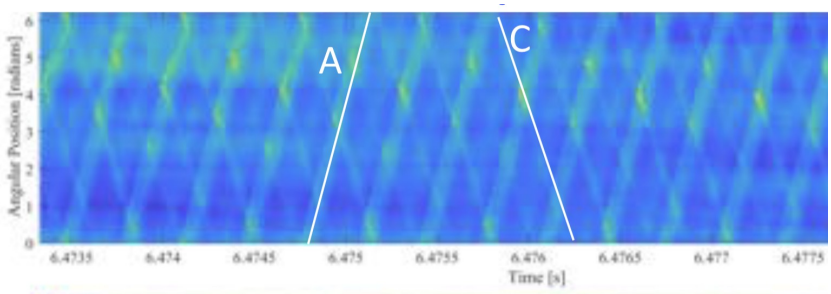

Figure 2 – Wave Dynamics observed using x-t diagrams, showing- A: Primary Detonation Wave, C: Secondary Wave System, traveling counter to the main detonation wave. Image reproduced from DOE UTSR Meeting 2018 presentation by M. Gamba.

The presence of counterpropagating waves is not surprising, as the impedance jump experienced by the wave as it traverses a fuel injector will generate a reflected shock or expansion wave. *Indeed, purely traveling wave solutions would only be expected in the ideal case of a perfectly azimuthally symmetric system, without any fuel injector features at discrete angles*. The "spin ratio" of an RDC must clearly be a function of wave amplitude, annular gap features, and injector impedance. Further elucidating these dependencies is one of the goals of this work. The observations above motivate the proposed work to understand the type and nature of rotating wave solutions that are possible in RDC environments.

Injector Response and Injector Shock Reflections

The transversely propagating shock waves induce large pressure drop fluctuations across the fuel/oxidizer injection system. Even in cases where the fuel injector is choked, the overpressure after the shock will usually be sufficient to unchoke it. If this occurs, then the fuel/oxidizer mass flow rate into the RDC is modulated. In addition, the presence of the fuel injector is "felt" by the transversely propagating wave and weakens the propagating wave by inducing a wave reflection. This tendency to partially reflect the traveling shock can lead to local counterpropagating waves, as discussed in the earlier section.

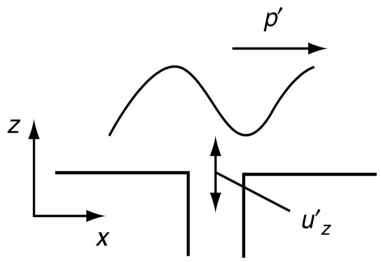

Figure 3 – Axial velocity oscillations induced at the interface of an injector (vertical passage) and the annulus (horizontal passage).

There is a large literature on injector response during transverse combustion instabilities in rockets (where injector coupling is a critical feature controlling whether the rocket is stable or

DISTRIBUTION A: Distribution approved for public release.

unstable), or in instabilities in annular combustors [[6]]. Critical to this feedback is the coupling between the annular chamber wave dynamics, and injector dynamics. A key piece of the injector coupling problem is the manner in which a transversely propagating shock, and the associated transverse velocities, induce oscillations in reactant flow rates (see Figure 3). This process is sometimes referred to as "pressure coupling", as the oscillatory pressure drop across the reactant supply system (assuming it is unchoked), induces an oscillatory reactant flow rate. The actual pressure coupling phenomenon is quite complex, as it is essentially a nonlinear shock refraction problem, as wave motions in the transverse direction in the combustor itself are refracted (or bent), so that they propagate into the reactant supply system. For low amplitude oscillations, the nature of this refraction problem is a strong function of:

(1) the impedance of the reactant supply system (this is controlled by the presence of volumes, tube lengths, flow bends/turns, and pressure drops in the injector system); and

(2) the nature of the wave motions that are inducing the oscillatory pressure (for example, injector dynamics behave very differently in the presence of travelling vs. standing waves).

Far less work has been done on the injector coupling/wave refraction problem in the large amplitude/shocked pressure case. Clearly, the nature of these interactions varies over the parts of the cycle where the injector is choked and where it is unchoked, as well as on the direction of the flow for a given part of the cycle. In addition, the presence of the shock wave bouncing back and forth in the fuel supply system can significantly alter the amplitude of the fluctuating fuel flow rate, depending upon its phasing with respect to the main detonation.

As noted earlier, the shock wave "feels" the presence of the nozzle and is weakened by partial reflection. Following Lighthill [[14]], it is possible to derive simplified expressions for the amplitude of the reflected waves as a function of injector impedance, shock amplitude and cross sectional area. Although not shown here, these equations show that the reflected wave amplitude is relatively weak in the realistic case where the injector cross sectional area is small relative to that of the annular gap, but still nonzero. In particular, the fact that such a wave will be excited at every injection point means that it must be considered. The one case where the injector can drive a significant impact on the transverse wave is when its impedance is adjusted (e.g., by upstream lengths, volumes, pressure drops, etc.), to drive the injector impedance to zero (i.e., no pressure fluctuation case). In such a case, very strong shock wave reflections can be induced by a very small injector [[15]].

Goals/Accomplishments

Computational Fluid Dynamics Simulation of AFRL Rotating Detonation Rocket Engine

Computational Fluid Dynamics (CFD) is a powerful tool for understanding the phenomena described above. When utilized properly, CFD provides access to the full spatiotemporal flow

DISTRIBUTION A: Distribution approved for public release.

field in a system, illuminating countless phenomena that are inaccessible to experiments. This is especially the case in RDEs, in which the incredibly short time scales (on the order of tens of microseconds for a single detonation cycle) and the intensity of the combustion and flow physics therein severely limit that which can be accessed experimentally. However, proper use of CFD is predicated on proper modeling assumptions – e.g. boundary conditions, physics models (choice of chemical mechanism, turbulence model, etc.), numerics (shock-capturing methods, etc.), and possible geometry simplifications (domain truncations, use of symmetries, etc.) – to capture the physics governing the system being modeled. Given our current lack of understanding of the critical physics governing rotating detonation combustion, then, it is unsurprising that CFD predictions show major discrepancies from experimental ones, as widely reported [[58]]. That the source of such discrepancies is still unknown indicates a clear deficiency in our understanding of RDE physics and the modeling choices needed to recapitulate them.

To help address this deficiency, as well as those mentioned in the preceding sections, our group has developed the capabilities to model the full spatiotemporal flow field within an RDE using CFD, specifically the commercial CFD code ANSYS Fluent. Due to the extreme computational cost of such models, we are limited to case-specific investigations; therefore, we have chosen to model the high mass flow rate test case from the methane-oxygen RDRE detailed by the 5th MVP workshop [[58]]. The initial and boundary conditions, geometry, and operating conditions for this test case were prescribed according to the instructions provided therein. Our model, hereafter referred to as the TLRG model, consists of 17.9 million tetrahedral elements and uses a fixed, global time step of 0.1 μs. The pressure-velocity coupling is captured via the Coupled algorithm in Fluent, and a second order implicit time discretization and second-order spatial discretization is used. The k-epsilon (i.e. RANS) turbulence model is used throughout the domain, and a 12-step reaction mechanism with laminar finite rate chemistry [[59]] is used to model the stiff detonation kinetics.

We have also continued an existing simulation developed by Dr. Hossam Elasrag of AFOSR, hereafter referred to as the AFRL model. Also developed in Fluent, this simulation uses 22.4 million hexahedral elements and employs a hybrid RANS-Large Eddy Simulation (LES) turbulence model together with the same 12-step reaction mechanism utilized by our own model, as well as the same time step. This model had already progressed beyond the point of stable rotating detonation and was validated against the experimental test case and other groups' CFD models. This second dataset is useful in several regards. Firstly, because of the similarity between our simulations (same chemical mechanism, boundary conditions, and CFD code, similar numerics and mesh size), the second dataset provides a useful point of comparison for addressing some of the aforementioned knowledge gaps. Secondly, because it was already validated and uses the same CFD code, it enabled easy analysis without the need to validate the results or become proficient with a new CFD code.

DISTRIBUTION A: Distribution approved for public release.

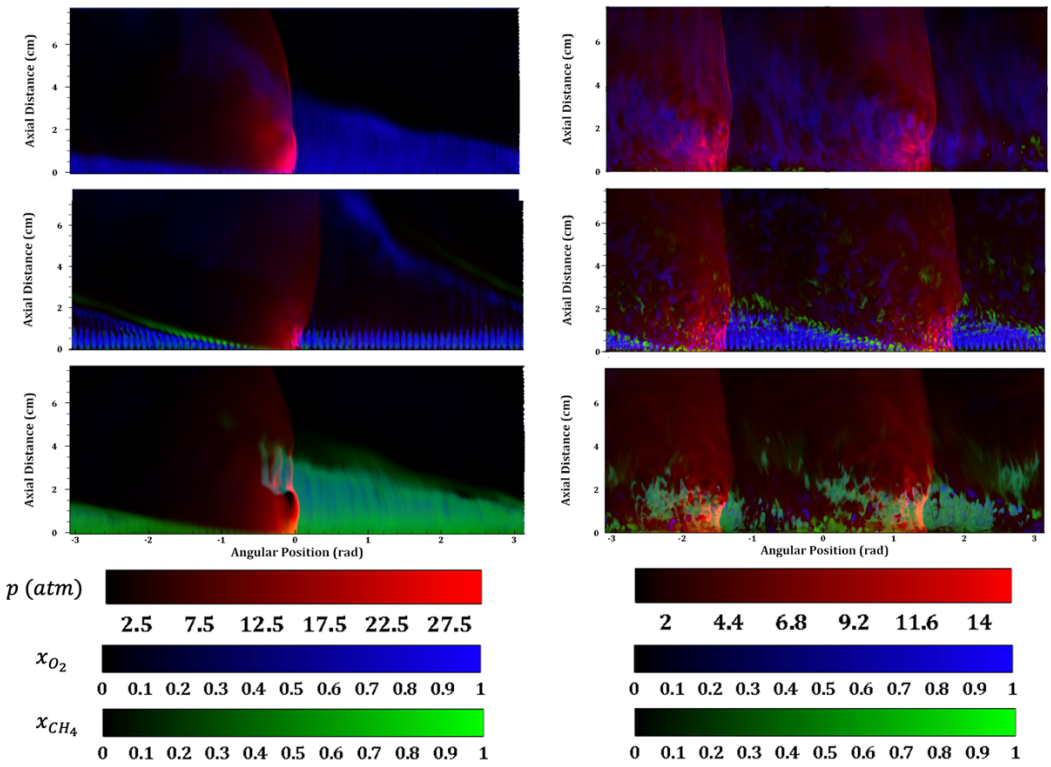

Figure 4 - Wave/reactant characteristics for TLRG (left) and AFRL (right) models at the inner chamber (top row), middle surface (middle row) and outer chamber (bottom row)

Figure 4 shows the wave and reactant characteristics for the TLRG and AFRL models during the steady regime. Despite the similarities between the two models, they exhibit different wave numbers. This is surprising but consistent with the lack of repeatability for this validation case observed by other computational groups. Nevertheless, this difference in wave number represents a confounding factor: this is the dominant source of differences in behavior between the two models, making it difficult to assess the roles of differing viscous models in producing such differences. For instance, examining the reactant characteristics observed in the blue and green channels of Figure 4, one observes a greater presence of unburnt reactants behind the detonations in the AFRL model than in the TLRG model. This is most likely because the single detonation wave of the TLRG model is stronger than the two detonations of the AFRL model, which are allotted half the reactants of the former. A stronger detonation has a higher post-wave temperature and, therefore, a greater ability to auto-ignite reactants. Furthermore, there is a greater portion of unburnt reactants near the outer (oxygen injector side) and inner (fuel injector side) chambers for both simulations, likely due to insufficient mixing in these regions. Observing the middle left frame of Figure 4, one observes that the mixture height seemingly reaches a constant value some distance behind the wave; this height, perplexingly, is shorter than that of the fuel and oxygen layers seen in the top and bottom rows. This is possibly an out of plane effect resulting from limited penetration of reactants into this plane, but this warrants further investigation. Also, one notices marked 3-dimensionality in the detonation; the shape of

DISTRIBUTION A: Distribution approved for public release.

the detonation varies considerably between the 3 radial locations sampled, particularly in the TLRG model.

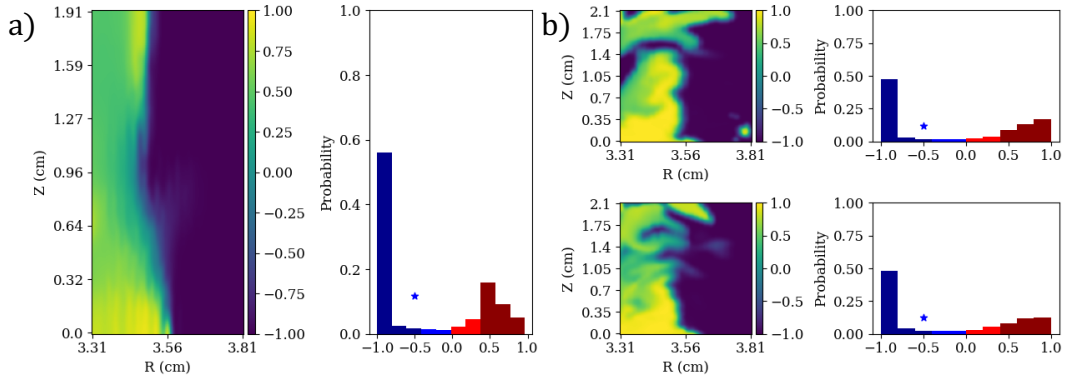

Figure 5 - Spatial and probability distribution of reduced equivalence ratio for a) TLRG and b) AFRL models ahead of the detonations. Histograms use the following color scale: dark blue - very lean [$\phi^* \in \left(-1, -\frac{1}{3}\right), \phi \in \left(0, \frac{1}{2}\right)$], blue - lean [$\phi^* \in \left(-\frac{1}{3}, 0\right), \phi \in \left(\frac{1}{2}, 1\right)$], red - rich [$\phi^* \in \left(0, \frac{1}{3}\right), \phi \in (1, 2)$], dark red – very rich [$\phi^* \in \left(\frac{1}{3}, 1\right), \phi > 2$]. A blue asterisk indicates that the majority of the domain is fuel-lean

The conditions of reactants supplied to the detonations can be further observed in Figure 5, which displays the *r-z* plane taken 2 injector locations ahead of the detonations for both simulations for a representative time step. Because equivalence ratio ϕ is unbounded, it is preferable to show the *reduced* equivalence ratio ϕ^*, defined as $\phi^* \equiv \frac{2\phi}{\phi+1} - 1$, such that negative ϕ^* indicates locally lean conditions and positive ϕ^* indicates locally rich conditions. Moreover, unlike ϕ, ϕ^* is bounded between -1 (pure oxidizer) and 1 (pure fuel), removing infinities due to pockets of pure fuel. In both simulations, most of the domain is fuel-lean for most instances sampled. Additionally, the reactants are highly stratified, with a distinct layer between pure fuel and pure oxidizer. This is especially pronounced in the TLRG model; the boundary between fuel and oxidizer appears to be much more distorted in the AFRL model. This may be due to the use of LES in the AFRL model, which enables the resolution of large turbulent eddies that would produce this distortion. This may lead to improved mixing in the AFRL model; the fact that there is still a relatively small portion of well-mixed (only slightly rich or lean) reactants in this case is likely a consequence of the greater wave number, meaning that reactants have less time to enter the chamber and mix before the arrival of a new detonation.

DISTRIBUTION A: Distribution approved for public release.

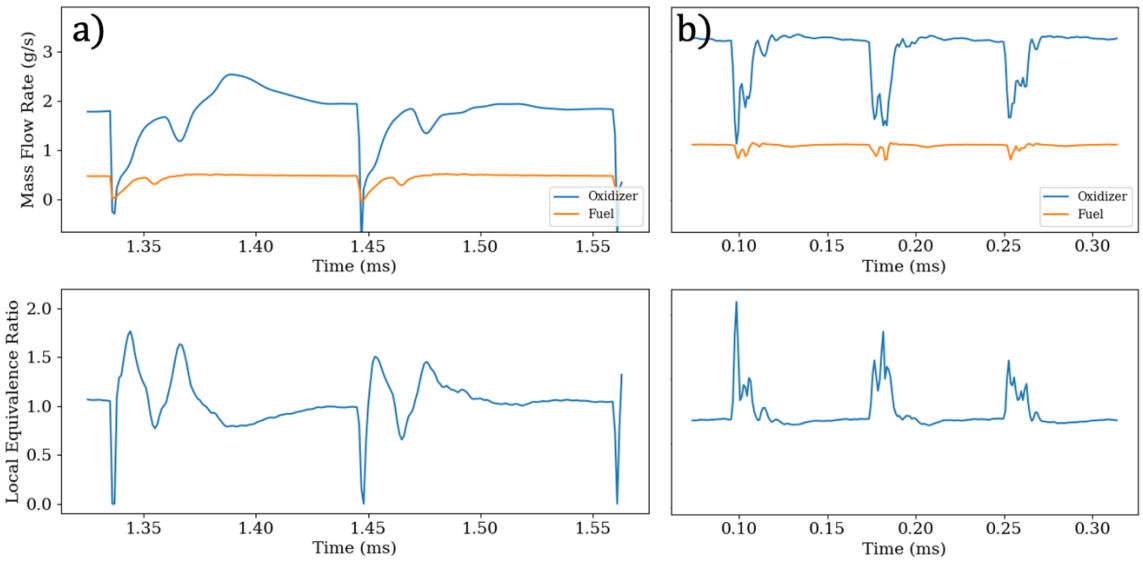

Figure 6 - Injector recovery process for a) TLRG and b) AFRL models. Mass flow rates are shown in the top row and local equivalence ratios are shown in the bottom row.

Figure 6 details the injector recovery process more closely. In the TLRG model, the detonation is strong enough to induce reversed flow, whereas neither of the two waves in the AFRL model are strong enough to accomplish this. In both simulations, the reactants become locally rich after the passage of the wave; this is consistent with the observation that the fuel mass flow rate recovers more quickly than that of the oxidizer due to the smaller fuel injector diameter. Also of note is that the recovery occurs in 2 stages; the mass flow rate reaches a local minimum after the detonation's passage, then increases before decreasing to a *second* trough and subsequently recovering to its nominal state. This process is examined more closely in Figure 7.

DISTRIBUTION A: Distribution approved for public release.

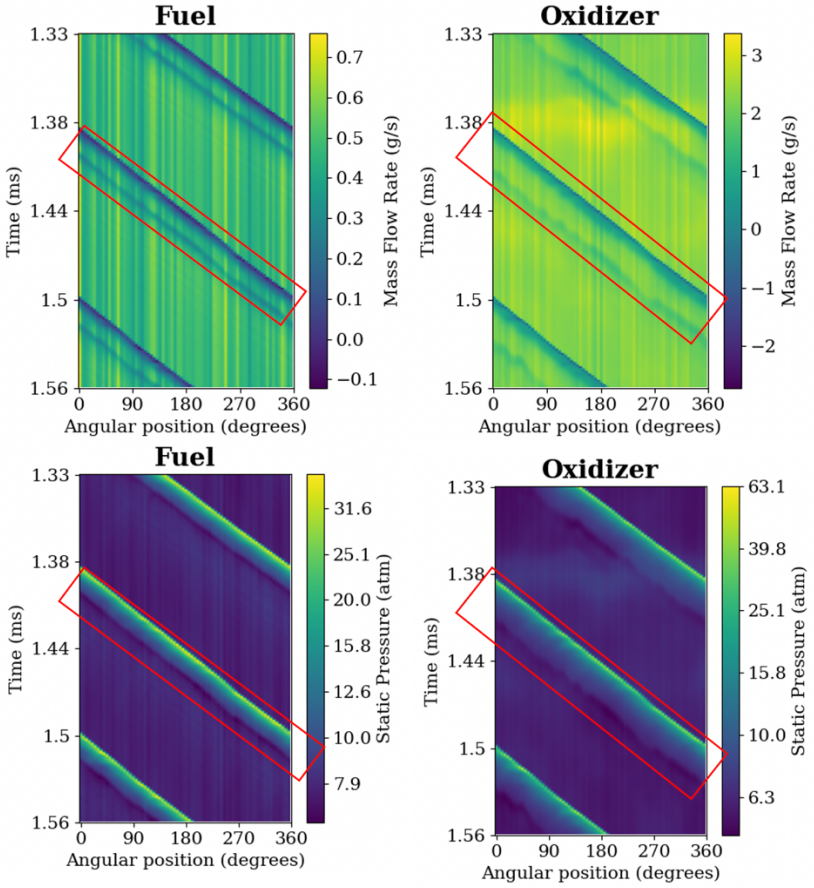

Figure 7 - 2-stage injector recovery process for the TLRG model, as illustrated by average mass flow rate (top row) and static pressure (bottom row) contours for the fuel and oxidizer injectors

Shown above, this second drop in mass flow rate is caused not by a *compression* wave, but by an *expansion* wave. This can be most clearly seen in the average pressure contours – while the first drop is due to a pressure *spike*, the second drop is due to a pressure *drop*. Said expansion wave reduces both the velocity and density of reactants, causing the mass flow rate to temporarily drop before a full recovery is made.

This work was partly motivated by the desire to better understand detonation wave dynamics and injector response. Concerning the first point, it is once again striking that, despite the apparent similarities between the two models, the wave modes are different. The sources of this discrepancy are far from obvious; for instance, the more-resolved turbulent eddies in the AFRL model (which used a hybrid RANS-LES approach) may promote more parasitic deflagration and, therefore, cause the detonations to have a greater propensity to split, or the improved reactant mixing they promote may lead to a better conditioned reactant layer capable of supporting more detonations. However, we believe it is more likely that this configuration can support multiple wave modes. We [inadvertently] tested this hypothesis when, to gain data from the first 1.5 ms of

DISTRIBUTION A: Distribution approved for public release.

operation in the AFRL model, we re-initialized the simulation. When this was done, 2 pairs of *counter-propagating* waves, rather than the 2 counter-clockwise waves observed in the original simulation, were produced in the steady-state regime. After careful investigation, this was found to be due to slight differences in initial conditions. Nevertheless, this informally demonstrates the possibility of multiple wave modes for a given set of operating conditions, a phenomenon observed in other simulations [[16]]. Formally demonstrating this possibility is the goal of future work.

Concerning the second point (injector response), this analysis yields several salient items. Firstly, that the injector recovery process occurs in two stages clearly motivates the fundamental studies of shock/injector interactions discussed later in this report. Lower-order models of RDEs (such as the "2D unwrapped" RDE models in several seminal works [[60], [61]]) routinely neglect phenomena of this nature (e.g., they assume that the mass flow rate is an instantaneous, monotonic function of chamber pressure), so their accuracy can be improved by accounting for them. Secondly, this analysis identifies at least two potential non-idealities in this configuration: inefficient mixing and uneven injector recovery. Both issues could potentially interfere with the establishment of a well-conditioned reactant layer ahead of the detonation, degrading detonative performance. However, it is unclear to what extent these issues should be adjusted to optimize performance. For instance, excessively promoting mixing could instead lead to greater parasitic deflagration ahead of the wave. Prior work suggests that pre-detonation deflagration harms performance considerably more than post-detonation deflagration [[62]], so some degree of inefficient mixing might be beneficial. Additional work on this topic is forthcoming.

Analysis of Detonation Energetics

Considering the preceding, and from the standpoint general combustion instabilities, a better understanding of wave energetics was needed. Thus, one goal of this project was to formally analyze the energetics of detonation waves. As a useful starting point for this investigation, we considered a general transport equation for the energy of disturbances.

$$\frac{\partial \boldsymbol{E}}{\partial \boldsymbol{t}} + \boldsymbol{\nabla \cdot \vec{I}} = \boldsymbol{\phi}$$

Here, E, $\vec{I}$, and ϕ represent the energy density, flux, and sources for the disturbances. The latter are of particular interest, as they are responsible for adding/removing energy from the detonation. Thus, a goal of this project was to identify dominant source terms and their relative scaling.

The precise form of the above energy transformation equation is traditionally derived from a perturbation expansion, as in Ch.2 of the PI's textbook "Unsteady Combustor Physics" [[63]]. This describes the transport of energy up to 2nd order in perturbation amplitude. For extremely large amplitude disturbances like detonations, however, it became pertinent to use a more generalized disturbance energy transport equation, specifically that of Brear et al [[64]]. To apply this formulation, we have initiated a collaboration with Prof. Poludnenko's group, using their DNS calculations and extracting the various terms in the energy transport equation. This work reveals some striking aspects of the problem under consideration, which we will briefly

DISTRIBUTION A: Distribution approved for public release.

summarize. For further details, please see the full proceedings from the 2022 Spring Technical Meeting [[65]].

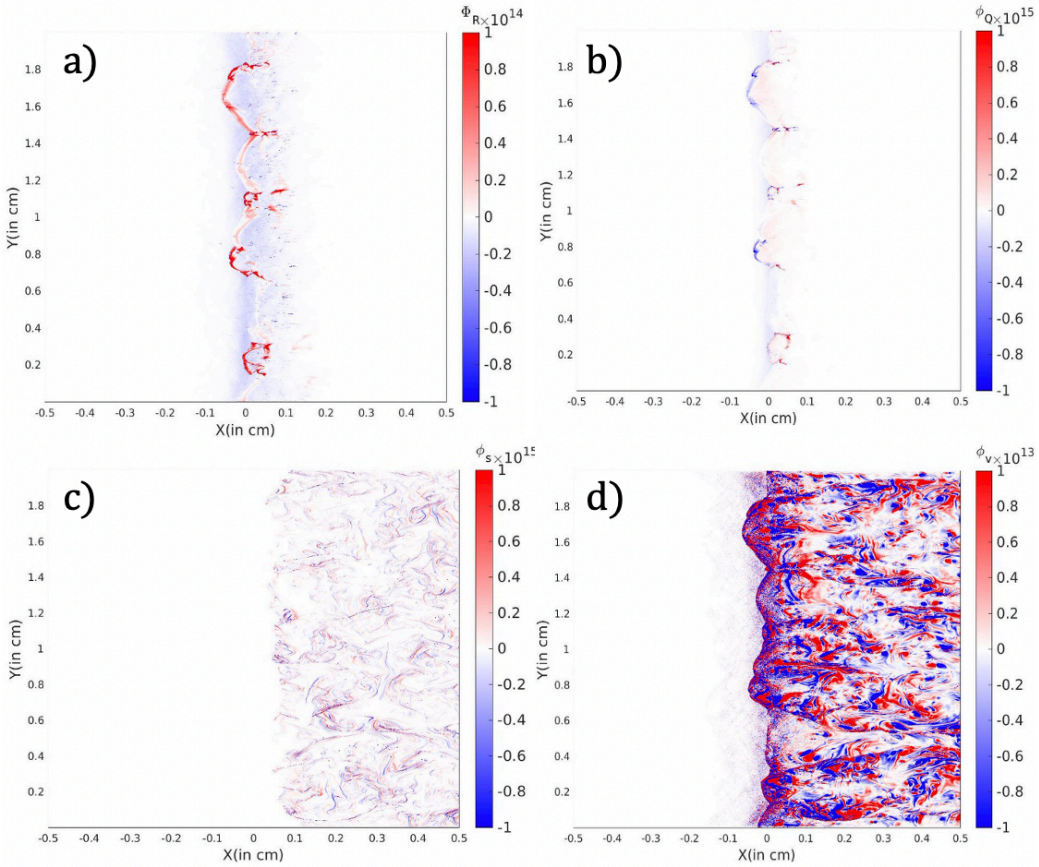

Figure 8 – Snapshots of instantaneous a) Rayleigh source term, b) heat release source term φ_Q, c) entropic source term φ_s, and d) vortical source term φ_Ω

Figure 8 shows the magnitude and sign of various sources in the detonation flow-field. Firstly, comparing frames a) and b), one observes that φ_Q is almost an order of magnitude larger than the Rayleigh source term. Since the former is speculated to be a source of both acoustic and entropic disturbances while the latter is only a source of acoustic disturbances, this result suggests that the bulk of energy produced by unsteady combustion contributes to the entropic disturbance field. Secondly, comparing frames b) and d), one notes that unsteady combustion produces nearly two order of magnitudes more disturbance energy than unsteady vorticity. However, as this is a 2-D computation, so 3-dimensional effects like vortex stretching and bending are unaccounted for, meaning that the vorticity source term φ_Ω is likely under-estimated.

DISTRIBUTION A: Distribution approved for public release.

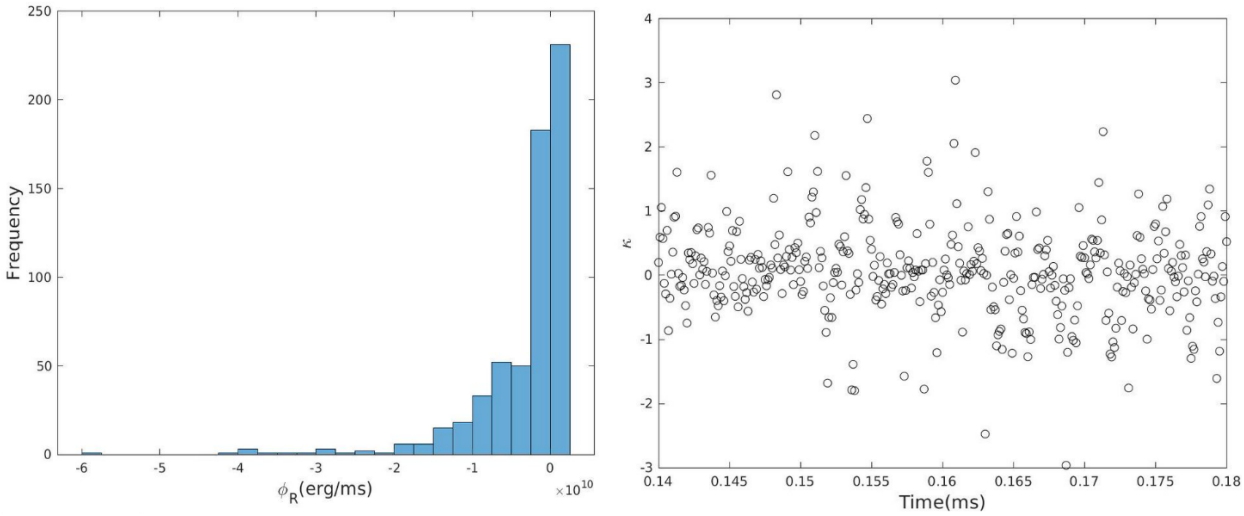

(a) (b)

Figure 9: (a) Distribution of volume integrated Rayleigh source, $\frac{(\gamma-1)}{\gamma p_0} p'q'$ in erg/ms, and (b) Normalized Rayleigh source term

In Figure 9 (a), the spatially integrated Rayleigh source term over 0.5cm behind the detonation front, which is approximately the region of chemical reaction zone in this case, is presented as a histogram of source term distribution with time. From this plot, it can be observed that the Rayleigh source term is largely negative behind the detonation front which implies that heat release fluctuations are removing energy from the disturbances. As stated previously, we wished to identify an appropriate scaling for these source terms. The importance of such a scaling is revealed by the smallness of the sources relative to the detonative heat release (~10^{10} vs. ~10^{17} erg/s on average). An appropriate choice is the intensity flux associated with these transversely propagating acoustic waves. It is well known that these transverse waves are critical for sustaining the detonation and hence the energy flux across them is used for source term normalization. This term can be estimated from the product of the transverse velocity fluctuations and fluctuating pressure at the duct centerline. Figure 9 (b) presents the spatially integrated Rayleigh source normalized by the energy flux across the transverse wave behind the detonation front for one channel width distance in the streamwise direction. It is observed that the Rayleigh source term achieves values ranging from zero to about four times the intensity flux across the transverse waves. The normalized Rayleigh source has a mean of about -2.5 and rms value of 6.6. This further indicates that the Rayleigh source is on average negative and almost twice as large as the energy flux across the transverse waves. The large rms value of the Rayleigh source suggests that it varies between large negative and large positive values with time.

DISTRIBUTION A: Distribution approved for public release.

Going forward, we wish to use these results, possibly in combination with those from model problems to lend insight into computations and experiments. For example, it is relatively straightforward to estimate the Rayleigh source term from simultaneous pressure and chemiluminescence measurements. We will work with existing experimental facilities – both air breathing and rocket – to obtain data sets of detonation wave amplitudes and determine the extent to which these amplitudes might be influenced by the parameters suggested by the above analyses, such as injector response functions. We also plan to apply our methods broader datasets consisting of varied reactants and detonation channel widths.

Determination of Acoustic Wave Modes from Periodic Injector Arrays

As mentioned above, a key phenomenon in RDEs is the interaction of a spinning shock with periodically spaced injectors. During this interaction, the shock is partly reflected, leading to a counter-propagating pressure wave. Recent work suggests that this mechanism can govern the direction of detonations in certain injector designs [[66]]. Furthermore, so-called "secondary waves" (non-reacting shocks traveling opposite to the direction of detonations) are widely known to influence the wave mode through collisions and blocking reactant injectors [[67], [68]]. Thus, we hypothesized that this mechanism could influence the dominant direction of pressure waves in the combustion chamber.

As a starting point toward understanding this phenomenon, we considered a purely acoustic scattering problem where a background pressure field was applied to an injector array. The resulting scattered wave comprises both a forward and counterpropagating component whose relative magnitudes can be compared. This provides a means to understanding how the number, spacing, and characteristics of the injectors can influence the dominant direction of waves. This preliminary work was not intended to make any broad statements about the case of detonations or even finite-amplitude waves; it is merely for pedagogical purposes to illustrate how one might proceed with the more general problem. However, we believe that our findings from this analysis are useful for several reasons. Firstly, they demonstrate the usefulness of such an approach toward tackling the more general problem at hand. Secondly, even acoustic waves can self-steepen into high-amplitude traveling waves in combustion chambers: this phenomenon has been noted as early as 1965 by Clayton et al, who even referred to it as "rotating detonation-like combustion" [[69]]. Indeed, several authors have noted the possibility of detonations to form from non-reacting pressure waves when they couple with deflagration zones [[66], [70]], and other authors have noted the similarities between rotating detonation and self-excited combustion instabilities seen elsewhere [[71]]. Thus, there's a strong possibility that even the purely acoustic case has bearing on the more general one.

We proceed by briefly describing our modeling approach. For initial simulations of the system to make initial observations and model comparisons, COMSOL was used to simulate the system under various conditions. The system was set up with the annulus represented unwrapped with a periodic boundary on both sides. The scattering injector surface is the lower boundary and is represented with a periodic impedance or a hard boundary with rectangular injectors. The

DISTRIBUTION A: Distribution approved for public release.

incident shock wave is represented as a background pressure field with an angle θ such that $\sin\theta = \frac{1}{M_s}$, where M_s is the Mach number of the incident shock. The resulting total pressure field p_{tot} can be decomposed as the sum of the incident wave p_{inc}, the reflected wave p_{refl} and the scattered field p_{sc}; that is,

$$p_{tot} = p_{tot} + p_{refl} + p_{sc}.$$

The geometric constraints of the system allow pressure solutions of certain wave numbers $k_{x,n}$ and $k_{y,n}$ in the transverse (x) and axial (y) directions.

$$p = \exp\left[i\left(k_{x,n}x + k_{y,n}y\right)\right]$$

$$k_{x,n} = \frac{2\pi n}{L}$$

$$k_{y,n} = \frac{2\pi}{L}\sqrt{(n_s M_s)^2 - n^2}$$

Here, n_s represents the number of waves. To find a measure of the system directivity, the scattered field can be decomposed via orthogonality:

$$p_{sc} = \sum \alpha_n \exp\left[i\left(k_x x + k_y y\right)\right], \text{ or}$$

$$\alpha_n e^{-ik_{y,n}y} = \int p_{sc} e^{-ik_{x,n}x} dx$$

This gives the amplitude of each allowed wave, of which the angles are already known. Averaged over the selected domain, this gives the field strength as a function of angle:

$$\alpha_n = \frac{\sum \frac{\int p_{sc} e^{-ik_{x,n}x} dx}{e^{-ik_{y,n}y}}}{N_y}$$

Here, N_y is the number of points in the axial direction.

For a more direct comparison to a simplified model, thin rectangular injectors were used such that they could be modeled as point sources. A periodic impedance with a different pattern would need a more sophisticated model. Shown below is a selected vector plot of this discrete directivity, as measured by the reflection angle $\boldsymbol{\theta_r}$.

DISTRIBUTION A: Distribution approved for public release.

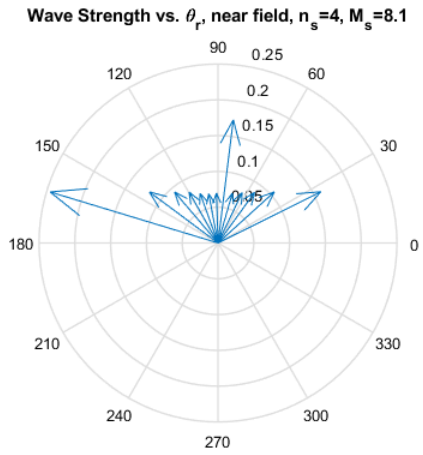

Figure 10 - Wave strength versus reflection angle θ_r for 4 waves traveling at $M_s = 8.1$.

A lower order model of this system is formed by representing the pressure field scattered from the injector surface as that scattered by a series of N injectors treated as point sources. In this case, the pressure field is the sum of the contributions from each point source m, phased with some angle ϕ_m relative to the others. For a periodic domain where the propagating detonation continues infinitely, there would be an infinite number of point sources contributing to the pressure field. If we assume a given detonation rotates J times through the RDE, we can represent the pressure in terms of a finite sum of contributions from the point sources:

$$P = -\frac{i}{4}\sum_{m=-J\cdot N}^{J\cdot N} H_0(kr_m)\exp\left(i\phi_m\right)$$

Here, k is the wave number, r_m is the distance from the point source, and H_0 is the Hankel function of the first kind. Taking this expression in the far field ($r_m \to \infty$ limit), the angles of maximum scattering are found to be

$$\theta_{max} = \sin^{-1}\left(\frac{1}{2n_s M_s J} - \frac{1}{M_s}\right)$$

This can be compared with the COMSOL data for the purpose of comparing the computed angles of Maximum scattering.

With this accelerated method of predicting the angle of maximum scattering, we can sweep of ranges of the parameters n_s, M_s, and N (number of waves, wave Mach number, and number of injectors). This gives us an idea of what injector system parameters favor certain travel directions for a given number of waves. For instance, consider Figure 11, which shows the dominant scattering direction for a variety of parameters.

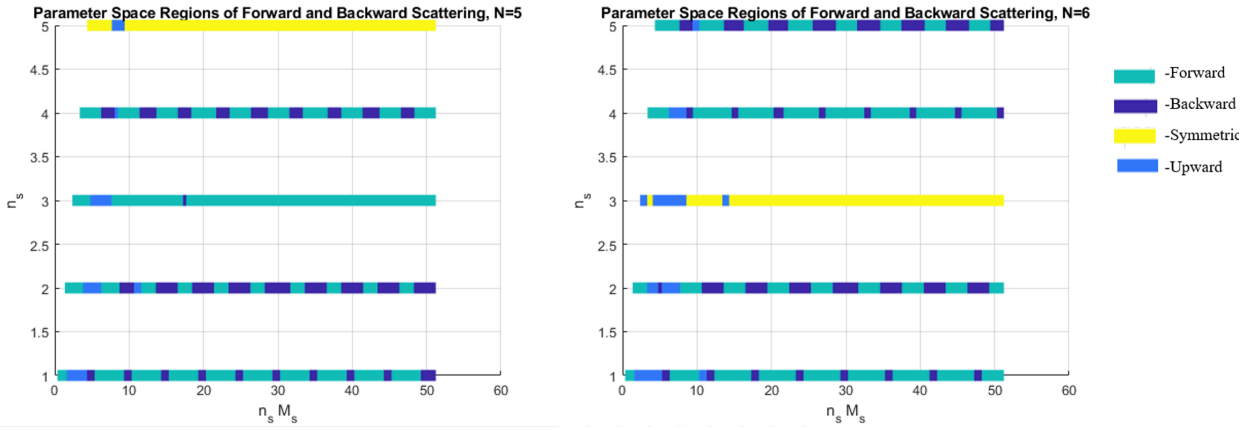

Figure 11 – Dominant wave directivity for $N = 5$ and $N = 6$ injectors for a range of wave numbers n_s and scaled wave speeds $n_s M_s$.

The above figure is striking for several reasons. Firstly, it suggests that, for most wave modes with a given number of injectors, there is no clear trend in preferred wave direction; it appears to vary erratically as wave speed increases. For RDEs, it generally isn't possible to predict the direction of wave travel [[67], [71]]; this work appears to suggest that, even in the simplified case considered here, this is still impossible. Secondly, it suggests that the number of injectors can affect the prevalence of certain wave directions, i.e., the symmetric mode occurs for different numbers of waves depending on the number of injectors. This is especially important from a design standpoint; it suggests that one can select a given injector count to avoid certain undesirable wave modes (such as counter-propagating waves).

Going forward, we wish to extend this problem to more realistic flows. To start, we'll consider the more realistic case with mean flow. A useful starting point toward this end would be the wave equation with mean flow, presented in Ch.2 of the PI's textbook "Unsteady Combustor Physics". We'll then consider the more general case of finite-amplitude waves and eventually detonations. Toward this end, there is a wealth of prior work on combustion instabilities involving shocks that may prove useful – see Section 5.1 of a recent review by Sirignano for further details [[72]].

Investigation of Shock Wave Transmission through Variable-Area Ducts

The injection system is critical to any combustor, governing many of the key physical processes leading to either beneficial or deleterious behavior. The preceding arguments show a need to better understand these processes in RDEs and how to leverage them for optimal behavior. As such, key questions we aimed to answer with this work included:

- "How can injection system dynamics be tuned to augment detonation wave strength, or at least to minimize the deleterious effects of injector coupling?"
- "How does injector coupling, as well as the nonlinear impedance of the injector system influence RDC characteristics?"

DISTRIBUTION A: Distribution approved for public release.

The preceding investigation helps address both questions by elucidating the connection between injector number/spacing and the dominant wave direction in RDEs. The following investigation addresses these questions by studying the transmission of shocks through a discrete change in area. This is a ubiquitous phenomenon within the injection system and is expected to strongly impact device behavior. It governs the degree of pressure feedback into the reactant plena, leading to several highly influential phenomena in RDEs. For one, it can produce a low-frequency instability whereby a system of trailing shocks and reflected expansion waves causes the base pressure to oscillate sinusoidally [[73], [74]]. This is one of several instabilities in RDEs caused by the injection system, as discussed by Anand et al. in a recent literature review [[71]]. Although stiff injectors are less prone to these instabilities, they also result in greater pressure drops across the injection system, thereby reducing performance [[75]]. Thus, studying the shock/area change interaction is necessary to determine the ideal injector geometry to balance these competing effects.

Although the acoustic case has been extensively characterized in literature [[63], [76]], the shocked case has received significantly less treatment. Studies by Rudinger [[77]] and Oppenheim [[78]] theoretically analyzed wave transmission and reflection resulting from the shock / area change interaction; these works were later expanded upon by Salas [[79]]. For this work, we utilized Rudinger's method for calculating quasi one-dimensional approximations to the flow. These studies apply conservation principles to the flows up and downstream of the multi-dimensional adjustment zone in the immediate vicinity of the area change. The key flow features in this interaction are shown in Figure 12.

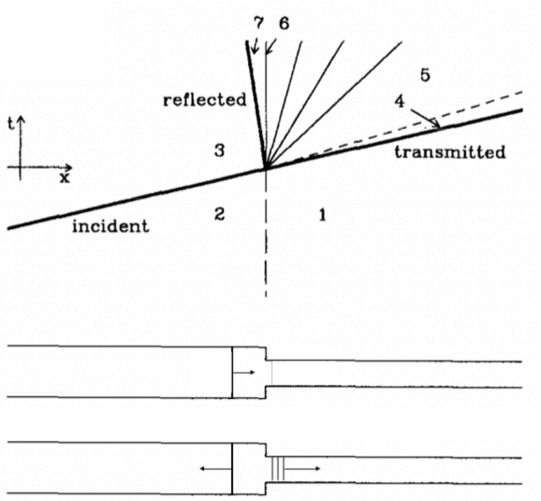

Figure 12 - Diagram of the key flow features resulting from a shock interaction with a discrete area change: an incident shock and a transmitted and/or reflected finite wave (either a shock or an expansion fan, depending on the shock strength and geometry).

While useful, these methods neglect the multidimensional "near-field" phenomena occurring near the area change. The nature of such phenomena, and the impact they have on estimates of reflected and transmitted wave strength, are not understood. There is some evidence that the

DISTRIBUTION A: Distribution approved for public release.

impact of such phenomena on the far-field is minimal [[80], [81]]. However, these works do not answer the question of how general results are and, even if they are generally true, *why* the discrepancies are small. To address this gap, we investigated the types of multi-dimensional, unsteady phenomena resulting from the shock / area change interaction and their impacts on the behavior of the reflected and transmitted waves. Toward this end, we studied the reflection and transmission of shocks of various strengths through channels with various area changes using both computational fluid dynamics (CFD), which can account for 2D transient effects, and quasi 1D methods, which do not.

Useful quantities to compare between the two models are the transmission and reflection coefficients, respectively defined as follows:

$$T = \frac{p_t - p_0}{p_i - p_0}$$

$$R = \frac{p_r - p_i}{p_i - p_0}$$

Here, p_i, p_t, p_r, and p_0 are the post shock [static] pressure, post transmitted wave pressure, post reflected wave pressure, and initial pressure of the quiescent gas in the tube. These are shown below for a variety of [left to right] area ratios and incident shock Mach numbers M_i:

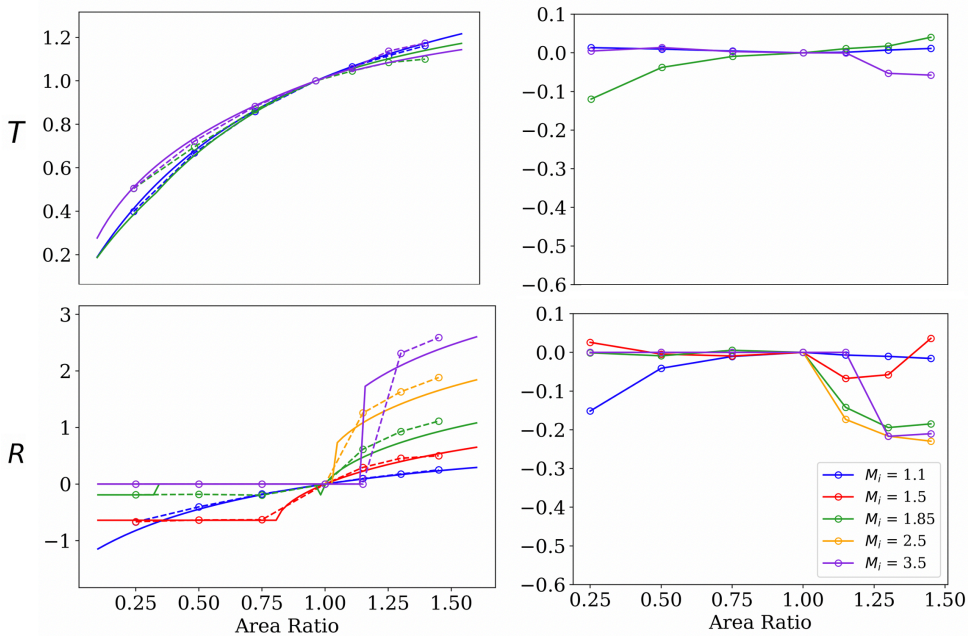

Figure 13 - Reflection and transmission coefficients over the range of cases studied. Left column: values calculated using quasi one-dimensional (solid line) and CFD (circles). Right column: difference in quasi one-dimensional value and CFD calculated.

Interestingly, the transmission coefficient is much less sensitive to the incident shock strength than the reflection coefficient. As expected, T is less than 1 for area divergences (area ratio < 1) and greater than 1 for area convergences. The reflection coefficient varies strongly with both area ratio

and shock strength. For a large enough area ratio (i.e. a sudden enough contraction), the reflection coefficient increases in a nearly linear manner with shock strength; this represents a limiting behavior for the reflection coefficient.

As might be expected, discrepancies between the two results grow as the area ratio deviates from unity in either direction (noting that the exact solution is one dimensional when the area ratio is unity). Overall, however, the quasi 1D calculations predict reasonably accurate values of R and T. This overall good agreement suggests that, while 2D disturbances have pronounced effects on the flow field close to the area jump, their lasting effects on the transmitted and reflected waves are minor. This result is not only fundamentally interesting but also consequential for reduced order models of the phenomenon, as it shows that quasi one-dimensional considerations can be used to accurately understand and quantify the effect of the area change on the reflected and transmitted shock waves.

The quasi-1D theory provides *implicit* expressions for quantities of interest that must be solved numerically. To provide more insightful, explicit expressions for these quantities and possibly provide boundary conditions for larger scale calculations, we used perturbation approaches for the weak shock ($M_i \approx 1$) limit. These are as follows:

$$T = \frac{2\alpha}{\alpha+1} + \frac{2\alpha(\alpha-1)(\gamma-3)}{(\gamma+1)(\alpha+1)^2}(M_i-1) + O(M_i-1)^2$$

$$R = \frac{\alpha-1}{\alpha+1} + \frac{2(\alpha-1)(\alpha\gamma+\alpha+4)}{(\gamma+1)(\alpha+1)^2}(M_i-1) + O(M_i-1)^2$$

Here, α represents the area ratio and γ the specific heat ratio. Clearly, these limit to their classical acoustic expressions (see [[82]]). Furthermore, they show that, for finite-amplitude waves, the strength of the transmitted and reflected waves depend on not only the area ratio but also the shock strength and the gas properties. Near-field effects can be incorporated into these expressions. For example, when a weak shock interacts with a diverging duct, the resulting flow separates with an associated entropy jump. An expression for this jump, developed by Isaacson, is as follows:

$$\Delta s = \frac{1}{2} C_v[(1-\alpha)^2 + (1-\alpha)^6]\gamma(\gamma-1)M^2$$

Here, M is the Mach number of the flow entering the area change. This jump, when incorporated into the quasi-1D expressions, yields analytic expressions for R and T like those provided above.

A natural extension of this work is to consider the more general case of an initial mean flow in the duct, as when a shock is transmitted into a reactant injector during device operation. We also wish to extend this work to other geometries encountered within an RDE: these include bifurcating ducts (as when a detonation passes over an injector element) and bends (as in the case of unlike impinging injectors commonly used in rocket engines). Preliminary investigation into these cases suggests that, for the quasi-1D theory, additional physics will need to be incorporated to close the problem: these can be discovered through 2D CFD analysis like what was performed for this work. Further, considering the predictive accuracy of the quasi-1D theory, future work could employ this theory to develop simplified boundary conditions for the injection system for use in reduced-order models.

DISTRIBUTION A: Distribution approved for public release.

Dynamics of Swirl Jets

Shifting gears now toward turbulent combustion under autoignition conditions, we considered the nonlinear dynamics of fully developed laminar annular jets with respect to the centrebody diameter Reynolds number and swirl ratio. Similar flows appear in numerous applications and feature a vibrant range of topological and dynamical characteristics associated with phenomena including shear layer separation and vortex breakdown. We began by investigating the non-monotonic evolution of the axisymmetric jet's steady topology under varying swirl ratio. In accord with earlier reports, the jet progresses through a sequence of wake, breakdown, and wall jet regimes in a qualitatively similar manner across a wide span of centrebody diameters and Reynolds numbers. In the wake regime, the nonswirling jet bifurcates to a plane-symmetric, but not axisymmetric, steady flow pattern beyond a diameter-dependent critical Reynolds number value. With further increase in Reynolds number, the steady nonswirling jet subsequently destabilises via multiple distinct Hopf bifurcations. Introducing positive swirl to the jet also induces unsteadiness by twisting the singly-azimuthally periodic, asymmetric wake structure and causing it to precess periodically in time about the central axis. Intermediate swirl stabilises these unsteady dynamics and restores the jet's axisymmetry. This stabilising effect is then reversed in the breakdown regime at higher swirl ratio, where a variety of period-1 and period-2 instabilities bifurcate from the steady flow as swirl ratio is increased. Several instances of hysteresis and subcritical behaviour are reported and discussed, including one that manifests precessing vortex core (PVC) oscillations.

This work is further detailed in a Journal of Fluid Mechanics paper noted in the list of publications.

Blowoff of Bluff Body Stabilized Flames

Another problem we wished to investigate was that of blowoff in bluff body stabilized flames. Flames at high density ratios blow off in at least two distinct stages: stage 1, where intermittent extinction occurs along the flame front, but the flame and flow remain qualitatively similar to stable conditions, and stage 2, where there is permanent downstream flame extinction and large-scale changes in dynamic flow characteristics. This this work focuses on stage 2 processes, with the goal of understanding what ultimately leads to irrecoverable flame blowoff. A test facility was developed with the flexibility to achieve two goals: (1) approach LBO by keeping the parameters that influence its hydrodynamic stability approximately constant, particularly flow velocity and gas expansion ratio (σ), and (2) compare near-LBO dynamics under conditions where, well away from blowoff, the flame is globally stable (high σ case) and globally unstable (low σ case, where the Bénard-Von Karman, BVK, instability of the flow is present). The latter case was of particular interest as most prior detailed diagnostic studies of LBO have been performed at high σ, BVK-

DISTRIBUTION A: Distribution approved for public release.

suppressed conditions. We found that the transient blowoff process remained largely unchanged in the high and low σ cases, apparently due to the fact that the BVK instability reappears in either case under conditions very close to LBO. In all cases, blowoff was preceded by permanent downstream extinction that moves progressively closer to the bluff body as LBO is approached. We also found that near-LBO dynamics are intrinsically three dimensional, due to both secondary instabilities of the shear layer and large out-of-plane motions believed to be due to confinement effects associated with bluff body-wall interactions. These three-dimensional structures often manifest themselves as burning reactant fingers which are caught in the backflow of the recirculation zone; under very near LBO conditions they impinge on the back of the bluff body and extinguish as well. At the very edge of blowoff, the recirculation zone is no longer composed of hot products and is unable to autoignite the oncoming reactant flow, leading to global extinction. The characteristic time associated with this feedback between downstream extinction and wake structure alteration that leads to blowoff is about two orders of magnitude larger than the characteristic flow time.

This work is further detailed in a Combustion and Flame paper noted in the list of publications.

Finite Thickness Effects on Turbulent Flame Speeds

We also considered turbulent flame dynamics in subsonic flows. As part of this work, we continue to analyze several fundamental issues around causality in turbulent flame physics- namely "why does the turbulent burning velocity increase with increases in turbulence intensity?". This seemingly obvious question is actually not obvious and has several important subtleties - naming whether the surface area/surface density increases are the *cause or the effect* of the increased turbulent burning velocity. As part of this, we continue to look at KPP wave solutions and their features. The chapter analyzes the effect of finite flame thickness and Arrhenius kinetics on wave solutions to reaction diffusion equations used to approximate turbulent flame speeds. KPP (Kolmogorov-Petrovsky-Piskunov) solutions of the averaged reaction-diffusion equation are commonly used in turbulent combustion to scale turbulent burning velocities. Subject to certain conditions on reaction rate profile through the flame brush and turbulent diffusivity, this theory relates the turbulent burning velocity to the derivative of the reaction rate ($\widetilde{\omega}$) at the leading edge of the flame brush ($d\widetilde{\omega}/d\tilde{c}|_{\tilde{c}=0}$). Such waves are often referred to as "pulled fronts". However, turbulent flames never actually satisfy the KPP conditions for a pulled front, as the turbulent flame brush, parameterized here by the thickness δ_t, consists of an ensemble of laminar flamelets of thickness δ, where $\epsilon = \delta/\delta_t \ll 1$ is very small, but nonzero, and $d\widetilde{\omega}/d\tilde{c}$ tends to zero at the brush leading edge for high activation energy, combustion-type kinetics. This chapter analyzes these effects on KPP wave solutions, parameterized by $\epsilon = \delta/\delta_t$ and Zeldovich number, Ze, focusing on whether turbulent flames retain their "pulled front" character and what the correction to the KPP wave speed is. Variational solutions of the reaction-diffusion equation show that the solution, can be expanded

in power of $1/|\ln \epsilon|$. Both numerical and asymptotic results are presented, showing that the wave still exhibits "pulled front" solutions but with significant corrections to the KPP result. The leading order correction is of the form $|\ln \epsilon|^{-2}$ and independent of Ze. Higher order corrections are function of both ϵ and Ze. However, the dominant factor influencing the wave speed correction is due to the finite ϵ, with Ze exhibiting a weaker effect.

This work is further detailed in a Physical Review E paper noted in the list of publications.

Permuted Proper Orthogonal Decomposition for Analysis of Advecting Structures

Finally, we analyzed coherent structures in high-Reynolds number flows using permuted proper orthogonal decomposition (PPOD). Flow data are often decomposed using proper orthogonal decomposition (POD) of the space-time separated form, which targets spatially correlated flow structures in an optimal manner. PPOD, on the other hand, decomposes data according to a separation of variables that naturally captures advecting structures. This chapter presents mathematical features of PPOD, followed by analysis of three experimental data sets from high Reynolds number, turbulent shear flows: a wake, a swirling annular jet, and a jet in cross flow (JICF). In the wake and swirling jet cases, the leading PPOD and space-only POD modes focus on similar features but differ in convergence rates and fidelity in capturing spatial and temporal information. In contrast, the leading PPOD and space-only POD modes for the JICF capture completely different features – advecting shear layer structures and flapping of the jet column, respectively. This example demonstrates how the different inner product spaces, which order the PPOD and space-only POD modes according to different measures of variance, provide unique "lenses" into features of advection-dominated flows, allowing complimentary insights.

This work is further detailed in a Journal of Fluid Mechanics paper noted in the list of publications.

References

[1] J. Shaw, J. Kildare, M. Evans, A. Chinnici, C. Sparks, S. Rubaiyat, R. Chin, and P. Medwell, *A Theoretical Review of Rotating Detonation Engines*. *Detonation – New Era for Engines*. IntechOpen, 2019. pp. 1-24.

[2] Sirignano, W.A., *A theoretical study of nonlinear combustion instability: longitudinal mode* 1964: PhD thesis.

[3] Moore , F.K. and Maslen, S.H., *Transverse oscillations in a cylindrical combustion chamber*. 1954, Technical Report NACA TN 3152.

DISTRIBUTION A: Distribution approved for public release.

[4] Krebs, W., Bethke, S., Lepers, J., Flohr, P., Prade, B., Johnson, C., and Sattinger, S., *Thermoacoustic design tools and passive control: Siemens power generation approaches*. 2005, Combustion Instabilities in Gas Turbine Engines Operational Experience, Fundamental Mechanisms and Modeling.

[5] Paschereit, C.O., Schuermans, B., Bellucci, V., and Flohr, P., *Implementation of instability prediction in design: Alstom approaches.* Combustion Instabilities in Gas Turbine Engines: Operational Experience, Fundamental Mechanisms and Modeling, 2005: p. 445-480.

[6] O'Connor, J., Acharya, V., and Lieuwen, T., *Transverse combustion instabilities: Acoustic, fluid mechanic and flame processes.* Progress in Energy and Combustion Science, 2015. **49**: p. 1-39.

[7] Bennewitz, J.W., Bigler, B.R., Pilgram, J.J., and Hargus, J., William A, *Modal transitions in rotating detonation rocket engines.* International Journal of Energetic Materials and Chemical Propulsion, 2019. **18**(2): p. 91-109.

[8] Lu, F.K. and Braun, E.M., *Rotating detonation wave propulsion: experimental challenges, modeling and engine concepts.* Journal of Popuslion and Power, 2014. **30**(5): p. 1125-1142.

[9] Wolanski, P. *Rotating Detonation Wave Stability*. in *Proc. of 23rd International Colloquium For Dynamics of Explosions and Reactive Systems*. 2011. Irvine, USA.

[10] Bennewitz, J.W., Bigler, B.R., Hargus, W.A., Danczyk, S.A., and Smith, R.D. *Characterization of Detonation Wave Propagation in a Rotating Detonation Rocket Engine using Direct High-Speed Imaging*. in *Joint Propulsion Conference*. 2018. Cincinnati, Ohio.

[11] Lin, W., Zhou, J., Liu, S., Lin, Z., and Zhuang, F., *Experimental study on propagation mode of H2 /Air continuously rotating detonation wave.* Int J Hydrogen Energy, 2015. **40**: p. 1980-1993.

[12] Bykovskii, F., Zhdan, S., and Vedernikov, E., *Continuous spin detonations.* Journal of Propulsion Power, 2006. **22**: p. 1204-16.

[13] Duvall, J., Chacon, F., Harvey, C., and Gamba, M. *Study of the effects of various injection geometries on the operation of a rotating detonation engine*. in *AIAA Aerospace Sciences Meeting*. 2018. Kissimmee, Florida.

[14] Lighthill, M.J., *Waves in Fluids*. 2001, New York: Cambridge University Press.

[15] Blimbaum, J., Zanchetta, M., Akin, T., Acharya, V., O'Connor, J., Noble, D., and Lieuwen, T., *Transverse to longitudinal acoustic coupling processes in annular*

DISTRIBUTION A: Distribution approved for public release.

combustion chambers. International Journal of Spray and Combustion Dynamics, 2012. **4**(4): p. 275-297.

[16] Sankaran, R., Im, H.G., Hawkes, E.R., and Chen, J.H., *The effects of non-uniform temperature distribution on the ignition of a lean homogeneous hydrogen–air mixture.* Proceedings of the Combustion Institute, 2005. **30**(1): p. 875-882.

[17] Mansfield, A.B. and Wooldridge, M.S., *High-pressure low-temperature ignition behavior of syngas mixtures.* Combustion and Flame, 2014. **161**(9): p. 2242-2251.

[18] Habisreuther, P., Galeazzo, F.C.C., Prathap, C., and Zarzalis, N., *Structure of laminar premixed flames of methane near the auto-ignition limit.* Combustion and Flame, 2013. **160**(12): p. 2770-2782.

[19] Longwell, J., *Flame stabilization by bluff bodies and turbulent flames in ducts.* Proceedings of the Combustion Institute, 1952. **4**(1): p. 90-97.

[20] Longwell, J.P., Frost, E.E., and Weiss, M.A., *Flame stability in bluff body recirculation zones.* Industrial & Engineering Chemistry, 1953. **45**(8): p. 1629-1633.

[21] Driscoll, J., *Turbulent premixed combustion: Flamelet structure and its effect on turbulent burning velocities.* Progress in Energy and Combustion Science, 2008. **34**(1): p. 91-134.

[22] Won, S.H., Windom, B., Jiang, B., and Ju, Y., *The role of low temperature fuel chemistry on turbulent flame propagation.* Combustion and Flame, 2014. **161**(2): p. 475-483.

[23] Bansal, G. and Im, H., *Autoignition and front propagation in low temperature combustion engine environments.* Combustion and Flame, 2011. **158**(11): p. 2105-2112.

[24] Gupta, S., Im, H., and Valorani, M., *Classification of ignition regimes in HCCI combustion using computational singular perturbation.* Proceedings of the Combustion Institute, 2011. **33**(2): p. 2991-2999.

[25] Chen, J.H., Hawkes, E.R., Sankaran, R., Mason, S.D., and Im, H.G., *Direct numerical simulation of ignition front propagation in a constant volume with temperature inhomogeneities: I. Fundamental analysis and diagnostics.* Combustion and flame, 2006. **145**(1): p. 128-144.

[26] Hawkes, E.R., Sankaran, R., Pébay, P.P., and Chen, J.H., *Direct numerical simulation of ignition front propagation in a constant volume with temperature inhomogeneities: II. Parametric study.* Combustion and Flame, 2006. **145**(1): p. 145-159.

DISTRIBUTION A: Distribution approved for public release.

[27] Zhang, H., Hawkes, E.R., Chen, J.H., and Kook, S., *A numerical study of the autoignition of dimethyl ether with temperature inhomogeneities.* Proceedings of the Combustion Institute, 2013. **34**(1): p. 803-812.

[28] Yoo, C.S., Lu, T., Chen, J.H., and Law, C.K., *Direct numerical simulations of ignition of a lean n-heptane/air mixture with temperature inhomogeneities at constant volume: Parametric study.* Combustion and Flame, 2011. **158**(9): p. 1727-1741.

[29] Cook, D.J., Pitsch, H., Chen, J.H., and Hawkes, E.R., *Flamelet-based modeling of auto-ignition with thermal inhomogeneities for application to HCCI engines.* Proceedings of the Combustion Institute, 2007. **31**(2): p. 2903-2911.

[30] Lipatnikov, A. and Chomiak, J., *Molecular transport effects on turbulent flame propagation and structure.* Progress in Energy and Combustion Science, 2005. **31**(1): p. 1-73.

[31] Nakahara, M. and Kido, H., *Study on the Turbulent Burning Velocity of Hydrogen Mixtures Including Hydrocarbon.* AIAA journal, 2008. **46**(7): p. 1569-1575.

[32] Kido, H., Nakahara, M., Nakashima, K., and Hashimoto, J., *Influence of local flame displacement velocity on turbulent burning velocity.* Proceedings of the Combustion Institute, 2002. **29**(2): p. 1855-1861.

[33] Cheng, R., Littlejohn, D., Strakey, P., and Sidwell, T., *Laboratory investigations of a low-swirl injector with H2 and CH4 at gas turbine conditions.* Proceedings of the Combustion Institute, 2009. **32**(2): p. 3001-3009.

[34] Littlejohn, D. and Cheng, R., *Fuel effects on a low-swirl injector for lean premixed gas turbines.* Proceedings of the Combustion Institute, 2007. **31**(2): p. 3155-3162.

[35] Fairweather, M., Ormsby, M., Sheppard, C., and Woolley, R., *Turbulent burning rates of methane and methane–hydrogen mixtures.* Combustion and Flame, 2009. **156**(4): p. 780-790.

[36] Daniele, S., Jansohn, P., Mantzaras, J., and Boulouchos, K., *Turbulent flame speed for syngas at gas turbine relevant conditions.* Proceedings of the Combustion Institute, 2011. **33**(2): p. 2937-2944.

[37] Kitagawa, T., Nakahara, T., Maruyama, K., Kado, K., Hayakawa, A., and Kobayashi, S., *Turbulent burning velocity of hydrogen–air premixed propagating flames at elevated pressures.* International Journal of Hydrogen Energy, 2008. **33**(20): p. 5842-5849.

[38] Cabra, R., Chen, J., Dibble, R., Karpetis, A., and Barlow, R., *Lifted methane–air jet flames in a vitiated coflow.* Combustion and Flame, 2005. **143**(4): p. 491-506.

DISTRIBUTION A: Distribution approved for public release.

[39] Cabra, R., Myhrvold, T., Chen, J., Dibble, R., Karpetis, A., and Barlow, R., *Simultaneous laser Raman-Rayleigh-LIF measurements and numerical modeling results of a lifted turbulent H2/N2 jet flame in a vitiated coflow.* Proceedings of the Combustion Institute, 2002. **29**(2): p. 1881-1888.

[40] Gordon, R.L., Masri, A.R., and Mastorakos, E., *Simultaneous Rayleigh temperature, OH- and CH2O-LIF imaging of methane jets in a vitiated coflow.* Combustion and Flame, 2008. **155**(1-2): p. 181-195.

[41] Gordon, R.L., Masri, A.R., Pope, S.B., and Goldin, G.M., *A numerical study of auto-ignition in turbulent lifted flames issuing into a vitiated co-flow.* Combustion Theory and Modelling, 2007. **11**(3): p. 351-376.

[42] Mastorakos, E., *Ignition of turbulent non-premixed flames.* Progress in Energy and Combustion Science, 2009. **35**(1): p. 57-97.

[43] Wu, Z., Masri, A.R., and Bilger, R.W., *An Experimental Investigation of the Turbulence Structure of a Lifted H2/N2 Jet Flame in a Vitiated Co-Flow.* Flow, Turbulence and Combustion, 2006. **76**(1): p. 61-81.

[44] Yoo, C.S., Sankaran, R., and Chen, J.H., *Three-dimensional direct numerical simulation of a turbulent lifted hydrogen jet flame in heated coflow: flame stabilization and structure.* Journal of Fluid Mechanics, 2009. **640**: p. 453.

[45] Duwig, C. and Dunn, M.J., *Large Eddy Simulation of a premixed jet flame stabilized by a vitiated co-flow: Evaluation of auto-ignition tabulated chemistry.* Combustion and Flame, 2013. **160**(12): p. 2879-2895.

[46] Zhang, F., Yu, R., and Bai, X.S., *Direct numerical simulation of PRF70/air partially premixed combustion under IC engine conditions.* Proceedings of the Combustion Institute, (0).

[47] Bandaru, R.V. and Turns, S.R., *Turbulent jet flames in a crossflow: effects of some jet, crossflow, and pilot-flame parameters on emissions.* Combustion and Flame, 2000. **121**(1-2): p. 137-151.

[48] Huang, R.F. and Yang, M.J., *Thermal and concentration fields of burner-attached jet flames in cross flow.* Combustion and Flame, 1996. **105**(1-2): p. 211-224.

[49] Tsue, M., Kadota, T., and Kono, M., *Detailed measurements of the structure of a jet diffusion flame in a cross flow.* Proceedings of the Combustion Institute, 2000. **28**(1): p. 295-301.

DISTRIBUTION A: Distribution approved for public release.

[50] Han, D. and Mungal, M.G., *Simultaneous measurements of velocity and CH distribution. Part II: deflected jet flames.* Combustion and Flame, 2003. **133**(1-2): p. 1-17.

[51] Grout, R.W., Gruber, A., Yoo, C.S., and Chen, J.H., *Direct numerical simulation of flame stabilization downstream of a transverse fuel jet in cross-flow.* Proceedings of the Combustion Institute, 2011. **33**(1): p. 1629-1637.

[52] Micka, D.J. and Driscoll, J.F., *Stratified jet flames in a heated (1364K) air cross-flow with autoignition.* Combustion and Flame, 2011.

[53] Mancini, M., Schwöppe, P., Weber, R., and Orsino, S., *On mathematical modelling of flameless combustion.* Combustion and flame, 2007. **150**(1): p. 54-59.

[54] Weber, R. and Smart, J.P., *On the (MILD) combustion of gaseous, liquid, and solid fuels in high temperature preheated air.* Proceedings of the Combustion Institute, 2005. **30**(2): p. 2623-2629.

[55] Tsuji, H., Gupta, A.K., Hasegawa, T., Katsuki, M., Kishimoto, K., and Morita, M., *High temperature air combustion: from energy conservation to pollution reduction*. 2002: CRC press.

[56] Gopalakrishnan, P., Bobba, M., and Seitzman, J., *Controlling mechanisms for low NOx emissions in a non-premixed stagnation point reverse flow combustor.* Proceedings of the combustion institute, 2007. **31**(2): p. 3401-3408.

[57] Choi, G.-M. and Katsuki, M., *Advanced low NOx combustion using highly preheated air.* Energy Conversion and Management, 2001. **42**(5): p. 639-652

[58] *Proceedings of the 5th model validation for propulsion (MVP 5) workshop*. AIAA SciTech Forum, 2021.

[59] H. Wang, *A physics-based approach to modeling real-fuel combustion chemistry - I. Evidence from experiments, and thermodynamic, chemical kinetic and statistical considerations*. Combustion and Flame, 2018. **193**, p. 502-519.

[60] D. Schwer and K. Kailasanath, *Numerical investigation of the physics of rotating-detonation-engines.* 50th AIAA Aerospace Sciences Meeting, 2012.

[61] M. Hishida, T. Fujiwara, and P. Wolanski, *Fundamentals of rotating detonations*. Shock Waves, 2009. **19**, p. 1-10.

[62] B. R. Bigler, J. R. Burr, J. W. Bennewitz, S. A. Danczyk, and W. A. Hargus, *Global performance effects of mode transitions in a rotating detonation rocket engine*. AIAA Propulsion and Energy Forum, 2020.

[63] T. C. Lieuwen, *Unsteady Combustor Physics*. 2012, New York: Cambridge University Press.

[64] M. Brear, F. Nicoud, M. Talei, A. Giauque, and E. Hawkes, *Disturbance energy transport and sound production in gaseous combustion*. Journal of Fluid Mechanics, 2012. **707**, p. 53-73.

[65] H. Rajagopalan, S. S. Dammati, V. Acharya, A. Y. Poludnenko, and T. Lieuwen, "Disturbance energy budget in gaseous detonations," in *2022 Spring Technical Meeting*, 2022.

[66] M. Ullma and V. Raman, *Impacts of Injection Scheme and Grid Resolution in Two-dimensinoal Rotating Detonation Engine Simulations*. AIAA SciTech Forum, 2024.

[67] A. Batista, B. R. Bigler, M. C. Ross, C. Lietz, and W. A. Hargus, *Detonation Wave Collision Study During Rotating Detonation Rocket Engine Counter-Propagating Modes*. AIAA Propulsion and Energy Forum, 2021.

[68] V. Raman, S. Prakash, and M. Gamba, *Nonidealities in Rotating Detonation Engines*. Annual Review of Fluid Mechanics, 2023. **55**, p. 639-74.

[69] R. M. Clayton, *Experimental Measurements on Rotating Detonation-Like Combustion*. JPL Technical Report, 1965. p. 32-788.

[70] M. Zhao and H. Zhang, *Origin and chaotic propagation of multiple rotating detonation waves in hydrogen/air mixtures*. Fuel, 2020. **275**.

[71] V. Anand and E. Gutmark, *Rotating detonation combustors and their similarities to rocket instabilities*. Progress in Energy and Combustion Science, 2019. **73**, p. 182-234.

[72] W. A. Sirignano, *Driving Mechanisms for Combustion Instability*. Combustion Science and Technology, 2015. **187**, p. 162-205.

[73] D. A. Schwer and K. Kailasanath, *Feedback into Mixture Plenums in Rotating Detonation Engines*. 50th AIAA Aerospace Sciences Meeting, 2011.

[74] V. Anand, A. St. George, and E. Gutmark, *Amplitude modulated instability in reactants plenum of a rotation detonation combustor*. "International Journal of Hydrogen Energy," 2017. **42**, p. 12,629-624.

[75] K. Kailasanath, *Recent Developments in the Research on Pressure-Gain Combustion Devices.* Innovations in Sustainable Energy and Cleaner Environment, 2020. p. 3-21.

[76] F. Fahy, *Foundations of Engineering Acoustics*. 2000. Academic Press.

DISTRIBUTION A: Distribution approved for public release.

[77] G. Rudinger, *Passage of shock waves through ducts of variable cross section*. Physics of Fluids, 1960. **3**, p. 449-455.

[78] A. K. Oppenheim, P. A. Urtiew, and R. A. Stern, *Peculiarity of shock impingement on area convergence*. Physics of Fluids, 1959. **2**, p. 427-431

[79] M. D. Salas, *Shock Wave Interaction with an Abrupt Area Change*. NASA Technical Paper 3113, 1991.

[80] R. Menina, R. Saurel, R. Zereao, and L. Houas, *Modelling gas dynamics in 1D ducts with abrupt area change*. Shock Waves, 2011. **21**, p. 451-466.

[81] G. V. Shoev, Y. A. Bondar, D. V. Khotyanovsky, A. N. Kudryavstev, K. Maruta, and M. Ivanov, *Numerical study of shock wave entry and propagation in a microchannel*. Thermophysics, 2012. **19.1**, p. 17-32.

[82] L. E. Kinsler, A. R. Frey, A. B. Coppens, and J. V. Sanders, *Fundamentals of Acoustics, vol. IV*. 200, John Wiley & Sons, Inc.

Impacts

Many of the impacts of this project were discussed in the previous sections. In this section, we'll summarize and elaborate them more succinctly.

Firstly, this work provides insight into the behavior of the injection system in RDEs. Considering how critical this system is to overall device behavior, such insights are highly valuable. For one, the large-scale computations for this work clarified multiple phenomena associated with the injection system: these include a two-stage flow recovery process associated with expansion waves emitted by the injectors, uneven recovery between the fuel and oxidizer injectors, and reactant stratification owing to incomplete radial mixing. The cost of such computations can be greatly reduced by using a "sub-model" for the injection system instead of modeling it explicitly. Incorporating the aforementioned phenomena into such models can improve their accuracy, leading to a cost-efficient tool for studying RDEs. All these phenomena can either support or degrade RDE performance. Therefore, this work presents a useful first step to promoting beneficial physics in RDEs and avoiding adverse physics.

Our analysis of acoustic wave modes arising from periodically spaced injectors clarified another important effect of the injection system in RDEs: "wake shedding," or wave reflections from individual injectors. We demonstrated that, depending on the number of injectors, the number of waves, and the speed of these waves, the injection system can dictate the dominant direction of these waves. This acoustic analysis is a novel tool toward understanding this phenomenon and will prove useful toward investigating the general case with detonations. Furthermore, since even acoustic waves can grow remarkably strong in the presence of coupled combustion, potentially even giving rise to traveling detonations, injector acoustics may prove important to RDEs.

DISTRIBUTION A: Distribution approved for public release.

Shock waves interact with discrete area changes in countless places within RDEs, particularly the injection system. This interaction is known to substantially impact device behavior. Therefore, our study into this phenomenon clarifies a ubiquitous and impactful phenomenon in RDEs. For the injection system, this sheds light on the proper sizing of injectors. To be specific, our results can help one determine the proper area ratios (both the combustion chamber / injector area ratio and the injector / plena area ratios) and injector lengths (which dictate the travel times of transmitted waves) that achieve desired behavior. The tools developed for our analysis can be used to study shock transmission through other geometries within RDEs, including split and bent ducts. This could lead to physics-based sub-models that help one study RDEs in a more cost-efficient manner.

Secondly, this work sheds light on the dynamics of detonation waves in rotating detonation engines. Our large-scale computations reveal how simulated detonation dynamics depend on the chosen turbulence model. These computations routinely employ the Large Eddy Simulation (LES) turbulence model, as opposed to the cheaper Reynolds-Averaged Navier-Stokes (RANS) model. While the latter can't resolve small-scale turbulent phenomena (whose precise effect on RDEs is still unknown), our analysis demonstrates that it can resolve large-scale, qualitative phenomena in RDEs convincingly. Further, it reveals many of the key qualitative differences in wave dynamics resolved by these models: this can better inform choices by experts when performing similar computations. These computations also demonstrate (empirically, at least) a striking phenomenon observed elsewhere: the possibility of multiple wave modes at a given set of operating conditions. Such a possibility warrants careful consideration by both experimental and computational RDE researchers in setting up their experimental design.

Detonation energetics is a scarcely investigated but hugely important topic in RDEs. Our analysis on this subject, therefore, is both novel and impactful. Understanding the fundamental science behind how detonations store and dissipate energy is paramount to understanding how they can be optimized by proper design. This work represents a valuable first step toward this end. Additionally, our investigation into acoustic wave modes produced by periodically spaced injectors elucidates a connection between the injection system and wave dynamics in RDEs. In this respect, this work contributes to the massive body of literature suggesting that RDE wave dynamics cannot be studied in a vacuum apart.

Work on swirl flow dynamics, bluff body flame blowoff, and orthogonal decompositions of dynamic combustion data has all contributed to improved fundamental understanding of controlling subsonic combustion-acoustic-flame interactions. All of this work has been published in leading journals in the field, including Journal of Fluid Mechanics and Physical Review E.

Finally, this work is valuable from a basic science standpoint. Detonation and shock dynamics remain one of the more elusive problems in fluid mechanics and in physics in general. The investigations performed in this work shed much needed light on these subjects. The interaction of acoustic waves with periodic injectors (or periodic obstacles in general) occurs in other situations besides RDEs: these include general combustors, concert venues, buildings, and countless imaginable scenarios. Therefore, the applications of this work extend well beyond what was considered in this work.

DISTRIBUTION A: Distribution approved for public release.

Changes

None to report.

Technical Updates

The previous sections briefly detailed our accomplishments in several areas. The following section reviews these in greater detail.

DISTRIBUTION A: Distribution approved for public release.

Chapter 1

Turbulent Markstein numbers for Harmonically Forced, Premixed Flames

1.1. Introduction

Turbulent flames in modern combustion devices exist in hydrodynamically unstable flows or in confined environments with acoustic background disturbances. These flames are inherently subjected to the superposition of broadband turbulence and narrowband hydrodynamic or acoustic oscillations [1].

An important property of turbulent flames propagating in turbulent flows is its average burning rate or burning velocity, referred to as the turbulent flame speed. Indeed, an important canonical problem in turbulent combustion is the turbulent flame speed in isotropic, stationary turbulent flows, a quantity that has been discussed extensively in the literature [2].

An important generalization of this problem is propagation of flames with both broadband turbulent fluctuations, and coherent large scale disturbances which can have their own space-time variations. This problem has received less treatment and we summarize these limited studies in the rest of this Introduction. Turbulent premixed flames subjected to harmonic velocity disturbance were analyzed computationally by Hemchandra. et. al [3], showing that harmonic flame wrinkles are dimished by kinematic restoration with the effect increasing with increasing turbulence intensity. Following this, a turbulent flame configuration with harmonically oscillating flame holder was analyzed numerically by Shin et. al. [4] and experimentally by Humphrey et. al. [5]. The ensemble averaged displacement turbulent flame speed, $S_{T,D}$ was defined using the G equation as [5]

$$\langle S_{T,D} \rangle \equiv \frac{\frac{\partial \langle \zeta \rangle}{\partial t} + \langle U_w \rangle \frac{\partial \langle \zeta \rangle}{\partial s} - \langle u_n \rangle}{\left(1 + \left(\frac{\partial \langle \zeta \rangle}{\partial s}\right)^2\right)^{\frac{1}{2}}} \tag{1.1}$$

where $\langle\zeta\rangle$ is the ensemble-averaged flame position, s and n are the coordinates along and normal to the flame for a coordinate system aligned with the time averaged flame position, $\langle U_w\rangle$ denotes the wrinkle convection speed, and $\langle u_n\rangle$ is the reactant conditioned velocity components along the n coordinate. Note that this definition differs from what was originally introduced by Shin and Lieuwen [4], who used $\langle u_s\rangle$, the reactant conditioned velocity along the 's' coordinate, in place of $\langle U_w\rangle$. However, Shin [6] showed that, while $\langle U_w\rangle = \langle u_s\rangle$, in the linear approximation, non-zero correlations between turbulent flow disturbances, ${u_s}'$, and flame wrinkle $\partial\zeta'/\partial s$, causes these two quantities to differ.

All of these results showed a clear negative correlation between the ensemble-averaged turbulent flame speed and ensemble-averaged curvature with the flame speed increasing in regions of negative curvature [4]:

$$\langle S_{T,D}\rangle = \langle S^0_{T,D}\rangle\left(1 - M_{T,D}\langle C\rangle\right) \tag{1.2}$$

where

$$\langle C\rangle = -\frac{\frac{\partial^2\langle\zeta\rangle}{\partial s^2}}{\left(1+\left(\frac{\partial\langle\zeta\rangle}{\partial s}\right)^2\right)^{\frac{3}{2}}} \tag{1.3}$$

The sensitivity of ensemble-averaged flame speed to ensemble-averaged curvature is quantified by the turbulent Markstein number $\left(M_{T,D}\right)$. Note that although it is analogous to the laminar Markstein number of stretch sensitive flames, they are fundamentally different quantities with completely different controlling physics. For example, the laminar Markstein number applies instantaneously, whereas the turbulent Markstein number defined above applies to ensemble averaged behavior. Moreover, it has been determined empirically and not derived from rigorous asymptotics.

A similar observation of the sensitivity of the turbulent flame speed to ensemble averaged curvature has been described for expanding, statistically spherical, premixed turbulent flames [7, 8]. The importance of large scale perturbations in turbulent flames in strongly affecting the flame speed is evident from these studies. In addition, Lipatnikov and Chomiak [7] have also noted some qualitative trends in the variation of Markstein numbers with various fluid and flame dynamics parameters like turbulence intensity, turbulent Reynolds number, etc.

Thus, both data and computations clearly show that the ensemble averaged turbulent flame speed is modulated in flows with coherent wrinkles, such as spherical or harmonically oscillating flames. However, a number of questions remain. First, while the linear model in Eq. 1.2 is a reasonable first order approximation to the data, it does not capture unsteady effects (i.e., it assumes that the time varying $\langle S_{T,D}\rangle$ and $\langle C\rangle$ are in phase, regardless of the disturbance frequency). The calculations by Shin and Lieuwen [4] suggest that there is some phase variation, but this point has not been

DISTRIBUTION A: Distribution approved for public release.

fully explored. Second, measurements also clearly indicate the shortcomings of a linear relationship between $\langle S_{T,D} \rangle$ and $\langle C \rangle$, particularly in regions of positive curvature. Finally, even within the approximations of the linear model, questions remain concerning the sensitivity of $M_{T,D}$ upon other coherent and turbulent flow parameters. Humphrey, et al. [5] had some success in correlating $M_{T,D}$ with a dimensionless ratio of turbulent flame brush thickness and coherent wrinkle wavelength, denoted as $\lambda_{\zeta,t}/\lambda_c$. Specifically, the turbulent Markstein number is shown to be sensitive to the ratio of turbulent length scale $\left(\lambda_{\zeta,t} = \frac{u'R}{u_0}\right)$ and convective length scale $(\lambda_c = u_0/f_0)$ for u'/S_L values higher than 2.5 [5], where u' is the rms axial velocity and S_L is the laminar flame speed. At low values of length scale ratio (0.1 – 0.7), the Markstein number increased monotonically, appearing to saturate at higher values of length scale ratio (> 0.7). However, for lower values of u'/S_L (< 2.5), the Markstein number was independent of length scale ratio. Moreover, Humphrey, et al. [5]'s correlation of $M_{T,D}$ with $\lambda_{\zeta,t}/\lambda_c$ showed significant scatter with several points that could not be reasonably removed as outliers, clearly showing the shortcomings of this correlation. As such, the dependency of $M_{T,D}$ on flow parameters should be regarded as an open question.

This work described in this chapter attempts to address some of the key remaining questions in the above mentioned studies specifically by extending the experimental conditions. In particular, efforts focused on extending the range of the parameter $\lambda_{\zeta,t}/\lambda_c$ and turbulence intenisities. In addition, we took data over a much denser experimental matrix.

The rest of the chapter is organized as follows. First, the experimental facility is described, including the method of harmonic forcing and diagnostics. Next, image and data processing methods used to evaluate ensemble-averaged flame position and velocity fields are detailed. Further, results related to ensemble-averaged flame speed, curvature and turbulent Markstein numbers are presented. Lastly, the conclusions of the present work are presented.

1.2. Experimental methods

1.2.1. Experimental facility

The experimental facility consists of a premixed methane-air turbulent flame attached to a mechanically forced, transversely oscillating flame holder, thus introducing coherent, convecting wrinkles on the flame [5]. It is shown in Figure 1.1. Methane and air at an equivalence ratio of 0.7 and at a nominal temperature of about 273 K are mixed in the mixing plenum consisting of ball bearings after entering the rig from the inlet ports. The mixture further passes through the settling plenum and then through a variable turbulence generation mechanism. The mechanism consists of two metal plates with pie-shaped slots. With the fixed bottom plate and a rotating top plate, the blockage ratio can be varied to generate turbulence intensities ranging from 8% to 38%. This turbulence generator allows for independent variation of mean flow velocity and turbulence intensity [9]. The rotation of the plates is controlled by a stepper motor through a connecting rod.

DISTRIBUTION A: Distribution approved for public release.

A part of the main air is diverted and seeded with 1 micron Titanium dioxide (TiO_2) particles to obtain Mie-scattering images. The seeded air remixes with the reactant mixture before the turbulence generator. A contoured nozzle with an exit jet diameter of 24.1 mm is used further to generate a uniform top-hat velocity profile.

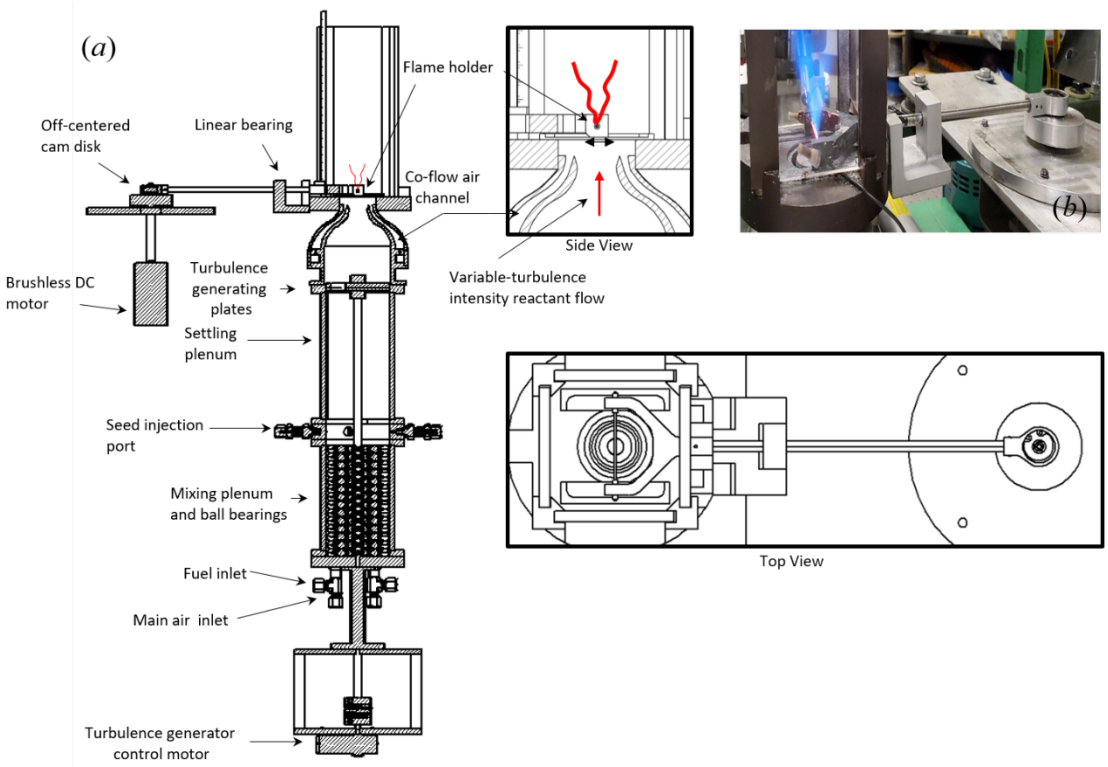

Figure 1.1: a) Schematic of experimental facility and b) Image of V-shaped flame and the direct drive oscillating mechanism

The mixture exits the nozzle into an atmospheric combustion chamber. The circular reactant jet is surrounded by a velocity matched, unseeded, annular co-flow with an outer diameter of 36.3 mm. A heated, 0.81 mm diameter Nichrome wire is used as the flame holder bisecting the circular jet. The wire is friction fitted into ceramic inserts attached to a metal fork. The ceramic ensures electric isolation of the two ends of the wire when electrically heated. The forcing mechanism consists of a brushless DC motor rated for maximum, no-load speed of 60,000 RPM connected to the metal fork through a push rod and an off-centered cam disk. This is a change from our previously reported facility, implemented to enable a constant oscillation amplitude (0.3 mm for the data reported here), independent of the frequency (motor RPM) in contrast to the speaker assembly used previously whose amplitude varied with varying frequency [5]. The motor speed is controlled by a PID feedback controller through LabVIEW.

The flame holder was oscillated at forcing frequencies ranging from 200 Hz to 800 Hz with mean reactant velocities ranging from 3m/s to 8m/s. The turbulence intensities were varied from 20% to

DISTRIBUTION A: Distribution approved for public release.

35% to navigate in the parametric space of u'/S_L and $\lambda_{\zeta,t}/\lambda_c$ as shown in Figure 1.2. Notice that the new experimental regime has been expanded by increasing the convective wavelength range and almost doubling the previous values of u'/S_L.

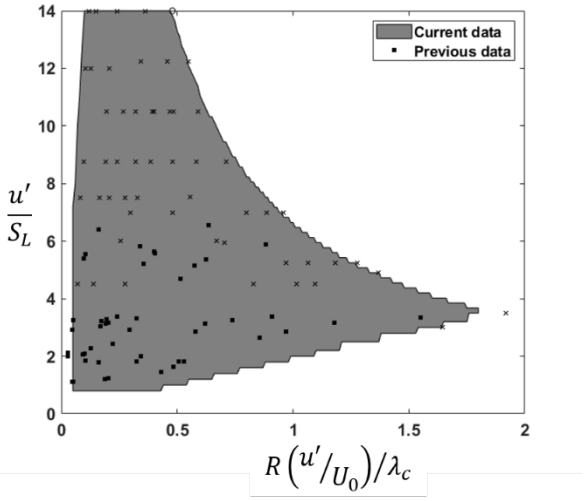

Figure 1.2: Experimental regime in parametric space showing previous data [5] (black dots), extended envelope (shaded region) and data points corresponding to the current data (crosses)

1.2.2. Diagnostics

Instantaneous velocity field was quantified using high speed particle image velocimetry (PIV). The same Mie-scattering images were also used to track flame edges based on the difference in seed density between regions containing reactants and products. Part of the data (low frequency cases (< 400 Hz)) were obtained with single camera whose lens plane is inclined at a low angle (~9^o) with respect to plane of the laser sheet for better optical access, obtaining two dimensional planar velocity field. Note that the inclination introduces a bias in the instantaneous velocity measurements due to the out-of-plane velocity component. However, the bias cancels out when ensemble-averaging since there is no convective component to the out-of-plane velocity. For the high frequency cases, stereo PIV is used to eliminate the above-mentioned bias and, in addition, to obtain all the three velocity components.

527 nm dual head, frequency doubled Nd:YLF laser is used to form a vertical sheet approximately 0.8 mm thick (optical set up shown in Figure 1.3). For low frequency cases, Photron SAZ high speed camera was used with a Tokina f =100 mm f/2.8 lens set to a resolution of 1024 x 1024 pixels whereas for high frequency cases, two Phantom v2640 cameras were used with Tokina f = 100 mm f/2.8 lenses with a resolution of 1024 x 976 pixels. Velocity vectors were obtained using LaVision Davis PIV software. The vector calculation uses an initial pass with a 48 x 48 pixel interrogation window and two subsequent passes of 16 x 16 pixel interrogation window with 50 % overlap. The acquisition rate was set to 10 times the forcing frequency, thus giving 10 samples per forcing cycle.

DISTRIBUTION A: Distribution approved for public release.

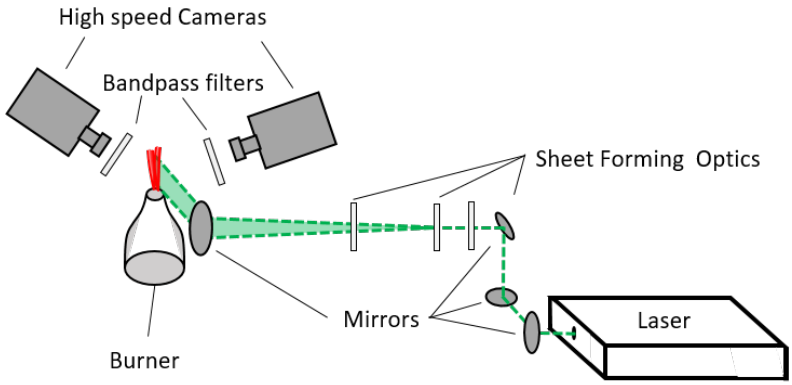

Figure 1.3: Optical diagnostics setup

1.2.3. Image and data processing

LaVision's Davis PIV processing software was used initially to de-warp the raw images, correcting for the distortion from the quartz window and the camera inclination. Further, a sliding minimum operation was performed to remove unwanted reflections/background by subtracting a weighted minimum over a set of images. Stream-wise variation of image intensity was corrected for by normalizing the image intensity using the pixels outside the flame region as reference. The images were smoothed first with a Gaussian filter and further with an edge preserving bilateral filter. Next, the images were cropped to remove regions outside of interest and were binarized using Otsu's method [10] to obtain a time series of instantaneous, binary images as shown in Figure 1.4. Binary images corresponding to the same phase with respect to the forcing cycle are ensemble-averaged to obtain ensemble-averaged progress variable field varying from unity in the reactants to 0 in products. Note that in this case, ensemble-averaging is the same as phase averaging. All quantities are defined at the progress variable value of 0.5 associated with the averaged, binarized image.

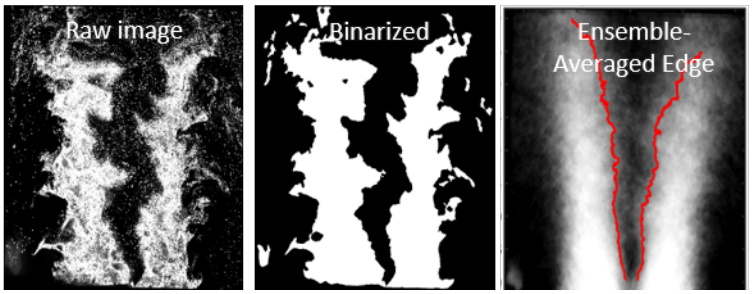

Figure 1.4: Illustration of image processing steps to obtain ensemble-averaged flame edges

Similar to the binary images, instantaneous velocity fields corresponding to the same phase with respect to the forcing frequency are averaged to obtain ensemble-averaged velocity fields. In addition, the fields are reactant conditioned by considering only the velocity vectors corresponding to the reactant region for averaging. Further, a coordinate system is defined based on the time

DISTRIBUTION A: Distribution approved for public release.

averaged flame with the s coordinate corresponding to the direction along the flame and n coordinate corresponding to the direction normal to it, as shown in Figure 1.5. Finally, the ensemble-averaged flame speed and curvature are obtained using Eqs. 1.1 and 1.3.

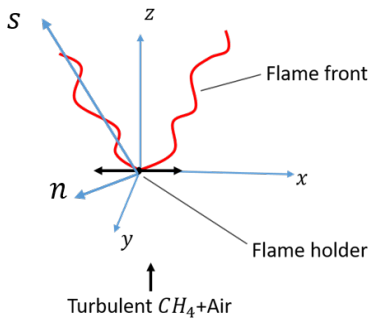

Figure 1.5: Coordinate system defined based on time –averaged flame used in analysis to determine ensemble-averaged flame speed and curvature.

1.3. Results and discussion

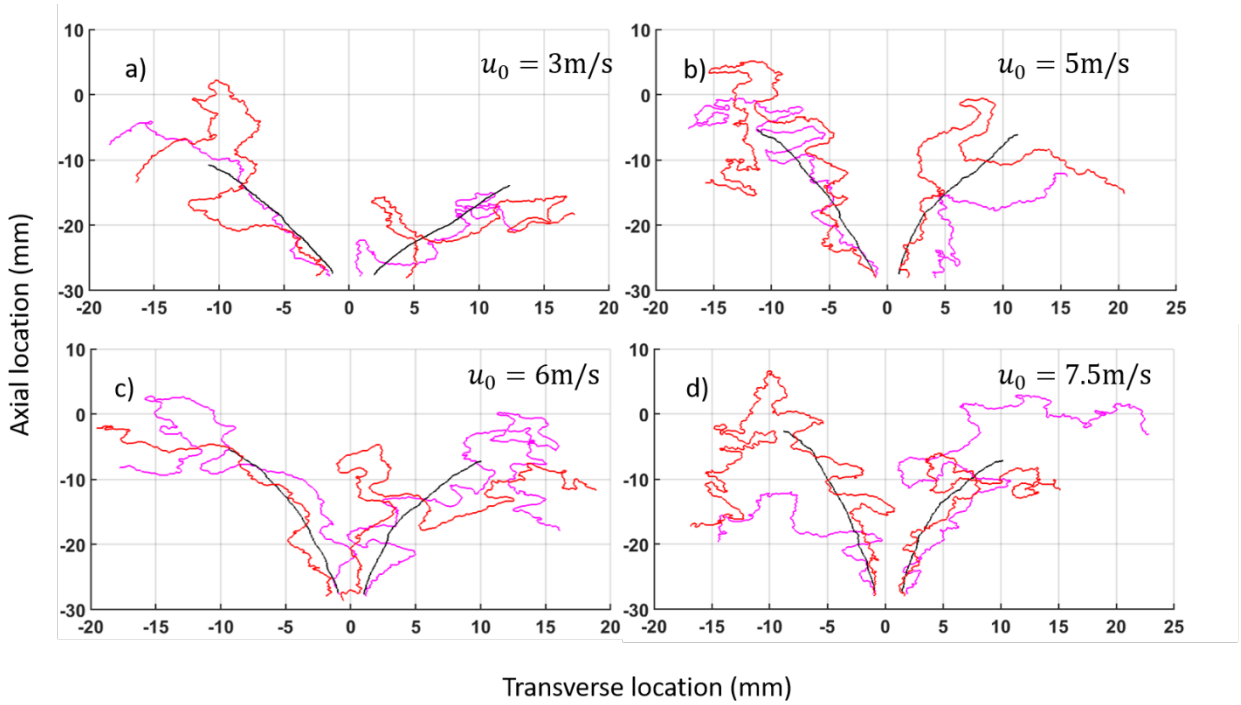

Figure 1.6: Ensemble-averaged edges (black), and two instantaneous edges (red, magenta) for f_0=600 Hz, $u'/u_0 = 37\%, 30\%, 35\%, 35\%$ from a) to d) respectively

Figure 1.6 shows instantaneous flame edges (red, magenta lines) overlaid on the ensemble-averaged edge (black line) for turbulent, premixed flame with the flame holder forced harmonically at a forcing frequency of 600 Hz and increasing mean axial velocity. Note that a) – d) also represents turbulent flames forced with increasing convective wave length defined as $\lambda_c =$

DISTRIBUTION A: Distribution approved for public release.

u_0/f_0. Notice that the high turbulence intensity smoothes the coherent flame wrinkles which otherwise would be apparent for low turbulence intensities due to enhanced effect of kinematic restoration at high turbulence intensities[5]. Also note that with the increasing mean axial velocity the average flame angle with respect to the horizontal increases with the flame bending away from the reactants [11].

1.2.4. Ensemble-averaged flame speed trends

Figure 1.7 plots the ensemble-averaged edges (black lines) overlaid on instantaneous edges (red and magenta lines) for $f_0 = 400\,Hz$, nominal velocity of ~5 m/s with increasing turbulence intensity from a) to b). Notice that the ensemble-averaged edge is smoothed out with increasing turbulence due to increased effect of kinematic restoration [5].

Figure 1.8 plots the correlation between ensemble-averaged flame speed and curvature for the same two cases as in Figure 1.7 with different turbulence intensities. The plot is obtained by binning the data according to curvature values and averaging the data corresponding to a particular bin to reduce the bias introduced by the large number of data points corresponding to the positively curved regions of the flame [5]. Notice that the correlation is negative for negative values of curvature with increased flame speed in the highly negatively curved regions of the flame. For positive values of curvature however, there exists a secondary weaker correlation even tending towards positive correlation, especially at higher turbulence intensity (Figure 1.8 b)). In addition, note the large asymmetry in the range of positive and negative curvature values for the lower turbulence intensity case. This is due to the presence of cusps with high negative curvature values in the ensemble averaged flame position at the lower turbulence intensity conditions, due to kinematic restoration [4] as explained previously (see Figure 1.7) . This asymmetry decreases with increasing turbulence intensity as seen from the variation of ratio of range of negative to positive ensemble-averaged curvature with the turbulence intensity plotted in Figure 1.9. Note that this ratio tends toward a value of unity at high turbulence intensities, which implies a symmetric range of positive and negative curvature. Symmetric wrinkling occurs in the linear limit (e.g., see Lieuwen [12]) as well, suggesting that there may be some analogies between the high turbulence intensity case and linear flame dynamics.

DISTRIBUTION A: Distribution approved for public release.

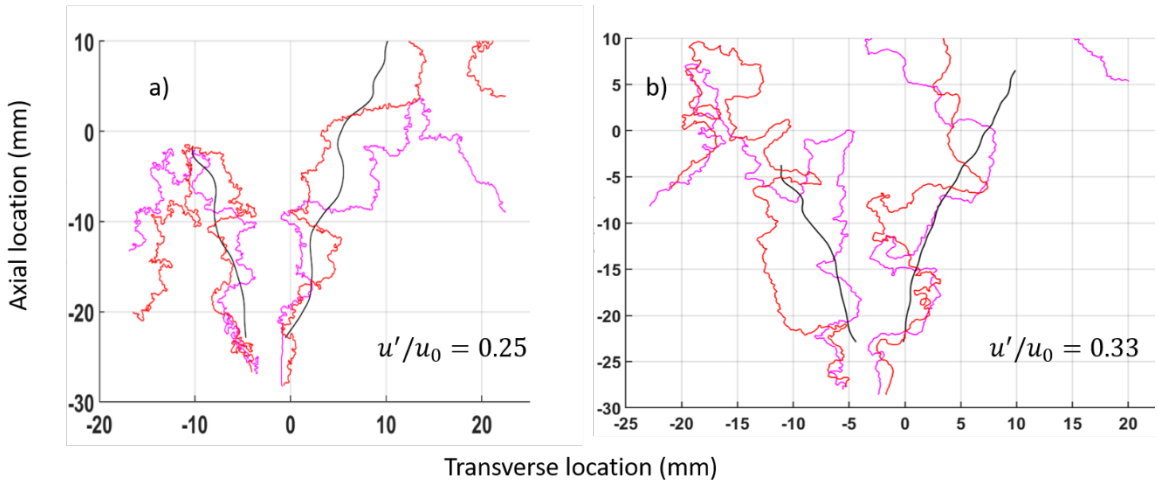

Figure 1.7: Ensemble-averaged edges (black) instantaneous edges (red, magenta) for f_0=400 Hz, a) $u_0 = 4.5$ m/s, $u'/u_0 = 25\%$ b) $u_0 = 5$ m/s, $u'/u_0 = 33\%$

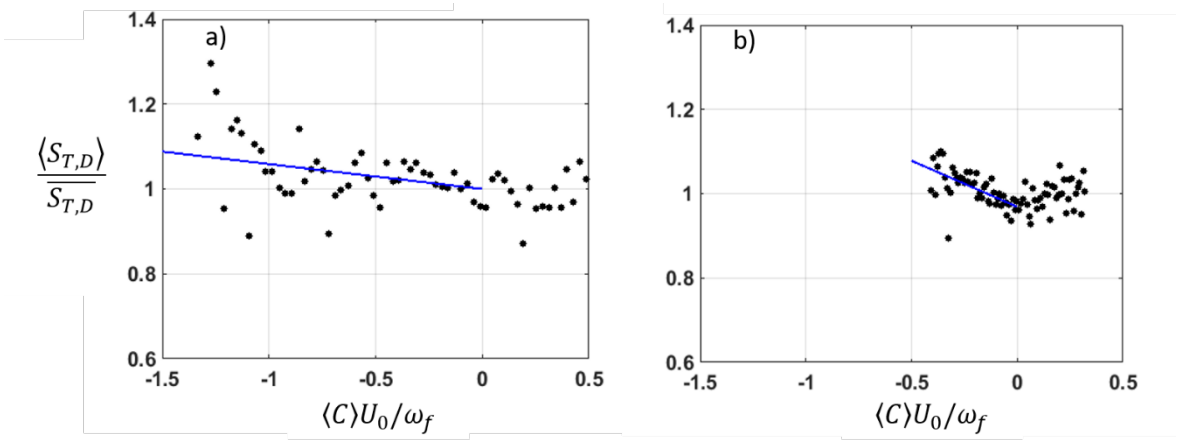

Figure 1.8: Correlation between ensemble-averaged flame speed (normalized by local time averaged flame speed ($\overline{S_{T,D}}$)) and ensemble-averaged curvature (normalized by mean axial velocity (u_0) and forcing frequency) for a) $f_0 = 400$ Hz, $u_0 = 4.5 ms^{-1}$ and $u'/u_0 = 0.25$ and b) $f_0 = 400$ Hz, $u_0 = 5$ ms^{-1} and $u'/u_0 = 0.33$ Linear fit for negative curvature values plotted as blue line

DISTRIBUTION A: Distribution approved for public release.

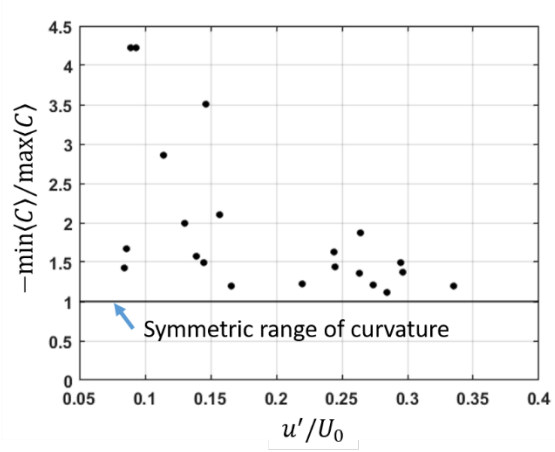

Figure 1.9: Variation of the ratio of range of negative curvature and positive curvature of the ensemble-averaged flame edge with turbulence intensity ($f_0 = 200$ Hz, 500 Hz, 600 Hz and nominal $u_0 \sim 5$m/s)

For the same case as in Figure 1.8 a), Figure 1.10 plots the three different components of $\langle S_T \rangle$ defined as $\langle S_{T,1} \rangle = \frac{\partial \langle \zeta \rangle}{\partial t} / [1 + (\partial \langle \zeta \rangle / \partial s)^2]^{1/2}$, $\langle S_{T,2} \rangle = \langle u_s \rangle \frac{\partial \langle \zeta \rangle}{\partial s} / [1 + (\partial \langle \zeta \rangle / \partial s)^2]^{1/2}$ and $\langle S_{T,3} \rangle = -\langle u_n \rangle / [1 + (\partial \langle \zeta \rangle / \partial s)^2]^{1/2}$. Note that the magnitude of flame speed is dominated by the ensemble-averaged normal velocity component ($\langle S_{T,3} \rangle$). However, the correlation itself seems to be dominated by the convective component along the averaged flame edge $\left(\langle S_{T,2} \rangle\right)$ since the normal velocity component appears to be not-correlated with ensemble-averaged curvature. For positive values of curvature however, the influence of $\langle S_{T,3} \rangle$ is apparent in the zero to positive correlation with the ensemble-averaged curvature.

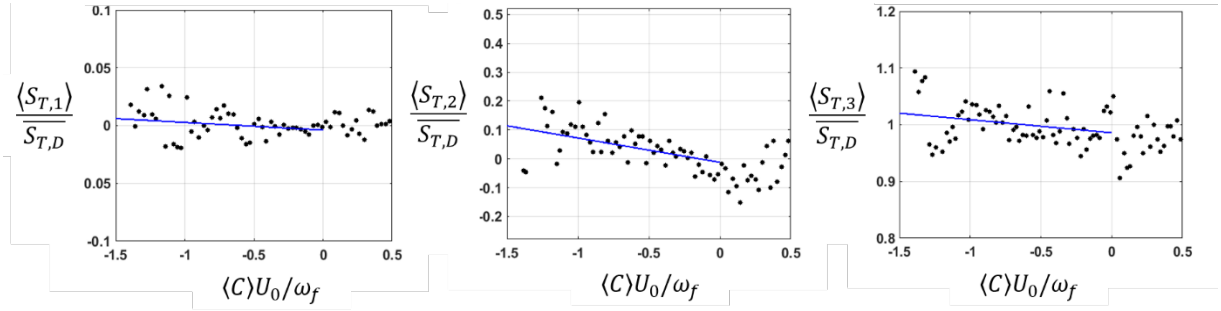

Figure 1.10: Components of $\langle S_T \rangle$ defined as above for the same parameters as in Figure 1.8

1.2.5. Negative curvature regions – turbulent Markstein numbers

DISTRIBUTION A: Distribution approved for public release.

Non-dimensional turbulent Markstein numbers are calculated as the slope of the linear fit to the correlation between ensemble-averaged flame speed and curvature in the negatively curved regions of the flame.

Figure 1.12 a) plots the variation of turbulent Markstein length upon the ratio of a turbulent flame scale, $\lambda_{\zeta,t} = u'/u_0$ and convective length scale ($\lambda_c = u_0/f_0$). Humphrey, et al. [5] originally suggested this scaling ratio, emphasizing the importance of the turbulence flame brush width and coherent wrinkle scale (see Figure 1.11). The monotonic increase with the decrease in convective wave length is to be expected since kinematic restoration is more prominent for smaller wrinkle wavelengths for a given wrinkle amplitude. As illustrated in Figure 1.11, in the negatively curved regions of the flame, the decreased wavelength makes the annihilation of flame surface due to its normal propagation become more prominent and thus increasing the flame speed. Similarly the opposite phenomenon occurs in the positively curved regions thus increasing the sensitivity of flame speed to curvature with decreasing wrinkle wavelength.

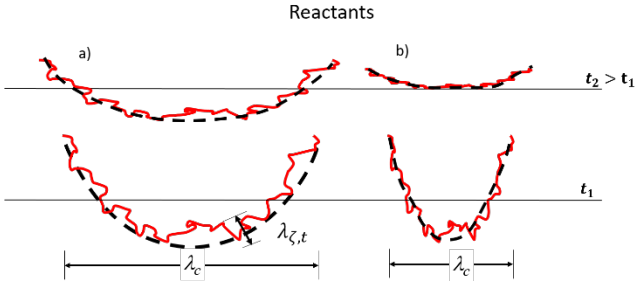

Figure 1.11: Illustration of turbulent flame brush and convective wave length scales. Image also shows action of kinematic restoration in smoothing flame wrinkle out

However, the turbulent flame brush varies with both downstream distance and turbulence intensity, and its functional dependence upon these quantities also changes near the flame holder and farther downstream. For example, several analyses show that the flame brush thickness for turbulent premixed flames scales linearly with turbulence intensity in near-field close to the flame holder but as the square root of turbulence intensity far downstream [13]. For this reason, we replot the data with $\lambda_{\zeta,t}$ defined in five ways as (a) $\lambda_{\zeta,t} = \frac{u'}{u_0}R$, (b) $\lambda_{\zeta,t} = \sqrt{\frac{u'}{u_0}}R$,(c) R, (d) $\lambda_{\zeta,t} = \left(\frac{u'}{u_0}\right)^{-1/2} R$ and (e) $\lambda_{\zeta,t} = \left(\frac{u'}{u_0}\right)^{-1} R$ (filled points indicate data from current campaign and unfilled points indicate data from Humphrey, et al. [5])). The burner exit radius, R, is used here as representative of the turbulent integral length scale. Note that Humphrey, et al. [5] used the first scaling in (a) and the scaling in (b) is what would be expected for large distances downstream. As neither of these scalings capture the turbulence intensity dependence, the other plots, (c)-(e) are used to show other velocity scalings. Note that the data points are conditioned based on the value of turbulence intensity. Several observations are evident from the plots: first, the Markstein numbers corresponding to each turbulence intensity bin form clear clusters, suggesting that the dependence on turbulence intensity is not fully captured by any of these scalings. Second, each of

DISTRIBUTION A: Distribution approved for public release.

the clusters seemingly increases linearly with the length scale ratio. The slopes of the linear best fit to each of the bins of turbulence intensities are plotted in Figure 1.13. Presumably, the best scaling exponent will be the one that is constant with different u'/u_0 bins. This slope is nearly constant for $\lambda_{\zeta,t} = \left(\frac{u'}{u_0}\right)^{-1/2} R$.

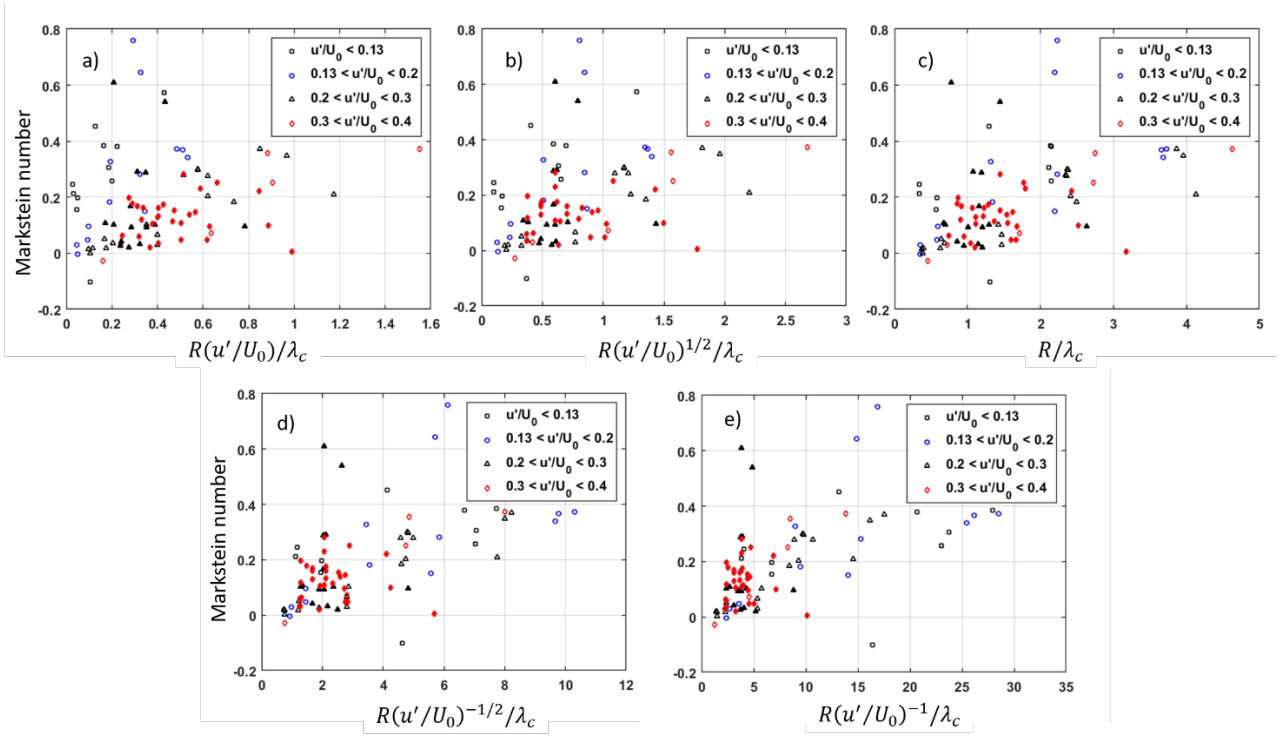

Figure 1.12: Variation of Turbulent Markstein number with $\lambda_{\zeta,t}/\lambda_c$ with $\lambda_{\zeta,t}$ defined as a) $R(u'/U_0)$ b) $R(u'/U_0)^{1/2}$ c) R d) $R(u'/U_0)^{-1/2}$ and e) $R(u'/U_0)^{-1}$ (filled points indicate data from current campaign and unfilled points indicate data from Humphrey, et al. [5])

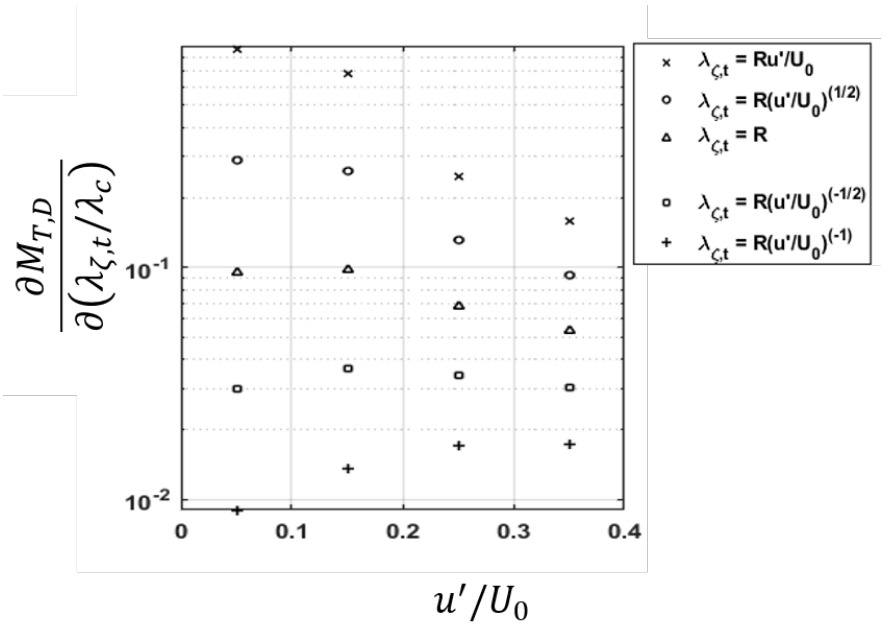

Figure 1.13: Variation of slope of the linear fits for the variation of $M_{T,D}$ with the ratio of turbulent and convective length scale for turbulence intensity bins as defined in Figure 1.12

Pulled together these results clearly indicate that the turbulent Markstein length increases with $1/\lambda_c$ – this can be seen most clearly from Figure 1.12 c), which has no turbulence intensity scaling and λ_c changes by a factor of nine. The turbulence intensity is more confusing – if the appropriate turbulent length scale is the flame brush thickness, then the best scaling should have a positive exponent (e.g.,$(u'/u_0)^{-1/2}$ and u'/u_0). However, Figure 1.13 clearly shows that a negative exponent is the best fit. Similar conclusions are reached when we evaluated a scaling of the form $R\ (Re_t)^n/\lambda_c$, where $Re_t = Ru'/\nu$. These also show a best fit for $n = -1/2$. This latter result does suggest a potential scaling, since the Taylor microscale scales as the product of integral length scale and $(Re_t)^{-1/2}$; i.e., as $R\ (Re_t)^{-1/2}$. This suggests that the turbulent Markstein length is a function of the ratio of the Taylor microscale and convective wavelength.

1.4. Summary

This chapter presents the correlation between ensemble-averaged flame speed and curvature for v-shaped turbulent premixed flame subject to harmonically oscillating flame holder. The experimental envelope is extended (compared to that presented by Humphrey, et al. [5]) using a direct drive mechanism for flame holder oscillation with a brushless DC motor. This provided for a constant oscillation amplitude independent of the forcing frequency. The ensemble-averaged flame speed and curvature show a clear negative correlation although only in the negatively curved regions of the flame dominated by the normal velocity component. However, there also exists a secondary correlation corresponding to the positively curved regions of the flame with a decreased sensitivity. The sensitivity parameter, turbulent Markstein number is shown to be clustered and

DISTRIBUTION A: Distribution approved for public release.

monotonically increasing with the ratio of turbulent and convective length scale when conditioned based on the turbulence intensity. The variation is best captured when turbulent length scale scales as inverse square root of turbulence intensity. Similar scaling results with turbulent Reynolds number indicate that the turbulent Markstein number is a function of the ratio of Taylor micro scale and convective wavelength.

DISTRIBUTION A: Distribution approved for public release.

Bibliography

[1] T. C. Lieuwen, *Unsteady combustor physics*. Cambridge University Press, 2012.

[2] J. F. Driscoll, "Turbulent premixed combustion: Flamelet structure and its effect on turbulent burning velocities," *Progress in Energy and Combustion Science,* vol. 34, no. 1, pp. 91-134, 2008.

[3] S. H. Preetham and T. C. Lieuwen, "Response of turbulent premixed flames to harmonic acoustic forcing," *Proceedings of the Combustion Institute,* vol. 31, no. 1, pp. 1427-1434, 2007.

[4] D.-H. Shin and T. Lieuwen, "Flame wrinkle destruction processes in harmonically forced, turbulent premixed flames," *Journal of Fluid Mechanics,* vol. 721, pp. 484-513, 2013.

[5] L. J. Humphrey, B. Emerson, and T. C. Lieuwen, "Premixed turbulent flame speed in an oscillating disturbance field," *Journal of Fluid Mechanics,* vol. 835, p. 102, 2018.

[6] D. H. Shin, "Premixed Flame Kinematics in a Harmonically Oscillating Velocity Field," PhD PhD, School of Aerospace Engineering, Georgia Institute of Techology, 2012.

[7] A. Lipatnikov and J. Chomiak, "Application of the Markstein number concept to curved turbulent flames," *Combustion Science and Technology,* vol. 176, no. 3, pp. 331-358, 2004.

[8] A. Lipatnikov and J. Chomiak, "Global stretch effects in premixed turbulent combustion," *Proceedings of the Combustion Institute,* vol. 31, no. 1, pp. 1361-1368, 2007/01/01/ 2007.

[9] A. Marshall, P. Venkateswaran, D. Noble, J. Seitzman, and T. Lieuwen, "Development and characterization of a variable turbulence generation system," *Experiments in Fluids,* vol. 51, no. 3, pp. 611-620, 2011.

[10] N. Otsu, "A Threshold Selection Method from Gray-Level Histograms," *IEEE Transactions On Systems, Man, And Cybernetics,* vol. 9, no. 1, pp. 62-66, 1979.

[11] S. Kheirkhah and O. L. Gulder, "Turbulent premixed combustion in V-shaped flames: Characteristics of flame front," *Physics of Fluids,* vol. 25, no. 5, p. 055107, 2013.

[12] T. C. Lieuwen, *Unsteady Combustor Physics*. Cambridge University Press, 2012, p. 488.

[13] A. N. Lipatnikov and J. Chomiak, "Turbulent flame speed and thickness: phenomenology, evaluation, and application in multi-dimensional simulations," *Progress in Energy and Combustion Science,* vol. 28, no. 1, pp. 1-74, 2002.

[14] M. Bauerheim, F. Nicoud, and T. Poinsot, "Progress in analytical methods to predict and control azimuthal combustion instability modes in annular chambers," *Physics of Fluids,* vol. 28, no. 2, p. 021303, 2016.

DISTRIBUTION A: Distribution approved for public release.

Chapter 2

Numerical and theoretical analysis of shock wave interactions with abrupt area changes

2.1 Introduction

This paper considers shock propagation through a channel with an area discontinuity. This problem is one subset of the more general problem of wave reflection, transmission, and dissipation in channels. A large knowledge base on this problem exists in the acoustics literature [20, 10], which is a useful starting point for the subsequent discussion. Assuming linear, one dimensional waves with no bulk flow, incident upon an area discontinuity with constant properties, approximate expressions can be developed for the wave reflection and transmission coefficients. These expressions are developed by assuming that the frequency is below the duct cutoff frequency (otherwise, multi-dimensional waves can be excited at the junction) and that the adjustment zone required for the multi-dimensional, evanescent disturbances to dissipate is small relative to an acoustic wavelength [21]. By integrating the momentum and energy equations over this adjustment zone, it can be shown that the unsteady pressure and volume flow rate are approximately constant, leading to the the resulting pressure reflection and transmission coefficients in terms of the area ratio α [19].

$$T \equiv \frac{\text{Transmitted wave amplitude}}{\text{Incident wave amplitude}} = \frac{2\alpha}{\alpha + 1} \tag{2.1}$$

$$R \equiv \frac{\text{Reflected wave amplitude}}{\text{Incident wave amplitude}} = \frac{\alpha - 1}{\alpha + 1} \tag{2.2}$$

Mean flow and nonlinearity add additional effects. The integral approach described above can be readily generalized to include mean flow but also requires determining the pressure distribution across the control surfaces. This pressure distribution is itself controlled by whether the unsteady flow attaches to the bounding walls or separates (such as when flow transitions rapidly from a smaller to larger cross-sectional area ducts). In either case, quasi-steady relations are typically invoked to develop analytical reflection and transmission coefficients. If there is no mean flow, unsteady flow separation causes the wave interaction problem to be intrinsically nonlinear (the acoustic wave dynamics themselves are linear, but the matching conditions are nonlinear) and dissipative, due to the conversion of some of the dilatational energy in the incident wave into rotational, vortical energy. In the presence of mean flow, the leading order dissipation term is linear in disturbance amplitude. This wave dissipation phenomenon, including its nonlinear amplitude dependence, has been extensively characterized in the literature [38, 11].

The propagation of shocks through varying channels has received significantly less treatment. This problem arises in several applications in which shocks move through channels, including rotating detonation engines [18], blast shelters [6], and supersonic wind tunnels [12]. The shock problem introduces two important processes that are not present in the above described acoustic analyses - first, the wave dynamics themselves are intrinsically nonlinear and non-isentropic and, second, the disturbance length scale is very short. Prior work suggests that, even for more complicated channels like bends and bifurcations, the area ratio between the primary and secondary duct dominates the strength of the transmitted shock wave [22]. Studies by Rudinger [29] and Oppenheim [28] theoretically analyzed wave transmission and reflection resulting from the shock / area change interaction; these works were later expanded upon by Salas [30]; we will utilize Rudinger's method [4] in this paper in calculating quasi one-dimensional approximations. These works can essentially be thought of as finite-amplitude generalizations of the work described above; i.e, they are quasi-1D analyses that apply conservation principles to the flows up- and down-stream

DISTRIBUTION A: Distribution approved for public release.

of the multi-dimensional adjustment zone in the immediate vicinity of the area change. As such, they neglect the multidimensional "near-field" phenomena occurring near the area change. These can include vortices, oblique shock diamonds, and transverse wave reflections [24]. The nature of such phenomena, and the impact they have on estimates of reflected and transmitted wave strength, are not understood. There is some evidence that the impact of such phenomena on the far-field is fairly minor; Shoev et al. [32], for instance, noted a roughly 5% discrepancy between the quasi-1D calculations employed by Rudinger and Salas and the 2D-averaged Euler equations when calculating the Mach numbers of transmitted shock waves through a microchannel. Similarly, Menina et al. [25] observed that, while these two methods show understandable discrepancies in the immediate vicinity of the area change after the shock's passage, these disagreements diminished sharply far beyond the area jump. However, these works do not answer the question of how general these results are and, even if they are generally true, *why* the discrepancies are small.

Furthermore, little is known about the energetics of this phenomenon. Traveling acoustic waves have the well known "equi-partition" property, where average energy density is evenly distributed between kinetic and internal energy associated with the "acoustic/compressional/dilatational" disturbance. Even in the linear acoustic case, dilatational energy in the acoustic wave is not fully converted into the dilatational reflected and transmitted acoustic waves; this is manifested in the fact that the acoustic energy flux of the reflected and transmitted acoustic waves is less than that of the incident wave. Rather, as noted above, some irrotational, dilatational disturbance energy is converted into vortical disturbances where the energy is exclusively kinetic and manifested in rotational, incompressible disturbances [20, 7]. Some energy is also transferred into entropy disturbances if the wave interacts with a temperature variation. For the shock problem, although the types of disturbances resulting from this interaction are documented in the literature [24], it is unknown how much energy is deposited in such disturbances and how much remains with the transmitted and reflected waves. These types of interactions between dilatational, vortical, and entropic disturbances is potentially much more significant in the shock-area change problem, due to the much higher flow velocities behind the shock (which, via the Kutta condition [8], lead to vortical disturbances), as well as the intrinsically non-isentropic nature of shock waves. Menina et al. [25] worked to address this gap by accounting for the transport of turbulent energy during a weak shock's interaction with an abrupt area expansion, but this type of analysis has yet to be generalized to a broad range of incident shock strengths and area changes, as well as entropy disturbances.

Analytical tools have been developed to quantify energy flux and source terms in flow disturbances that can be brought to bear for this problem. Specifically, Myers [26] has developed formal expressions that explicitly show the form of disturbance energy for arbitrary amplitude disturbances. This work has been generalized by Brear et al. [5] to include the effects of species transport and chemical reactions. These formulations are now routinely applied in thermo-acoustic problems [35, 23], but this formalism has not yet been applied to the shock-area change problem to the authors' knowledge.

The primary goal of this work is to study the propagation of shocks through channels with discontinuous area changes. Within this larger goal, we have the following specific aims. First, we wish to further understand the types of multi-dimensional, unsteady phenomena resulting from the shock / area change interaction and their impacts on the behavior of the reflected and transmitted waves. Toward this end, we studied the reflection and transmission of shocks of various strengths through channels with various area changes using both computational fluid dynamics (CFD), which can account for 2D transient effects, and quasi 1D methods, which do not. These phenomena are characterized across five different "regimes" governing the shock-area change interaction depending on the area ratio and incident Mach number. We also quantified the discrepancies between CFD and quasi-1D theory and show that they are in surprisingly good agreement, showcasing the viability of quasi-1D methods to predict the asymptotic strength of reflected and transmitted shocks despite neglecting near-field phenomena. Second, we perform an asymptotic analysis of the quasi 1D expressions (which are generally implicit expressions) to derive explicit expressions for reflected and transmitted wave energy, as well as accumulation and dissipation of energy in the near-field. The latter results are not only insightful in being presented in explicit form, but can also serve as boundary conditions for larger scale calculations. Finally, we analyze the energetics of the interaction. To accomplish this, we use Myer's expressions for disturbance energy and analyze the relative changes in dilatational energy associated with the area change and look at the excited vortical and entropic disturbances.

DISTRIBUTION A: Distribution approved for public release.

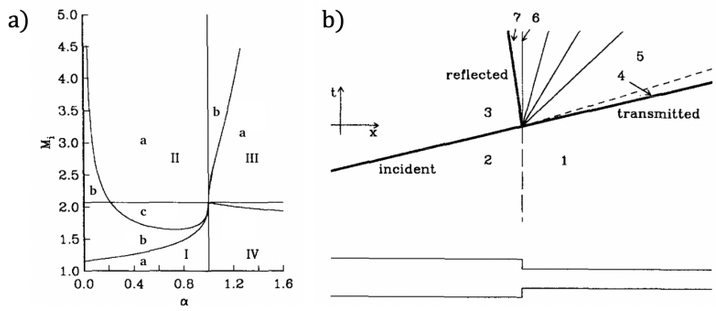

Figure 2.1: a) Diagram of wave patterns in parameter space. b) Wave diagram for the case of a reflected shock wave and a transmitted shock and expansion wave (Zone IIIa). —; shock, —, expansion wave; - - -, contact surface. Adapted from [30].

2.2 Methods

This section is organized as follows. We begin by describing the aforementioned modeling approaches used in this work: the quasi-1D theory and 2D CFD. We then describe the methods used to analyze the energetics of the flow field in this problem. This includes a review description of disturbance energy as it pertains to this problem and the methods we employ to decompose disturbance energy into three modes.

2.2.1 Modeling Approaches

This subsection describes the quasi-1D and 2D methods used to analyze the flow field in this problem.

Quasi-1D Theory

For this work, we used Rudinger's method to perform quasi-1D calculations of the flow field resulting from the shock / area change interaction. Rudinger's method relies on formal application of the Rankine-Hugoniot relations, coupled with physical arguments on the nature of the contact surface, reflected shock wave, and transmitted shock wave(s). In other words, before a solution can be obtained, one must first determine the structure of reflected and transmitted waves resulting from the shock's passage, either through experiment or appeals to physical principles to screen out physically unrealistic patterns. Second, as with most approaches relying on integral jump conditions, *quasi-steady* relations are used to match the wave characteristics of the incident, reflected, and transmitted shocks far up and downstream of the area change where these disturbances are one-dimensional, implicitly neglecting the accumulation terms.

Results are a function of two parameters: the incident shock wave Mach number M_i and the ratio of upstream to downstream channel areas α, as shown in figure 2.1. This parameter space is naturally divided into 4 quadrants separated by two lines: the space to the left of the vertical line (located at $\alpha = 1$) represents area decreases, while the space to the right of this line represents area increases. Meanwhile, the space below the horizontal line (located at $M_i = \left[\frac{(7-\gamma)+\sqrt{(7-\gamma)^2-16(2-\gamma)}}{4(2-\gamma)}\right]^{1/2} \approx 2.068$ for air) contains cases for which the flow behind the incident shock is subsonic, while the space above the horizontal line contains cases for which the flow behind the incident shock is supersonic. Within each quadrant are various zones corresponding to specific wave structures - one such pattern is shown in figure 2.1b; this corresponds to the case of a single reflected and transmitted shock as well as an expansion wave transmitted from the area change. These structures are described next.

Zone Ia corresponds to the case of a weak shock (i.e., subsonic flow behind the incident shock) and an area increase. In this case, the resulting interaction produces a reflected expansion wave and a transmitted shock. As the strength of the shock increases at a given area ratio, one moves into wave zone Ib. In this zone, the expansion wave is strong enough to produce sonic flow upstream of the area decrease. The resulting flow through the area decrease is choked, producing a standing shock wave within the area expansion, in addition to the waves described in the previous case. Further increasing the shock strength moves one into zone Ic. For this case, the pressure ratio across the area change is sufficiently strong to unchoke it, causing the standing shock to exit the area change as a second transmitted normal shock. If the incident shock is strengthened further

DISTRIBUTION A: Distribution approved for public release.

still, quadrant II is reached. For sufficiently large area ratios, the pattern corresponds to zone IIa, in which case the expansion wave in the previous case is no longer possible, due to the supersonic flow behind the incident shock, leaving only the two transmitted shocks. If the area ratio is too small, however, the wave pattern becomes that of zone IIb, in which case the pressure ratio across the area change is too small to un-choke the area increase, resulting in a standing shock and a transmitted shock.

Zone IV corresponds to the case of a weak shock and a contracting duct. In this case, the resulting interaction produces a reflected and transmitted shock only. If the incident shock wave is strengthened, then the flow behind the area change is accelerated to sonic conditions. In this case, a transmitted expansion wave is generated in addition to the waves present in the previous case, resulting in a type IIIa pattern. For large enough area ratios, this pattern is also present in quadrant III. If however, the area ratio is small enough, i.e., zone IIIb, there is only a transmitted expansion wave and a transmitted shock.

To lay the foundation for the later section on the approximate (small $(M_i - 1)$ limit) theory, we summarize the key equations next.

$$\rho_1 u_1 A_1 = \rho_2 u_2 A_2 \tag{2.3}$$

$$(p_1 + \rho_1 u_1^2) A_1 = (p_2 + \rho_2 u_2^2) A_2 \tag{2.4}$$

$$h_1 + \frac{u_1^2}{2} = \frac{c_1^2}{\gamma - 1} + \frac{u_1^2}{2} = \frac{c_2^2}{\gamma - 1} + \frac{u_2^2}{2} \tag{2.5}$$

Equations 2.3-2.5 describe the conservation of mass, momentum, and energy across an area discontinuity given by the upstream and downstream areas A_1 and A_2. The quantities p, ρ, u, c, and γ denote the pressure, density, velocity, sound speed, and specific heat ratio (assumed to be constant in this work), respectively. The final expression makes use of the ideal gas law to relate enthalpy h to sound speed. For conciseness, we define:

$$\delta \equiv \left(\frac{\gamma - 1}{2} \right), \quad \kappa \equiv \left(\frac{\gamma + 1}{2} \right) \tag{2.6}$$

Rudinger's method involves decomposing the fluid domain into zones separated by finite compression (shock) and expansion waves, contact surfaces, and the area change. To relate conditions across shock waves, the above conservation equations can be transformed into the Rankine-Hugoniot relations [1].

$$\frac{p_2}{p_1} = \frac{\gamma M_1^2 - \delta}{\kappa} \tag{2.7}$$

$$\frac{\rho_2}{\rho_1} = \frac{u_1}{u_2} = \frac{\kappa M_1^2}{\delta M_1^2 + 1} \tag{2.8}$$

$$M_2^2 = \frac{\delta M_1^2 + 1}{\gamma M_1^2 - \delta} \tag{2.9}$$

It should be noted that velocities and Mach numbers M are in the frame of the shock. For expansion waves, the following Riemann invariants were utilized.

$$J_+ = c + \delta u = const \tag{2.10}$$

$$J_- = c - \delta u = const \tag{2.11}$$

The above two relations hold for left- and right-moving isentropic waves, respectively. For isentropic state changes (i.e. changes throughout the expansion wave and area change, provided there is no standing shock), the following equation was used.

$$\frac{p}{\rho^\gamma} = const \tag{2.12}$$

This expression can be combined with the ideal gas law and appropriate conservation relations (i.e. the Riemann invariants for finite waves and conservation of mass/energy for the area change) to relate flow variables between two points. Finally, to relate conditions across a contact surface,

DISTRIBUTION A: Distribution approved for public release.

we equated the pressure and velocity on either side. Thus, although there is no explicit relation between other flow variables across the contact surface, they could still be implicitly related by fixing either pressure or velocity, solving for the corresponding velocity or pressure, and iterating this process until both pressure and velocity were continuous.

While the solution must generally be implemented computationally, Rudinger's method can be explicitly solved in the weak shock limit using perturbation approaches. We detail the approach in the Appendix, and refer to these solutions later in interpreting computational results.

2.2.2 Two-Dimensional Computations

This section presents details of the inviscid simulations used to compute the two-dimensional domain, implemented with ANSYS Fluent 2020 R1. Fluent has increasingly robust tools for simulating shocks and has been employed toward this end in numerous works [16, 36]. The pressure-flow coupling was captured using the COUPLED algorithm. The temporal discretization used a second-order bounded implicit transient scheme with a time step such that the Courant number in the flow behind the incident shock = 0.5. The spatial discretization uses a 2nd order scheme for pressure and a second order upwind scheme for density; the latter is recommended for improved accuracy for shock capturing [3]. Further information on these settings can be found in the Fluent User's Guide [3] and Theory Guide [2]. Structured geometry conforming mesh elements (quad cells) were used with a uniform size of 0.5 mm (1/20th the tube width); this size was determined from a mesh sensitivity study.

The width of the small duct was selected to be 10 mm, the width of the larger duct was determined from the area ratio, and both ducts were given lengths of at least 300 mm (that is, 30 times the tube width) to capture the transmitted and reflected shocks far enough from the area change for them to become one-dimensional. The criteria we used for "one-dimensionality" was that there be negligible transverse variations along the shock. In order to determine if the the length was sufficient to fully develop the transmitted shock, we also performed a second set of identical calculations in which the duct lengths were increased by a factor of three and found the results to be insensitive to the changes. In general, the domain length required for the flow to return to one-dimensionality increases with incident shock strength.

Shocks were generated by fixing the static pressure p_i, total pressure $p_{t,i}$, and total temperature $T_{t,i}$ at the inlet to the appropriate values, which were calculated using the following equations.

$$p_i = p_0 \frac{\gamma M_i^2 - \delta}{\kappa} \tag{2.13}$$

$$p_{t,i} = p_i \left(1 + \delta M_d^2\right)^{\frac{\gamma}{2\delta}}, \quad M_d = \frac{M_i^2 - 1}{\sqrt{(\delta M_i^2 + 1)(\gamma M_i^2 - \delta)}} \tag{2.14}$$

$$T_{t,i} = T_i \left(1 + \delta M_d^2\right), \quad T_i = T_0 \frac{(\delta M_i^2 + 1)(\gamma M_i^2 - \delta)}{\kappa^2 M_i^2} \tag{2.15}$$

The above equations are merely re-expressions of the Rankine-Hugoniot relations (equations 2.7-2.9) evaluated for the conditions upstream and downstream of the incident shock. Here, p_0 and T_0 represent the initial pressure and temperature in the domain, set at 1 atm and 300 K, respectively. All other surfaces were treated as walls with zero normal velocity and heat flux. The exit boundary condition is unimportant provided that the duct is long enough (i.e. the shock can travel a sufficient distance to develop fully before interacting with the exit) and the pressure and velocity at the wall match that of the exit duct. The duct was initialized with quiescent, atmospheric air.

Shock pressure reflection and transmission coefficients were extracted from these calculations, defined as [29].

$$T = \frac{p_4 - p_1}{p_3 - p_2} \tag{2.16}$$

$$R = \frac{p_7 - p_3}{p_3 - p_2} \tag{2.17}$$

where the subscripts denote zones in the channel, as summarized in figure 2.2.

State variables of interest were taken to be the average in each of the zones in figure 2.2. Zone 4 was taken sufficiently far from the near-field zone that disturbances had returned to one-dimensional. CFD simulations were performed over a range of values for M_i and α in all of the zones shown in figure 2.1.

DISTRIBUTION A: Distribution approved for public release.

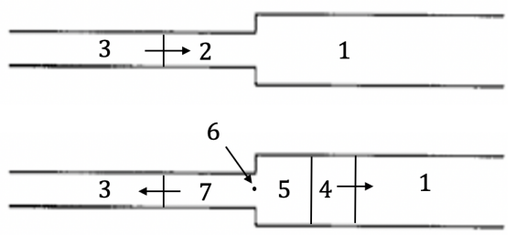

Figure 2.2: Fluid zones in a channel for a type Ia pattern. Zones are numbered as follows: 1) the right side of the area discontinuity not reached by the transmitted shock, 2) the left side of the area discontinuity not reached by the incident shock, 3) the region upstream of the incident shock not reached by a reflected wave, 4) the region upstream of the transmitted shock not reached by the contact surface, 5) the region between the contact surface and the area discontinuity, 6) the region immediately downstream of the area discontinuity, and 7) the region between the reflected wave and the area discontinuity

2.2.3 Disturbance Energy Quantification

This section describes the approach used to quantify energy and energy flux during the shock / area change interaction. This energetics-based approach has been useful in several fields of study, particularly combustor noise [5] and combustion instabilities [27, 34]. Consider an energy equation of the following form.

$$\frac{\partial E}{\partial t} + \nabla \cdot \vec{I} = \phi \tag{2.18}$$

where $\vec{I}$ represents the energy flux and ϕ represents energy sources/sinks. Furthermore, consider again the flow in the channel after the incident shock passes through the area change, as outlined in figure 2.2. Integrating over a control volume V across the incident shock and making use of the divergence theorem, we have the following relation.

$$\begin{aligned} \frac{1}{A_L}\frac{\partial}{\partial t}\int_V E dV &= \frac{1}{A_L}\int_V \frac{\partial E}{\partial t} dV \\ &= \frac{1}{A_L}\left[\int_V \phi dV - \int_S (\vec{I}\cdot\vec{n}) dA\right] \\ &= \frac{1}{A_L}\int_V \phi dV + I_{3,x} - I_{1,x} \\ &\equiv I_i \end{aligned} \tag{2.19}$$

In the above, A_L represents the area on the left (incident) side of the duct, while $I_{3,x}$ and $I_{1,x}$ represent x-components of the energy fluxes in zones 1 and 3 as defined in figure 2.2 (that is, the unperturbed zone upstream of the area discontinuity and the zone upstream of the incident shock, respectively). We define I_i to be the *intensity* of the incident shock and define the intensities of the transmitted and reflected waves in the same manner. To evaluate E, $\vec{I}$, and ϕ, we use the following expressions from Myers [26]:

$$E \equiv \rho[h_T - h_{T0} - T_0(s - s_0)] - \rho_0\vec{u}_0 \cdot (\vec{u} - \vec{u}_0) - (p - p_0) \tag{2.20}$$

$$\vec{I} \equiv (\rho\vec{u} - \rho_0\vec{u}_0)[h_T - h_{T0} - T_0(s - s_0)] + \rho_0\vec{u}_0(T - T_0)(s - s_0) \tag{2.21}$$

$$\phi \equiv (\rho\vec{u} - \rho_0\vec{u}_0) \cdot [\vec{\Omega}\times\vec{u} - \vec{\Omega}_0\times\vec{u}_0 + (s - s_0)\nabla T_0] - (s - s_0)\rho_0\vec{u}_0 \cdot \nabla(T - T_0) \tag{2.22}$$

Here, h_T, s, and Ω represent the total enthalpy, entropy, and vorticity, respectively, while $\vec{u} \equiv (u, v)$ defines the fluid velocity vector. $()_0$ represents the unperturbed state of the fluid, taken in this case to be the state before the arrival of the incident shock. Because the fluid is initially homogeneous and stationary, the source terms are identically zero. Hence, the intensity of the incident shock equals the jump in energy flux before and after it.

Equation 2.18 - with the given definitions of E, $\vec{I}$, and ϕ - is an extension of the familiar acoustic energy relation to arbitrary wave disturbance amplitudes. This enables us to define the *power* reflection and transmission coefficients, given below.

DISTRIBUTION A: Distribution approved for public release.

$$R_\Pi = R_I \equiv \frac{I_r}{I_i} \tag{2.23}$$

$$T_\Pi = \frac{1}{\alpha} T_I \equiv \frac{I_t}{\alpha I_i} \tag{2.24}$$

Here, $I_i \equiv |\vec{I}_i|$, $I_t \equiv |\vec{I}_t|$, and $I_r \equiv |\vec{I}_r|$ are the incident, transmitted, and reflected wave intensities respectively. Partitioning the domain into the zones shown in figure 2.2, define these as follows.

$$\vec{I}_i \equiv \vec{I}_3, \quad \vec{I}_t \equiv \vec{I}_4, \quad \vec{I}_r \equiv \vec{I}_7 - \vec{I}_3 \tag{2.25}$$

We expand more on the characteristics of Myers' disturbance energy and analyze them with respect to the finite amplitude energy quantification approaches from Jenvey [17] and Doak [9] in Appendix B.

Returning to the problem at hand, consider how to use these results for comparisons of quasi-1D and 2D results. There exists some zone before and after the area change where transient and 2D effects persist; we refer to this as the near-field zone V_n. Considering this zone, we have the following.

$$\begin{aligned} \frac{1}{A_L I_i} \int_{V_n} \frac{\partial E}{\partial t} dV &= -\frac{1}{A_L I_i} \int_{\partial V_n} (\vec{I} \cdot \vec{n}) dA \\ &= -\frac{1}{\alpha I_i} (I_4 - I_6) \end{aligned} \tag{2.26}$$

Define the *accumulation coefficient*, C_e, to be the normalized disturbance energy flux transferred from the incident shock to disturbances other than the transmitted and reflected finite waves during the interaction:

$$\begin{aligned} C_e &\equiv \frac{A_L I_i - A_R I_t - A_L I_r}{A_L I_i} \\ &= 1 - T_\Pi - R_\Pi \end{aligned} \tag{2.27}$$

Substituting equations (2.25) and (2.26) into the above relation produces the following.

$$\begin{aligned} C_e &= \frac{1}{A_L I_i} \left[(A_L I_7 - A_R I_6) + \int_{V_n} \frac{\partial E}{\partial t} dV \right] \\ &= \frac{\text{Flux through area change} + \text{Accumulation in near-field zone}}{\text{Incident disturbance energy}} \end{aligned} \tag{2.28}$$

We will quantify this accumulation coefficient in the subsequent calculations. The above relations reveal insights into the relationship between quasi-1D and general results. For instance, the only sources of energy flux between states 4 and 6 in the quasi-1D theory are a contact surface and possible secondary transmitted waves. This contrasts with the general result, in which the transient, higher-dimensional behavior in the near-field may result in disturbance energy flux. This expression provides a convenient means to assess the magnitude of these discrepancies and their impact on the wave behavior.

Decomposition into Acoustic, Vortical, and Entropic Components

For this work, we wished to understand not only the *amount* of disturbance energy deposited into 2D phenomena but the *distribution* of this disturbance energy. A useful taxonomy for disturbances is to categorize them as acoustic/dilatational, vortical, and entropy disturbances [7]. These disturbances manifest themselves in the dilation $\Lambda \equiv \nabla \cdot \vec{u}$, the vorticity $\Omega \equiv \nabla \times \vec{u}$, and the entropy s. We also calculated the instantaneous spatial distribution of the total disturbance energy flux $F \equiv \nabla \cdot \vec{I}$. While these definitions are unique, note that these fields are not independent as they are in the linear case but strongly coupled through nonlinearities [7]. In addition, evaluating their contribution to energy transfer becomes more nuanced in the finite amplitude case because energy flux is a quadratic quantity and such disturbances are nonlinearly coupled [20]. In order to provide insights into how the energy flux is distributed across dilatational, vortical, and entropy disturbances, we also compared it to the corresponding space/time distribution of the dilatation, vorticity, and entropy fields. This comparison can be done qualitatively (by visualizing the regions where large energy flux is coincident with regions of large disturbance amplitude of a given mode), or quantitatively by calculating the normalized correlation coefficient between fields as follows.

DISTRIBUTION A: Distribution approved for public release.

$$\text{Correlation Coefficient} \equiv \frac{\sum_{i=0}^{N}(F_i - \bar{F})(\psi_i - \bar{\psi})}{\sqrt{\sum_{i=0}^{N}(F_i - \bar{F})^2 \sum_{i=0}^{N}(\psi_i - \bar{\psi})^2}} \tag{2.29}$$

The above sums are evaluated over each point $i = 1, \ldots, N$ in the flow-field. Here, ψ represents one of the 3 variables noted above (Λ, Ω and s). R was calculated at each instant in time, then time-averaged over a representative time window in which near-field effects reached a steady structure.

We also analyzed the disturbance energy density distribution using methods suggested by Jenvey [17] and Doak [9], which have been employed in past aero-acoustics studies [33] where one wishes to understand energy transfer between highly nonlinear vortical disturbances and far-field acoustic wave propagation. We perform this decomposition for disturbance energy density as follows. First, split the disturbance energy density into "internal" and "kinetic" energy contributions for reasons discussed later:

$$\begin{aligned} E &= \rho[h - h_0 - T_0(s - s_0)] - (p - p_0) + \frac{1}{2}\rho\vec{u}\cdot\vec{u} \\ &= e_D + \frac{1}{2}\rho\vec{u}\cdot\vec{u} \end{aligned} \tag{2.30}$$

Define the internal energy contribution e_D and density ρ to be functions of p and s. Using the following relations [26]

$$dh = TdS + \frac{1}{\rho}dp, \quad dp = \frac{c^2\rho\beta T}{c_p}ds + c^2 d\rho \tag{2.31}$$

differentiate with respect to time and apply the chain rule accordingly to obtain the following decomposition for e_D.

$$\frac{\partial e_D}{\partial t} = \left.\frac{\partial e_D}{\partial p}\right|_{s=s_0}\frac{\partial p}{\partial t} + \left.\frac{\partial e_D}{\partial p}\right|_{p=p_0}\frac{\partial s}{\partial t} \tag{2.32}$$

$$\left.\frac{\partial e_D}{\partial p}\right|_{s=s_0} = \frac{1}{c^2}\left[h - h_0\right] \tag{2.33}$$

$$\left.\frac{\partial e_D}{\partial s}\right|_{p=p_0} = -\frac{\rho\beta T}{c_p}\left[\left(h - \frac{c_p}{\beta}\right) - (h_0 - T_0 s_0) - T_o\left(s - \frac{c_p}{\beta T}\right)\right] \tag{2.34}$$

To handle the kinetic energy term, perform the following decomposition. First, following Jenvey and Doak, define the following quantities.

$$\nabla\cdot\vec{u}_\Lambda \equiv -\frac{1}{\gamma p}\frac{Dp}{Dt}, \quad \nabla\cdot\vec{u}_s \equiv \frac{1}{c_p}\frac{Ds}{Dt} \tag{2.35}$$

Further defining these vector fields to be curl-free, define the curl-free velocity $\vec{u}_D$ as $\vec{u}_D \equiv \vec{u}_\Lambda + \vec{u}_s$. The following relationships then hold.

$$\begin{aligned} \nabla\cdot\vec{u}_D &= \nabla\cdot\vec{u}_\Lambda + \nabla\cdot\vec{u}_s \\ &= -\frac{1}{\gamma p}\frac{Dp}{Dt} + \frac{1}{c_p}\frac{Ds}{Dt} \\ &= -\frac{1}{\rho}\frac{D\rho}{Dt} \\ &= \nabla\cdot\vec{u} \end{aligned} \tag{2.36}$$

Finally, define the divergence-free velocity $\vec{u}_\Omega$ as $\vec{u}_\Omega \equiv \vec{u} - \vec{u}_D$, so that $\vec{u} = \vec{u}_\Lambda + \vec{u}_s + \vec{u}_\Omega$. Given the above properties of $\vec{u}_D$, one has that $\nabla\cdot\vec{u}_\Omega = \nabla\cdot\vec{u} - \nabla\cdot\vec{u}_\Lambda = 0$ and $\nabla\times\vec{u}_\Omega = \nabla\times\vec{u} = \vec{\Omega}$. Thus, this procedure decomposes the velocity into components associated with pressure, vorticity, and entropy as desired; thus, we refer to $\vec{u}_\Lambda$, $\vec{u}_\Omega$, and $\vec{u}_s$ as "acoustic," "vortical," and "entropic" velocity components, respectively. The procedure for solving for these fields is as follows.

1. Solve the Poisson problem $\nabla^2\phi = -\frac{1}{\rho}\frac{D\rho}{Dt}$ with the Neumann condition $\nabla\phi\cdot\hat{n} = \vec{u}\cdot\hat{n}$ on the boundary for the velocity potential ϕ. Inherent in this boundary condition is the assumption that $\vec{u}$ is irrotational at the boundaries, consistent with the inviscid calculation, which prevents the generation of vorticity at the walls. Because of convecting vortical disturbances, it is also

DISTRIBUTION A: Distribution approved for public release.

important to place the downstream boundary sufficiently far downstream. It was found that neglecting to do so had the effect of introducing noise in the spatial contours of the disturbance accumulation terms. However, this had minimal impact on their relative magnitudes, provided that the domain boundary was far enough downstream to include the flow structures.

2. Solve the Poisson problem $\nabla^2\phi_\Lambda = -\frac{1}{\gamma p}\frac{Dp}{Dt}$ with the Neumann condition $\nabla\phi_\Lambda \cdot \hat{n} = \vec{u} \cdot \hat{n}$ on the boundary. This boundary condition implicitly defines $\vec{u}_s \cdot \vec{n}$ to be zero at the walls.

3. Calculate $\vec{u}_\Lambda$ and $\vec{u}_D$ as $\nabla\phi_\Lambda$ and $\nabla\phi$, respectively.

4. Calculate $\vec{u}_s$ as $\vec{u}_D$ - $\vec{u}_\Lambda$.

5. Calculate $\vec{u}_\Omega$ as $\vec{u}$ - $\vec{u}_D$.

Making use of the regular, rectangular grid for the domain, we solved the above Poisson problems numerically using 2nd-order finite differencing and solving the resulting system of equations using SciKit's UMFPACK direct solver.

With this decomposition, we partition the kinetic energy accumulation in a similar manner. We have the following:

$$\begin{aligned}\frac{\partial}{\partial t}\left(\frac{1}{2}\rho\vec{u}\cdot\vec{u}\right) &= \frac{\vec{u}\cdot\vec{u}}{2}\frac{\partial\rho}{\partial t} + \rho\vec{u}\cdot\frac{\partial\vec{u}}{\partial t} \\ &= \frac{(\vec{u}_\Lambda+\vec{u}_\Omega+\vec{u}_s)\cdot(\vec{u}_\Lambda+\vec{u}_\Omega+\vec{u}_s)}{2}\left(\frac{1}{c^2}\frac{\partial p}{\partial t} - \frac{\rho\beta T}{c_p}\frac{\partial s}{\partial t}\right) \\ &+ \rho(\vec{u}_\Lambda+\vec{u}_\Omega+\vec{u}_s)\cdot\frac{\partial}{\partial t}(\vec{u}_\Lambda+\vec{u}_\Omega+\vec{u}_s)\end{aligned} \tag{2.37}$$

We now define the acoustic, vortical, and entropic contributions to the disturbance energy density to be those terms that are *strictly* associated with the three fields; that is, those associated with *pure* multiples of $\frac{\partial p}{\partial t}$ and/or $\vec{u_\Lambda}$, $\vec{u_\Omega}$, and $\frac{\partial s}{\partial t}$ and/or $\vec{u_s}$, respectively. In doing so, we expand on the methods of Jenvey and Doak by excluding combinations of such terms ($\vec{u}_s \cdot \vec{u}_\Lambda$, for instance) from these categories and group them into a four additional *coupled* terms. Thus, we have the following definitions for each of the seven contributions to the disturbance energy accumulation $\dot{E} \equiv \partial E/\partial t$:

$$\dot{E}_\Lambda \equiv \frac{1}{c^2}\left(h - h_0 + \frac{\vec{u}_\Lambda\cdot\vec{u}_\Lambda}{2}\right)\frac{\partial p}{\partial t} + \rho\vec{u}_\Lambda\cdot\frac{\partial\vec{u}_\Lambda}{\partial t} \tag{2.38}$$

$$\dot{E}_\Omega \equiv \rho\vec{u}_\Omega\cdot\frac{\partial\vec{u}_\Omega}{\partial t} \tag{2.39}$$

$$\dot{E}_s \equiv -\frac{\rho\beta T}{c_p}\left(\left[h - \frac{c_p}{\beta}\right] - (h_0 - T_0 s_0) - T_o\left[s - \frac{c_p}{\beta T}\right] + \frac{\vec{u}_s\cdot\vec{u}_s}{2}\right)\frac{\partial s}{\partial t} + \rho\vec{u}_s\cdot\frac{\partial\vec{u}_s}{\partial t} \tag{2.40}$$

$$\dot{E}_{\Lambda,\Omega} \equiv \frac{2\vec{u}_\Lambda\cdot\vec{u}_\Omega + \vec{u}_\Omega\cdot\vec{u}_\Omega}{2c^2}\frac{\partial p}{\partial t} + \rho\left(\vec{u}_\Lambda\cdot\frac{\partial\vec{u}_\Omega}{\partial t} + \vec{u}_\Omega\cdot\frac{\partial\vec{u}_\Lambda}{\partial t}\right) \tag{2.41}$$

$$\dot{E}_{\Lambda,s} \equiv \frac{2\vec{u}_\Lambda\cdot\vec{u}_s + \vec{u}_s\cdot\vec{u}_s}{2c^2}\frac{\partial p}{\partial t} - \rho\beta T\frac{2\vec{u}_\Lambda\cdot\vec{u}_s + \vec{u}_\Lambda\cdot\vec{u}_\Lambda}{2c_p}\frac{\partial s}{\partial t} + \rho\left(\vec{u}_\Lambda\cdot\frac{\partial\vec{u}_s}{\partial t} + \vec{u}_s\cdot\frac{\partial\vec{u}_\Lambda}{\partial t}\right) \tag{2.42}$$

$$\dot{E}_{\Omega,s} \equiv -\rho\beta T\frac{2\vec{u}_\Omega\cdot\vec{u}_s + \vec{u}_\Omega\cdot\vec{u}_\Omega}{2c_p}\frac{\partial s}{\partial t} + \rho\left(\vec{u}_\Omega\cdot\frac{\partial\vec{u}_s}{\partial t} + \vec{u}_\Omega\cdot\frac{\partial\vec{u}_s}{\partial t}\right) \tag{2.43}$$

$$\dot{E}_{\Lambda,\Omega,s} \equiv \frac{\vec{u}_\Omega\cdot\vec{u}_s}{c^2}\frac{\partial p}{\partial t} - \rho\beta T\frac{\vec{u}_\Lambda\cdot\vec{u}_\Omega}{c_p}\frac{\partial s}{\partial t} \tag{2.44}$$

To analyze this exchange during the shock / area change interaction, we calculated each of the seven terms and examined their spatial structures and relative importance over the range of cases studied.

In closing, it should be emphasized that that, ultimately, it is the actual flow and thermodynamic variables that are fundamentally defined. We then impose the acoustic, entropic, and vortical decomposition upon the data; e.g., the quantities $\vec{u}_s$ and $\vec{u}_\Lambda$ are defined quantities. The question for this decomposition approach is not whether it is "correct;" that is, this decomposition is exact, but there are other possible definitions resulting in exact decompositions. Rather, because such decompositions are non-unique, a more appropriate question is whether it is "useful" for extracting insights into the modal coupling processes at the area expansion.

DISTRIBUTION A: Distribution approved for public release.

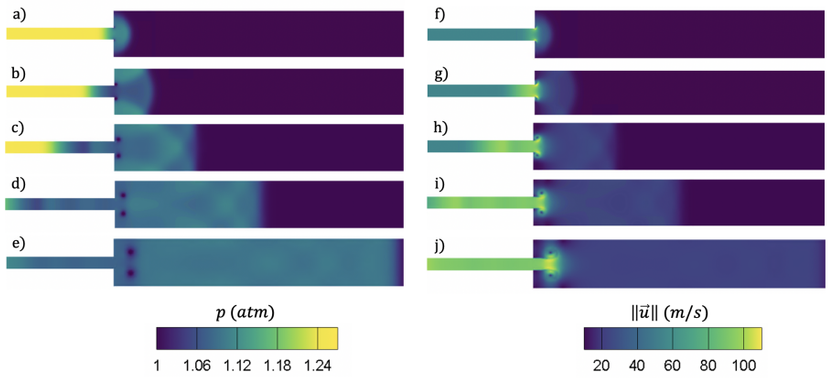

Figure 2.3: Time series of pressure (a-e) and velocity (f-j) fields for $M_i = 1.1$, $\alpha = 0.25$. Time elapsed: 0.68 ms.

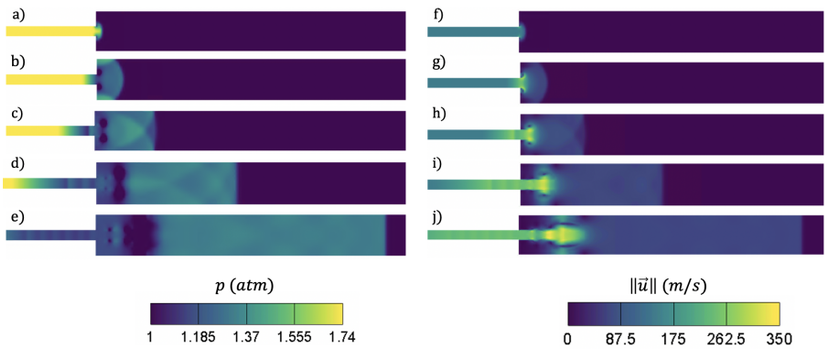

Figure 2.4: Time series of pressure (a-e) and velocity (f-j) fields for $M_i = 1.5$, $\alpha = 0.25$. Time elapsed: 0.57 ms.

2.3 Results & Discussion

2.3.1 Flow-Field Description

Figures 2.3 - 2.6 display the transient, 2D pressure and velocity magnitude for four representative cases with the same expanding area ratio, but increasing shock strength. Figure 2.7 shows a single case for a diverging duct. The reasons for selecting these conditions will be discussed later. In the first four cases where the duct expands, the shock spherically diffracts into the larger duct before reaching its walls. This results in a series of wave reflections off the duct walls, the transverse components of which dissipate with time and the axial components of which eventually coalesce with the original shock into a planar front. Comparing figures 2.3 - 2.6, note that, owing to the increased strength of the initial transmitted shock, this transverse wave system takes more time/distance to dissipate as the incident shock strength increases; thus, the transmitted shock must travel over a greater distance before coalescing into a planar front. The reflected wave, meanwhile, remains nearly planar. In the contracting duct case, the transmitted shock remains planar. In this case, shocks reflected from the corners of the junction undergo a similar process of transverse wave reflection before coalescing into a planar reflected shock. Portions of this transverse wave system also trail behind the transmitted shock before dissipating.

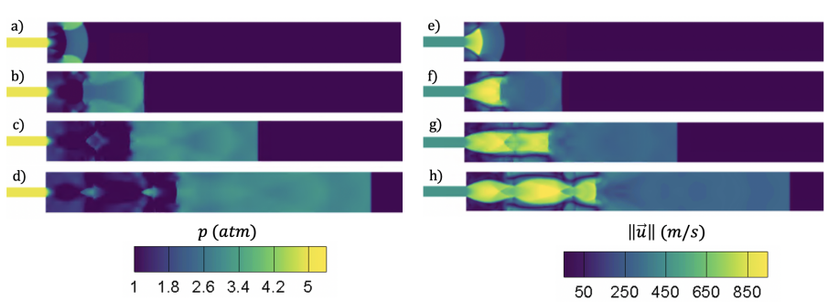

Figure 2.5: Time series of pressure (a-e) and velocity (f-j) fields for $M_i = 2.1$, $\alpha = 0.25$. Time elapsed: 0.51 ms.

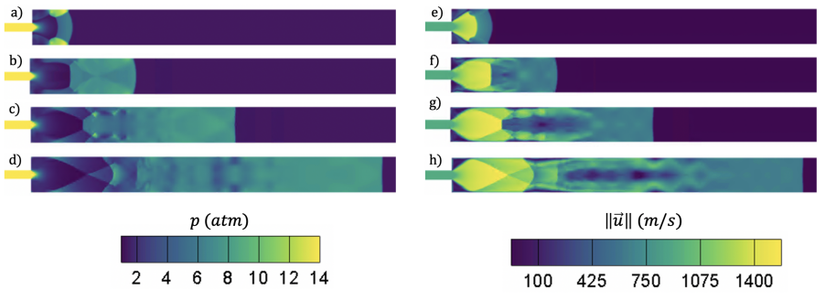

Figure 2.6: Time series of pressure (a-e) and velocity (f-j) fields for $M_i = 3.5$, $\alpha = 0.25$. Time elapsed: 0.4 ms.

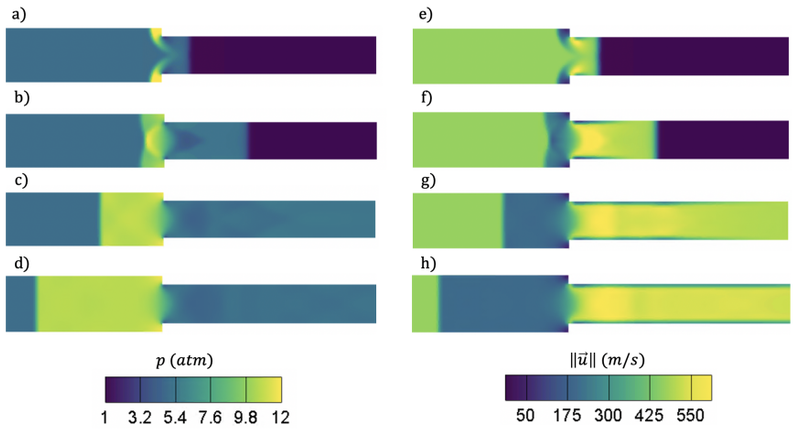

Figure 2.7: Time series of pressure (a-e) and velocity (f-j) fields for $M_i = 2.1$, $\alpha = 1.45$. Time elapsed: 0.096 ms.

Besides nonlinear waves, there are several noteworthy flow features whose characteristics depend on the incident shock strength and area ratio. For area divergence, a pair of eddies is clearly visible at the jet edges, such as shown in figure 2.3. Some time after the passage of the incident shock, these eddies form permanent recirculation zones whose streamwise/spanwise length ratio appears to be proportional to that of the area change. This appears to be the familiar phenomenon of vortex shedding from an impulsive starting jet. Also, for a sufficiently strong incident shock, the flow entering the area change becomes sonic, producing the supersonic jet shown in figure 2.4, whose characteristics depend on the static pressure of the exiting fluid jet. This is the familiar case of the supersonic diverging nozzle whose behavior is controlled by a back pressure; in this case, the back pressure is governed by the area ratio and incident shock strength. This jet is surrounded by recirculation zones and contains the familiar "shock diamond" pattern of alternating oblique shocks and expansion fans.

These five different conditions shown in Figures 2.3-2.7 were chosen as they are each representative of at least five categories of two-dimensional behavior; these categories are summarized in figure 2.8. This classification is distinct from that shown in figure 2.1, obtained from Salas et al., as it depends on 2D flow features and is further detailed in the following section. In brief, regime 1 transitions to regime 2 when the flow entering the area change becomes choked, regime 3 when the resulting supersonic jet becomes under-expanded, and regime 4 when the jet expands to the confines of the secondary duct. Regime 5 encompasses all contracting duct cases.

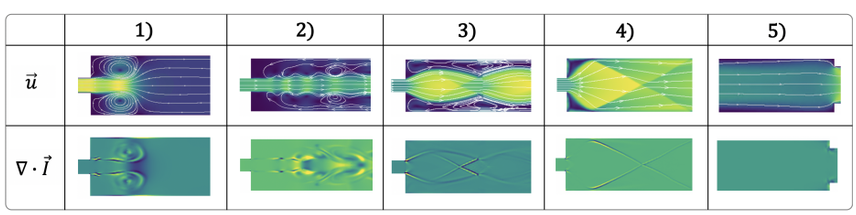

Figure 2.8: Near field flow regimes. Snapshots are taken from 1) $M_i = 1.1, \alpha = 0.25$ (see figure 2.3), 2) $M_i = 1.5, \alpha = 0.25$ (see figure 2.4), 3) $M_i = 2.1, \alpha = 0.25$ (see figure 2.5), 4) $M_i = 3.5, \alpha = 0.25$ (see figure 2.6), and 5) $M_i = 2.1, \alpha = 0.25$ (see figure 2.7).

DISTRIBUTION A: Distribution approved for public release.

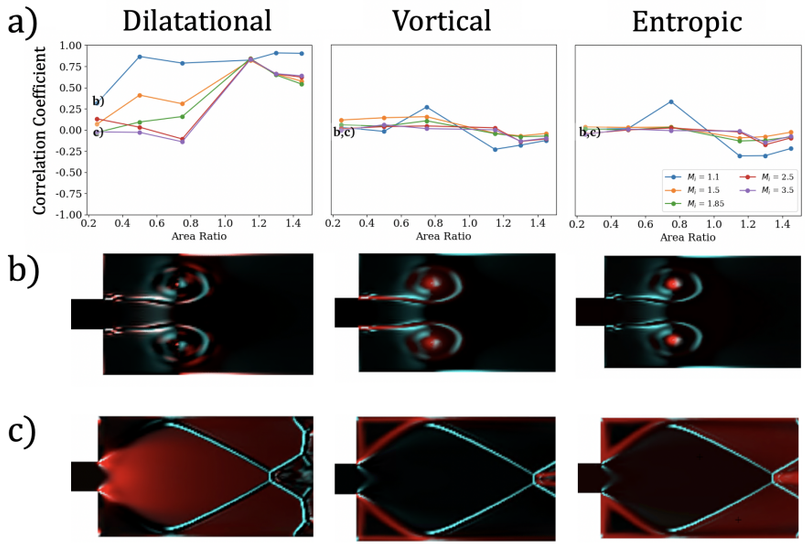

Figure 2.9: a) Time-averaged normalized correlation coefficient between disturbance energy flux field and dilation, vorticity, and entropy fields over the cases studied. Spatial overlap (white) between flux (cyan) and dilatation, vorticity, and entropy (red) for b) $M_i = 1.1$, $\alpha = 0.25$ case and c) $M_i = 2.5$, $\alpha = 0.25$ case.

The disturbance energy characteristics are correlated with prominent flow features. First, consider regime 1, detailed further in figure 2.3. In this case, the disturbance energy flux in the near-field zone is associated with the pair of eddies at the far end of the resulting fluid jet, as shown by figure 2.8. If the fluid entering the jet is sonic or supersonic, the dominant sources of disturbance energy flux are either the recirculation zones outside the fluid jet or the oblique shocks / expansion fans within the jet itself. The former appear to dominate in regions where the exiting fluid is either over-expanded (that is, the pressure of the exiting jet is less than ambient, producing regime 2 in figure 2.8) or only slightly under-expanded, in which case the jet expands slightly before contracting repeatedly, forming a shock-diamond pattern (regime 3 in figure 2.8). In cases where the jet is sufficiently under-expanded that the resulting jet fills the channel and doesn't contract, the oblique shocks / expansion fans are coincident with locations of strongest flux (regime 4 in figure 2.8). Moreover, there appear to be little to no near-field phenomena of particular note for the converging duct cases (regime 5 in figure 2.8).

Figure 2.9 shows the correlation between the disturbance energy flux field and dilatation, vorticity, and entropy fields. In most cases, the disturbance energy flux field correlates most strongly with the dilatation field and correlates weakly with the vorticity and entropy fields. As an example, consider the case shown in figure 2.9b, where elevated energy flux is correlated most strongly with regions of vortex rollup. One can clearly observe, however, that of the three fields, the dilatational field has the greatest correspondence with the disturbance energy flux. These results suggest that most disturbance energy lies in the dilatational mode. The reasons for this can be understood from the leading order energy flux term, $F_1 \equiv \nabla \cdot (p_1 \vec{u}_1)$. The 1st-order pressure fluctuation p_1 only has a dilatational component [20]; thus, at first order, the disturbance energy flux results from the dilatational mode *only*. Therefore, any disturbance energy flux from the vortical or entropic disturbances would have to result from higher-order effects whose magnitude is dominated by this first-order effect.

For $\alpha < 1$, this trend weakens as the jet becomes less expanded; that is, as both α and M_i increase such that the jet pattern shifts from 2 to 4. The reason for this can be seen in figure 2.9c: for flow regimes 2 - 4, dilation values peak in the oblique wave train, whereas the disturbance energy flux reaches local extrema in both the oblique waves and in the surrounding flow separation zone. As the jet pattern shifts to regime 4, the greatest disturbance energy flux values are found in the oblique shocks; however, the disturbance energy reaches local maxima joined to local minima, whereas the dilation field has local minima only. This is why, as shown in figure 2.9a, the flux field becomes more *negatively* correlated with the dilation field for increasing α for the $M_i = 2.5$ and 3.5 cases. Visually inspecting figure 2.9b, the disturbance energy extrema corresponding to the recirculation zones coincide most strongly with those of the vorticity field and, to a lesser extent, the entropy field. Combining these observations, for cases where the area change leads to choked flow, the dilatation field (strongest in the oblique wave train), vorticity field (strongest at the edges of the jet,

DISTRIBUTION A: Distribution approved for public release.

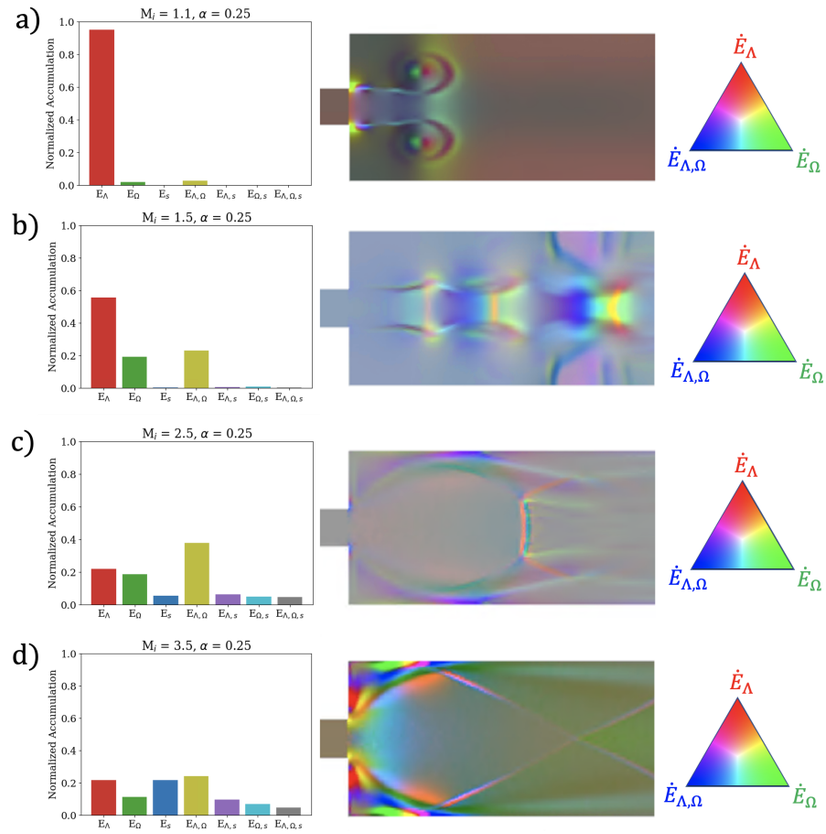

Figure 2.10: Relative magnitudes and spatial structures of the dominant disturbance energy accumulation terms for a) regime 1, b) pattern 2, c) regime 3, and d) regime 4. The terms shown in the red, green, and blue channels are indicated by the color triangles in the rightmost column.

where shear layers exist), and entropy field (strongest in the area surrounding the jet) are dominant in different spatial structures that rank differently in disturbance energy strength depending on M_i and α. The dilatation field produces proportionally more disturbance energy with increasing M_i and α.

Further insight into the disturbance energy flux distribution can be gained by quantifying the terms in the disturbance energy decomposition laid out in equations (2.39) - (2.44). For the diverging ducts, this information is summarized in figure 2.10. The bar graphs detail the relative magnitudes of the time- and space-averaged disturbance energy accumulation terms. The contours showcase the spatial distribution of the 3 accumulation terms of greatest interest. Taken together, these elucidate the relative importance of various disturbance energy accumulation terms (acoustic, vortical, acoustic-vortical, etc.) and the flow structures with which they're correlated. For the case of a weak shock (that is, regime 1 discussed in the previous paragraphs), acoustic disturbances are responsible for the bulk of the disturbance energy accumulation, with the other fields contributing little to none. This agrees with the information in figure 2.9a, in which the disturbance energy flux was most correlated with the dilatation field. Similarly, comparing the RGB contour of figure 2.10a with those of figure 2.9b, the various accumulation terms coincide spatially with their respective fields (i.e. the acoustic accumulation, the red channel of figure 2.10a, aligns with the dilatation field; the same holds for the vorticity and entropy fields).

As the incident shock increases in strength, we reach the "regime 2" under-expanded jet of figure 2.10b, at which point $\dot{E}_\Lambda$ (acoustic disturbance energy accumulation), $\dot{E}_\Omega$ (vortical accumulation) and $\dot{E}_{\Lambda,\Omega}$ (acoustic-vortical accumulation) have similar magnitudes (although the acoustic is roughly double the other two) and are the dominant contributors to the accumulation. As the incident shock strengthens and the resulting jet becomes more expanded (i.e. "regime 3" jet of figure 2.10c), the latter two terms overwhelm the acoustic accumulation and become the dominant contributors. This shows that the disturbance energy accumulation is dominated by acoustic-vortical products. Additionally, the other four terms ($\dot{E}_s$, $\dot{E}_{\Lambda,s}$, $\dot{E}_{\Omega,s}$, and $\dot{E}_{\Lambda,\Omega,s}$) become increasingly important, until, in the fully-expanded case of figure 2.10d, disturbance energy accumulation is deposited roughly equally between the seven terms. This would appear to result from the emerging entropic mode seen in figure 2.10c, reflecting the growing strength of entropy disturbances and, consequently, the growing magnitude of modal cross products with entropy (i.e. $\dot{E}_{\Lambda,s}$, $\dot{E}_{\Omega,s}$, and $\dot{E}_{\Lambda,\Omega,s}$) in the overall

DISTRIBUTION A: Distribution approved for public release.

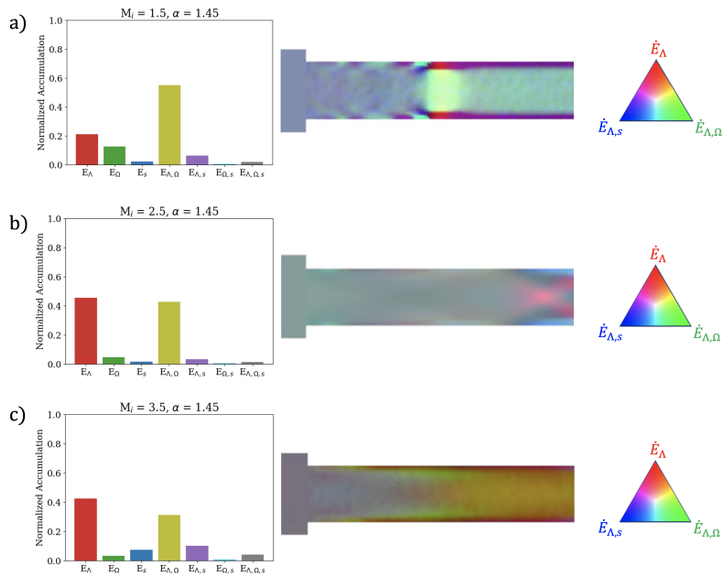

Figure 2.11: Relative magnitudes and spatial structures of the dominant disturbance energy accumulation terms for contracting ducts for 3 different incident shock strengths. The terms shown in the red, green, and blue channels are indicated by the color triangles in the rightmost column.

accumulation. This result explains the increased decorrelation of the disturbance energy flux with $\nabla \cdot \vec{u}$, $\nabla \times \vec{u}$, and s shown in figure 2.9 with increased incident shock strength increases; i.e., the energy flux is increasingly dominated by products of these canonical disturbances.

Examining the RGB contours of figure 2.10b-d, acoustic energy accumulation is strongest at the oblique shocks within the supersonic jet, while vortical accumulation is strongest at the edges of the jet, where recirculation zones exist. Examining the entropic accumulation (blue channel) of figure 2.10d, the entropic accumulation is also maximized on the jet edges and has large values between shock diamonds. This last case agrees with figure 2.9c; that is, the acoustic, vortical, and entropic accumulations once again appear to coincide with their respective fields as expected. The acoustic-vortical accumulation ($\dot{E}_{\Lambda,\Omega}$), the other dominant contributor for the supersonic jets, is maximized in the Mach disks that separate successive shock diamonds, where the flow is simultaneously expanded and turned. These results suggest that these processes within the jet increase the amount of acoustic-vortical disturbance energy accumulation as the jet expands.

For contracting ducts, the distribution of disturbance energy accumulation is summarized in figure 2.11. Even for weak incident shocks, the acoustic energy accumulation is always smaller than the acoustic-vortical accumulation. The former appears to be strongest at the transverse shocks that persist shortly after transmission into the smaller duct, while the latter appears to dominate in the interior of these shocks. Thus, for contracting ducts, the acoustic-vortical accumulation is a significant contributor to the overall disturbance energy. Also present is the acoustic-entropic accumulation, which appears to be strongest near the duct boundaries. As the incident shock is strengthened, the entropic and acoustic-entropic accumulations outweigh the acoustic-vortical accumulation, while the acoustic accumulation maintains its relative importance. This may explain why the correlation between the disturbance energy flux and dilatation fields remains constant with increasing shock strength, as shown in figure 2.9a. Combined with the diminishing importance of the vortical accumulation, these observations suggest that vortical disturbances become overwhelmed by entropic ones as incident shock strength increases; these entropic disturbances, in conjunction with strong pressure gradients (acoustic disturbances), produce strong acoustic-entropic disturbance energy.

Combining the above observations, the differing jet patterns in the near-field zones have varying strengths in each of the seven disturbance energy accumulation terms. Acoustic disturbances are strong for all jet patterns observed; as the incident shock increases in strength and produces stronger jets, these disturbances work in tandem with emerging vortical and entropic disturbances to produce cross-product disturbance energy accumulation. Energy accumulation is dominated by acoustic and vortical disturbance products for contracting ducts; the bar graph of figure 2.11b suggests that even relatively weak vortical disturbances are responsible for a significant portion of the energy accumulation when acoustic disturbances are present. Furthermore, these decompositions provide further insight into the alternative visualization approach of determining the correlation of instantaneous disturbance energy flux with the dilatation, vorticity and entropy fields.

DISTRIBUTION A: Distribution approved for public release.

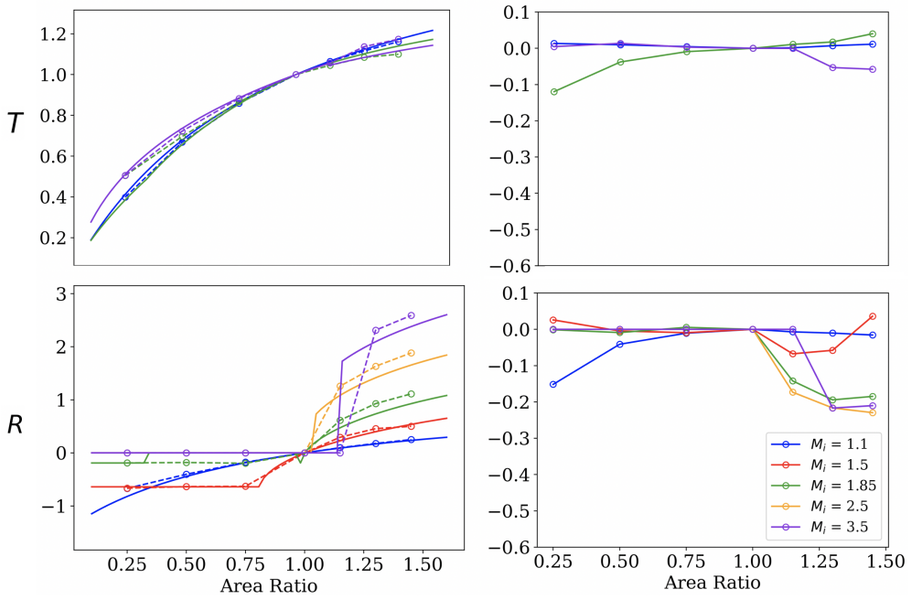

Figure 2.12: Reflection and transmission coefficients over the range of cases studied. Left column: values calculated using quasi one-dimensional (solid line) and CFD (circles). Right column: difference in quasi one-dimensional value and CFD calculated.

2.3.2 Quantitative Shock Behavior

Numerical Calculations

Figure 2.12 plots the dependence of R and T on area ratio at different incident Mach numbers, showing both quasi one-dimensional and the full CFD calculations. The right plot shows the difference between the two calculation approaches. Interestingly, the transmission coefficient is much less sensitive to the incident shock strength than the reflection coefficient. As expected, T is less than 1 for area divergences ($\alpha < 1$) and greater than 1 for area convergences. The reflection coefficient varies strongly with both α and M_i. For a large enough area ratio (i.e. a sudden enough contraction), the reflection coefficient increases in a nearly linear manner with M_i; this represents a limiting behavior for the reflection coefficient.

As might be expected, discrepancies between the two results grow as the area ratio deviates from unity in either direction (noting that the exact solution is one dimensional when the area ratio is unity). Overall, however, the quasi 1D calculations predict reasonably accurate values of R and T . This overall good agreement suggests that, while 2D disturbances have pronounced effects on the flow field close to the area jump, their lasting effects on the transmitted and reflected waves are fairly minor. This result is not only fundamentally interesting but also consequential for reduced order models of the phenomenon, as it shows that quasi one-dimensional considerations can be used to quite accurately understand and quantify the effect of the area change on the reflected and transmitted shock waves.

We next consider power reflection, transmission, and accumulation. Here the story is more nuanced in terms of errors in the dissipation predicted by quasi one-dimensional results. The dependence of R_Π, T_Π, and C_e upon area ratio, showing results for both flow models, are shown in figure 2.14. The deviation between the quasi 1D and CFD results are again plotted on the right. Once again, the values are quite similar between the two models. Moreover, as with T, T_Π and C_e, the largest deviations appear for larger area changes. Unlike T, however, T_Π varies with both M_i and α. Furthermore, R_I shows little variation between the two results except in the case of very strong and very weak shocks' interacting with a large area divergence; this contrasts with the behavior of R noted in the previous section.

Unlike T, T_Π exceeds unity for sufficiently strong shocks for diverging ducts with certain area ratios. This does not indicate that energy conservation is violated; it merely indicates the presence of stronger energy accumulation terms in the region between the shocks owing to the transient nature of the problem (see equations (2.27) and (2.28)). For instance, consider the balance of *total* energy between the waves in the weak shock case. By employing the perturbation methods discussed in the next section, the following can be demonstrated for the quasi-1D method:

$$\frac{\text{Transmitted total power}}{\text{Incident total power}} = \frac{\rho_4 u_4 h_{T4} A_t}{\rho_3 u_3 h_{T3} A_i} = \frac{2}{\alpha + 1} + \mathcal{O}(M_i - 1) \tag{2.45}$$

DISTRIBUTION A: Distribution approved for public release.

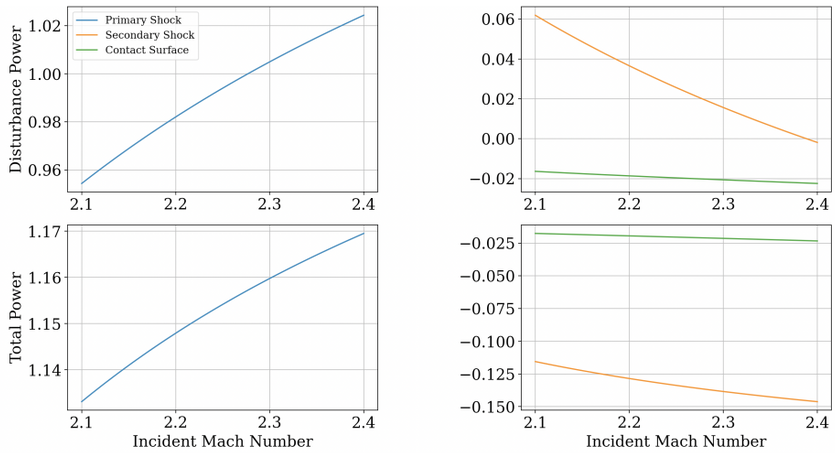

Figure 2.13: Total and disturbance power transmission coefficients for the primary shock, secondary shock, and contact surface for $\alpha = 0.5$ calculated using the quasi-1D method.

$$\frac{\text{Reflected total power}}{\text{Incident total power}} = \frac{\rho_3 u_3 h_{T3} - \rho_7 u_7 h_{T7}}{\rho_3 u_3 h_{T3}} = \frac{\alpha - 1}{\alpha + 1} + O(M_i - 1) \tag{2.46}$$

$$\frac{\text{Incident - Transmitted - Reflected total power}}{\text{Incident total power}} \propto (\alpha - 1)(M_i - 1)^5 + O(M_i - 1)^6 \tag{2.47}$$

One notes the following from the above expressions. First, even in the acoustic ($M_i = 1$) limit, the total power transmission ratio exceeds unity, but this is balanced by a negative total power reflection coefficient, such that the two sum to unity up to $O(M_i - 1)$. This unfamiliar result pertains to the *total* energy, not the *disturbance* energy; the latter produces the more familiar result for linear acoustics, as discussed in Appendix B. Second, the third expression indicates that, at $O(M_i - 1)$, the power of the transmitted and reflected waves exceed that of the incident wave for diverging ducts (since (α - 1) < 0). This discrepancy is due to the contact surface present in the quasi-1D model. Such flow disturbances (the reflected wave and contact surface in this example) supply the necessary power to allow the transmitted power to exceed that of the incident shock. As stated before, this is possible due to the transient nature of the physics; the disturbances accumulate or dissipate the necessary power required to maintain convective energy balance. Finally, we note that this phenomenon is caused by the *frontal* nature of the shocks; that is, the post-shock state persists indefinitely and does not return to its condition it was at before the shock arrived. The case of shock "pulses," in which the fluid behind the shock eventually returns to rest (when, for example, a piston compresses the gas by a certain length) represents an entirely different phenomenon whose energy flux physics should be the subject of future work.

With this in mind, consider the power balance highlighted in figure 2.13. For the quasi-1D method, the disturbance power transmission coefficient exceeds unity when $M_i \approx 2.277$. Observing the top right plot, one notes that the contact surface has negative power flux (that is, the power flow of the downstream flow *exceeds* that of the upstream flow) and the secondary shock has positive disturbance power flux up to $M_i \approx 2.389$. As M_i increases, the power fluxes of both waves decrease, enabling a corresponding increase in that of the transmitted wave. As noted in the preceding discussion, the *total* power transmission coefficient exceeds unity in all cases. Unlike the disturbance power transmission coefficient, the total power transmission coefficient for the secondary shock is always negative; there are some values of M_i for which the disturbance power flux decreases across the shock but the total power flux increases. Again, it should be emphasized that total energy and disturbance energy are distinct quantities with wholly different qualitative and quantitative characteristics. For both energy metrics, however, the transmission coefficients for the three flow disturbances (the primary shock, secondary shock, and contact surface) sum to unity. In other words, their *combined* power flux equals that of the incident shock, thereby preserving energy conservation.

C_e is *over*-predicted by the quasi-1D theory in nearly every case except those for weak shocks. Thus, despite not explicitly accounting for 2D, near-field disturbances, the quasi-1D theory partially captures the disturbance energy accumulation (the secondary transmitted shock of zone Ic in figure 2.1, for instance, is one phenomena responsible for this) not seen in the 2D results.

These quasi one-dimensional calculations can be generalized by adding additional physics to partially capture two-dimensional effects. For example, consider the recirculation patterns exhibited

DISTRIBUTION A: Distribution approved for public release.

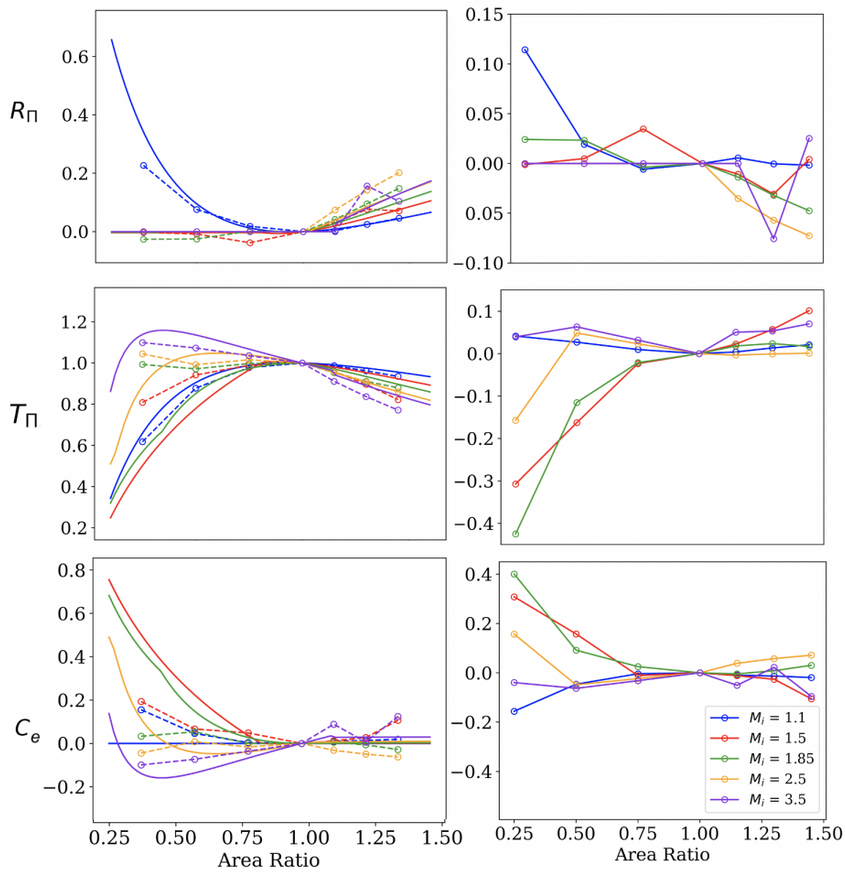

Figure 2.14: Power reflection, transmission, and accumulation coefficients over the cases studied. Left column: values calculated using quasi one-dimensional (solid line) and CFD (circles) approaches. Right column: difference in quasi one-dimensional and CFD values.

for weak shock interactions with a diverging duct (behavior i in figure 2.8). This flow separation associated with a sudden flow expansion causes the flow to increase in entropy. Flow separation can be incorporated into the quasi 1D approach by accounting for this entropy jump. Using the entropy jump value previously developed by Isaacson [15], valid for $\alpha \in (0.2, 1)$, leads to:

$$\Delta s = \mathscr{C}_v[(1-\alpha)^2 + (1-\alpha)^6]\gamma\delta M_7^2 \tag{2.48}$$

Here, $\mathscr{C}_v$ is the constant volume specific heat. This can be combined with the steady energy conservation equation and Gibb's relations to obtain a more accurate set of relations between the pre- and post-area change conditions. The effects of such a correction can be most clearly seen in R_Π, as shown in figure 2.15 below; for the most severe area increase studied, errors between quasi 1D and CFD was reduced from 50% to 6%.

Analytical Results for Weak Shocks

The results of the previous section can be further interpreted by writing explicit solutions from the quasi 1D theory, obtained by a perturbation expansion in powers of $(M_i - 1)$. We present results with the leading order nonlinear corrections for T, R, T_Π, R_Π, and C_e from their linear acoustic relations next (see the Appendix for details):

DISTRIBUTION A: Distribution approved for public release.

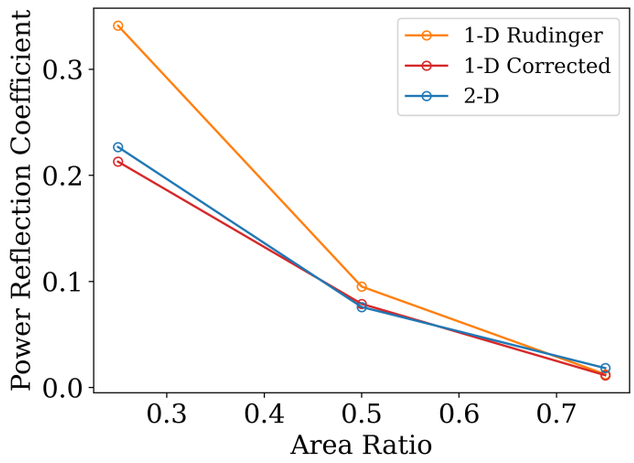

Figure 2.15: Power reflection coefficient for various diverging ducts calculated using the quasi-1D method, corrected quasi-1D method accounting for flow separation, and 2D CFD.

$$T = \frac{2\alpha}{\alpha+1} + \frac{2\alpha(\alpha-1)(\delta-1)}{\kappa(\alpha+1)^2}(M_i-1) + O(M_i-1)^2 \tag{2.49}$$

$$R = \frac{\alpha-1}{\alpha+1} + \frac{2(\alpha-1)(\alpha\kappa+2)}{\kappa(\alpha+1)^2}(M_i-1) + O(M_i-1)^2 \tag{2.50}$$

$$T_\Pi = \frac{4\alpha}{(\alpha+1)^2} + \frac{4\alpha(\alpha-1)(\delta-1)}{\kappa(\alpha+1)^3}(M_i-1) + O(M_i-1)^2 \tag{2.51}$$

$$R_\Pi = \left(\frac{\alpha-1}{\alpha+1}\right)^2 - \frac{4\alpha(\alpha-1)(\delta-1)}{\kappa(\alpha+1)^3}(M_i-1) + O(M_i-1)^2 \tag{2.52}$$

$$C_e = \begin{cases} \frac{64\delta(\alpha-1)\alpha^2(1+\alpha[4+7\alpha])}{3\kappa^3(\alpha+1)^6}(M_i-1)^4 + O(M_i-1)^5, & \alpha < 1 \\ \\ \frac{128\delta(\alpha-1)\alpha^3}{\kappa^3(\alpha+1)^5}(M_i-1)^4 + O(M_i-1)^5, & \alpha > 1 \end{cases} \tag{2.53}$$

Several important observations can be made from these equations. First, all of the expressions limit to their classical acoustic expressions (see [19]). While the above terms only depend on α in the acoustic limit, nonlinear corrections depend on the incident shock strength and the specific heat ratio of the gas, γ. Second, while nonlinear corrections to T, R, T_Π, R_Π, occur at leading order in (M_i-1), the correction to C_e occurs at $O(M_i-1)^4$, implying that it is very weak at low Mach numbers. Since the quasi 1D theory only accounts for dilatational and entropy disturbances (i.e., not vortical), energy exchange only occurs between these two disturbances in the quasi 1D problem. Moreover, since at $O(M_i-1)^2$ and lower there is no entropy produced by shocks, energy in the dilatational disturbances are conserved to that order. The area change rearranges the energy in the incident shock between the reflected and transmitted shock, but the power carried away by these reflected/transmitted waves exactly equals that of the incident wave up to $O(M_i-1)^3$. To further understand this point for this specific problem, consider equation (2.28). In this case, the area change is isentropic and steady, so there it has no net disturbance energy flux, leaving only the unsteady accumulation in the near-field zone, given by equation (2.26). The leading order contribution to the power accumulation is the jump in stagnation enthalpy flux across the contact surface. Because the pressure and velocity are continuous across the contact surface, this reduces to the following.

$$\rho_4 u_4 h_{T4} - \rho_5 u_5 h_{T5} = \frac{u_4^3}{2}(\rho_4 - \rho_5) \tag{2.54}$$

This expression explicitly shows that u_4^3 is $O(M_i-1)^3$ in magnitude. Since the contact surface only exists at $O(M_i-1)^3$ and higher, the jump in density across the contact surface is $O(M_i-1)^3$ in magnitude; thus, the unsteady accumulation of disturbance energy in the near-field zone is only $O(M_i-1)^6$ in magnitude. Because I_i is $O(M_i-1)^2$ in magnitude, C_e is $O(M_i-1)^4$ in magnitude. Summarizing the above points, the quasi-1D theory only accounts for entropy and acoustic disturbances; thus, there is disturbance energy accumulation up to the order at which entropy disturbances

DISTRIBUTION A: Distribution approved for public release.

appear. Consequently, transfer of energy out of the shock into other disturbances only occurs at very high order (i.e. its magnitude is quite small). This result was noted more generally by Jenvey [17] who stated that acoustic energy transport due to mass flux fluctuations is conserved to arbitrary order for irrotational, homentropic flow; and Doak [9], who noted that such flows exist in a "local fluctuating dynamical equilibrium" in which the net power flux is zero.

These quasi-1D near-field power accumulation results can be similarly modified to account for flow separation using the correction developed in equation (2.48). If this equation is added to the system to be solved, one obtains the following new expressions for the above variables:

$$T = \frac{2\alpha}{\alpha+1} + \left[\frac{2\alpha(\alpha-1)(\delta-1)}{\kappa(\alpha+1)^2} - \frac{4\alpha F(\alpha)}{\kappa(1+\alpha)^3}\right](M_i-1) + O(M_i-1)^2 \tag{2.55}$$

$$R = \frac{\alpha-1}{\alpha+1} + \left[\frac{2(\alpha-1)(\alpha\kappa+2)}{\kappa(\alpha+1)^2} + \frac{4F(\alpha)}{\kappa(1+\alpha)^3}\right](M_i-1) + O(M_i-1)^2 \tag{2.56}$$

$$T_\Pi = \frac{4\alpha}{(\alpha+1)^2} + 4\alpha\left[\frac{(\alpha-1)(\delta-1)}{\kappa(\alpha+1)^3} - \frac{4F(\alpha)}{\kappa(1+\alpha)^3}\right](M_i-1) + O(M_i-1)^2 \tag{2.57}$$

$$R_\Pi = \left(\frac{\alpha-1}{\alpha+1}\right)^2 - 4\alpha(\alpha-1)\left[\frac{\delta-1}{\kappa(\alpha+1)^3} - \frac{2F(\alpha)}{\kappa(\alpha+1)^4}\right](M_i-1) + O(M_i-1)^2 \tag{2.58}$$

$$C_e = \frac{8F(\alpha)}{\kappa(1+\alpha)^3}(M_i-1) + O(M_i-1)^2, \tag{2.59}$$

where $F(\alpha) \equiv (1-\alpha)^2 + (1-\alpha)^6$. This equation has noteworthy consequences. First, the accumulation coefficient is now $O(M_i-1)$ in magnitude. Thus, although this coefficient is small in both cases, Rudinger's method under-predicts the accumulation by orders of magnitude in the weak shock case (in the framework of equation (2.48)). Second, the aforementioned discrepancies in T, R, T_Π, and R_Π are first-order effects. It is also worth noting that using equation (2.48) correctly predicts the sign of this discrepancy; neglecting these effects causes one to over-predict T, T_Π, and R_Π and under-predict R. Furthermore, because of the form of $F(\alpha)$, these effects are most significant at lower α (that is, more severe area increases), but their prominence diminishes sharply with increasing α (that is, for less severe area increases).

2.4 Conclusions

The interactions between shock waves and discrete area changes have been studied using both computational fluid dynamics and quasi-steady, quasi-one dimensional calculations (Rudinger's Method). The former method reveals five categories of 2D, transient "near-field" phenomena that persist near the area change after the passage of the incident shock; these categories, which depend on 2D flow features, are distinct from those used in the quasi-1D theory, which depend on the structure of the 1D wave patterns (contact surfaces, reflected shocks or expansion waves, transmitted shocks). The observed flow regime depends on the incident shock strength and the area ratio. The transfer of disturbance energy from the shock waves to such near-field disturbances was also analyzed. This revealed that disturbance energy is spatially correlated with flow regimes in the near field (vortex roll-up, shock diamonds, etc.). The flow regime responsible for the greatest disturbance energy flux depends on the incident Mach number and area ratio.

This work represents the first study, to our knowledge, investigating how disturbance energy is produced by acoustic, vortical, and entropic disturbances of arbitrary magnitude during the shock/area change interaction. Correlating the disturbance energy flux with dilation, vorticity, and entropy reveals that the dominant disturbance depends on the category of near-field behavior. For example, for a weak shock, dilatational disturbances are strongest. Formally decomposing the disturbance energy further reveals the relative importance of these disturbances, and that they interact to produce disturbance energy in nonlinear cross-products. For diverging ducts, such interactions eventually cause disturbance energy to change at nearly equal rates across all disturbances and their cross-products. For contracting ducts, vortical disturbances contribute less disturbance energy than entropy disturbances with increasing shock strength; these disturbances interact with ever-present acoustic disturbances to produce energy in cross-product terms.

Comparison between CFD and the quasi-1D method reveals good agreement between the two. This suggests that quasi-1D methods accurately capture the asymptotic behavior of wave reflections and transmissions, an important observation considering the vast differences in computational complexity between these methods. However, the near-field power accumulation resulting from the

DISTRIBUTION A: Distribution approved for public release.

traveling shock waves can be off by orders of magnitude for weak shocks, as discussed in the next section. Furthermore, we show how to resolve some of the aforementioned quantitative differences by accounting for the entropy rise associated with flow separation in the near field.

These results show that shock transmission is primarily effected by area ratio, while shock reflection is greatly influenced by both area ratio and incident Mach number. For large enough area contractions, the reflection coefficient is influenced by incident Mach number only. Using perturbation methods, we quantified the order of magnitude of important physical effects like power accumulation and provide analytic, asymptotic expressions for variables of interest. We demonstrated that accumulation has a notably low order of magnitude in the weak shock case. However, this order of magnitude, while low in both cases, is severely under-predicted when near-field phenomena are neglected. This is because the quasi-1D method only accounts for dilatational and entropic disturbances; because the latter only appear at high orders, this method conserves dilatational energy in the shocks to 3rd order. This showcases the readiness of physical insight and ease of calculation provided by such methods, improving both the simplicity and transparency of quasi-1D methods.

2.5 Appendix: Perturbation Expansion for Weak Shocks

In this section, we present asymptotic, quasi one-dimensional results referred to in section 2.1. In general, one cannot obtain an analytical expression for R and T using Rudinger's method. However, such expressions can be obtained by expanding the governing equations in powers of (M_i - 1). During this interaction, we have the following system of equations.

$$\alpha = \frac{M_5}{M_7}\left(\frac{1+\delta M_7^2}{1+\delta M_5^2}\right)^{\frac{\kappa}{2\delta}} \tag{2.60}$$

$$p_5 = p_7\left(\frac{1+\delta M_7^2}{1+\delta M_5^2}\right)^{\frac{\gamma}{2\delta}} \tag{2.61}$$

$$u_5 = M_5 c_5 = M_5 c_7\left(\frac{1+\delta M_7^2}{1+\delta M_5^2}\right)^{\frac{1}{2}} \tag{2.62}$$

$$u_5 = u_4 = \frac{c_1}{\kappa}\left(\sqrt{\frac{\kappa p_5 + \delta p_1}{\gamma p_1}} - \sqrt{\frac{\gamma p_1}{\kappa p_5 + p\delta p_1}}\right) \tag{2.63}$$

The first equation is obtained by combining the conservation equations for mass and energy with the Poisson adiabat (that is, equations (2.3), (2.5), and (2.12)), the second equation simply states that the total pressure is conserved throughout the area discontinuity (consistent with isentropic flow), and the third equation is an alternate expression of the energy conservation equation. The final equation is obtained from the normal shock relations across the transmitted shock after some algebra. The numerical subscripts are summarized in figure 2.2. The type of reflected wave depends on whether the area increases (resulting in a reflected expansion wave) or decreases (resulting in a reflected shock). For now, we limit consideration to the former case, wherein we have the following equations for p_7 and c_7.

$$p_7 = p_3\left(\frac{1+\delta M_3}{1+\delta M_7}\right)^{\frac{\gamma}{\delta}} \tag{2.64}$$

$$c_7 = c_3\left(\frac{1+\delta M_3}{1+\delta M_7}\right) \tag{2.65}$$

This results in a system of four nonlinear equations for the variables M_5, M_7, p_5, and u_5. Although this cannot be solved explicitly in general, explicit solutions can be determined to the desired order of accuracy by expanding each variable in the following manner.

$$M_7 \equiv \nu_0 + \nu_1 + \ldots + \nu_n, \quad M_5 \equiv \mu_0 + \mu_1 + \ldots + \mu_n$$
$$\Pi_5 \equiv \frac{p_5}{p_1} - 1 \equiv \pi_0 + \pi_1 + \ldots + \pi_n, \quad u_5 \equiv v_0 + v_1 + \ldots + v_n$$

DISTRIBUTION A: Distribution approved for public release.

At order n, we have the following system of linear equations for $(\nu, \mu, \pi, v)_n$.

$$\begin{bmatrix} A_C B_C & A_C C_C & 1 & 0 \\ A_V B_V & A_V C_V & 0 & 1 \\ B_A & C_A & 0 & 0 \\ 0 & 0 & -D_W(2\gamma + \kappa P_n) & 1 \end{bmatrix} \begin{bmatrix} \nu_n \\ \mu_n \\ \pi_n \\ v_n \end{bmatrix} = \begin{bmatrix} A_C - P_n - 1 \\ M_n A_V - V_n \\ A_A \alpha - 1 \\ 2P_n D_W(\gamma + \kappa P_n) - V_n \end{bmatrix} \tag{2.66}$$

$$N_n \equiv \sum_{k=0}^{n-1} \nu_k, \quad M_n \equiv \sum_{k=0}^{n-1} \mu_k, \quad P_n \equiv \sum_{k=0}^{n-1} \pi_k, \quad V_n \equiv \sum_{k=0}^{n-1} v_k,$$

$$A_C \equiv \frac{p_3}{p_1} \left(\frac{1 + \delta M_3}{1 + \delta N_n} \right)^{\frac{\gamma}{\delta}} \left(\frac{1 + \delta N_n^2}{1 + \delta M_n^2} \right)^{\frac{\gamma}{2\delta}},$$

$$A_V \equiv a_3 \left(\frac{1 + \delta M_3}{1 + \delta N_n} \right) \left(\frac{1 + \delta N_n^2}{1 + \delta M_n^2} \right)^{\frac{1}{2}}$$

$$A_A \equiv \frac{N_n}{M_n} \left(\frac{1 + \delta M_n^2}{1 + \delta N_n^2} \right)^{\frac{\kappa}{2\delta}},$$

$$B_C \equiv \frac{\gamma(1 - N_n)}{(1 + \delta N_n)(1 + \delta N_n^2)}, \quad B_V \equiv \frac{\delta M_n (1 - N_n)}{(1 + \delta N_n)(1 + \delta N_n^2)}, \quad B_A \equiv \frac{N_n^2 - 1}{N_n (1 + \delta N_n^2)},$$

$$C_C \equiv \frac{\gamma M_n}{1 + \delta M_n^2}, \quad C_V \equiv -\frac{1}{1 + \delta N_n^2}, \quad C_A \equiv \frac{1 - M_n^2}{M_n (1 + \delta M_n^2)},$$

$$D_W \equiv \frac{c_1}{2\gamma^2} \left(\frac{\gamma}{\gamma + \kappa P_n} \right)^{\frac{3}{2}}$$

Solving for M_5, M_7, p_5, and u_5 closes the system.

One can obtain simplified expressions for certain terms of interest by expanding them in a Taylor series in M_i centered about 1. The first 2 terms in the expansions for each variable are $O(M_i - 1)$ and $O(M_i - 1)^2$, respectively, while the 3rd term in each expansion is $O(M_i - 1)^3$. For comparison, consider the entropy jump across the incident shock, given by the below expression.

$$\begin{aligned} \Delta s &= \mathscr{C}_v \left[\log\left(\frac{p_3}{p_1} \right) - \gamma \log\left(\frac{\rho_3}{\rho_1} \right) \right] \\ &= \mathscr{C}_v \left[\log\left(\frac{\gamma M_i^2 - \delta}{\kappa} \right) - \gamma \log\left(\frac{\kappa M_i^2}{\delta M_i^2 + 1} \right) \right] \end{aligned} \tag{2.67}$$

Here, $\mathscr{C}_v$ is the constant volume specific heat. Making use of the aforementioned series expansion, note that this expression is $O(M_i - 1)^3$ in magnitude. Similarly, if one calculates s_5 and s_4 (the entropy after the area change and before the transmitted shock, respectively), note that the difference between the two is also $O(M_i - 1)^3$ in magnitude. The pressure jump across the shock, meanwhile, is $O(M_i - 1)$ in magnitude. This type of analysis yields equations (2.50) - (2.53) in the main text. We note the difficulty in grouping terms of the same order in $(M_i - 1)$ in the above procedure. For this reason, we utilized Wolfam Mathematica 12, which has powerful tools for this purpose. We strongly advise others to use a similar tool in reproducing the results of this paper. To demonstrate the convergence of this method toward the numerical results, figure 2.16 plots the absolute difference between the two against $(M_i - 1)$ and iteration number in the aforementioned iterative method. The left plot demonstrates the legitimacy of the approximation, as the errors have the correct slope on the log-log plot.

To understand how near-field effects alter the solution, consider equation (2.48), which accounts for the entropy jump resulting from the flow separation phenomena, neglected by Rudinger's method. In this case, making use of equation (2.67), we replace A_C, A_A, B_C, and B_A in equation (2.66) with A'_C, A'_A, B'_C, and B'_A given by the below equations.

$$A'_C \equiv \frac{p_3}{p_1} \left(\frac{1 + \delta M_3}{1 + \delta N_n} \right)^{\frac{\gamma}{\delta}} \left(\frac{1 + \delta N_n^2}{1 + \delta M_n^2} \right)^{\frac{\gamma}{2\delta}} \exp\left(-\frac{1}{2} \gamma N_n^2 F(\alpha) \right) \tag{2.68}$$

$$A'_A \equiv \frac{N_n}{M_n} \left(\frac{1 + \delta M_n^2}{1 + \delta N_n^2} \right)^{\frac{\kappa}{2\delta}} \exp\left(-\gamma N_n^2 F(\alpha) \right) \tag{2.69}$$

DISTRIBUTION A: Distribution approved for public release.

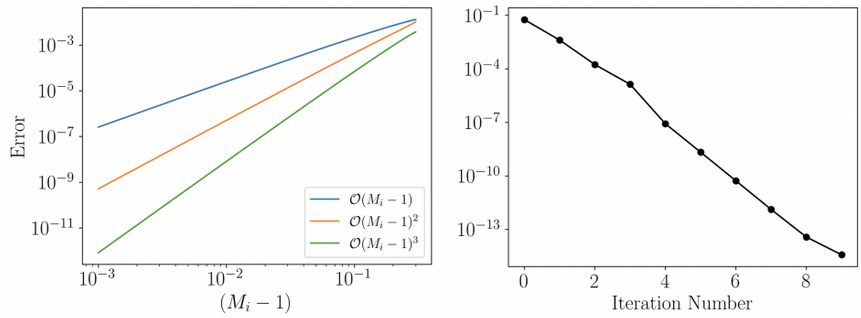

Figure 2.16: Absolute difference between the series approximation and numerical solution for transmitted Mach number M_t vs. $(M_i - 1)$ (left) and iteration number (right).

$$B'_C \equiv \frac{\gamma(1 + N_n[F(\alpha)(1 + \delta N_n)(1 + \delta N_n^2) - 1])}{(1 + \delta N_n)(1 + \delta N_n^2)} \tag{2.70}$$

$$B'_A \equiv \frac{[1 - 2\gamma F(\alpha)]N_n^2 - 2\delta\gamma F(\alpha)N_n^4 - 1}{N_n(1 + \delta N_n^2)} \tag{2.71}$$

$$F(\alpha) \equiv (1 - \alpha)^2 + (1 - \alpha)^6$$

If this new system is solved, one obtains equations (2.56) - (2.59).

If the area decreases, the system must be modified as follows. The reflected wave is now a shock, in which case we have the following equations for p_7 and c_7.

$$p_7 = p_3 \frac{\gamma(M_3 + \frac{W}{a_3})^2 - \delta}{\kappa} \tag{2.72}$$

$$c_7 = c_3 \frac{\sqrt{\left(\gamma[M_3 + \frac{W}{a_3}]^2 - \delta\right)\left(\delta[M_3 + \frac{W}{a_3}]^2 + 1\right)}}{\kappa(M_3 + \frac{W}{a_3})} \tag{2.73}$$

Here, W is the speed of the reflected wave, which represents a new unknown variable. Rather than solving for this new variable in terms of those of the original system, it is more convenient to include the following equation in the system and solve for it along with the others.

$$M_7 = \frac{1 + (M_3 + \frac{W}{a_3})(\delta M_3 - \frac{W}{a_3})}{\sqrt{\left(\gamma[M_3 + \frac{W}{a_3}]^2 - \delta\right)\left(\delta[M_3 + \frac{W}{a_3}]^2 + 1\right)}} \tag{2.74}$$

Because this system contains nonlinear multiples of W when expanded in a power series, is it necessary to replace it with the variable $\Omega \equiv 1 - \frac{W}{a_3}$, after which the expansion $\Omega \equiv \omega_0 + \omega_1 + ... + \omega_n$ can be utilized. The system is than successively solved at higher orders, starting from zeroth order. This results in the following system of linear equations for $(\omega, \nu, \mu, \pi, \nu)_n$.

$$\begin{bmatrix} F_N & 1 & 0 & 0 & 0 \\ A_C F_C & A_C B_C & A_C C_C & 1 & 0 \\ A_V F_V & A_V B_V & A_V C_V & 0 & 1 \\ 0 & B_A & C_A & 0 & 0 \\ 0 & 0 & 0 & -D_W(2\gamma + \kappa P_n) & 1 \end{bmatrix} \begin{bmatrix} \omega_n \\ \nu_n \\ \mu_n \\ \pi_n \\ \nu_n \end{bmatrix} = \begin{bmatrix} A_N - N_n \\ A_C - P_n - 1 \\ M_n A_V - V_n \\ A_A \alpha - 1 \\ 2P_n D_W(\gamma + \kappa P_n) - V_n \end{bmatrix} \tag{2.75}$$

DISTRIBUTION A: Distribution approved for public release.

$$N_n \equiv \sum_{k=0}^{n-1} \nu_k, \quad M_n \equiv \sum_{k=0}^{n-1} \mu_k, \quad P_n \equiv \sum_{k=0}^{n-1} \pi_k, \quad V_n \equiv \sum_{k=0}^{n-1} v_k, \quad W_n \equiv \sum_{k=0}^{n-1} \omega_k$$

$$A_N \equiv \frac{\delta M_3^2 + (2 - W_n)W_n + (\delta - 1)M_3(1 - W_n)}{\sqrt{(\gamma[M_3 + 1 - W_n]^2 - \delta)(\delta[M_3 + 1 - W_n]^2 + 1)}},$$

$$A_C \equiv \frac{\gamma(M_3 + 1 - W_n)^2 - \delta}{\kappa} \left(\frac{1 + \delta N_n^2}{1 + \delta M_n^2}\right)^{\frac{\gamma}{2\delta}},$$

$$A_V \equiv a_3 \frac{\sqrt{(\gamma[M_3 + 1 - W_n]^2 - \delta)(\delta[M_3 + 1 - W_n]^2 + 1)}}{\kappa(1 + M_3 - W_n)} \left(\frac{1 + \delta N_n^2}{1 + \delta M_n^2}\right)^{\frac{1}{2}}$$

$$A_A \equiv \frac{N_n}{M_n} \left(\frac{1 + \delta M_n^2}{1 + \delta N_n^2}\right)^{\frac{\kappa}{2\delta}},$$

$$B_C \equiv -\frac{\gamma N_n}{1 + \delta N_n^2}, \quad B_V \equiv -\frac{\delta M_n N_n}{1 + \delta N_n^2}, \quad B_A \equiv \frac{N_n^2 - 1}{N_n(1 + \delta N_n^2)},$$

$$C_C \equiv \frac{\gamma M_n}{1 + \delta M_n^2}, \quad C_V \equiv -\frac{1}{1 + \delta M_n^2}, \quad C_A \equiv \frac{1 - M_n^2}{M_n(1 + \delta M_n^2)},$$

$$D_W \equiv \frac{c_1}{2\gamma^2} \left(\frac{\gamma}{\gamma + \kappa P_n}\right)^{\frac{3}{2}},$$

$$F_N \equiv -\frac{\partial}{\partial \omega_n} M_7 \bigg|_{w_n = 0}, \quad F_V \equiv \frac{\delta M_n (1 + \gamma[1 + M_3 - W_n]^4)}{(1 + \delta[M_3 + 1 - W_n]^2)(\gamma[M_3 + 1 - W_n]^2 - \delta)(1 + M_3 - W_n)}$$

This system, when solved, yields the same expressions for T, R, T_Π, and R_Π up to $O(M_i - 1)^2$ as those for the increasing area case. Observing the definitions of these terms, one notes that the order at which certain physics affect these terms is one less than the order at which it affects the waves. For instance, consider the expression for the transmitted Mach number M_t.

$$M_t = 1 + \frac{2\alpha}{\alpha + 1}(M_i - 1) + \frac{2\alpha(\alpha - 1)(\delta - 1)}{\kappa(\alpha + 1)^2}(M_i - 1)^2 + O(M_i - 1)^3 \tag{2.76}$$

Comparing this with equations (2.50) - (2.53), one observes that the area ratio affects M_t at 1st order and the specific heat affects M_t at 2nd order; this is one order higher than the order at which these factors affect the above coefficients. Similarly, because the entropy jump across the wave is a 3rd-order quantity, the fact that the reflected wave is no longer isentropic when $\alpha > 1$ affects the coefficients at the 2nd order. As a consequence, the leading-order expression for C_e is also changed as follows.

$$C_e = \frac{128\delta(\alpha - 1)\alpha^3}{\kappa^3(\alpha + 1)^5}(M_i - 1)^4 + O(M_i - 1)^5 \tag{2.77}$$

Thus, although C_e varies with area ratio differently depending on whether the reflected wave is a shock or an isentropic expansion wave, its order of magnitude (in terms of shock strength) is the same in both cases.

DISTRIBUTION A: Distribution approved for public release.

Bibliography

[1] Anderson, J. D. Jr. 1990 *Modern Compressible Flow With Historical Perspective*, pp. 64-74 McGraw-Hill Publishing Company

[2] ANSYS, Inc 2020 Chapter 28: Solver Theory *Fluent 2020 R1 Theory Guide, Fluent Documentation*

[3] ANSYS, Inc 2020 Chapter 37: Using the Solver *Fluent 2020 R1 User's Guide, Fluent Documentation*

[4] Ben-Dor, G. and Elperin, T. 2001 *Handbook of Shock Waves, vol. II*, pp. 181-396, Academic Press.

[5] Brear, M., Nicoud, F., Talei, M., Giauque, A. and Hawkes, E. 2012 Disturbance energy transport and sound production in gaseous combustion *J. Fluid Mech.*, **707**, pp 53-73

[6] Cacoilo, A., Teixeira-Dias, F., Mourao, R., Belkassem, B., Vantomme, J. and Lecompte, D. 2018 Blast wave propagation in survival shelters: experimental analysis and numerical modeling *Shock Waves*, **28**, pp 1169-1183.

[7] Chu, B. T. and Kovasznay, L. S. G. 1957 Non-linear interactions in a viscous heat-conducting compressible gas *J. Fluid Mech.*, **3.5**, pp. 494-514.

[8] Crighton, D. G. 1985 The Kutta condition in unsteady flow *Annu. Rev. Fluid Mech*, **17**, pp 411-445

[9] Doak, P. E. 1989 Momentum potential theory of energy flux carried by momentum fluctuations, *J. Sound Vib.*, **131.1**, pp 67-90

[10] Fahy, F. 2000, *Foundations of Engineering Acoustics*, Academic Press.

[11] Ingard, U. and Singhal, V. 1975 Effect of flow on the acoustic resonances of an open-ended duct *J. Acoust. Soc. Am.*, **58**, 788-793.

[12] Gounko, Y. P. and Kavun, N. I. 2018 Starting Processes at Testing Inlets in Impulse Wind Tunnels, *ICMAR*.

[13] Hai-Tao, B. 2010 Numerical analysis on hydraulic system shockwave, *ICIC 2010*

[14] Hunter, J. K. and Keller, J. B. 1984 Weak Shock Diffraction *Wave Motion*, **6**, pp 79-89

[15] Isaacson, L. K. 2011 Deterministic prediction of the Entropy Increase in a Sudden Expansion, *Entropy*, **13**, pp 402-421

[16] Janardhanraj, S., Abhishek, K. and Jagadeesh, G. 2021 Insights into the shockwave attenuation in miniature shock tubes *J. Fluid Mech.* **910**, A3.

[17] Jenvey, P. L. 1989 The sound power from turbulence: a theory of the exchange of energy between the acoustic and non-acoustic fields, *J. Sound Vib.*, **131.1**, pp 37-66

[18] Kailasanath, K. 2020 Recent Developments in the Research on Pressure-Gain Combustion Devices, *Innovations in Sustainable Energy and Cleaner Environment*, pp 3-21

[19] Kinsler, L. E., Frey, A. R., Coppens, A. B. and Sanders, J. V. 2000 F̂undamentals of Acoustics, vol. IV, pp 149-150, 288-289, John Wiley & Sons, Inc

[20] Lieuwen, T.C. 2012 *Unsteady Combustor Physics*, pp 124-186 Cambridge University Press

DISTRIBUTION A: Distribution approved for public release.

[21] Lighthill, J. 1978 *Waves in Fluids*, pp 418-421, Cambridge University Press

[22] Marty, A., Daniel, E., Massoni, J., Biamino, L., Houas, L., Leriche, D. and Jourdan, G. 2018 Experimental and numerical investigations of shock wave propagation through a bifurcation, *Springer Nature, Shock Waves*, **29**, pp 285-296

[23] Meadows, K. R., 1997 A Study of Fundamental Shock Noise Mechanisms *NASA Technical Paper 3605*

[24] Mendoza, N. and Bowersox, R. D. W. 2013 On the Unsteady Shock Wave Interaction with a Backward-Facing Step: Viscous Analysis, *ISSW*, pp 1373-1378

[25] Menina, R., Saurel, R., Zereq, M. and Houas, L. 2011 Modelling gas dynamics in 1D ducts with abrupt area change *Shock Waves*, **21**, pp 451-466.

[26] Myers, M. K. 1991 Transport of energy by disturbances in arbitrary steady flows *J. Fluid Mech.*, **226**, pp 383-400

[27] Noiray, A. and Denisov, A. 2017 A method to identify thermoacoustic growth rates in combustion chambers from dynamic pressure time series *Proc. Combust. Inst*, **36.3**, pp 3840-3850

[28] Oppenhein, A. K., Urtiew, P. A. and Stern, R. A. 1959 Peculiarity of shock impingement on area convergence, *Phys. Fluids* **2**, pp 427-431.

[29] Rudinger, G. 1960 Passage of shock wave through ducts of variable cross section, *Phys. Fluids*, **3**, pp 449-455.

[30] Salas, M. D. 1991 Shock Wave Interaction with an Abrupt Area Change, *NASA Technical Paper 3113*

[31] Sekutkovski, B., Kostic, I., Stefanovic, Z., Simonovic, A., and Kostic, O. 2015 A hybrid RANS-LES method with compressible k-omegaSSTSAS turbulence model for high reynolds number flow applications *Teh. Vjesn.*, **22.5**

[32] Shoev, G. V., Bondar, Y. A., Khotyanovsky, D. V., Kudryavtsev, A. N., Maruta, K. and Ivanov, M. S. 2012 Numerical study of shock wave entry and propagation in a microchannel, *Thermophys.*, **19.1** pp 17-32

[33] Unnikrishnan, S., Gaitonde, D. V. 2021 Instabilities and transition in cooled wall hypersonic boundary layers *J. Fluid Mech.*, **915**, A26

[34] Urbano, A., Selle, L., Staffelbach, G., Cuenot, B., Schmitt, T., Ducruix, S. and Candel, S. 2016 Exploration of combustion instability triggering using Large Eddy Simulation of a multiple injector liquid rocket engine *Combust Flame*, **169**, pp 129-140

[35] Weiczorek K., Sensiau, C., Polifke, W. and Nicoud F. 2011 Assessing non-normal effects in thermoacoustic systems with mean flow *Phys. Fluids*, **23.10**, 107103.

[36] Wen, C., Karvounis, N., Walther, J. H., Ding, H. and Yang, Y. 2020 Non-equilibrium condensation of water vapour in supersonic flows with shock waves, *Int. J. Heat Mass Transf.*, **149**, 11910.

[37] Whitham, G. B. 1956 On the propagation of weak shock waves *J. Fluid Mech.*, **1**, pp 290-318

[38] Zinn, B. 1970 A theoretical study of non-linear damping by helmholtz resonators *J. Sound Vib.*, **13.3**, pp 347-356

DISTRIBUTION A: Distribution approved for public release.

Chapter 3

Simultaneous multiple laser beam intensity profile correction and its application to a vitiated bluff body combustor field

3.1 Introduction

Lean blowoff sets important operational limits on modern combustion systems. Being able to predict when it will occur, as well as how to delay its occurrence is an important scientific and engineering problem. A large literature on the problem exists for premixed and non-premixed systems, for a variety of flow configurations including jet flames [1-4], bluff body flames [5-10], swirl flames [11-15], and non-premixed flames [16-19].

Lean blowoff in recirculation stabilized flames is not a single step process – it occurs in at least 2 stages [20]. As flames approach blowoff, say by decreasing equivalence ratio or increasing flow velocity, they first enter "stage 1", where local extinction zones appear along the flame front. However, the overall flame and flow features remain relatively similar to a healthy, stable flame and the flame can persist indefinitely at this stage. Closer to blowoff, "stage 2" occurs where large sections of the flame are intermittently or permanently extinguished, there is large scale entrainment of reactants into the recirculating flow, and there is large scale disruption of the baseline fluid mechanics and hydrodynamic stability of the flow due to this entrainment.

Early studies established empirical blowoff correlations that were a function of operational parameters such as equivalence ratio, velocity, preheat temperature, jet/bluff body diameter, and so forth [5, 8, 9, 21-23]. Later work showed that these correlations are all essentially ratios of global chemical and fluid mechanic time scales, i.e., a Damköhler number [24]. Indeed, these global time scales based upon average properties have been largely successful at correlating blowoff, a somewhat surprising result given the complexity of the phenomenon, range of different competing processes, and the local spatio-temporal dependencies. It has been hypothesized that these correlations are essentially predictors of when extinction on the flame front starts to occur (which essentially involves a ratio of flow stretch rate and extinction strain rate), or "stage 1" of blowoff. It has been further argued [20] that correlations of "stage 1 onset" are successful because

DISTRIBUTION A: Distribution approved for public release.

this initial extinction stage is a necessary precursor to the following stage 2, and then ultimate blowoff.

Nonetheless, the "stage 2" phenomenon involves significantly more physics than simply local, stretch-induced extinction. For example, the recirculating shear flows used to stabilize flames in high velocity flows, such as wakes or backward facing steps, are generally subject to convective and global instability in the absence of combustion; e.g., the Bénard-Von Karman (BVK) global instability is a prominent feature of nonreacting wakes. Flames with sufficiently high density ratio, $\sigma = \frac{\rho_u}{\rho_b} = \frac{T_b}{T_u}$ (where the subscripts u and b denote the unburnt (pre-flame) and burnt (post flame) regions respectively, and ρ and T represent the density and temperature)) usually profoundly alter these isothermal hydrodynamic stability characteristics, often slowing the growth of the Kelvin-Helmholtz instability in shear layers, and stabilizing the global instability. For example, above a reactant to product density ratio of $\sigma \sim 2 - 3$ (exact value depending upon shear layer thickness, flame position, confinement effects, etc.), the BVK instability is suppressed in reacting wakes [25]. The BVK instability is present in lower density ratio stable flames, such as those encountered with highly preheated reactants. Moreover, a prominent feature of bluff body flames near blowoff is a profound change in the apparent stability of the flow. Even in high density wakes where the BVK instability is suppressed in stable flames, large scale sinuous flapping of the flame/flow is observed near blowoff, suggesting a re-emergence of the BVK instability [20].

A second prominent feature of recirculation stabilized flames near blowoff is permanent flame extinction at some downstream location as blowoff is approached. This behavior is reminiscent to what is observed in piloted flows where the presence of the pilot forces ignition at the burner lip but further downstream, presumably away from the influence of the pilot, extinction occurs [26-29]. As long as the pilot remains, such flames never really blowoff. Rather the downstream permanent extinction point moves progressively closer to the piloting point as flow velocities are increased or the equivalence ratio is decreased.

In recirculation stabilized flames, the role of the pilot is played by the recirculating combustion products which act as an ignition source in the nearfield. As a result, the flame generally stays attached to the burner/bluff body lip all the way to total extinction – an observation common to several studies [20, 30-32]. The only exception to this behavior that the authors are aware of are very small diameter bluff body stabilized flames [10] where the flame lifts off the bluff body. We hypothesize that this behavior occurs when the piloting recirculation zone (whose length scales with bluff body diameter) becomes the same size as the thermal zone over which the bluff body quenches the flow. Nonpremixed flames begin to blow off in a matter that is opposite to these premixed flames; the flame lifts off the burner with the liftoff height progressively increasing as blowoff is approached [2, 16, 17, 19].

As noted above, hydrodynamic stability and vorticity dynamics interact with flame extinction and hot product recirculation phenomena near blowoff. This vorticity comes from two sources. First, it flows into the domain from the separating bluff body boundary layer, where it is organized into concentrated vortices due to the Kelvin-Helmholtz instability. The interaction of the two bluff body shear layers further downstream results in further concentration and reorganization of this

DISTRIBUTION A: Distribution approved for public release.

vorticity into the staggered vortex street in nonreacting or low density ratio flames. Gas expansion, baroclinic vorticity, and increased gas viscosity alter these vorticity dynamics. However, gas expansion and enhanced viscosity act on existing vorticity, spreading out concentrated vorticity regions and preserve overall circulation. The second vorticity source is baroclinic production, which acts as a source or sink of vorticity and circulation. In flows with favorable pressure gradients where the flow is accelerated on average, the baroclinic-generated vorticity is of opposite sign to the background shear vorticity, causing a change in sign of vortical structures at some point downstream; alternatively but equivalently, it turns a confined wake flow into a jet flow because of flow acceleration [33]. Flames near blowoff are at high velocities and/or low flame speeds and generally interact much more prominently with the high stretch, shearing regions than stable flames, as shown in several works [22, 32, 34-37].

To fix notation going forward, we will consider the coordinate system shown in Figure 3.1. Most studies of the bluff body blowoff problem have confined their phenomenological explanations to two-dimensional (XY) vortex dynamics. However, a recent study from Fugger et al. [38, 39] demonstrated for the first time that three-dimensional vortex effects become increasingly prominent near blowoff. Additionally, three-dimensional secondary instabilities associated with reorientation of concentrated vortex tubes in the X direction are well known features associated with axially developing, initially two-dimensional shear layer instabilities. Finally, prominent three-dimensional effects also occur in the bluff body near field in cases where the bluff body is confined. As such, we will briefly summarize the nonreacting literature on three dimensional effects.

Consider first the configurations where the bluff body diameter (D) is small relative to its length (L), i.e., $\frac{L}{D} \gg 1$. These flows consist of three distinct regions – the wake, the shear layer and the bluff body boundary layer. Three-dimensional effects within the wake begin to manifest via two instability modes [40-43]. The first mode (mode A) causes the formation of vortex loops (about 3D – 4D apart) between the BVK vortex tubes. A deformed BVK vortex tube is pulled by the vortex tube upstream and stretched to form braids oriented in the X direction. The second mode (mode B) causes the formation of vortex pairs oriented in the X direction. It requires the induced velocity associated with already existing vortex tubes (through mode A) to imprint onto a newly forming vortex braid. During its transition to turbulence the wake also sees "spot-like" vortex dislocations/mismatches which can also contribute to the deviation from two dimensionality as viewed on the Z=0 plane [44]. Several studies have also looked at how end effects (stemming from the span walls at $Z = \pm\frac{L}{2}$) can lead to oblique vortex shedding instead of parallel shedding [45]. Finally, shear layer vortices can also contribute towards streamwise vorticity generation via a similar mechanism [46].

Nonreacting flows over confined bluff bodies ($\frac{L}{D} < 10$) see the presence of two unsteady spectral modes. The first, mode-I is the primary shedding mode associated with the BVK instability. The second, mode-II is driven by the periodic separation of the span wall boundary layer [47, 48]. As noted earlier, one of the effects of combustion is to reduce the interaction of the

two bluff body shear layers. This is somewhat analogous to the presence of a splitter plate in nonreacting flows which has been studied in detail. The presence of a splitter plate allows for mode-I to change from "roller-style" shedding having vortex tubes oriented along the Z direction to a tail anchored vortex (TAV) structure having vortex tubes oriented along the Y direction. The TAV is hypothesized to form a part of a larger hoop-like flow structure that results in spanwise non-uniformity in the XZ plane or a three-dimensional recirculation zone. Evidence of a similar structure was recently found in reacting flows over confined bluff bodies [38, 39, 49, 50]. These TAVs (or corner vortical structures) are part of a three-dimensional recirculation zone, where, as the equivalence ratio is decreased and blowoff is approached, the strength of the corner vortical structures increases, out of plane (+/-Z) motions within the recirculation zone increase, and flame extinction occurs more significantly near the span walls than the Z = 0 centerline. Interestingly, these studies found that once global extinction had occurred the corner vortical structures vanished. These studies highlighted that confined bluff body flames include not only 3D effects of the shear layers, but large 3D effects of the combustion and velocity fields within and near the recirculation zone seemingly due to the spanwise confinement of the bluff body flame.

At present, a number of questions remain about what ultimately causes a flame to irrecoverably blow off, both in terms of flow and flame dynamics. In particular, the majority of studies of near blowoff dynamics use OH PLIF, which is a useful diagnostic in cases where the flame is continuous, but its interpretation becomes more confusing with significant levels of coexisting reaction sheets and nonreacting reactant-product interfaces. This work increases the confidence in OH PLIF based techniques by incorporating simultaneous formaldehyde (CH_2O) PLIF measurements, which in addition to being useful in its own right, can also be used to calibrate interpretations from OH PLIF, via the computation of a heat release marker. Second, all prior blowoff studies have approached blowoff by reducing the equivalence ratio or increasing the flow velocity. This approach, however, simultaneously changes the underlying hydrodynamic stability characteristics of the flow. Great effort was put into this study to approach blowoff while fixing its underlying hydrodynamic stability features, by maintaining nearly constant product to reactant gas expansion ratio and flow velocity. Finally, these measurements were obtained with simultaneous stereo-PIV to correlate the scalar OH and CH_2O structures with three-dimensional flow features.

3.1 Experimental description

3.1.1 Facility

The facility shown in Figure 3.1, is horizontal and consists of three parts – the vitiator, the flow conditioning section and the reacting bluff body test section. The building air supply is sourced from a compressor, which supplies air for the vitiator ($\dot{m}_{air,vit}$) and dilution ($\dot{m}_{air,dilution}$) separately; the air for the vitiator first passes through an in-line flow heater (Watlow 50 kW) which preheats the air up to 616 K (T_{ph}). The vitiator burns natural gas ($\dot{m}_{fuel,vit}$) which is premixed

with the air more than 1 m (150 diameters) upstream of the 4 tangential injection points at the vitiator. After combustion in the vitiator, the combustion products are mixed with dilution air and bluff body fuel in the first part of the flow conditioning section, as marked in Figure 3.1. The bluff body fuel (natural gas) ($\dot{m}_{fuel,bb}$) is injected coaxial with the dilution air to mitigate autoignition of the fuel at the injection site; fuel is injected 1.2 m (13 hydraulic diameters) upstream of the bluff body test section. The mixture of combustion products, air and fuel then flows through a ceramic flow straightener (ACI Versagrid, consisting of 5 mm x 5 mm passages each 12.7 cm long with a wall thickness of 1.4 mm) which conditions the flow and ensures that a nominally parallel, fully developed flow enters the bluff body test section. The bluff body test section has a cross section measuring 12.7 cm (L) wide and 7.6 cm (H) tall. The bluff body, shown in Figure 3.1 along with the coordinate system, spans the width of the test section and has a diameter (D) of 1.91 cm, implying that L/D = 6.6. Ignition at the bluff body is achieved using a diffusion hydrogen torch. This section features fused quartz windows (Technical Glass Products Heraeus Type TSC-3) for optical access.

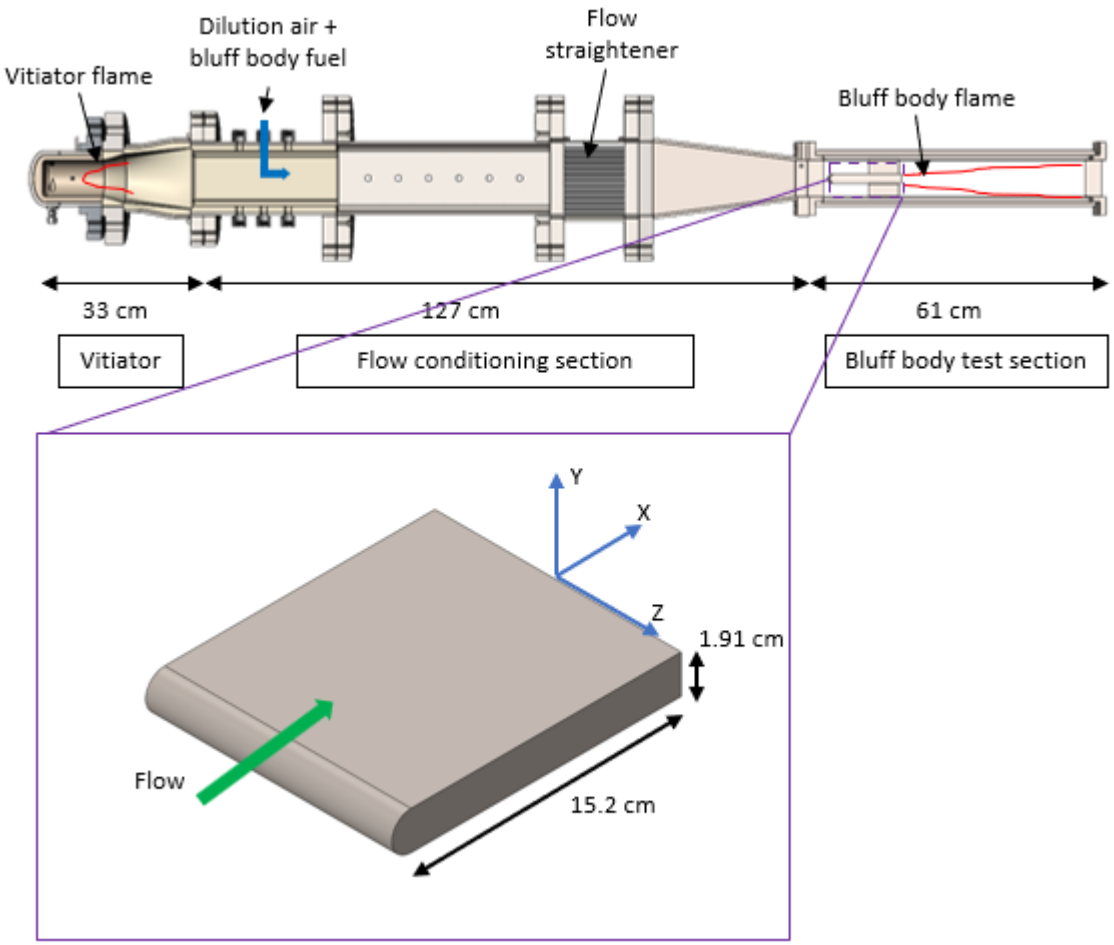

Figure 3.1: Rig schematic with bluff body (enlarged) and coordinate system

DISTRIBUTION A: Distribution approved for public release.

Cross stream variations in bluff body (ϕ_{bb}) and vitiator (ϕ_v) equivalence ratios were measured at the bluff body lip location using a CO_2 gas analyzer (Horiba PG300) and were found to be under 3%. Air and fuel flow metering for the vitiator and the bluff body was done independently using calibrated sub-critical orifice assemblies. This allowed for independent control of the two combustors. The uncertainties on these measurements are under 2% [51]. Static pressure was measured using Omega PX309 pressure transducers accurate to 0.25%, differential pressure measurements were made with Omega PX771A or Rosemount 3051 sensors accurate to 0.15%. Unburned temperatures were measured using K type thermocouples and were accurate to within 0.75% (or 2.2°C, whichever is greater).

The pre-flame temperature (T_u) was measured in the reactant stream upstream of the bluff body. We define an average reference axial velocity as $u_{bulk} = \frac{\dot{m}_{total}}{\rho_u A}$ (where A is the cross sectional area of the reactant stream at the bluff body lip and ρ_u is the pre-flame density calculated using the ideal gas law). The bluff body Reynolds number (Re_D) was calculated using u_{bulk} and the upstream reactant viscosity (ν) calculated from Sutherland's law as $Re_D = \frac{u_{bulk}D}{\nu}$. A reference post flame temperature (T_b) is calculated from the equilibrium temperature, obtained from an adiabatic mixing calculation of the vitiated products with the dilution air and bluff body fuel. Turbulence intensities (I, normalized by the total mean velocity) were determined from a 3 pixel x 3 pixel window in the reactant stream, well away from the bluff body shear layers. The integral length scale (L_{xx}) is also calculated within this window from the temporal autocorrelation function, assuming Taylor's frozen turbulence hypothesis. Several of these quantities are provided in Table 3.3 and discussed later.

3.1.1.1 Diagnostics description

This work carried out simultaneous 10 kHz stereo-PIV, OH PLIF and CH2O PLIF at several conditions. Brief descriptions of the imaging systems and laser sources used are summarized in Table 3.1 and Table 3.1: Image acquisition details respectively. The setup has been described in

detail in an earlier work [52] and is briefly summarized here. A schematic of the setup is shown in Figure 3.2.

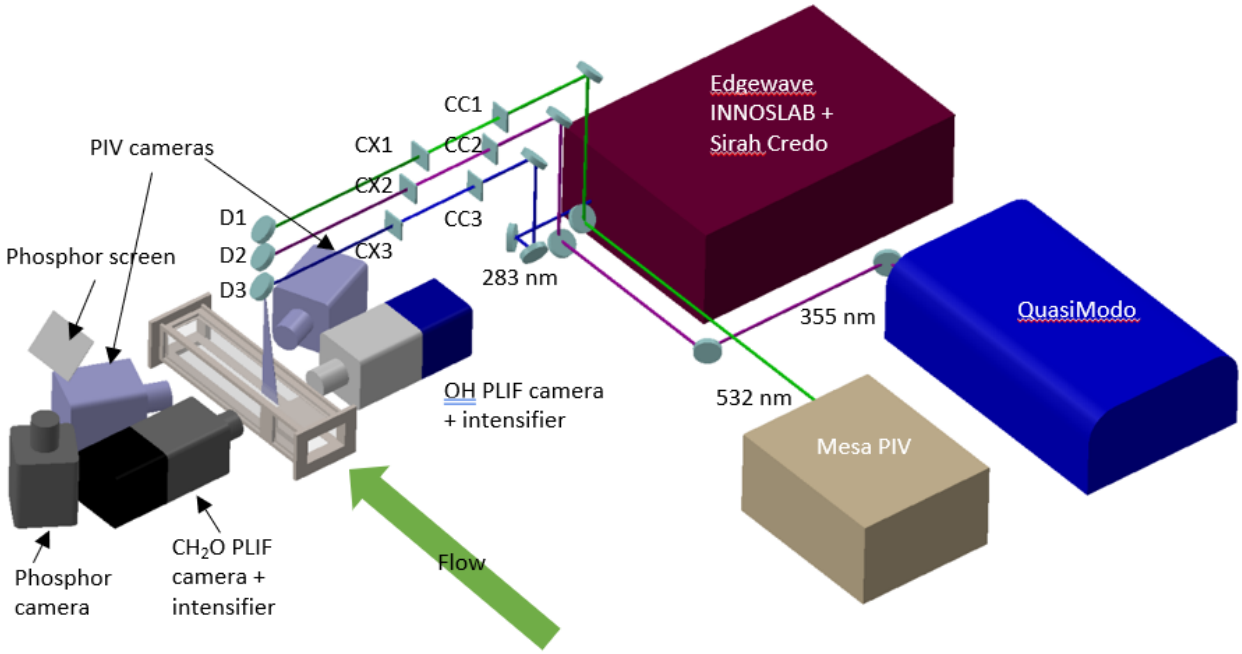

Figure 3.2: Diagnostics setup

Diagnostic	**Camera**	**Intensifier**	**Intensifier exposure [ns]**	**Lens**	**Filter(s)**
sPIV	Phantom v2640	N/A	N/A	100 mm, f/2.8	532/3 bandpass
OH PLIF	Photron SAZ	LaVision HS-IRO	150	100 mm, f/2.8	320/40 bandpass + 340 absorption
CH_2O PLIF	Photron SAZ	Lambert HiCATT	100-150	100 mm, f/2.8	364 longpass + 439/154 bandpass

Table 3.1: Image acquisition details

Diagnostic	**Laser**	**Wavelength [nm]**	**Pulse energy [mJ]**	**Beam waist [µm]**
sPIV	Continuum Mesa-PIV	532	N/A	400
OH PLIF	Edgewave INNOSLAB + Sirah Credo	283	0.25	300
CH_2O PLIF	Spectral Energies QuasiModo	355	150	380

Table 3.2: Laser source specifications

3.1.1.2 PLIF setup

The CH_2O PLIF system used a hybrid pumped (flashlamp and fiber amplified), pulsed burst mode Nd:YAG laser (Spectral Energies QuasiModo). The laser provided 355-nm third-harmonic laser pulses at 10 kHz for 10.5 ms approximately every 12 s. Average 355 nm pulse energy was maintained at approximately 150 mJ/pulse to avoid damage to the quartz windows. Sheet forming optics consisted of a cylindrical concave lens (CC2, f=-200mm) and a cylindrical convex lens (CX2, f=+1000mm) with perpendicular principal axes, that resulted in a 50 mm wide expanding sheet with a beam waist thickness (full width at half maximum, FWHM) of 380 μm, measured using the scanning knife edge technique. The laser sheet was located on Z = 0. The beam waist (placed at Y = 0) was measured in the center of the field of view (FOV) inside the test section. Fluorescence images were obtained perpendicular to the sheet using a high-speed CMOS camera (Photron FASTCAM SA-Z) coupled with an intensifier (Lambert HiCATT) that used a 100 mm visible lens (Tokina, f/2.8). A combination of longpass (Semrock 364LP) and bandpass (Semrock 439/154) filters were placed in front of the camera lens for spectral filtering. Images were recorded at 10 kHz at a resolution of 1024 pixels × 1024 pixels. Depending on the particular case, the intensifier exposure was varied between 100 ns – 150 ns. The system had a raw spatial resolution of 44 μm/pixel. While we were constrained in how far we could tune the exact 355 nm wavelength, we still tuned it to maximize the CH_2O signal.

The OH PLIF system used a diode-pumped, frequency doubled Nd:YAG laser (Edgewave INNOSLAB) to pump a frequency doubled dye laser (Sirah Credo) operating with Rhodamine 6G dye. The pump laser delivered 532 nm pulses at a pulse energy of 3 mJ/pulse at 10 kHz. The dye laser delivered pulses at 0.25 mJ/pulse and was tuned to excite the $A^2\sum \leftarrow X^2\Pi$ (1,0) Q1(7) transitions near 283 nm. Sheet forming optics consisted of a cylindrical concave lens (CC3, f=-500mm) and a cylindrical convex lens (CX3, f=+750mm) with their axes perpendicular to one another. The resulting expanding sheet had a width of 40 mm and a FWHM beam waist thickness of 300 μm, placed in the center of the FOV within the test section. Images were collected perpendicular to the laser sheet using a high-speed CMOS camera (Photron FASTCAM SA-Z) coupled with an intensifier (LaVision HS-IRO) that used a lens extender (Nikon PK-13, 27.5 mm) and a 100 mm UV lens (Sodern Cerco, f/2.8). A spectral bandpass filter (Semrock 320/40) was placed in front of the camera lens. Additionally, an absorption filter (Newport FSQU340) was placed in front of the 320/40 filter and was necessary to remove stray 355 nm reflection by the bandpass filter (320/40) into the CH_2O imaging system on the opposite side of the test section (ref. Figure 3.2). The intensifier was gated at 150 ns. Images were recorded at 10 kHz, at a resolution of 1024 pixels × 1024 pixels. The system had a raw spatial resolution of 44 μm/pixel.

Acetone PLIF images were acquired to provide time averaged intensity profile correction for the OH PLIF images. A technique using blue phosphor was used to perform shot-to-shot intensity profile correction for the CH_2O PLIF images. In this technique, the transmitted portion of the 355 nm sheet through optic D2 is imaged onto a plate coated with a uniform layer of blue phosphor. As the transmitted and reflected sheets are identical in intensity profiles, the plate is placed at the

DISTRIBUTION A: Distribution approved for public release.

beam waist of the transmitted sheet to enable simultaneous profile measurements. Both these techniques are compared and discussed in detail in an earlier work [52].

3.1.1.3 Stereo-PIV setup

The stereo PIV system used a diode-pumped, dual oscillator/single head, frequency doubled Nd:YAG laser (Continuum Mesa-PIV) which provided doublet 532 nm pulses at 10 kHz for particle illumination. Sheet forming optics consisted of a cylindrical concave lens (CC1, f=-200mm) and a cylindrical convex lens (CX1, f=+1000 mm), which resulted in the formation of an expanding sheet, nearly 50 mm wide, having a FWHM beam waist thickness of 400 μm. Light scattering images were obtained perpendicular to the laser sheet in a side scatter configuration using two high-speed CMOS cameras (Phantom v2640) operating in frame straddling mode at 20 kHz, that were fixed with Schiempflug adaptors, and utilized 100 mm visible lenses (Tokina, f/2.8). A narrow bandpass spectral filter (Semrock 532/3) was placed in front of each camera lens. A fluidized bed style seeder was used to seed the flow with 1 μm alumina particles. The seeder was connected in parallel to the dilution air line. Alumina was chosen to minimize spectral interference with the 355 nm laser [53]. Seed particle agglomeration was minimized by drying the seed in an oven at 533 K for 24 hours before every test run. The minimum cutoff frequency of the particles in the flow, assuming a flow temperature of 300 K is 13 kHz for the unvitiated cases and 28 kHz for the vitiated cases [54], both in the reactant stream. This value increases in the post flame region.

Images of a two-sided, two-level dot calibration plate (LaVision 058-5) were used to perform camera registration and calibration using DaVis 8.3.1.

3.1.1.4 Simultaneous imaging and timing

A series of three beam combining dichroic mirrors were used to combine the 532 nm, 355 nm and 283 nm sheets and are shown in Figure 3.2. This was done by reflecting the 532 nm sheet using optic D1 (Lattice Electro Optics (LEO) R532/T608), into optic D2 (LEO T532/R355), which in turn transmitted 532 nm and reflected 355 nm into optic D3 (LEO T532/T355/R283), which finally transmitted 532 nm and 355 nm, reflecting 283 nm into the test section. The three sheets entered from the top of the test section and were placed immediately behind the bluff body, overlapped and equidistant from the span walls. Sheet orthogonality, final placement and spatial overlap was verified using laser levels and precisely machined reference plates that were mounted to the rig.
The two PIV laser pulses were separated by 30 μs. The 355 nm pulse was delayed 15.24 μs after the first PIV pulse. The 283 nm pulse was delayed 760 ns after the 355 nm pulse. The timing box (Quantum Composer 9530) on board the QuasiModo served as the master clock and was used to drive the two other lasers. A second timing box (Berkeley Nucleonics 577), driven by the master clock, controlled the operation of the cameras and the intensifiers. Timing was verified using a digital oscilloscope (Tektronix TDS 3014).

DISTRIBUTION A: Distribution approved for public release.

3.1.1.5 Test Matrix and operating conditions

This section details the operating conditions as well as the approach used for designing the test matrix. The rig was developed with a number of operator specified controls which include $\dot{m}_{air,vit}, \dot{m}_{air,dilution}$, ϕ_v, ϕ_{bb}, T_{ph} and T_u, that could be adjusted to reach a host of different operating conditions as summarized in Table 3.3. As noted earlier, the goals of the test matrix design were two-fold: (1) to approach blowoff by keeping the parameters that influence its hydrodynamic stability approximately constant, particularly flow velocity (u_{bulk}) and gas expansion ratio (σ), and (2) to compare near LBO dynamics under conditions where, well away from blowoff, the flame is globally stable (high σ case) and globally unstable (low σ case). The latter case was of particular interest as most prior detailed diagnostic studies of LBO have been performed at high σ, BVK suppressed conditions. Given the observations that "BVK-like features" appear near LBO in these cases, it is of interest to look at the LBO process in flames that are already manifesting the BVK instability.

Conditions U1, V1 and NR1 are statistically stationary whereas conditions U2 and V2 are transient, capturing a flame in the process of blowoff. The blowoff equivalence ratio (ϕ_{LBO}) at these conditions was estimated by slowly dropping ϕ_{bb} and allowing the flame to stabilize with each change, until finally the flame proceeded to global extinction spontaneously; the resultant value of ϕ_{bb} was averaged over 5 repetitions to estimate ϕ_{LBO}. To obtain data at the transient conditions, the flame was first brought as close to blowoff as possible while remaining statistically stationary, specifically, ϕ_{bb} was set to $\sim\phi_{LBO} + 0.02$ after which the fuel valve was turned off. A number of prior numerical studies have similarly introduced step changes into the equivalence ratio to compute a blowoff transient [55-59]. Experimentally, such a step change is not possible because of fuel supply system dynamics (e.g., "capacitance" in the supply system), and the actual time variation of the equivalence ratio of the bluff body flame dropped much slower over the ~1 s test duration. The fuel measurement system, which has a 250 ms response time, showed that ϕ_{bb} fell to a value of $\sim\phi_{LBO} - 0.01$ after ~ 2 s. Table 3.3 summarizes the conditions at the start of the data record, along with other quantities as and when they are introduced through the rest of the paper.

Simultaneous 10 kHz (Fs) stereo-PIV, OH PLIF and CH_2O PLIF were recorded at all conditions. For conditions U1, U2 and NR1, stereo-PIV and OH PLIF were recorded for ~ 0.6 s and ~ 0.5 s respectively, while for conditions V1 and V2 they were recorded for ~ 1.2 s and ~ 1 s respectively. CH_2O PLIF was recorded for the first 10.5 ms of the data record at all conditions.

DISTRIBUTION A: Distribution approved for public release.

Property	Case U1 (stable, unvitiated)	Case U2 (near blowoff, unvitiated)	Case V1 (stable, vitiated)	Case V2 (near blowoff, vitiated)	Case NR1 (non-reacting)
u_{bulk} [m/s]	8	8	22	19	7
$\dot{m}_{air,vit}$[g/s]	25	32	18	18	32
ϕ_v	0	0	0.5	0.5	0
$\dot{m}_{air,dilution}$ [g/s]	42	38	79	49	38
ϕ_{bb}	0.62	0.47	0.52	0.46	0
T_u [K]	300	300	539	640	300
T_b [K]	1710	1440	1605	1555	300
σ	5.7	4.8	2.9	2.4	1
Re_D	9700	9700	9800	6400	8500
T_{ph} [K]	300	300	353	353	300
I [%]	9.5	5.6	5.1	5.2	7.3
$\frac{L_{RZ}}{D}$	1.4	2.9	2.6	1.8	1.3
$\mathcal{F}_{si}$ [%]	5	10	55	45	30
L_{xx}/D	0.3	0.3	0.3	0.4	0.3

Table 3.3: Operating conditions

3.2 Data reduction

This section summarizes the different analysis methodologies used in this work.

3.2.1 Velocity field processing

As a pre-processing step, the raw seeded images were subjected to a 4 x 4 particle intensity normalization filter and a 2 x 2 pixel window sliding background subtraction to improve the sensitivity of the algorithm, implemented using LaVision's DaVis 8.3.1. The PIV processing involved a multi-pass cross-correlation algorithm with decreasing interrogation window sizes, starting at 64 x 64 pixels, all the way down to 24 x 24 pixels with a 50% overlap, to reduce axial loss of pair error. Vector post processing involved two passes of a median filter using the "strongly remove and iteratively replace" option where a vector is removed if it is more than 1.5 standard deviations away from the mean of its neighbors. If removed, a new vector (calculated from the next highest correlation peak) can replace it, if it lies less than 2 standard deviations from the mean of its neighbors. This yielded a final vector spacing of 0.54 mm. The final instantaneous vector field is denoted as $\vec{V} = u(x,y,t)\,\hat{\imath} + v(x,y,t)\,\hat{\jmath} + w(x,y,t)\,\hat{k}$ where $\hat{\imath}, \hat{\jmath}$ and $\hat{k}$ represent the unit vectors in the X, Y and Z direction respectively (defined in Figure 3.1). Any subscript corresponds to the case name as introduced in Table 3.3; e.g., u_{U1} refers to the X component of the instantaneous velocity field for case U1. Time averages are denoted as $\overline{(.)}$ and fluctuating quantities as $(.)'$. Instantaneous in-plane PIV uncertainty [60] was calculated to be 1.5% and 3.5% of u_{bulk} for the unvitiated (U1, U2) and vitiated (V1, V2) cases respectively. Out of plane

uncertainty was 25% and 10% of u_{bulk} for unvitiated (U1, U2) and vitiated (V1, V2) cases respectively. In addition to the higher uncertainty that is expected from the out of plane component in stereo-PIV, the increased out of plane activity (discussed later) is another contributing factor for these values.

The spectral content of the signal was quantified via a Fourier transform of the transverse velocity fluctuations, $\hat{v}(x, y, f)$. The Nyquist frequency (f_{nyq}) is 5 kHz and the minimum frequency resolution (Δf_{raw}) lies in the 0.8 Hz – 1.6 Hz range, depending on the case (ref. Section 3.1.1.5). For the statistically stationary cases, averaging is performed over 3 ensembles (of the data record) to reduce noise. Fourier spectra presented hereafter for these cases are always ensemble averaged. For the transient cases, the Fourier spectra is computed over the entire data record. In order to analyze the varying time-frequency dynamics of these cases, a continuous wavelet transform of the non-stationary signals is computed using a Morse analytic wavelet ($\psi_{P,\gamma}$) which has the generalized frequency domain form, expressed in terms of the Strouhal number, $St = fD/u_{bulk}$

$$\psi_{P,\gamma}(St) = \left(\frac{2\pi u_{bulk}}{D}\right)^{P/\gamma} H(St)\, a_{P,\gamma}\, St^{P/\gamma} e^{-\left(\frac{2\pi u_{bulk} St}{D}\right)^{\gamma}} \tag{3.1}$$

where $H(St)$ is the Heaviside step function and $a_{P,\gamma} = \left(\frac{e\gamma^2}{P^2}\right)^{P^2/\gamma^2}$ is a normalizing constant. The Morse analytic wavelet family is parametrized by the time-bandwidth product (P) and the symmetry parameter (γ) which have values of 60 and 3, respectively [61].

3.2.2 PLIF processing

Time-synchronized, raw images of OH PLIF and CH_2O PLIF are subjected to the following: (1) laser pulse energy correction, (2) laser pulse profile correction, and (3) coordinate transform to real world coordinates. The instantaneous signal-to-noise (SNR) is defined as the ratio of the PLIF signal in a region of known species presence to that of the background noise level in a region of known species absence, both averaged over a 5 x 5 pixel window. The OH PLIF images of cases U1 and U2 have an SNR of 15 and cases V1 and V2 have an SNR of 10.

Following this, the CH_2O images are subjected to the following processes in order: (1) a 7 x 7 pixel Weiner filter [62], and (2) two consecutive bilateral filters [63]. The OH images are subjected to the following steps in order: (1) a 7 x 7 median filter, (2) a 5 x 5 Weiner filter, and (3) a single bilateral filter to perform edge preserving noise reduction. The CH_2O PLIF images of cases U1 and U2 have an SNR of 8 whereas cases V1 and V2 have an SNR of 6. The final CH_2O and OH time series are defined as $\boldsymbol{C(x, y, t)}$ and $\boldsymbol{O(x, y, t)}$ respectively where any subscript once again denotes the case name. Sample composite images showing $\boldsymbol{O(x, y, t)}$ and $\boldsymbol{C(x, y, t)}$ in red and green respectively for all the cases are shown in Figure 3.6.

3.2.3 Edge detection

Reliable edge detection of the OH PLIF images is a necessary first step in several analysis techniques presented in this work. Beginning with the final processed OH images, $O(x, y, t)$, the following steps are followed in order: (1) contrast enhancement is achieved by using histogram equalization [64], (2) noise reduction and smoothing is achieved with a 5 x 5 Weiner filter and a 5 x 5 Gaussian filter [62], (3) binarization is achieved using a threshold obtained using Otsu's method [65] and finally (4) a morphological thinning process is iteratively applied until the result no longer changes [66], to obtain a single pixel wide, mathematically tractable contour representing the OH edge. In general, these steps allow for reliable unsupervised edge detection with high accuracies. Several examples are shown in the time snapshots of Section 3.3. Special care needs to be taken for cases V1 and V2 especially in the presence of transient extinction (introduced later), as oftentimes there is no "edge" in its vicinity.

3.2.4 Reactant volume identification

Flames near blowoff frequently see the presence of reactants within the wake/recirculation zone [20, 32, 67, 68]. While analyzing OH PLIF images of such flames, the highest signal levels correspond to flame reaction zones (superequilibrium OH levels), the next highest levels correspond to post flame combustion zones comprising of hot combustion products, while the lowest levels correspond to unburnt reactants or cooled combustion products. An unsupervised algorithm to identify volumes of reactants in an OH PLIF field was devised using intensity thresholding and segmentation. It involves the following steps:

1. Beginning with $O(x, y, t)$, edge detection steps (1) through (3) (from Section 3.2.3) are applied. The binarized field serves as a mask to identify the first field of reactant volumes.
2. A segmentation algorithm utilizing a maximally stable extremal regions (MSER) routine [69] is used to search for low intensity regions that lie within the detected high intensity regions. This gave rise to the second field of reactant volumes.
3. A union of the two fields of reactant volumes then gives the final reactant volume field.

Figure 3.3(a) and (b) show instances of $O_{U2}(x, y, t)$ while Figure 3.3(c) shows an instant of $O_{V2}(x, y, t)$. Figure 3.3(d)-(f) show the algorithm performance for Figure 3.3(a) – (c) respectively.

DISTRIBUTION A: Distribution approved for public release.

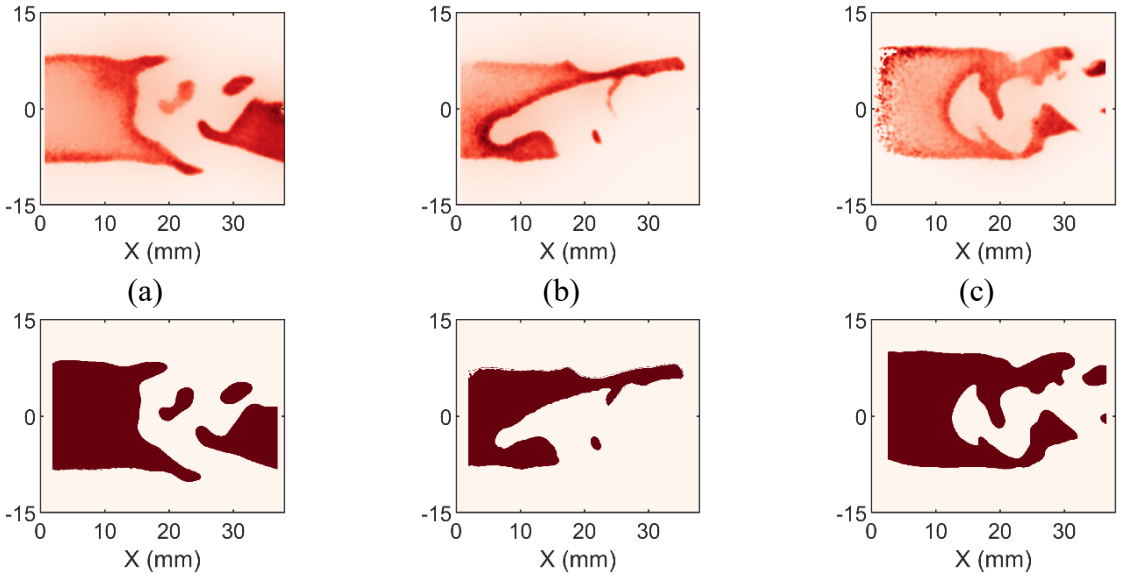

Figure 3.3: Reactant volume identification algorithm performance showing OH fields, $\boldsymbol{O(x,y,t)}$ ((a)-(c)) and the respective binarized fields ((d) – (f)) with reactants (light) and products (dark) for case U2 ((a),(b),(d),(e)) and case V2 ((c),(f)).

3.2.5 Edge classification – reaction surfaces vs extinction

In recirculation stabilized flames such as these, the edge of $O(x,y,t)$ can be thought of as an interface that separates reactants from products. This interface may be reacting or non-reacting. The former denotes the presence of a flame or reaction surface through which reactants must pass to become products on the other side, whereas the latter denotes an extinction zone or the lack of a flame. This may allow for either/both (1) reactant/product mixing, and (2) reactant pockets to pass into the product zone without burning. There are multiple approaches to assess the nature of the interface. First, one can look for regions of super-equilibrium OH in their vicinity; reaction surfaces will have such regions, as seen in Figure 3.3(a)-(c). Second, one can look for regions of high gradients of the OH field, $|\nabla O|\ (x,y,t)$ normal to the reactant/product interface. Third, one can estimate local heat release rates. Heat release in hydrocarbon flames is known to correlate well with concentrations of the HCO radical [70, 71]. As direct, high-speed PLIF measurements of HCO is difficult [71], oftentimes a heat release marker, Q computed as $Q(x,y,t) = O(x,y,t) \times C(x,y,t)$ is used as a proxy, motivated by the fact that the forward reaction rate of the HCO formation reaction, $OH + CH_2O \rightarrow H_2O + HCO$, is proportional to $[OH][CH_2O]$. The Q field was calculated from the $O(x,y,t)$ and $C(x,y,t)$ fields and investigated 2 mm on either side of each point on the detected OH edge in the flame normal direction. A peak detection routine then identifies peaks in this flame normal Q profile. The presence of a peak with a prominence greater or less than a certain threshold τ_p, classifies the point on the edge as a reaction surface or extinction zone, respectively. Figure 3.4(a) shows a sample OH field, $O(x,y,t)$ (red), the CH_2O field,

DISTRIBUTION A: Distribution approved for public release.

$C(x, y, t)$ (green) with the detected edge of $O(x, y, t)$ classified into reaction surface (yellow) and extinction zone (black) using this technique.

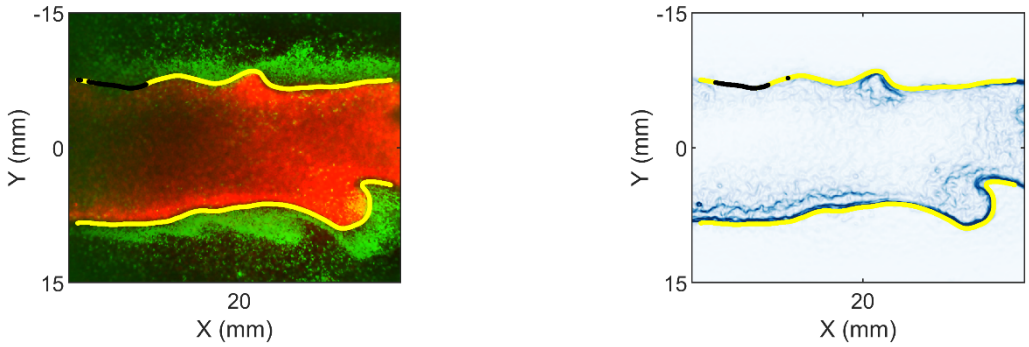

Figure 3.4: Edge classification into reaction surface (yellow) and extinction zone (black) using (a) heat release marker, and (b) OH gradient based detection techniques. OH field, $\boldsymbol{O(x, y, t)}$ is shown in red, CH_2O field, $\boldsymbol{C(x, y, t)}$ in green and OH gradient field, $\boldsymbol{\nabla O(x, y, t)}$ in blue.

Unsupervised classification was achieved by performing a sensitivity analysis that involved a study of the variation in length of the detected extinction zone as a function of chosen threshold, and then choosing a threshold value in the range that is relatively insensitive to the threshold variation. Such a technique, though extremely reliable, requires a CH_2O PLIF measurement which is only available for a fraction of the entire data record for the LBO transient cases. However, it can be used to analyze the first two approaches (based on OH fields) to calibrate them over time intervals where all measurements are available. Evidence of the potential of such a technique is seen in Figure 3.5 which plots the detected peaks of Q versus those of $|\nabla O|$, denoted as Q_{max} and $|\nabla O|_{max}$ respectively, in the vicinity of each point on the OH edge. The correlation between them is clear when $Q_{max} < 0.1$; beyond this, the noise associated with the $|\nabla O|$ computation increases the spread significantly while still suggesting a positive correlation.

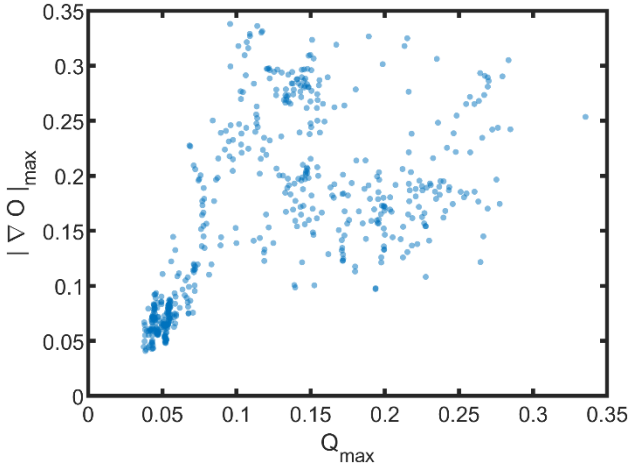

Figure 3.5: Scatter plot showing OH gradient magnitude maxima, $|\boldsymbol{\nabla O}|_{\max}$ vs Q_{max} for all points on the OH edges of 85 snapshots

DISTRIBUTION A: Distribution approved for public release.

The OH gradient based technique could be used if selection of the peak prominence threshold, τ_p was tuned to ensure similar classification performance as the heat release marker based technique. Figure 3.4(b) shows the OH gradient field, $\nabla O(x,y,t)$ (blues) with the detected edge of $O(x,y,t)$ classified into reaction surface (yellow) and extinction zone (black) using this technique. Comparing Figure 3.4(a) and Figure 3.4(b), it is easy to see that both the heat release marker and the *tuned* OH gradient based techniques have similar classification performance.

This tuned OH gradient based technique was used for edge classification for the entire data record. As the calibration was extracted from data obtained at the beginning of the non-stationary data record (i.e., over the time interval over which CH_20 PLIF data is also available), it is important to verify that it is appropriate to use over the entire time record, particularly very near LBO. To evaluate the validity of the tuning across the entire dataset, the following process was followed: (1) the entire data record was divided into five sequential parts, and (2) the probability density function (PDF) of $|\nabla O|(x,y,t)$ for portions of the OH layer where the flame existed was determined for each of these segments. The objective of this analysis was to determine if this PDF itself was non-stationary. We did not find it to be, i.e., the PDF of $|\nabla O|(x,y,t)$ for flame regions was approximately constant for each of the five sections of the time record. Moreover, this observation agrees with visual examinations of $O(x,y,t)$ at different time intervals within the data record. Section 3.3 later discusses several images that identify extinction zones using this technique.

3.3 Results and discussion

3.3.1 Instantaneous characteristics

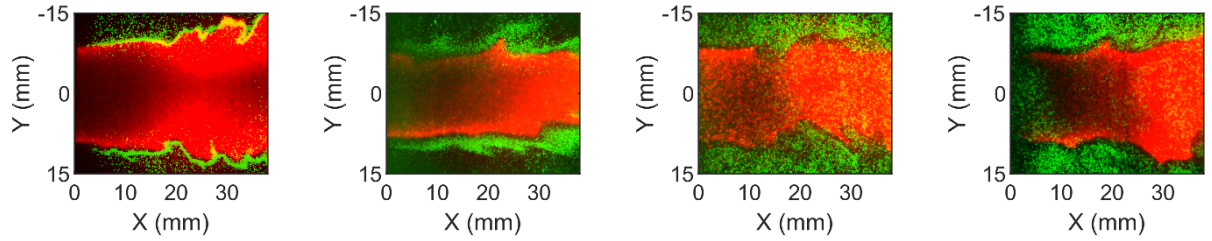

(a) Case U1 (b) Case U2 (c) Case V1 (d) Case V2

Figure 3.6: Instantaneous images depicting OH fields, $\boldsymbol{O(x,y,t)}$ (red) and CH_2O fields, $\boldsymbol{C(x,y,t)}$ (green) for (a) case U1 (unvitiated, stable) , (b) case U2 (unvitiated, near blowoff) at $\boldsymbol{t^* \sim -223}$, (c) case V1 (vitiated, stable) and (d) case V2 (vitiated, near blowoff) at $\boldsymbol{t^* \sim -300}$. The transient cases are shown at particular values of $\boldsymbol{t^*}$ which is a measure of proximity from global extinction that happens at $\boldsymbol{t^* = 0}$.

DISTRIBUTION A: Distribution approved for public release.

Figure 3.6 (a) – (d) shows instantaneous contour plots of $O(x, y, t)$ and $C(x, y, t)$ for cases U1, U2, V1 and V2 respectively. The transient cases are shown at particular values of normalized time from blowoff, $t^* = \frac{t - t_{BO}}{\frac{D}{u_{bulk}}}$, where t_{BO} denotes the time instant of global extinction as imaged within the FOV. Case U1 shows thin, concentrated CH_2O fields that lie on the reactant side of the flame, with strongly burning reaction surfaces at all axial locations; this is typical of stable, unvitiated flames. Both fields also show evidence of small scale roll up of the flame by shear layer vortices. Case U2 shows a broader spatial extent of CH_2O on the reactant side of the flame, similar to that observed in previous studies for near LBO flames [12, 72, 73]. Interestingly, the CH_2O layer lies inside the average shear layer location, which could be another reason for their broad spatial distribution (discussed in Section 3.3.2). Owing to a lower equivalence ratio (and lower turbulence intensity), the reduced flame speed of case U2 causes flame spreading at a smaller angle relative to the flow compared to case U1. Both cases show a low intensity OH region immediately behind the bluff body. This appears to be a manifestation of the thermal interaction zone between the bluff body and recirculating flow. Presumably this is due to cooling of the recirculating products as they interact with the back of the bluff body; this causes a drop in temperature and, consequently equilibrium OH concentrations. This low intensity region is larger at instances when there is an extinction zone in its vicinity. On average, these regions measure between 15 mm – 20 mm (~ 1D) in length depending on the case.

The vitiated cases (Figure 3.6 (c) – (d)) show markedly different fields. In both cases, the CH_2O fields are broadly distributed all across the reactant side of the flame. This is due to the high temperatures that the fuel is subject to at these conditions which leads to fuel breakdown well ahead of the bluff body. The larger scale sinuous flapping of the flame is also evident, due to the BVK instability. Finally, both cases show similar low intensity regions behind the bluff body like the unvitiated cases.

3.3.2 Time averaged characteristics

Figure 3.7 shows time averaged profiles of vorticity magnitude, $\overline{|\omega|}$ (blue), OH fields, $\bar{O}$ (red) and CH_2O fields, $\bar{C}$ (green) at three axial locations of X = 5 mm, 15 mm and 30 mm for cases U1, U2 and V1. The time averages for the transient cases (Case U2 and Case V2) are computed over the time interval before which significant downstream extinction is observed (see Figure 3.14 and Figure 3.19).

DISTRIBUTION A: Distribution approved for public release.

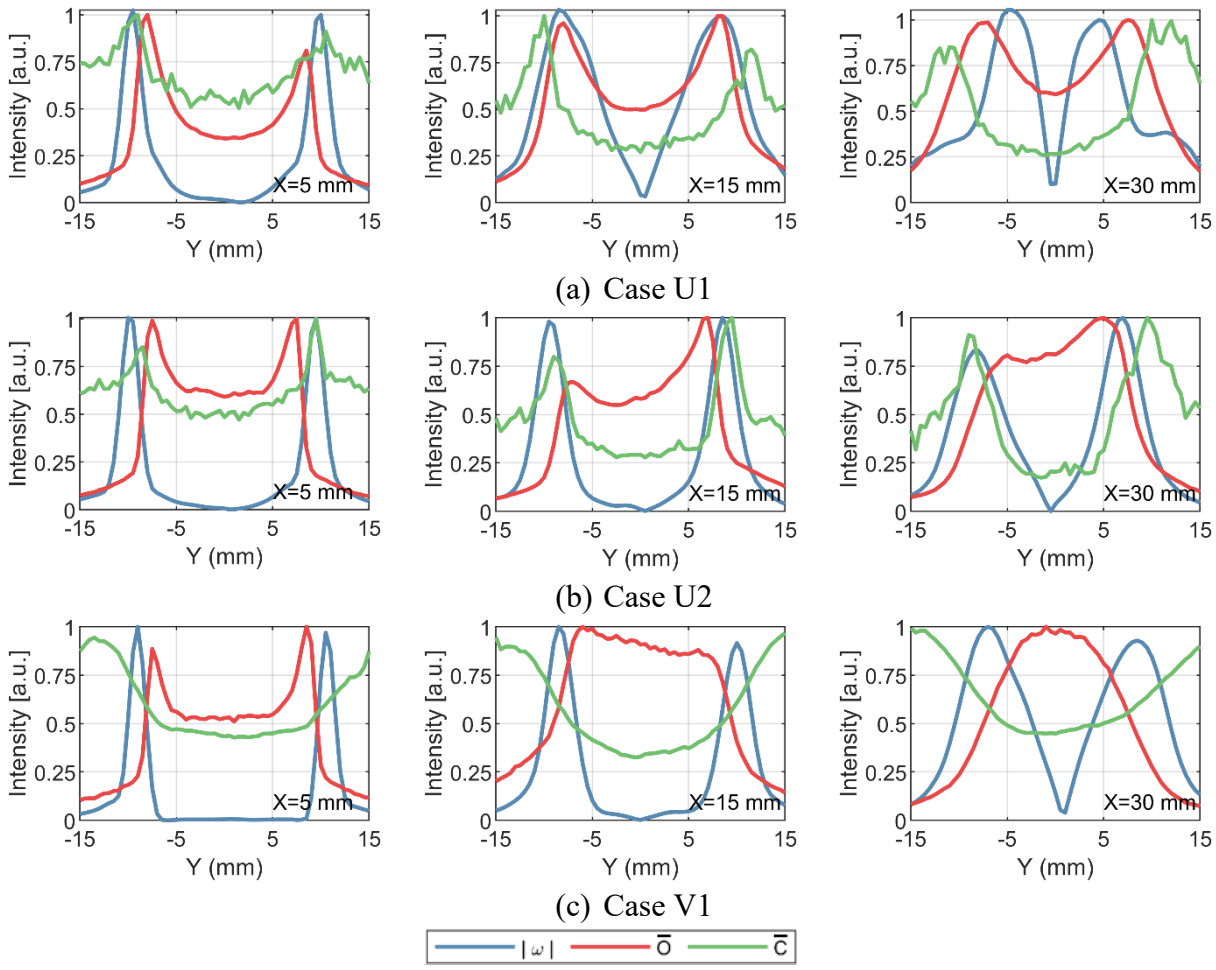

Figure 3.7: Time average profiles of vorticity magnitude, $\overline{|\boldsymbol{\omega}|}$, OH field, $\bar{\boldsymbol{O}}$ and CH_2O field, $\bar{\boldsymbol{C}}$ at axial positions of X = 5 mm, 15 mm and 30 mm for (a) case U1 (unvitiated, stable), (b) case U2 (unvitiated, near blowoff) and (c) case V1 (vitiated, stable).

For case U1, near X = 5 mm, the flame (denoted by the rising edge of $\bar{O}$, moving towards Y = 0 from either side) lies on the inside of the bluff body shear layers (denoted by the $\overline{|\omega|}$ peaks). At this axial location, the CH_2O layers lie within the shear layers. Moving downstream, the shear layer thickens (as seen by the increasing FWHM of the $\overline{|\omega|}$ peaks) and moves closer towards the centreline. At the same time, the flame moves away from the centerline, reaching a point where it lies within the shear layers and eventually outside of it (beyond X/D ~ 15), while the CH_2O layer moves further away from the centerline continually with the flame. For case U2, the flame starts off similarly, lying on the inside of the shear layer. The reduced flame speed results in a smaller angle with the flow (ref. Figure 3.6(b)), causing the flame to lie within the shear layers, subjecting it to higher levels of vorticity all along its length.

The vitiated cases (V1 and V2) show similar characteristics with the exception of the CH_2O layer which has a broad spatial distribution on the reactant side of the flame that decays in the post

DISTRIBUTION A: Distribution approved for public release.

flame region – Figure 3.7(c) shows profiles for case V1 as an example. At sufficiently downstream axial locations, the $\bar{O}$ profile starts becoming unimodal (ref. Figure 3.7(c), X= 30 mm). This happens due to the two shear layer stabilized flames coming closer together towards the end of the recirculation zone. All these observations merely describe the time average characteristics of the flame relative to the flow field and are not representative of its instantaneous behavior. Finally, Table 3.3 shows the normalized length of the recirculation zone, L_{RZ}/D, (defined as the axial distance at which $\bar{u}(x, y = 0)$ switches sign) for the different cases considered; it is also visualized in Figure 3.10 later.

3.3.3 Dynamic Flow Analysis

3.3.4

Figure 3.8 shows normalized Fourier spectra of the fluctuating velocity in the Y direction at (X,Y) = (35 mm, 0 mm) for cases U1, U2, V1 and V2. It indicates a clear spectral peak at $St \sim 0.22$ in the low density ratio, stable case, V1, but no prominent narrowband feature in the high density ratio, stable case, U1. Both results were expected and consistent with prior data [74]. Note also that a variety of non-reacting wake studies with different bluff bodies have demonstrated similar global mode frequencies [20, 75, 76].

Also evident is the clear peak in this same frequency range in both transient blowoff cases. In other words, these data strongly suggest that the BVK instability re-emerges in the high □ , near blowoff case, as argued in earlier studies from qualitative flame imaging [20, 77, 78]. The quantitative agreement of dominant Strouhal number reported here lends significant evidence that this is, indeed, the case. These disturbances and the consequent sinuous (i.e., asymmetric) flame flapping grow with downstream distance, particularly near and after the end of the recirculation zone as discussed later in this section.

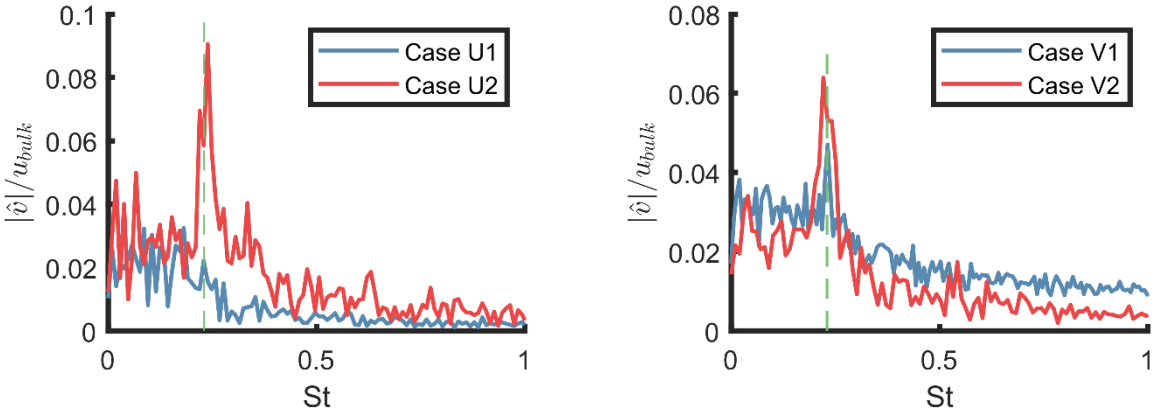

(a) (b)

Figure 3.8: Fourier spectra of vertical velocity fluctuations ($|\widehat{\boldsymbol{v}}|$) normalized by the bulk flow velocity ($\boldsymbol{u_{bulk}}$) at (X,Y) = (35 mm, 0 mm) for (a) unvitiated (U1, U2) and (b) vitiated (V1, V2) cases, as a function of Strouhal number, St. St=0.22 line is shown in dashed green.

As described in Section 3.2.1, a wavelet analysis was performed on the non-stationary cases U2 and V2.

Figure 3.9 plots wavelet transform magnitudes of the normalized vertical velocity ($\tilde{v}$) as a function of Strouhal number (St) and normalized time t^*, for case U2 (a) and case V2 (b), at (X,Y) = (35 mm, 0 mm) with $St = 0.22$ line shown in dashed black. Stage 2 of blowoff has a phenomenological characterization that includes large scale flame flapping, increased reactant entrainment, wake composition modification, etc. [20]. For case U2, it is interesting to note a few instances of high narrowband activity (near St = 0.22) that appear at the beginning of the dataset whereas after $t^* \sim -50$, sustained narrowband activity is evident. This would suggest that stage 2 of blowoff begins at $t^* \sim -50$ after a sufficient change in the global density ratio of the flow field has occurred. Case V2 on the other hand shows intermittent instances of narrowband activity from the beginning of the dataset. This intermittent behavior was previously noted by Emerson et al. [74] for stable, reacting wake flows at transitional σ values between 2 and 3. However, after $t^* \sim -125$, narrowband activity permanently sets in. This work will refer to the onset of stage 2 as the time after which narrowband disturbances permanently set in.

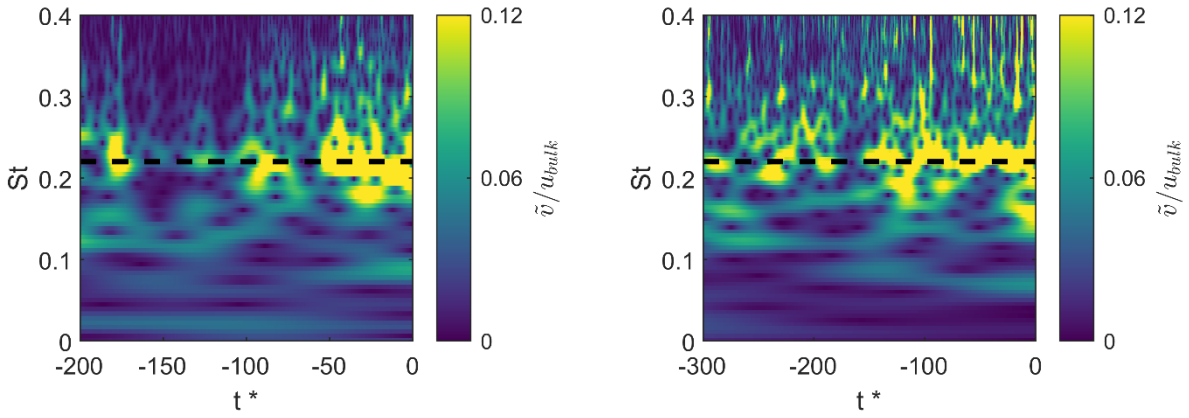

Figure 3.9: Magnitude of the wavelet transform of the vertical velocity ($\boldsymbol{V_{cwt}}$) at (X,Y) = (35 mm, 0 mm) normalized by the bulk flow velocity ($\boldsymbol{u_{bulk}}$) plotted as a function of Strouhal number (St) and normalized time from blowoff ($\boldsymbol{t^*}$) for case U2 (a) and case V2 (b). St = 0.22 line is shown in dashed black.

Further insight into the spatial distribution of the activity around $St = 0.22$ is presented in Figure 3.10(a)-(e) which shows contour plots of the Fourier spectra of the vertical velocity fluctuations integrated over the 0.19<St<0.24 range for cases U1, U2, V1, V2 and NR1 respectively, with the extent of the recirculation zone marked in black and in-plane velocity vectors overlaid. Case U1 (Figure 3.10(a)) shows little to no activity in this Strouhal number range, even downstream of the recirculation zone, signifying a complete suppression of the BVK instability, as is expected at $\sigma = 5.7$. All the other cases show some activity in this *St* number range, mostly clustered around the end of the recirculation zone; see Figure 3.10(b), (c), (d), and (e). In all the cases, this activity grows with axial distance and reaches large levels towards the end of the recirculation zone (and beyond, if applicable), with clear saturation occurring at downstream axial locations in case NR1.

DISTRIBUTION A: Distribution approved for public release.

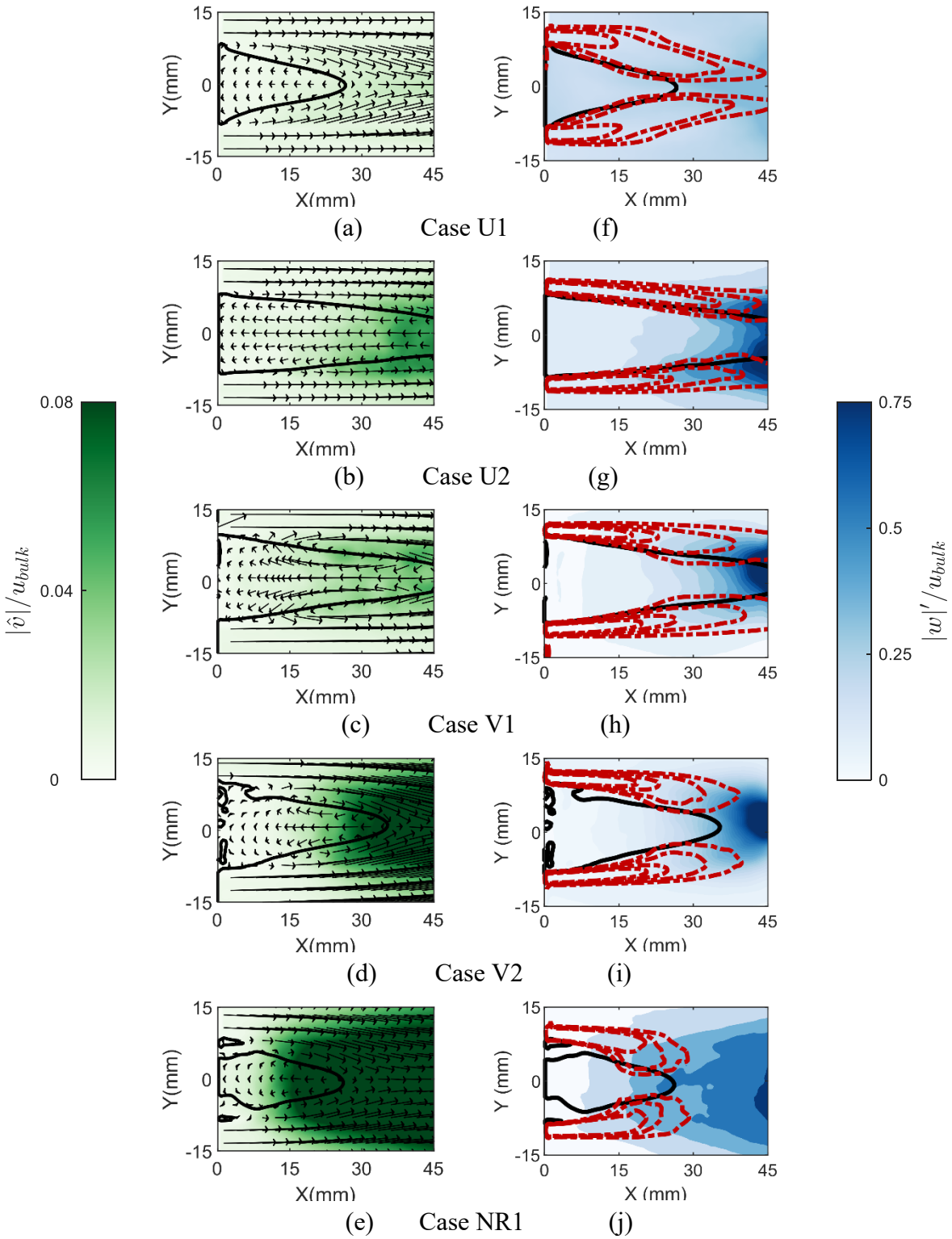

Figure 3.10: Magnitude of the Fourier spectra of vertical velocity fluctuations ($|\hat{\boldsymbol{v}}|$, greens) integrated over the $\boldsymbol{0.19 < St < 0.24}$ range and standard deviation of the out of plane velocity magnitude ($|\boldsymbol{w}|'$, blues) both normalized by the bulk flow velocity ($\boldsymbol{u_{bulk}}$), for cases U1

DISTRIBUTION A: Distribution approved for public release.

(unvitiated, stable), U2 (unvitiated, near blowoff), V1 (vitiated, stable), V2 (vitiated, near blowoff) and NR1 (non-reacting) ((a) – (e), respectively and (f) – (j) respectively). Plots show zero axial velocity contour (black), representative contours of average vorticity magnitude (red) and in-plane velocity vectors overlaid.

Figure 3.10(f) – (j) show standard deviation fields of the out of plane, normalized velocity magnitude ($|w|'$), for cases U1, U2, V1, V2 and NR1, respectively, with representative contours of the average vorticity overlaid in red. This quantity ($|w|'$) provides a useful metric for the magnitude of three-dimensional disturbance field effects. Beginning with the non-reacting case NR1 (Figure 3.10(j)), note that peak out of plane velocity magnitude fluctuations are around 70% of the bulk velocity. Wall/confinement effects could be one source of these fluctuations. Evidence of such out of plane activity, especially towards the end of the recirculation zone has been seen in a previous work [49]. Though the CVS has been observed in non-reacting confined flows when they feature splitter plates as discussed in the Introduction, this is not necessarily the case [79], suggesting that the exact conditions that cause this structure to manifest in confined flows are not very well understood. If present, these CVS could induce velocity across the Z = 0 plane, as suggested by previous works [38, 47]. Another source (not arising out of a confinement effect) of these fluctuations could be the streamwise vortices (oriented in the X direction) that form from secondary instabilities of the shear layer and/or BVK instability [40, 42, 43] that is prevalent in case NR1. The relative contribution of these two sources for each of the cases is discussed later in the section.

Consider next the stable, reacting flow cases. In contrast to NR1, there are significantly lower out of plane velocity magnitude fluctuations in the stable, high gas expansion ratio case U1 (Figure 3.10(f)); their peak values are 30% of u_{bulk}. Presumably, the significant gas expansion in this case suppresses unsteady three-dimensional structures. Consistent with this hypothesis is the much larger out of plane motions in the stable, low gas expansion ratio case V1, where peak out of plane velocity magnitude fluctuations are 100% of u_{bulk}.

Finally, much more significant out of plane motion occurs in both transient blowoff cases – case U2 (Figure 3.10(g)) and case V2 (Figure 3.10(i)), with peak values of 70% and 100% of u_{bulk} respectively. These results agree with the observations and results from Fugger et al. [38, 39], namely that blowoff in nominally two-dimensional bluff-body flames is an intrinsically three-dimensional phenomenon.

The Fourier spectra of the fluctuating velocity in the Z direction ($\widehat{w}$, not pictured here) is broadband and has no spectral peaks, gradually rolling off with increasing *St*. Even so, there is clear spatial coincidence between regions of elevated narrowband activity in $|\hat{v}|$ and elevated broadband activity in $|w|'$ as shown in Figure 3.10. This point is clearly shown in Figure 3.11, which plots the normalized standard deviation of the out of plane velocity magnitude versus the normalized Fourier spectra magnitudes of the vertical velocity fluctuations, along the upper shear layer. The indicated trendline (black) corresponds to $|w|' \sim |\hat{v}|^{0.5}$. This data suggests that the out

DISTRIBUTION A: Distribution approved for public release.

of plane velocity fluctuations are correlated with secondary instabilities of the primary BVK instability.

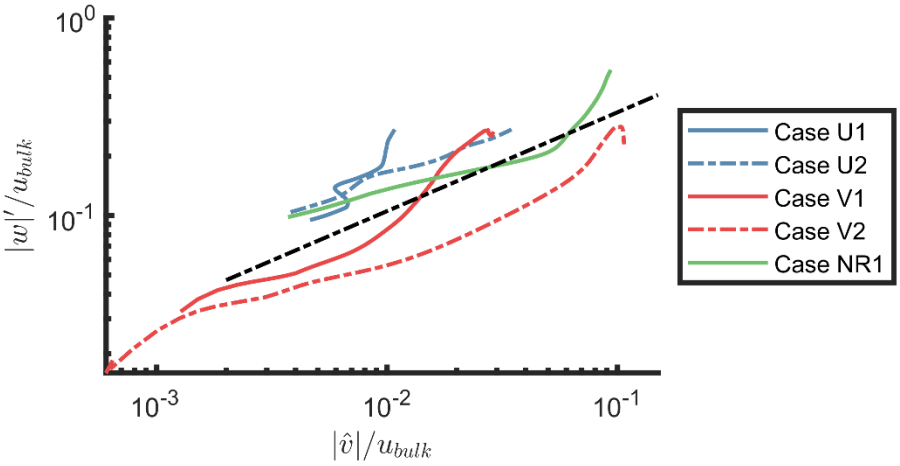

Figure 3.11: Normalized standard deviation of the out of plane velocity magnitude ($\frac{|\boldsymbol{w}|'}{\boldsymbol{u_{bulk}}}$) versus the normalized Fourier spectra magnitudes of the vertical velocity fluctuations ($\frac{|\hat{\boldsymbol{v}}|}{\boldsymbol{u_{bulk}}}$), both within the upper shear layer along Y ~10 mm, for all the cases considered. Trendline, $\boldsymbol{|w|'\sim|\hat{v}|^{0.5}}$ is shown in dashed black.

Next, consider Figure 3.12 which plots the normalized out of plane velocity ($\frac{w}{u_{bulk}}$) at representative time instants for cases U2, V1, and V2. Starting with cases V1 and V2, further evidence of secondary instabilities of the shear layer or BVK structures is evident, where the out of plane velocity demonstrates clear staggered patterns of alternating sign. This structure is reminiscent of the secondary instabilities of initially two-dimensional shear layers, which lead to the formation of streamwise oriented vortex tubes that manifest as alternating regions of $+w$ and $-w$ velocity as observed in an XY-plane [40-43]. In the transient case V2, this manifestation is consistent as blowoff is approached; the time instants denote proximity from blowoff which happens at $t^* = 0$. Case U2, however, does not show such clearly coherent staggered patterns, a point we discuss later in this section when we attempt to differentiate secondary shear layer instability and confinement effects on these three-dimensional disturbance fields.

DISTRIBUTION A: Distribution approved for public release.

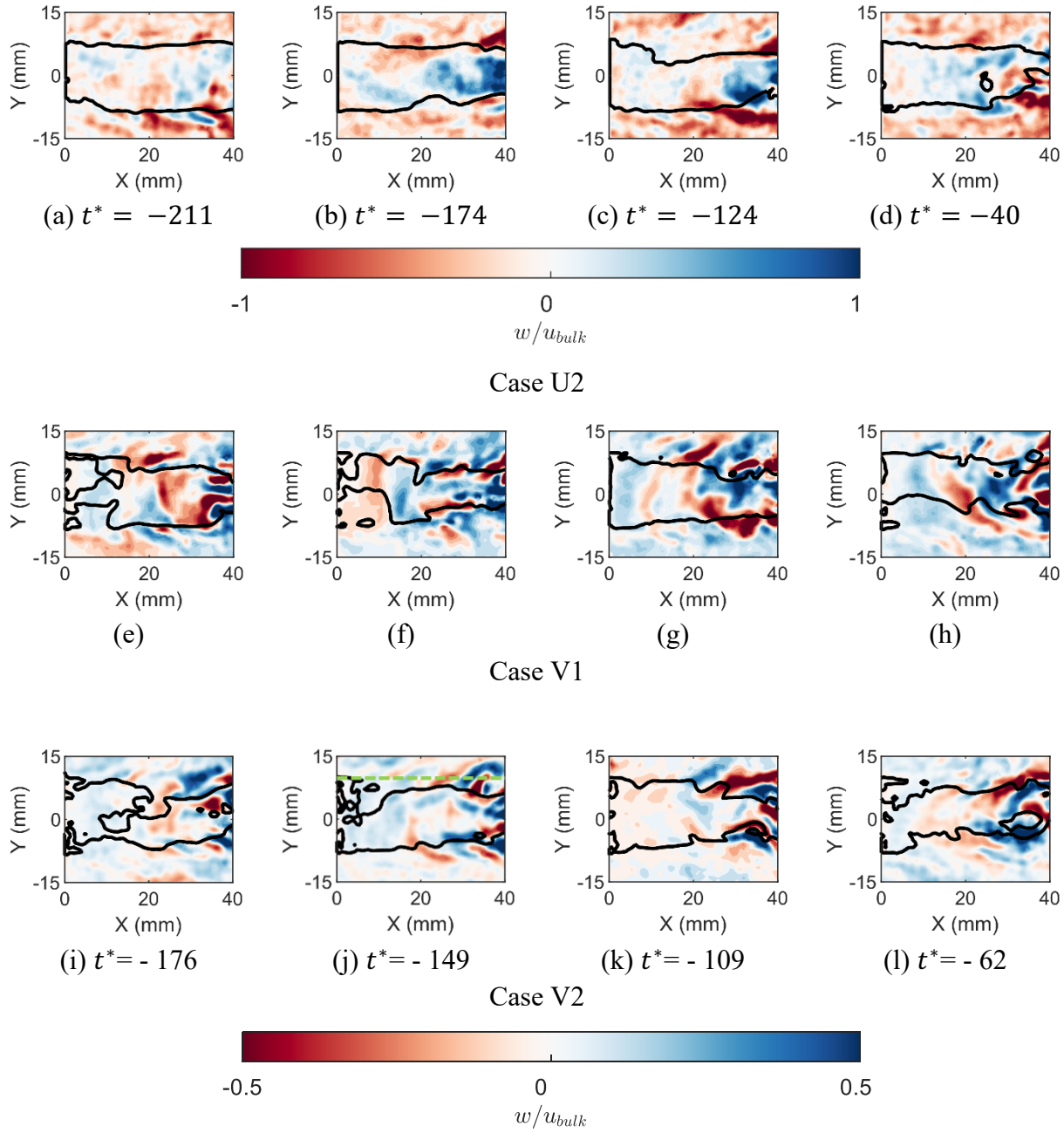

Figure 3.12 Normalized out of plane velocity ($\frac{w}{u_{bulk}}$) overlaid with the instantaneous zero axial velocity contour (black), for case U2 ((a)-(d)) at several normalized time instances from blowoff (t^*), case V1 ((e) – (h)) and case V2 ((i)-(l)) at several normalized time instances from blowoff (t^*). Dashed green line in (j) corresponds to $Y = 0.6D$.

The axial convection of these structures in the shear layers can be visualized from the cross correlation of $w\left(\frac{X}{D}, \frac{Y}{D} = y_o, t^*\right)$, denoted as $R\left(\frac{\Delta X}{D}, \Delta t^*\right)$, (where y_o = 0.6 is chosen to lie within the upper shear layer, ref. Figure 3.12(j) dashed green line). This is visualized in Figure 3.13 (solid

DISTRIBUTION A: Distribution approved for public release.

lines) for case V2. The angle made by the space-time correlation surface (with the Δt^* axis) represents the convection velocity, $u_{convect}$ (indicated by the black dashed line), of these alternating in and out of plane structures. Its value is $\frac{u_{convect}}{u_{bulk}} = 0.7 = \overline{u\left(\frac{X}{D}, \frac{Y}{D} = 0.6, t^*\right)}/u_{bulk}$, close to the shear layer velocity at this location. Following the dashed line, the correlation drops to 1/e of its maximum at $(\Delta t^*, \frac{\Delta x}{D})$ = (0.45, 0.30), quantifying the time/distance over which they remain correlated. The spatial size of these structures can be analogously worked out from the $(1/e)$ width of the space-time correlation surface at $\Delta t^* = 0$, to be about $0.18D$. Similarly computed cross correlation of $w\left(\frac{X}{D}, \frac{Y}{D} = 0.6, t^*\right)$ for case U2 is also shown in Figure 3.13 (colored dashed lines). There is a clear absence of a similarly oriented space-time correlation surface that would be indicative of axial convection, quantifying qualitative observations from Figure 3.12(a)-(d).

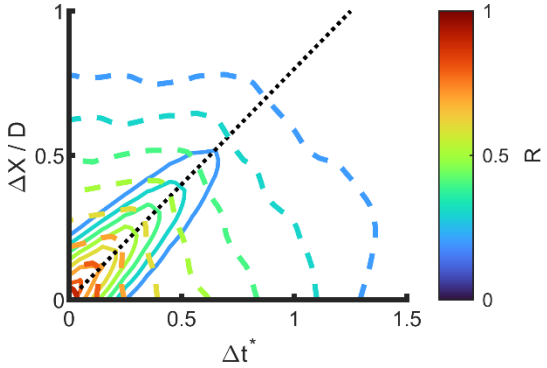

Figure 3.13: Iso-contours of cross-correlation function, $\boldsymbol{R\left(\frac{\Delta x}{D}, \Delta t^*\right)}$ of $\boldsymbol{w\left(\frac{x}{D}, \frac{y}{D} = 0.6, t^*\right)}$ for case V2 (solid lines: vitiated, near blowoff) and case U2 (dashed lines: unvitiated, near blowoff).

It is clear that there are two potential sources of three-dimensional effects in the near wake region – confinement and secondary instability of the shear layer. Understanding the relative roles of these is potentially important as presumably the former is a function of geometry and confinement details (particularly the aspect ratio L/D), while the latter is applicable to unconfined and confined bluff body flows. In order to attempt a differentiation of their relative contributions, we developed the following filtering approach, built upon the idea that the secondary instability structures will be coincident with shear layers/regions of high narrowband activity. It must be noted that this technique is a rudimentary attempt at attributing flow features; while the general classification approach is robust, the attributions of the classification to one source of instability or another ("confinement" or "secondary instability" driven) is admittedly speculative. Nonetheless, given this caveat, we believe that this classification approach yields interesting insights into the different processes at play in the different cases. Specifically, we identify regions with high out of plane activity ($\Omega_1: |w| > w_{thresh}$) that are also coincident with regions of high Z vorticity magnitude ($\Omega_2: |\omega| > \omega_{thresh}$) and label these as "secondary instability driven" (i.e., $\Omega_1 \cap \Omega_2$). High out of plane activity outside of regions of high Z vorticity magnitude are labeled

as "confinement driven" (i.e., $\Omega_1 - (\Omega_1 \cap \Omega_2)$. The time averaged percentage contribution of secondary instability ($\mathcal{F}_{si}$) can be calculated as $\mathcal{F}_{si} = \frac{ar(\Omega_1 \cap \Omega_2)}{ar(\Omega_1+\Omega_2)} \times 100$, where ar(.) denotes the area of the region. These are presented in Table 3.3 for all the cases (using w_{thresh} =0.5u_{bulk} and ω_{thresh}= 0.5$\overline{\omega}_{max}$). Naturally, the contribution from confinement driven effects is given by, $\mathcal{F}_c = 100 - \mathcal{F}_{si}$. This categorization approach suggests that secondary instabilities are almost completely suppressed in cases U1 and U2 (only 5% and 10% contribution respectively); presumably, most of the out of plane activity is due to structures (e.g., the corner vortex structures as reported in [38, 39]) associated with bluff body wall interactions, i.e., confinement effects. This is in line with Figure 3.12 ((a)-(d)) where we do not see significant structures with alternating signs for case U2. For cases V1 and V2, there is a significantly increased contribution from secondary instabilities (55% and 45% respectively), in line with the alternating out of plane structures discussed in the context of Figure 3.12. Finally, the non-reacting case NR1 (calculated within an X-span truncated close to the end of its recirculation zone) shows 30% contribution from secondary instabilities.

3.3.5 Analysis of Case U2: Unvitiated flame blowoff

Flames near blowoff see extinction zones along the flame surface and reactants within the otherwise product dominated recirculation zone. Throughout this data, and consistent with prior studies, we see two different kinds of extinction zones. The first, are referred to as "transient extinction zones" due to the fact that they are followed by a reaction surface, and get bigger/smaller as the edge flame located next to them retreats or advances. The second kind are characterized by complete extinction (or absence of a reaction surface) beyond a certain axial distance, and are referred to as "permanent extinction zones" in this work.

We can quantify the different types of extinction with two characteristic length scales. First, we define L_{ez} as the total length of the individual extinction zones that are contained within the flame surface on both the top and bottom flame branches, shown in Figure 3.14 as a function of normalized time (t^*). Second, we define a reference length scale at which permanent extinction occurs, L_f, by dividing the volume of the combustion products by the bluff body test section's cross-sectional area as

$$L_f = \frac{V_p}{DL} = \frac{A_p L}{DL} = \frac{A_p}{D} \tag{3.2}$$

where L is the span width of the test section, A_p is the area projection of V_p in the plane of the OH laser sheet, and D is the bluff body diameter. A value of $\frac{L_f}{D} \geq 2$ indicates that the flame does not permanently extinguish at some downstream axial location, or if it does, that it is outside of the FOV. Normalized time traces of L_f are shown in Figure 3.14 (blue). Figure 3.14 also depicts the instant of global extinction as imaged within the FOV (orange).

DISTRIBUTION A: Distribution approved for public release.

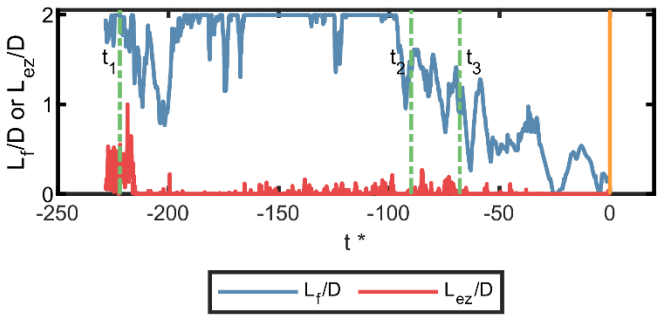

Figure 3.14: Normalized length scale at which permanent extinction occurs ($\frac{L_f}{D}$) and normalized total length of transient extinction zones ($\frac{L_{ez}}{D}$) as a function of normalized time from blowoff (t^*) denoted by the orange vertical line, for case U2. Time instants of interest are denoted by dashed (green) vertical lines.

Figure 3.14 shows how the U2 flame at $t^* <$ ~-100 usually spans the entire axial field of view (~2D) which is expected given its similarity to stable flames at this stage of blowoff (i.e., stage 1). There are instances where the point of extinction moves upstream (between 1D-2D); however these are temporary, and the flame recovers to span the FOV almost entirely. One potential source of the bursts of extinction observed could be the damped pulsations of the fuel supply system introduced by the sharp change in ϕ_{bb} as described in Section 3.1.1.5. Past t* ~ - 100, the flame length progressively shortens as the point of permanent extinction moves closer to the bluff body as it approaches global extinction. This progressive shortening is indicative of departure from stage 1 characteristics to the permanent, irrecoverable stage 2 of blowoff dynamics at t* ~ -50 (ref. Figure 3.9). The defining characteristic of stage 1 of blowoff is the first appearance of transient extinction zones along the flame surface [20]. While these transient extinction zones are observed in this case ($-240 < t^* < -100$), it is unclear why their occurrence reduces as the flame approaches global extinction. When present, they rarely have total lengths over $0.5D$. Closer to global extinction, they get much smaller (well under $0.5D$) suggesting that the shortened flame at this stage sees large levels of permanent downstream extinction beyond a certain axial location, but sees few transient extinction zones. Finally, the observed intermittency in the time trace of L_{ez} is due to frequent extinction/reignition processes that are prevalent at this stage and have been observed in previous studies [12, 68, 78].

The size and lifetime of these transient extinction zones can also be estimated in an average fashion from their space-time cross-correlation. To calculate this, we first define a binarized function along the lower OH edge, $I\left(t^*, \frac{x}{D}\right)$, where:

DISTRIBUTION A: Distribution approved for public release.

$$I\left(t^*,\frac{x}{D}\right)=\begin{cases}1, if\ \left(t^*,\frac{x}{D},\frac{y}{D}\right)\in\Phi\\0, otherwise\end{cases} \tag{3.3}$$

where Φ is the set of all space-time coordinates of all transient extinction zones that lie along the lower OH edge (ref. Figure 3.16) of case U2. The autocorrelation of this field, $A\left(\Delta t^*,\frac{\Delta x}{D}\right)$ is shown in Figure 3.15 (isocontours: dashed lines).

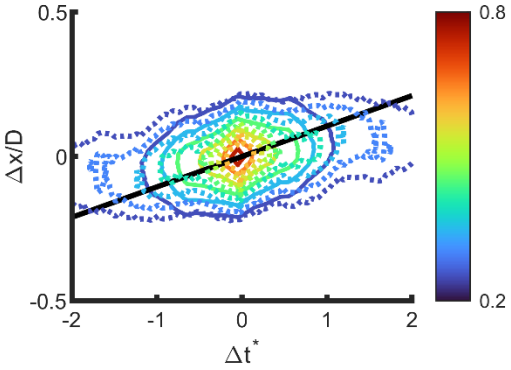

Figure 3.15: Isocontours of the autocorrelation, $\boldsymbol{A\left(\Delta t^*,\frac{\Delta x}{D}\right)}$ of the binarized function, $\boldsymbol{I\left(t^*,\frac{x}{D}\right)}$ for case U2 (dashed) and case V2 (solid) with the average axial convection speed line (black)

The angle that this space-time correlation surface makes with the Δt^* axis quantifies the average axial convection speed, u_{ez} of the transient extinction zones. Its value of $\frac{u_{ez}}{u_{bulk}}=0.1$ (denoted by the black line) agrees with the axial velocity at the nominal location of the detected transient extinction zones within the shear layer, suggesting convection by the local flow field. The correlation drops to $1/e$ of its maximum at $\left(\Delta t^*,\frac{\Delta x}{D}\right)=(1.3,0.13)$ which quantifies the average space-time lifetime of these extinction zones. Their length can be inferred from the $(1/e)$ width of the space-time correlation surface at fixed Δt^* to be about 0.1D. It is interesting to note that the shape of the space-time correlation surface for $|\Delta t^*|, \left|\frac{\Delta x}{D}\right| \ll 1$ is rhombus shaped, rather than the elliptical shape that it has for larger times/distances. Similar to how the orientation of the major axis of that ellipse denoted the average axial convection speed (u_{ez}), the orientation of the major axis of the rhombus can be related to a velocity, which comes out to $\frac{u^*_{ez}}{u_{bulk}}\sim 8$. Note that this high apparent velocity does not correspond to any flow velocity within the FOV, but is presumably the speed of the reaction edges, reflecting the rapidly changing length of the transient extinction zone.

Next, we consider the ways in which burnt products/unburnt reactants can enter the recirculation zone near blowoff, and the ways in which they will manifest themselves in planar measurements. In the OH PLIF fields, unburnt reactants can appear as low intensity “islands” that

DISTRIBUTION A: Distribution approved for public release.

are surrounded by a flame or combustion products. First, these islands could be a part of an out of plane, continuous reaction sheet. These manifest themselves in planar images as being surrounded by a reaction sheet, that has a "ring" of superequilibrium OH around them; they actively add heat to the wake. We see repeated instances of these "burning reactant fingers" inserting themselves into the planar sheet in this work, as presented later. Another mechanism is for the reactants to be entrained (i.e., entrained reactants) into the recirculation zone from within the measurement plane. In this case, the entrained reactant islands can either continue to burn (adding heat to the wake) as they mix with the hotter combustion products or they may stay as unburned reactants (and do not add heat to the wake as they are not burning, thus cooling the wake down). If the reactant islands are not surrounded by a flame, one hypothesized method for entering the recirculation zone in the measurement plane is through a transient extinction zone [12, 20, 78]. Interestingly, as discussed more later, we see little evidence of reactant islands originating from passing through extinction locations in the measurement plane. We do see, however, creation of non-burning reactant islands originating from the interaction of the out-of-plane burning reactant fingers with the backside of the bluff body, as discussed later. Moreover, in the presence of permanent extinction, when a "short flame" has the recirculation zone downstream of it (described later), unburnt reactant volumes also can directly enter the recirculation zone through purely two-dimensional effects.

Consider next, several snapshots around times of interest (t_1, t_2, t_3) denoted by the green dashed lines on Figure 3.14. These snapshots plot the edge of $O(x, y, t)$ with the reaction surface (green), transient extinction zone (orange), the magnitude of the Z component of vorticity, $|\omega|(x, y, t)$, and regions with out of plane velocity magnitude greater than 50% of u_{bulk} are shown in red (positive) and yellow (negative).Starting around $t^* = t_1$, we start off in stage 1 of blowoff dynamics (ref. Figure 3.16(a)-(f)). The flame spans the entire field of view at this stage. We see several instances of transient extinction zones along the flame surface, especially near the anchor point. Figure 3.16(a) – (f) follows one such extinction zone (orange) as it grows in size due to the retreat of the edge flame adjacent to it. At some point, under favorable local conditions (Figure 3.16(c), (d)), the retreating flame front transitions into a propagating one, reducing the size of the extinction zone and sometimes even healing it completely (Figure 3.16(e)). Such behavior is typical of flames in stage 1 of blowoff dynamics [78]. The high out of plane activity regions do not significantly display an alternating pattern (as discussed earlier) and several instances show large regions that are not coincident with high vorticity regions (e.g., Figure 3.16(c)-(e)). This suggests that they may be driven by confinement effects and not secondary instabilities, as argued earlier.

DISTRIBUTION A: Distribution approved for public release.

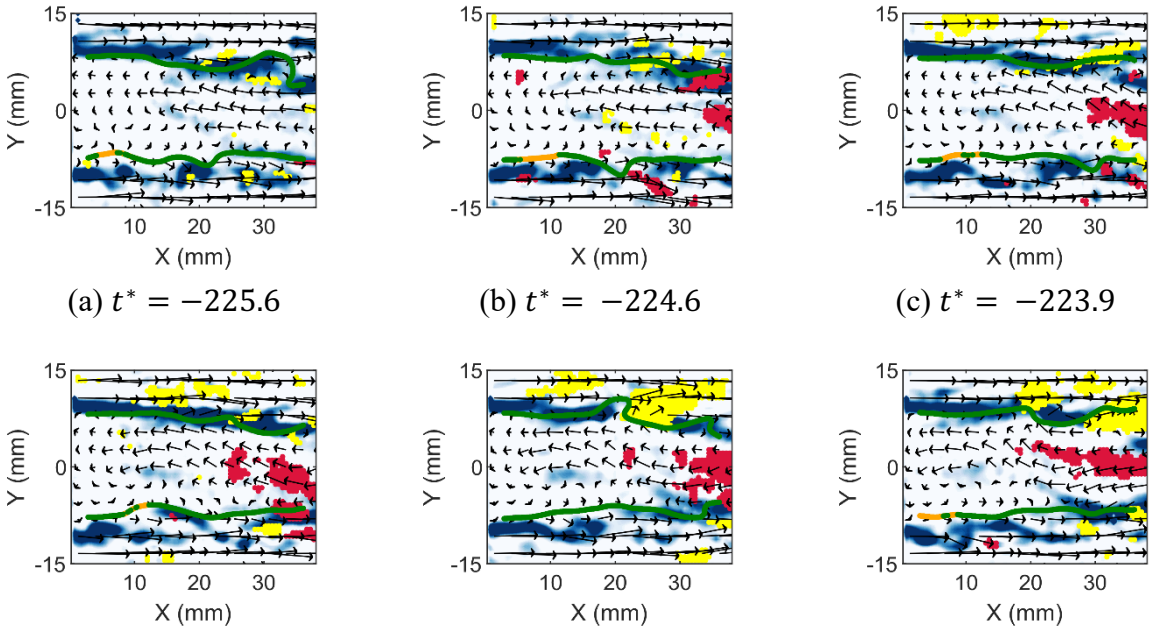

(a) $t^* = -225.6$ (b) $t^* = -224.6$ (c) $t^* = -223.9$

(d) $t^* = -223.1$ (e) $t^* = -222.2$ (f) $t^* = 221.4$

Figure 3.16 Images depicting the initial instances of a flame undergoing blowoff as a function of normalized time from blowoff ($\boldsymbol{t^*}$). Each image consists of vorticity magnitude field, $|\boldsymbol{\omega}|(\boldsymbol{x, y, t})$ overlaid with regions having out of plane velocity magnitude greater than 50% of $\boldsymbol{u_{bulk}}$ (red-positive, yellow-negative), reaction surfaces (green), extinction zones (orange), and in-plane velocity vectors.

Transient extinction zones have been previously proposed to create paths for non-reacting volumes of reactants to enter the recirculation zone [20]. Though we observe several instances of transient extinction zones throughout the dataset, we see no evidence of such reactant entrainment through extinction zones within the measurement FOV. The location of transient extinction needs to be considered; for example, significant backflow towards the end of the recirculation zone can create conditions favorable for reactant entrainment. However, at this point, we begin to see small volumes of burning reactant fingers within the recirculation zone (not pictured here). They are caught in the backflow associated with the recirculation zone and always burn out completely before reaching the bluff body. There is significant out of plane activity towards the end of the recirculation zone (X > 25 mm) whereas closer to the bluff body, the out of plane activity is almost absent.

As the flame comes closer to blowoff, there comes a point where there are large volumes of reactants present within the recirculation zone, say around $t^* = t_2$. These may be in the form of either burning reactant fingers (Figure 3.17(b)) or intermittent instances of downstream extinction of the flame (Figure 3.17(a) – (f), bottom shear layer X > 20 mm).

We begin to see increased levels of out of plane activity, largely coincident with the reactants-only region of the recirculation zone. Once again, their lack of organization in the form of alternating in and out of plane motion, coupled with the fact that they are not coincident with high vorticity

DISTRIBUTION A: Distribution approved for public release.

regions typical of the shear layers suggests that they are due to confinement effects. This out of plane activity seems to be responsible for introducing reactants into the imaged plane which are immediately caught in the reverse flow of the recirculation zone and convected towards the back of the bluff body. The fact that the out of plane motion continually introduces reactants, and not products, into the imaged plane suggests that much of the off centerplane regions could already have been replaced by reactants, i.e., permanent extinction has already set in earlier away from the centerline. This hypothesis is consistent with the imaging results from [38] that showed that bluff body flames near and at LBO encounter significantly more flame sheet extinguishment closer to the span wall (located at +/- Z) than near the centerline (Z=0). As discussed later in the context of Figure 3.23(d), (f) and (h), this would mean that the imaged centerplane is not representative of what is happening in planes parallel to it due to spanwise (along Z) non-uniformity of both the recirculation zone velocity field and the combustion [39]. Together with the out of plane activity, this would point towards the role of permanent extinction in driving blowoff in confined bluff body flames by moving reactants from planes away from the centerplane into it, a conclusion also drawn in [38]. This sometimes manifests as burning reactant fingers. Figure 3.17(a) – (f) show how flame propagation effects lead to the creation of a burning reactant finger that reacts as it convects towards the bluff body, while continually reducing in size. However, we also see other images where these burning reactant fingers impinge upon the back of the bluff body before burning out, after which portions of their burning surface are quenched (e.g., Figure 3.17(e)). This is a comparatively rare outcome for a burning reactant finger; only 15% of the total observed burning reactant fingers around this time reach the back of the bluff body, the rest are consumed as they convect towards it.

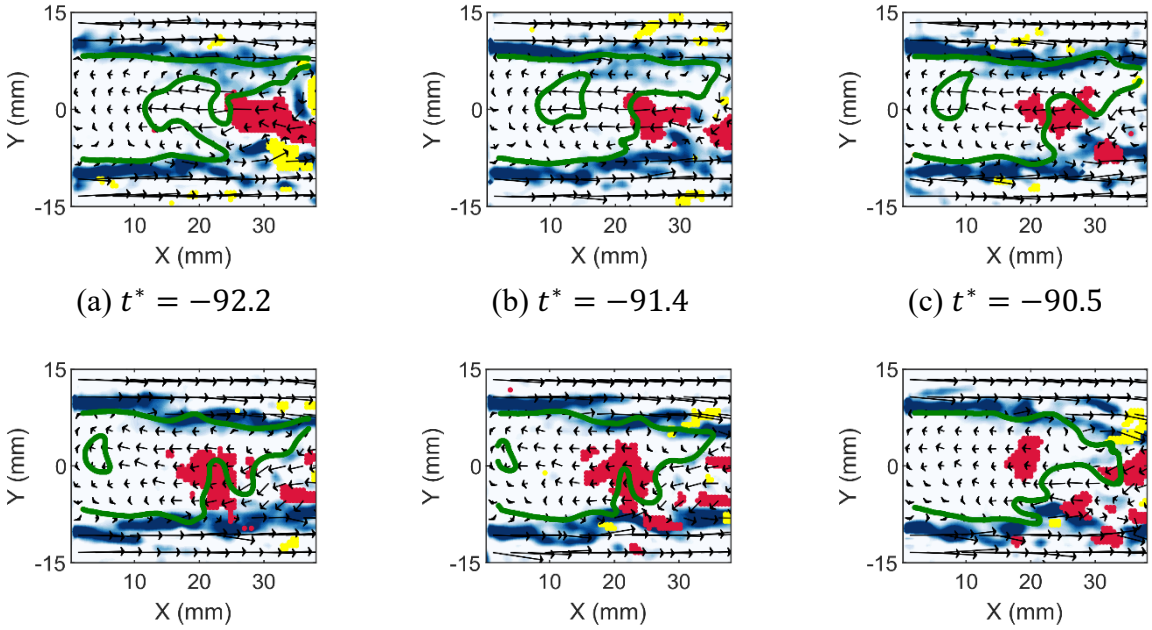

(a) $t^* = -92.2$ (b) $t^* = -91.4$ (c) $t^* = -90.5$

(d) $t^* = -89.7$ (e) $t^* = -88.7$ (f) $t^* = -88.3$

Figure 3.17 Images depicting large reactant volumes within the recirculation zone as a function of normalized time from blowoff ($\boldsymbol{t}^*$). Each image consists of vorticity magnitude field,

DISTRIBUTION A: Distribution approved for public release.

$|\boldsymbol{\omega}|(\boldsymbol{x}, \boldsymbol{y}, \boldsymbol{t})$ overlaid with regions having out of plane velocity magnitude greater than 50% of $\boldsymbol{u_{bulk}}$ (red-positive, yellow-negative), reaction surfaces (green), extinction zones (orange), and in-plane velocity vectors.

As already noted, permanent extinction appears at some downstream location, and moves closer to the bluff body as the flame approaches blowoff. Figure 3.18(a) – (c) clearly illustrates this short flame stage, around $t^* = t_3$. The out of plane field now shows some activity with alternating regions of in and out of plane motion but most of it seems to lie within the recirculation zone, not coincident with high vorticity regions.

Some insight into this behavior can be gained from downstream extinction observed in other works. Piloted jet flames, which normally have a closed tip and consume all incoming reactants over a range of conditions, similarly exhibit downstream extinction that progressively moves upstream as the equivalence ratio is lowered [26-29]. These flames are autoignited by the pilot at the jet exit, however further downstream where the effect of the pilot is reduced, they extinguish. In bluff body flames like ours, the role of the pilot is played by the hot combustion products within the recirculation zone and is a function of the flow/flame dynamics downstream, which is in contrast to the pilots in these studies, that are imposed by the operator.

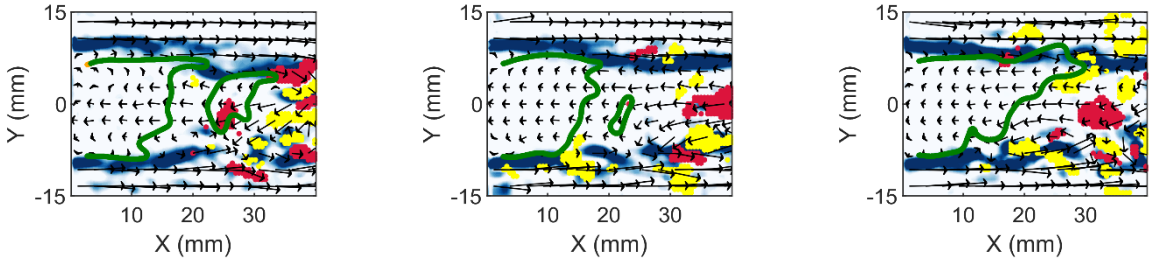

(a) $t^* = -71.7$ (b) $t^* = -67.6$ (c) $t^* = -66.3$

Figure 3.18 Images depicting a flame with significant levels of permanent downstream extinction behind the bluff body as a function of normalized time from blowoff ($\boldsymbol{t}^*$). Each image consists of vorticity magnitude field, $|\boldsymbol{\omega}|(\boldsymbol{x}, \boldsymbol{y}, \boldsymbol{t})$ overlaid with regions having out of plane velocity magnitude greater than 50% of $\boldsymbol{u_{bulk}}$ (red-positive, yellow-negative), reaction surfaces (green), extinction zones (orange), and in-plane velocity vectors.

Past this step, more of the recirculation zone is replaced by reactants and it slowly loses its piloting ability. The short flame observed before reduces to a V shaped flame stabilized within the near shear layers; these quickly blow off.

3.3.6 Analysis of Case V2: Vitiated flame blowoff

This section presents a description of the blowoff process for the vitiated flame, where the BVK instability is present both far from blowoff and near blowoff. Figure 3.19 plots $\frac{L_f}{D}$ and $\frac{L_{ez}}{D}$ for case

V2 with global extinction denoted by the orange line; it paints a similar picture to case U2. A value of $\frac{L_f}{D} \geq 2$ indicates that the flame does not see permanent extinction at any axial location downstream, or if it does, it is outside the measurement plane FOV. Once again, $\frac{L_f}{D}$ is close to 2 during the initial stages of the dataset (i.e., stage 1 of blowoff) indicating that the flame spans the entire FOV. Stage 2 of blowoff completely sets in by $t^* \sim -125$ (ref.

Figure 3.9(b)). Transient extinction zones appear frequently only during stage 1 of blowoff. Even then, they are rarely over 0.5D in length, quite similar in behavior to case U2. During stage 2 and the final instances of blowoff, their frequency of occurrence and lengths drop significantly.

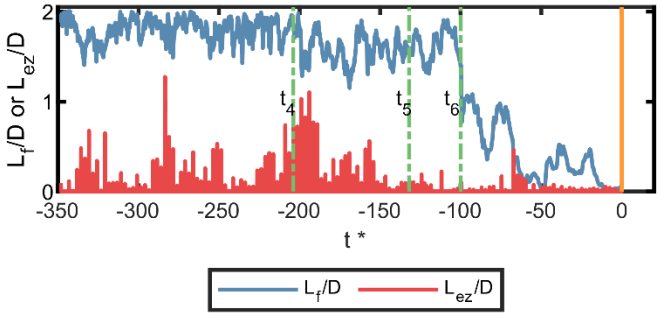

Figure 3.19 Normalized length scale at which permanent extinction occurs ($\frac{L_f}{D}$) and normalized total length of transient extinction zones ($\frac{L_{ez}}{D}$) as a function of normalized time from blowoff (t^*) denoted by the orange vertical line, for case U2. Time instants of interest are denoted by dashed vertical lines.

Figure 3.15 (dashed lines) shows isocontours of the autocorrelation, $A\left(\Delta t^*, \frac{\Delta x}{D}\right)$ of the binarized function, $I\left(t^*, \frac{x}{D}\right)$ computed in a manner similar to Equation 3 for case V2. It depicts the average axial convection speed of the transient extinction zones to be $\frac{u_{ez}}{u_{bulk}} \sim 0.1$. Once again, this value is in agreement with the nominal axial velocity in the vicinity of the bulk of the detected transient extinction zones within the shear layer, suggesting that they are convected by the local flow field. The correlation drops to 1/e of its maximum at $\left(\Delta t^*, \frac{\Delta x}{D}\right) = (0.75, 0.07)$ quantifying the average space-time lifetime of these extinction zones while also suggesting a shorter lifetime than case U2. Their length, inferred from the (1/e) width of the space-time correlation surface is about 0.1D, similar to case U2. Once again, the space-time correlation surface has a rhombus-like shape for $|\Delta t^*|, \left|\frac{\Delta x}{D}\right| \ll 1$, and its inclination can be used to compute an edge speed of $\frac{u_{ez}^*}{u_{bulk}} \sim 4$. This is attributed to the rapidly changing length of the transient extinction zone.

DISTRIBUTION A: Distribution approved for public release.

Next, we consider several snapshots around the times t_4, t_5, t_6 denoted by the green dashed lines on Figure 3.19. These snapshots show the edge of $O(x, y, t)$ with the reaction surface (green), transient extinction zone (orange) overlaid on the magnitude of the Z component of vorticity, $|\omega|(x, y, t)$. Regions with out of plane velocity magnitude greater than 50% of u_{bulk} are shown in red (positive) and yellow (negative).

The flame once again starts off exhibiting characteristics of stage 1 of blowoff dynamics, as expected (around $t^* = t_4$). Transient extinction zones are observed along the reaction surface. Figure 3.20(a) – (c) shows instances of the inception and growth of the transient extinction zone, similar to case U2. The out of plane activity appears to be more organized than case U2 at the same stage presumably due to the reduced gas expansion levels in this case, which potentially does not suppress shear flow structures as much as case U2.

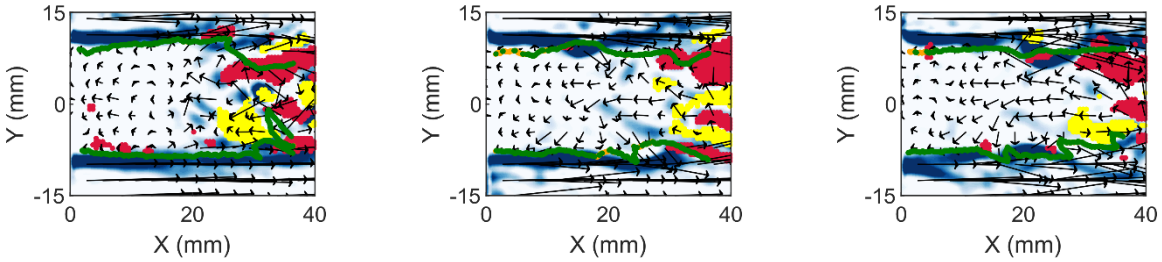

(a) $t^* = -205.4$ (b) $t^* = -204.2$ (c) $t^* = -203.8$

Figure 3.20 Images depicting the initial instances of a flame (case V2) undergoing blowoff as a function of normalized time from blowoff ($\boldsymbol{t^*}$). Each image consists of OH field, $\boldsymbol{O(x, y, t)}$ (red) overlaid with regions having out of plane velocity magnitude greater than 50% of $\boldsymbol{u_{bulk}}$ (red-positive, yellow-negative) and in-plane velocity vectors.

As the flame approaches global extinction, it reaches a point (around $t^* = t_5$) where large volumes of reactants are present within the recirculation zone, in the form of burning reactant fingers (Figure 3.21(d)) or intermittent downstream extinction, quite similar to case U2. Figure 3.21 (a) – (f) shows the life cycle of a burning reactant finger as it is caught in the backflow of the recirculation zone, burns and reduces in size as it convects towards the back of the bluff body and eventually completely burns out before hitting the back of the bluff body. The out of plane activity once again seems to be restricted to the reactants-only regions of the field or towards the end of the recirculation zone where the BVK instability becomes dominant (ref. discussion around Figure 3.10). Such behavior involving the entrance of unburnt reactants from near the end of the recirculation zone was similarly observed in an earlier work involving an axisymmetric bluff body [67], though their exact origin was not clear.

DISTRIBUTION A: Distribution approved for public release.

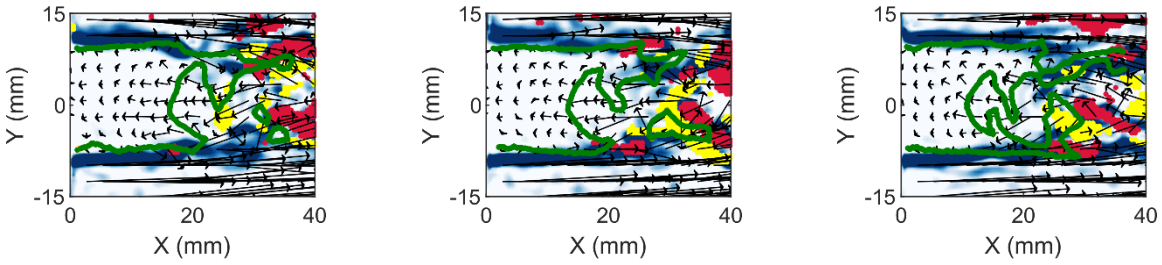

(a) $t^* = -133.4$ (b) $t^* = -132.9$ (c) $t^* = -132.6$

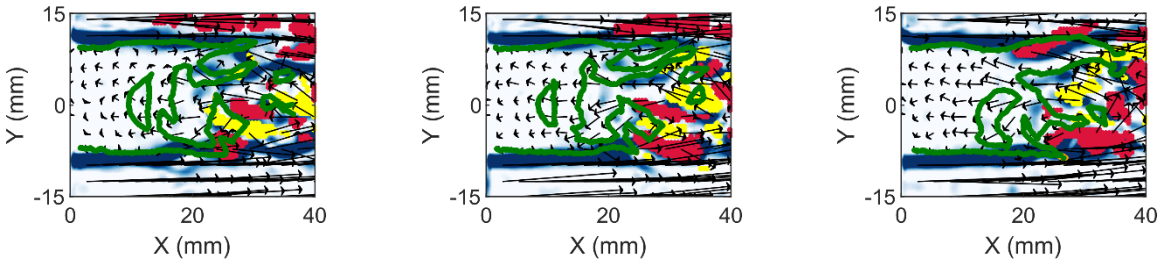

(d) $t^* = -132.4$ (e) $t^* = -132.1$ (f) $t^* = -131.7$

Figure 3.21 Images depicting large volumes of reactants within the recirculation zone (case V2) as a function of normalized time from blowoff ($\boldsymbol{t^*}$). Each image consists of OH field, $\boldsymbol{O(x, y, t)}$ (red) overlaid with regions having out of plane velocity magnitude greater than 50% of $\boldsymbol{u_{bulk}}$ (red-positive, yellow-negative) and in-plane velocity vectors.

Around $t^* = t_6$, the flame is quite short and there is a large zone of permanent downstream extinction, as shown in Figure 3.22(a) – (c). Shortly after this stage, global extinction is reached. In all, the blowoff transient of this low σ case are broadly similar to that of the high σ flame. This is an important result due to the very limited data in the open literature characterizing the detailed time-series dynamics of the blowoff transient in globally unstable, low σ flames. However, we do not see any fundamentally different features of the near LBO flame behavior between cases U2 and V2. This may be a manifestation of the fact that even the high σ flame becomes globally unstable near blowoff.

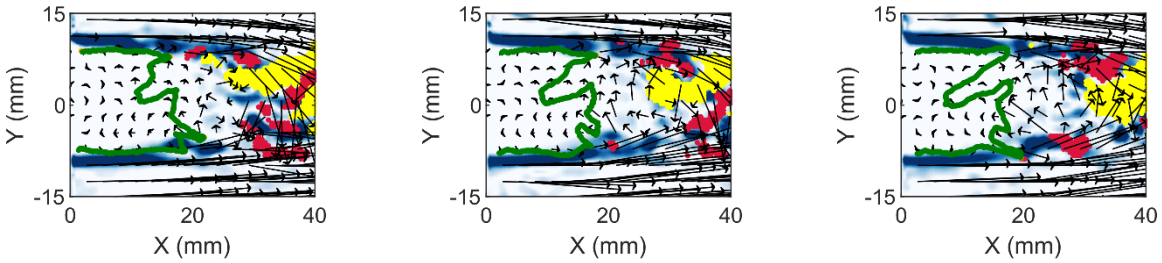

(a) $t^* = -100.1$ (b) $t^* = -99.9$ (c) $t^* = -99.7$

Figure 3.22 Images depicting a short flame behind the bluff body (case V2) as a function of normalized time from blowoff ($\boldsymbol{t^*}$). Each image consists of OH field, $\boldsymbol{O(x, y, t)}$ (red) overlaid with regions having out of plane velocity magnitude greater than 50% of $\boldsymbol{u_{bulk}}$ (red-positive, yellow-negative) and in-plane velocity vectors.

3.4 Discussion

This section summarizes the results of this work. First, the above discussions clearly indicate that blowoff is a "process", culminating in the actual complete extinction of the flame. It is clearly precipitated by feedback between recirculating hot products that ignite (or fail to ignite) incoming reactants and downstream extinction. A characteristic blowoff time, τ_{ext} associated with this feedback can be extracted from Figure 3.14 and Figure 3.19. Following a convention from previous works [67, 68], we define it as the time taken for $\frac{L_f}{D}$ to drop from 90% of its maximum value to 10% of its maximum value. It works out to be similar for the two cases; $93\frac{D}{u_{bulk}}$ and $86\frac{D}{u_{bulk}}$ for cases U2 and V2 respectively. Several other studies report varying lengths of the blowoff transient; for e.g., $40\frac{D}{u_{bulk}}$ (swirl flame) [18], ~ $120\frac{D}{u_{bulk}}$ [35] and $15 - 26\frac{D}{u_{bulk}}$ [67, 68] for various bluff body flames. All of these values are one to two orders of magnitude higher than the characteristic flow time scale $\left(\frac{D}{u_{bulk}}\right)$ which is, again, indicative of the negative feedback that requires several flow time scales to lead to complete extinction. Such behavior is completely different from flames stabilized by a kinematic balance between flame speed and flow velocity where a change in flame speed/flow velocity would immediately cause the flame to begin adjusting itself to maintain the kinematic balance. This point is significant for computations of blowoff, as it indicates that a large number of flow through times is needed to predict blowoff. Similarly, these results indicate that computations of bluff body LBO must be fully three dimensional. This is also an important point; e.g., the only review of LBO computations focused its attention on two-dimensional simulations [59]. Finally, these results emphasize the importance of downstream permanent extinction, which gradually moves backward towards the bluff body, emphasizing the importance of resolving the entire axial extent of the flame.

It is also helpful to contextualize these findings within the larger literature, particularly the recent publications of Fugger et al. [38, 39, 49]. They examined blowoff for two different bluff body widths, over a range of u_{bulk} for low and high σ confined bluff body flames using two kinds of fuels. As noted above, it seems that the different steps involved in the process of blowoff are the same in both high and low σ cases, implying that we can discuss both cases together. To describe this, we will draw illustrative sketches from two views – the midplane XY (Z=0) plane as presented in this work, and the spanwise XZ (Y=0) plane, based upon the prior PIV and chemiluminescence imaging work of Fugger et al. [38, 39]. These depict the span of the

recirculation zone (green), separating or wall bounded shear layers (blue) and the flame (red), and are pictured in Figure 3.23. These are not intended to capture the changing size of the recirculation zone, but focus on the relative positions of the flame, shear layers and recirculation zone. Representative streamlines are shown in Figure 3.23((e),(f)).

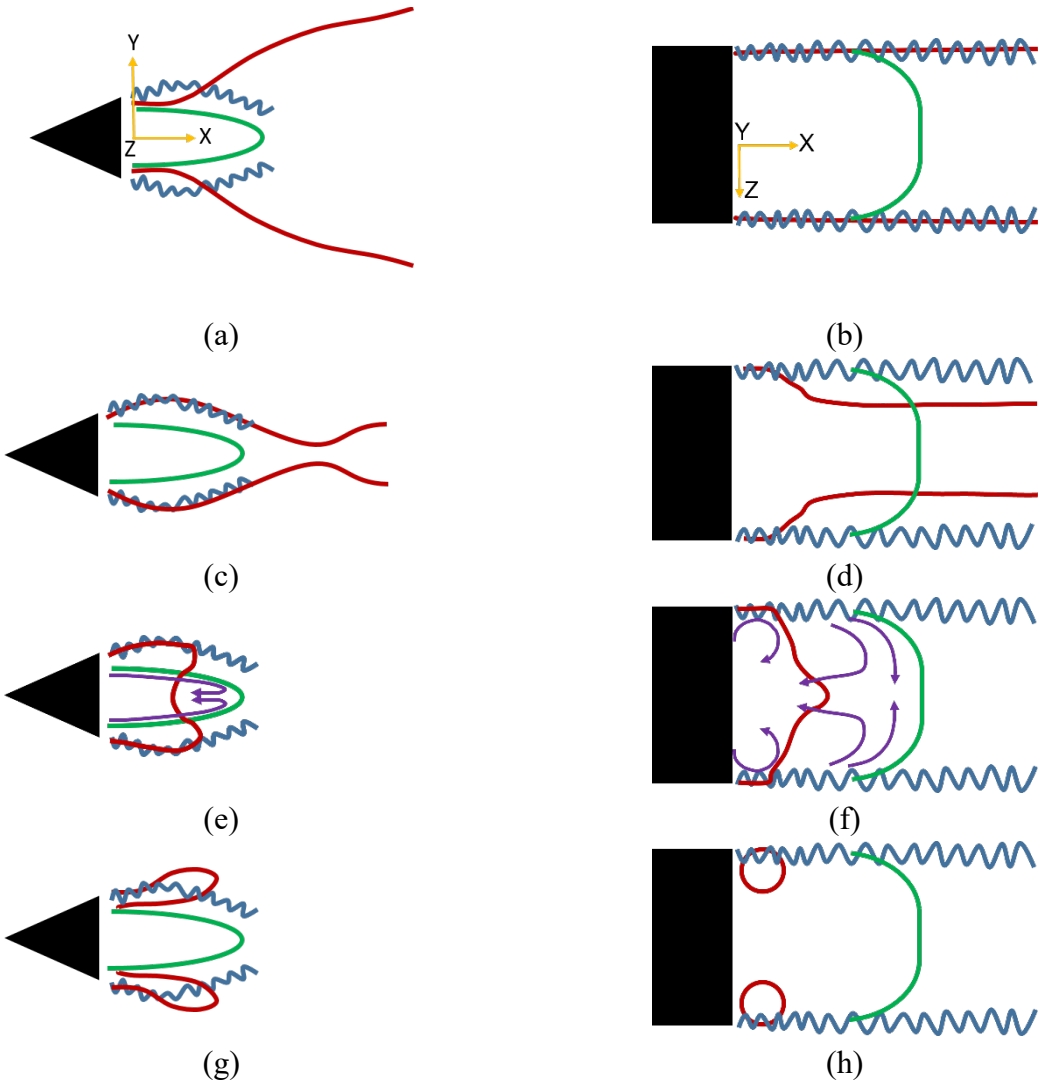

Figure 3.23 Illustration of a flame at different instances on the way to blowoff as seen on the Z=0 plane ((a), (c), (e), (g)), and the Y=0 plane ((b),(d), (f), (h)), depicting the recirculation zone (green), shear layers (blue) and the flame (red). Coordinate system is depicted in (a) and (b). Representative streamlines are indicated in violet.

Figure 3.23 (a) shows a flame far away from blowoff. The flame spans the full width of the section, as shown in the Y=0 plane in Figure 3.23 (b). At this stage, the presence of three-

DISTRIBUTION A: Distribution approved for public release.

dimensional structures is largely dictated by the gas expansion levels, i.e., they increase monotonically with downstream distance and reduced gas expansion, σ. Their presence is due to secondary instabilities of the shear layer/BVK instability (as characterized in the current study) and in part the spanwise nonuniform recirculation zone and the corner vortical structures (i.e., confinement effects) as detailed in recent previous work [38, 39, 49]. They result in large out of plane velocities in the Z=0 plane and transport material (combustion products, in this case) across the span.

As bluff body flames approach blowoff, they move into the high shear regions where they experience high values of flame stretch over the flame length [32, 35] (ref. Figure 3.23(c)). This causes the formation of transient extinction zones along the reaction surface which marks the onset of stage 1 of blowoff dynamics. One key hypothesis suggested earlier (and supported by recent previous works [38, 39]) is that the Z=0 plane is not representative of what is happening across the span of confined bluff body flames, especially close to blowoff. In particular, the visualizations of Fugger et al. [38, 39] show that permanent extinction sets in earlier away from the Z=0 plane. A possible explanation is that the inception of permanent extinction starts close to the span walls, due to some combination of wall quenching from heat losses to the side wall, stretch based extinction due to its proximity to the wall boundary layer, and stretch based extinction due to three dimensional structures associated with the bluff body/confining wall interaction (i.e., the corner vortical structures located with the recirculation zone as described in the Introduction). Figure 3.23(d) illustrates how such a flame would look as viewed on the Y=0 plane. Unburnt reactants could enter the backflow of the recirculation zone in other Z planes at this stage as shown in Figure 3.17 and Figure 3.21, through three dimensional structures and then manifest as burning reactant fingers. At this point, the majority of the burning reactant fingers burn out before reaching the back of the bluff body. It is worthwhile to note that the wake is still composed primarily of hot products; enough permanent extinction has not set in for there to be a strong enough *global* density ratio change to cause the BVK instability to manifest/get stronger if already present.

As already mentioned, three-dimensional structures play an important role in transport of materials in the spanwise (Z) direction; there may be a self-amplifying feedback as the strength of these structures grows as extinction increases. Closer to blowoff, this brings in cold reactants from the near wall regions and takes out hot products from regions closer to the centerline (see Figure 3.23(f) streamlines). This, along with the increased reactant entrainment levels close to blowoff, will exacerbate the width of permanent extinction in the spanwise (Z) direction, i.e., permanent extinction spreads away from the walls (Figure 3.23(f)) and also towards the bluff body leading to the formation of a short flame (Figure 3.23(e)). Enough of the wake/recirculation zone has been replaced with cold reactants for the global density ratio to now drop to levels sufficiently low for the BVK instability to set in (if it was not present in the stable case) or get stronger (if it was already present). It is worthwhile to note that permanent extinction causes the presence of a flame downstream of which the recirculation zone persists (ref. Figure 3.23(e)). The backflow associated with the recirculation zone is now composed of reactants and is fast enough (relative to the flame

DISTRIBUTION A: Distribution approved for public release.

speed) to push the flame front closer to the back of the bluff body, thereby filling more of the recirculation zone with unburnt reactants.

Permanent downstream extinction appears to play a pivotal role in the blowoff process. As expected, these flames rely on the piloting ability of the recirculation zone to ignite and stabilize a flame. Near blowoff, the recirculation zone is replaced by cold reactants (instead of hot products); this causes the recirculation zone to lose its piloting ability, pictured in Figure 3.23(g). Similar behavior is seen in both vitiated and unvitiated flames undergoing blowoff. The final vestiges of a flame undergoing blowoff, even after extinction in the Z=0 plane lies in close proximity to the corner vortical structures as represented in Figure 3.23(h), as shown by Fugger et al. [38].

3.5 Conclusion

This work investigated the process of blowoff at fundamentally different base hydrodynamic states (high and low density ratios) using simultaneous stereo PIV, OH PLIF and CH_2O PLIF. It found a similar series of steps leading to blowoff at both conditions and prescribed a phenomenological description of a blowoff mechanism including what ultimately contributed towards making the process of blowoff irrecoverable after a certain point. The flame approaches blowoff by sitting atop the shear layers where it experiences high values of flow strain induced flame stretch. This causes transient extinction zones to form along the reaction surface - a process which marks the onset of stage 1 of blowoff dynamics. As the flame progresses towards global extinction, BVK instability permanently sets in, marking the onset of stage 2 of blowoff dynamics. High levels of out of plane activity are prevalent either due to secondary instabilities of the shear layer/BVK instability or presumed confinement effects. This out of plane motion is responsible for introducing reactant volumes into/ removing product volumes out of the mid-plane recirculation zone thereby exacerbating permanent downstream extinction and moving it closer to the bluff body. With this, the flame within the recirculation zone is pushed towards the back of the bluff body by the backflow within the recirculation zone. As this happens more of the recirculation zone is replaced by reactants and there comes a point where all of the combustion products within the recirculation zone are completely replaced by cold reactants, causing it to lose its piloting ability. In its absence, the autoignition of the flame anchor point is no longer possible and flame stabilization is hindered, causing ultimate blowoff.

Several follow on studies are suggested by this work, in particular, to further explore three-dimensional effects such as quantifying the out of plane unburned reactant motions. This suggests more careful analysis of LBO dynamics at other planes, as well as varying the bluff body aspect ratio, *L/D*. In addition, it also suggests performing comparative 2-D and 3-D computational studies of the same nominal geometry, to further explore the dynamical significance of the three-dimensional effects noted here.

DISTRIBUTION A: Distribution approved for public release.

Bibliography

[1] Y.C. Chao, Y.L. Chang, C.Y. Wu, T.S. Cheng, An experimental investigation of the blowout process of a jet flame, Proc. Combust. Inst. 28 (2000) 335-342.

[2] T. Chen, L. Goss, D. Talley, D. Mikolaitis. Stabilization zone structure in jet diffusion flames from liftoff to blowout. 27th Aerospace Sciences Meeting,1989, 153.

[3] G.T. Kalghatgi, Blow-Out Stability of Gaseous Jet Diffusion Flames. Part I: In Still Air, Combust. Sci. Technol. 26 (2007) 233-239.

[4] A. Verdier, J. Marrero Santiago, A. Vandel, G. Godard, G. Cabot, B. Renou, Local extinction mechanisms analysis of spray jet flame using high speed diagnostics, Combust. Flame 193 (2018) 440-452.

[5] A.E. Potter Jr, E.L. Wong, Effect of pressure and duct geometry on bluff-body flame stabilization, National Advisory Committee for Astronauts, Cleveland, OH, USA, 1958.

[6] K.R. Anderson, J. Hertzberg, S. Mahalingam, Classification of absolute and convective instabilities in premixed bluff body stabilized flames, Combust. Sci. Technol. 112 (1996) 257-269.

[7] J.R. Hertzberg, I.G. Shepherd, L. Talbot, Vortex Shedding Behind Rod Stabilized Flames, Combust. Flame 86 (1991) 1-11.

[8] J. Longwell. Flame stabilization by bluff bodies and turbulent flames in ducts. Symposium (International) on Combustion,1953, 90-97.

[9] J.P. Longwell, E.E. Frost, M.A. Weiss, Flame Stability in Bluff Body Recirculation Zones, Ind. Eng. Chem. 45 (1953) 1629-1633.

[10] E.E. Zukoski, F.E. Marble, Experiments concerning the mechanism of flame blowoff from bluff bodies, (1983).

[11] Q. An, A.M. Steinberg, The role of strain rate, local extinction, and hydrodynamic instability on transition between attached and lifted swirl flames, Combust. Flame 199 (2019) 267-278.

DISTRIBUTION A: Distribution approved for public release.

[12] R.M. Kumar, I. Chterev, D. Stepien, M. Sirignano, B.L. Emerson, C.A. Fugger, N. Jiang, S. Roy, T.C. Lieuwen, Near blowout dynamics of a premixed, swirl stabilized flame, Proc. Combust. Inst. 38 (2021) 6067-6075.

[13] S. Nair, T. Lieuwen. Acoustic Detection of Imminent Blowout in Pilot and Swirl Stabilized Combustors. ASME turbo expo,2003, 55-65.

[14] R. Yuan, J. Kariuki, E. Mastorakos, Measurements in swirling spray flames at blow-off, International Journal of Spray and Combustion Dynamics, (2018) 185-210.

[15] B. Zhou, Q. Li, Y. He, P. Petersson, Z.S. Li, M. Alden, X.S. Bai, Visualization of multi-regime turbulent combustion in swirl-stabilized lean premixed flames, Combust. Flame 162 (2015) 2954-2958.

[16] K. Lyons, K. Watson, C. Carter, J. Donbar, On flame holes and local extinction in lifted-jet diffusion flames, Combust. Flame 142 (2005).

[17] K.M. Lyons, Toward an understanding of the stabilization mechanisms of lifted turbulent jet flames: experiments, Prog. Energ. Combust. 33 (2007) 211-231.

[18] D.E. Cavaliere, J. Kariuki, E. Mastorakos, A Comparison of the Blow-Off Behaviour of Swirl-Stabilized Premixed, Non-Premixed and Spray Flames, Flow Turbul. Combust. 91 (2013) 347-372.

[19] W.M. Pitts. Assessment of theories for the behavior and blowout of lifted turbulent jet diffusion flames. Symposium (international) on combustion,1989, 809-816.

[20] S.J. Shanbhogue, S. Husain, T. Lieuwen, Lean blowoff of bluff body stabilized flames: Scaling and dynamics, Prog. Energ. Combust. 35 (2009) 98-120.

[21] E. DeZubay, Characteristics of disk-controlled flames, Aero Digest 61 (1950) 54-56.

[22] S. Chaudhuri, B.M. Cetegen, Blowoff characteristics of bluff-body stabilized conical premixed flames in a duct with upstream spatial mixture gradients and velocity oscillations, Combust. Sci. Technol. 181 (2009) 555-569.

[23] B.R. Chowdhury, B.M. Cetegen, Effects of free stream flow turbulence on blowoff characteristics of bluff-body stabilized premixed flames, Combust. Flame 190 (2018) 302-316.

[24] I. Glassman, R.A. Yetter, N.G. Glumac, Combustion, Academic press2014.

[25] R. Erickson, M. Soteriou, The influence of reactant temperature on the dynamics of bluff body stabilized premixed flames, Combust. Flame 158 (2011) 2441-2457.

[26] R. Rajaram, T. Lieuwen, Parametric studies of acoustic radiation from premixed flames, Combust. Sci. Technol. 175 (2003) 2269-2298.

DISTRIBUTION A: Distribution approved for public release.

[27] M.J. Dunn, A.R. Masri, R.W. Bilger. Lifted turbulent premixed flames issuing into a hot coflow, imaging of temperature and OH. Proc. of the 16th Australasian Fluid Mechanics Conference,2007.

[28] M.J. Dunn, A.R. Masri, R.W. Bilger, A new piloted premixed jet burner to study strong finite-rate chemistry effects, Combust. Flame 151 (2007) 46-60.

[29] M.J. Dunn, A.R. Masri, R.W. Bilger, R.S. Barlow, Finite rate chemistry effects in highly sheared turbulent premixed flames, Flow, turbulence and combustion 85 (2010) 621-648.

[30] B.J. Lee, H.G. Im, Dynamics of bluff-body-stabilized lean premixed syngas flames in a meso-scale channel, Proc. Combust. Inst. 36 (2017) 1569-1576.

[31] B.J. Lee, C.S. Yoo, H.G. Im, Dynamics of bluff-body-stabilized premixed hydrogen/air flames in a narrow channel, Combust. Flame 162 (2015) 2602-2609.

[32] S. Chaudhuri, S. Kostka, M.W. Renfro, B.M. Cetegen, Blowoff dynamics of bluff body stabilized turbulent premixed flames, Combust. Flame 157 (2010) 790-802.

[33] T.C. Lieuwen, Unsteady Combustor Physics, Cambridge University Press, Cambridge, 2012.

[34] S. Chaudhuri, S. Kostka, M.W. Renfro, B.M. Cetegen, Blowoff mechanism of harmonically forced bluff body stabilized turbulent premixed flames, Combust. Flame 159 (2012) 638-640.

[35] S. Chaudhuri, S. Kostka, S.G. Tuttle, M.W. Renfro, B.M. Cetegen, Blowoff mechanism of two dimensional bluff-body stabilized turbulent premixed flames in a prototypical combustor, Combust. Flame 158 (2011) 1358-1371.

[36] A.J. Morales, T. Genova, J. Reyes, I. Boxx, K.A. Ahmed, Turbulence-Driven Blowout Instabilities of Premixed Bluff-Body Flames, Flow, Turbulence and Combustion 108 (2022) 213-236.

[37] A.J. Morales, I.M. Lasky, M.K. Geikie, C.A. Engelmann, K.A. Ahmed, Mechanisms of flame extinction and lean blowout of bluff body stabilized flames, Combust. Flame 203 (2019) 31-45.

[38] C.A. Fugger, T.P. Gallagher, J.P. Sykes, A.W. Caswell, Spanwise recirculation zone structure of a bluff body stabilized flame, Combust. Flame 216 (2020) 58-61.

[39] C.A. Fugger, A.W. Caswell, The influence of spanwise nonuniformity on lean blowoff in bluff body stabilized turbulent premixed flames, Proc. Combust. Inst. 38 (2021) 6327-6335.

[40] C. Williamson, The existence of two stages in the transition to three-dimensionality of a cylinder wake, Physics of fluids 31 (1988) 3165-3168.

[41] A. Prasad, C.H. Williamson, Three-dimensional effects in turbulent bluff-body wakes, J Fluid Mech. 343 (1997) 235-265.

DISTRIBUTION A: Distribution approved for public release.

[42] C. Williamson, Three-dimensional wake transition, J Fluid Mech. 328 (1996) 345-407.

[43] C.H. Williamson, Vortex dynamics in the cylinder wake, Annu. Rev. Fluid Mech. 28 (1996) 477-539.

[44] C. Williamson, The natural and forced formation of spot-like 'vortex dislocations' in the transition of a wake, J Fluid Mech. 243 (1992) 393-441.

[45] C.H. Williamson, Oblique and parallel modes of vortex shedding in the wake of a circular cylinder at low Reynolds numbers, J Fluid Mech. 206 (1989) 579-627.

[46] A. Prasad, C.H.K. Williamson, The instability of the shear layer separating from a bluff body, J Fluid Mech. 333 (1997) 375-402.

[47] R. Ruderich, H. Fernholz, An experimental investigation of a turbulent shear flow with separation, reverse flow, and reattachment, J Fluid Mech. 163 (1986) 283-322.

[48] C.L. Ford, P.M. Winroth, On the scaling and topology of confined bluff-body flows, J Fluid Mech. 876 (2019) 1018-1040.

[49] C.A. Fugger, J. Sykes, T. Gallagher, B. Rankin, A.W. Caswell. Corner Vortex Structures: Spanwise Imaging of a Confined, Premixed Bluff Body Stabilized Flame. AIAA Scitech 2020 Forum,2020, 0435.

[50] J. Sykes, T. Gallagher, C.A. Fugger, A.W. Caswell, B.A. Rankin. Corner Vortex Structures: Large Eddy Simulations of a Confined, Premixed Bluff Body Stabilized Flame. AIAA Scitech 2020 Forum,2020, 0436.

[51] M. Reader-Harris, Orifice plates and venturi tubes, Springer2015.

[52] R.M. Kumar, S. Adhikari, O. Bibik, B.L. Emerson, C.A. Fugger, T.C. Lieuwen, Simultaneous multiple laser beam intensity profile correction and its application to a vitiated bluff body combustor field, Applied Optics 61 (2022) 532-539.

[53] C.A. Fugger, B. Paxton, J.R. Gord, B.A. Rankin, A.W. Caswell. Measurements and Analysis of Flow-Flame Interactions in Bluff-Body-Stabilized Turbulent Premixed Propane-Air Flames. AIAA Scitech 2019 Forum,2019.

[54] R. Mei, Velocity fidelity of flow tracer particles, Exp. Fluids 22 (1996) 1-13.

[55] P.C. Ma, H. Wu, J.W. Labahn, T. Jaravel, M. Ihme, Analysis of transient blow-out dynamics in a swirl-stabilized combustor using large-eddy simulations, Proc. Combust. Inst. 37 (2019) 5073-5082.

[56] L. Esclapez, P.C. Ma, E. Mayhew, R. Xu, S. Stouffer, T. Lee, H. Wang, M. Ihme, Fuel effects on lean blow-out in a realistic gas turbine combustor, Combust. Flame 181 (2017) 82-99.

DISTRIBUTION A: Distribution approved for public release.

[57] A. Tyliszczak, D.E. Cavaliere, E. Mastorakos, LES/CMC of blow-off in a liquid fueled swirl burner, Flow, Turbulence and Combustion 92 (2014) 237-267.

[58] H. Zhang, E. Mastorakos, Prediction of global extinction conditions and dynamics in swirling non-premixed flames using LES/CMC modelling, Flow, Turbulence and Combustion 96 (2016) 863-889.

[59] W.-W. Kim, J.J. Lienau, P.R. Van Slooten, M.B. Colket III, R.E. Malecki, S. Syed, Towards modeling lean blow out in gas turbine flameholder applications, (2006).

[60] B. Wieneke, PIV uncertainty quantification from correlation statistics, Measurement Science and Technology 26 (2015) 074002.

[61] J.M. Lilly, S.C. Olhede, Generalized Morse wavelets as a superfamily of analytic wavelets, IEEE Transactions on Signal Processing 60 (2012) 6036-6041.

[62] J.S. Lim, Two-dimensional signal and image processing, Englewood Cliffs, (1990).

[63] C. Tomasi, R. Manduchi. Bilateral filtering for gray and color images. Sixth international conference on computer vision (IEEE Cat. No. 98CH36271),1998, 839-846.

[64] K. Zuiderveld, Contrast limited adaptive histogram equalization, in: S.H. Paul (Ed.), Graphics gems IV, Academic Press Professional, Inc.1994 474-485.

[65] N. Otsu, A threshold selection method from gray-level histograms, IEEE transactions on systems, man, and cybernetics 9 (1979) 62-66.

[66] A. Favre, Parallel syntactic thinning by recoding of binary pictures, Computer Vision, Graphics, and Image Processing 23 (1983) 99-112.

[67] J. Kariuki, J.R. Dawson, E. Mastorakos, Measurements in turbulent premixed bluff body flames close to blow-off, Combust. Flame 159 (2012) 2589-2607.

[68] J. Dawson, R. Gordon, J. Kariuki, E. Mastorakos, A. Masri, M. Juddoo, Visualization of blow-off events in bluff-body stabilized turbulent premixed flames, Proc. Combust. Inst. 33 (2011) 1559-1566.

[69] D. Nistér, H. Stewénius. Linear time maximally stable extremal regions. European Conference on Computer Vision,2008, 183-196.

[70] H.N. Najm, P.H. Paul, C.J. Mueller, P.S. Wyckoff, On the adequacy of certain experimental observables as measurements of flame burning rate, Combust. Flame 113 (1998) 312-332.

[71] P.H. Paul, H.N. Najm. Planar laser-induced fluorescence imaging of flame heat release rate. Symposium (International) on Combustion,1998, 43-50.

DISTRIBUTION A: Distribution approved for public release.

[72] C.A. Fugger, S. Roy, A.W. Caswell, B.A. Rankin, J.R. Gord. Structure and dynamics of CH2O, OH, and the velocity field of a confined bluff-body premixed flame, using simultaneous PLIF and PIV at 10 kHz. Proc. Combust. Inst.,2019, 1461-1469.

[73] B. Ayoola, R. Balachandran, J. Frank, E. Mastorakos, C. Kaminski, Spatially resolved heat release rate measurements in turbulent premixed flames, Combust. Flame 144 (2006) 1-16.

[74] B. Emerson, J. O'Connor, M. Juniper, T. Lieuwen, Density ratio effects on reacting bluff-body flow field characteristics, J Fluid Mech. 706 (2012) 219-250.

[75] J. Derakhshandeh, M.M. Alam, A review of bluff body wakes, Ocean Eng. 182 (2019) 475-488.

[76] Y. Nakamura, Vortex shedding from bluff bodies and a universal Strouhal number, Journal of fluids and structures 10 (1996) 159-171.

[77] B. Kiel, K. Garwick, J. Gord, J. Miller, A. Lynch, R. Hill, S. Phillips. A detailed investigation of bluff body stabilized flames. 45th AIAA Aerospace Sciences Meeting and Exhibit,2007, 168.

[78] S. Nair, T. Lieuwen, Near-blowoff dynamics of a bluff-body stabilized flame, Journal of Propulsion and Power 23 (2007) 421-427.

[79] N.A. Ozturk, A. Akkoca, B. Sahin, PIV measurements of flow past a confined cylinder, Exp. Fluids 44 (2008) 1001-1014.

DISTRIBUTION A: Distribution approved for public release.

Chapter 4

Dynamics and bifurcations of laminar annular swirling and nonswirling jets

4.1 Introduction

This paper considers the dynamical behaviour of laminar swirling jets exhausting from an annular pipe into a semi-infinite reservoir. Similar flow situations are commonplace in a variety of industrial applications, such as combustors used for power and propulsion. In such systems, the cylindrical core of the annulus serves as a bluff centrebody, forming a central flame-stabilising recirculation region that promotes mixing and deters flashback [1]. As swirl is introduced, interactions between this centrebody wake and phenomena such as vortex breakdown can manifest a wide range of possible flow and flame topologies, often with significant impacts on the system's performance and stability [2].

The main objective of this work is to expose the state-space dynamics underlying the relationships between distinct flow morphologies in swirling and nonswirling annular jets, especially in regards to the size of the centrebody. Swirling flows in particular often exhibit extensive intervals of multistability and hysteresis [3, 4], making parameter space characterisation difficult via experiments and transient simulations. With such methods, repeatability becomes a challenge unless the initial and boundary conditions are carefully controlled, and unstable connections between stable solution manifolds cannot be identified. In this regard, branch continuation methods, which form the basis of our study, offer a distinct advantage as they can explicitly control variations in the flow configuration and converge to unsteady solution manifolds [5].

Much like swirling circular jets, which do not possess an inner wall, swirling annular jets feature a complex suite of physical processes that drive their underlying dynamics. In both cases, these mechanics include prominent axial and azimuthal shear effects, centrifugal forces, and inertial waves [6]. However, the presence of the wake region that forms behind the centrebody leads to greater complexity in the case of annular jets compared to their circular analogues. For example, even in the absence of swirl, laminar annular jets spontaneously lose their axisymmetry [7, 8] and express a Bénard–von Kármán wake vortex street pattern [9]. Spatiotemporally coherent structures resembling these laminar flow patterns are also known to persist well into the turbulent regime [10, 11]. While a major focus of our work is dedicated to swirling jets, this paper will show that these dynamics at zero swirl are triggered by a sequence of separate Hopf bifurcations: an initial sub- or supercritical zero-frequency Hopf bifurcation to a 3D plane symmetric steady state followed by subsequent unsteady Hopf bifurcations. Such dynamics are shown to correspond to unsteady plane-symmetric vortex shedding or plane-asymmetric wake wobbling. It will also be shown that any finite amount of swirl causes the steady asymmetry to twist and precess in the azimuthal direction, leading to more elaborate space-time dynamics.

Sheen et al. [12] performed one of the first studies to directly explore the dynamics of swirling annular jets by using an experimental jet configuration with an inner-to-outer diameter ratio of 0.48 and adjustable swirl vanes under laterally confined and unconfined conditions for laminar to transitional ($O(10)$ to $O(1000)$) Reynolds numbers. Using a planar smoke visualisation technique, they identified a variety of distinct flow states that exchanged dominance as the flow rate and swirl vane angles were varied. Their main results for the unconfined case are briefly recounted here. At low swirl, they described the bluff body wake as a steady axisymmetric feature at low Reynolds numbers, which became unsteady and non-axisymmetric at higher Reynolds numbers. With increasing swirl, they observed that the unsteady and asymmetric flow patterns disappeared, leaving a steady, axisymmetric annular wake vortex for all Reynolds numbers. As they further

DISTRIBUTION A: Distribution approved for public release.

increased the swirl, the wake underwent a sequence of topological changes whereby a secondary vortex (the 'inverted triangle zone') located within the wake vortex along the centrebody wall and rotating in the opposite direction emerged, grew, and eventually penetrated the wake vortex, resulting in a steady axisymmetric flow without an internal stagnation point along the centreline. After this sequence, a threshold level of swirl was reached where vortex breakdown occurred downstream of the wake region, leading to the formation of an isolated recirculation "bubble" on the central axis. Further increasing swirl caused this isolated recirculation zone to progress upstream towards the centrebody, until at the highest swirl levels considered, the vortex breakdown bubble and the bluff body wake merged to create a single, large recirculation region attached to the centrebody. Though Sheen et al. [12] focused primarily on quasi-laminar dynamics, it is important to note that a similar overall picture of the annular jet's evolution with swirl holds for the turbulent mean flow, as shown, for example, by Vanierschot and Van den Bulck [13]. The same is true even at Reynolds numbers approaching 10^5, as reported in the large eddy simulations of García-Villalba and Fröhlich [14]. Similar observations were also reported in a combustor nozzle by Wang et al. [15], who noted how distinct or merged recirculation zones were present, depending upon the swirl number.

One important aspect of the description by Sheen et al. [12] is the single-valued nature of the reported swirling annular jet parameter space. However, using a stepped-conical annular nozzle with a diameter ratio of 0.65, Ogus et al. [9] were able to computationally and experimentally demonstrate a steady, axisymmetric open wall jet state that occurred under laminar conditions at swirl numbers beyond those examined by Sheen et al. [12]. Furthermore, this wall jet state persisted at lower swirl numbers due to the Coandă effect, thereby demonstrating hysteresis with respect to the various wake and vortex breakdown states reported earlier. Similar bistable behaviours involving a wall jet state have also been reported for swirling annular jets in the turbulent regime [16, 17, 18, 19]. The dynamics of this wall jet state will be plainly seen in our results, and are further discussed in the context of circular jets elsewhere [20, 21].

In addition to their description of parameter hysteresis, Ogus et al. [9] also gave an account of the unsteady structures they observed as the swirl was varied. We have already mentioned their description of the wake dynamics present in the nonswirling jet. As the swirl was increased from zero, Ogus et al. [9] described a quasiperiodic oscillation associated with regular Bénard–von Kármán-like vortex shedding and a slower precession of the asymmetric recirculation zone due to swirl. This unsteady behaviour disappeared as the swirl increased and the flow underwent a sequence of steady topology changes similar to that reported by Sheen et al. [12]. After the swirl increased beyond the threshold for vortex breakdown, a singly azimuthally-periodic ($|m| = 1$) precessing vortex core (PVC) spiral appeared. As swirl increased further, the central recirculation zone spread open, and the flow transitioned to a steady wall jet. No additional unsteady behaviour was reported, and the wall jet remained steady throughout the hysteresis region.

The fluid dynamics considered in earlier studies and further explored in this paper have significant implications on combustion systems, where this geometry is almost ubiquitous. In premixed combustion, flame shapes and locations are governed by a kinematic balance between the flow velocity and flame propagation normal to itself. Stagnation points and recirculation zones typically serve to stabilise such flames. In annular jets, flames can stabilise in either or both of the inner and outer shear layers and/or in front of the central recirculation zone (if one exists), giving rise to at least four completely different families of flame shapes [22]. The presence or absence of two of these four families is controlled by the presence of central stagnation zones, where the flame can aerodynamically stabilise well away from any physical hardware. Indeed, the complex nature of predicting when and where such aerodynamically stabilised flames exist was a key motivator for our interest in this geometry. This paper will show that the number and location of stagnation points in the steady flow is a strong function of the swirl ratio, centrebody diameter, and Reynolds number, thereby demonstrating the significant parameter sensitivities that underlie the complex and very different observations of mean flame configurations in various combustion experiments and simulations [15, 23, 24]. Furthermore, this paper will explore the birth of non-axisymmetric and unsteady flow solutions such as centrebody wake vortices and PVCs, which govern the asymmetries often observed in combustion system flames [22].

The fluids community has invested significant theoretical efforts towards understanding and modelling the dynamics of many swirling flows. Though a detailed bifurcation analysis of swirling annular jets is lacking, similar analyses have been performed for several laminar swirling flow configurations including the Grabowski–Berger vortex model [25, 26] and [27, 28, 29, 20, 21] swirling circular jets. Classical linear stability analyses of parallel swirling jets and wakes have

DISTRIBUTION A: Distribution approved for public release.

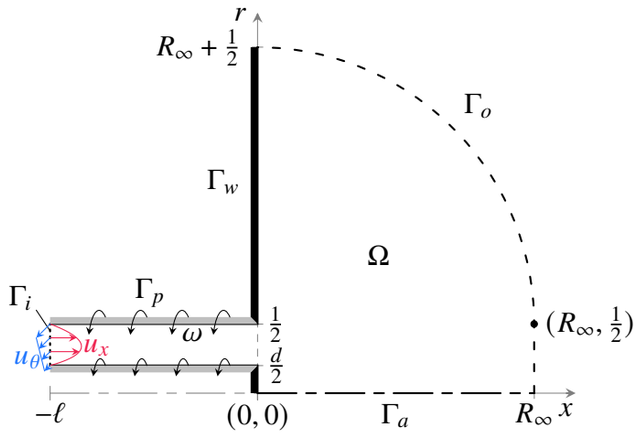

Figure 4.1: Schematic of the meridional plane of the axisymmetric domain Ω with boundary Γ.

also been performed [30, 31]. In turbulent swirling jets, linear [32, 33, 34, 35, 36, 37] and weakly-nonlinear [38] mean flow stability analysis techniques have explained the so-called "global modes" that seem to underlie many of the observed coherent structures [39]. While several existing mean flow stability studies do consider swirling annular jets, none of the existing studies resolve the parameter space with enough detail to provide a comprehensive description of swirling annular jet behaviours. Furthermore, mean flow linear stability analysis cannot predict oscillation amplitudes, and its validity is subject to several conditions [40, 41, 35, 42] that may not be robust to changes in parameters. Hence, at present, such studies do not yield a holistic understanding of the global dynamics of swirling annular jets. The current study aims to fill this void by exhaustively surveying the swirling annular jet parameter space under laminar conditions. Such knowledge will also serve as a starting point from which to develop a fundamental understanding of the key physics and dynamics at play in the turbulent regime.

The remainder of this paper is organised as follows. Section 4.2 describes the flow configuration and solution methodology. The main results are presented in Section 4.3, beginning with an overview of the steady flow topologies in Section 4.3.1. A discussion of the dynamics of the nonswirling jet is given in Section 4.3.2. Section 4.3.3 considers the effect of rotation on the wake behind the centrebody. Section 4.3.4 describes the dynamics of vortex breakdown and analyses relationships between the various flow topologies and the centrebody diameter. Section 4.3.5 discusses the significance of the wall jet regime and other possible implications of confinement. Finally, concluding remarks are given in Section 4.4.

4.2 Problem formulation

4.2.1 Flow configuration

We consider the flow of an incompressible Newtonian fluid of constant density and viscosity as it passes from a long, straight, rotating annular pipe into a stationary semi-infinite reservoir as shown in Figure 4.1. Aside from the annular cross-section of the pipe, the configuration studied in this paper is essentially identical to that of our earlier investigation of circular swirling jets [20]. As in that study, we here adopt a cylindrical coordinate system centred at the exit of the pipe such that $\boldsymbol{x} = (x, r, \theta)$ and reference all quantities to the outer diameter of the pipe $D = 2R$ and the volume-averaged velocity U through the pipe. Using these length and velocity scales, three independent parameters are introduced that fully specify the system: the Reynolds number $Re = DU/\nu$, the kinematic swirl ratio $S = \omega R/U$, and the inner-to-outer diameter ratio $d = D_i/D$. Here, $\nu > 0$ is the fluid's kinematic viscosity, $\omega \geq 0$ is the pipe's rotation rate, and $0 < D_i < D$ is the annulus' inner diameter.

The evolution of the velocity $\boldsymbol{u} = (u_x, u_r, u_\theta)^{\mathrm{T}}$ and pressure p within the axisymmetric domain Ω is governed by the incompressible Navier-Stokes equations,

$$\frac{\partial \boldsymbol{u}}{\partial t} + \boldsymbol{u} \cdot \boldsymbol{\nabla} \boldsymbol{u} = -\boldsymbol{\nabla} p + \frac{1}{Re} \nabla^2 \boldsymbol{u}, \tag{4.1a}$$

$$0 = \boldsymbol{\nabla} \cdot \boldsymbol{u}. \tag{4.1b}$$

Along the domain's border Γ, the boundary conditions listed in table 4.1 are enforced to model the configuration described above. On solid surfaces, no-slip conditions are enforced for all velocity

DISTRIBUTION A: Distribution approved for public release.

Boundary		Constraints			
Inlet,	Γ_i	$u_x = u_x^P(r)$	$\partial_x u_r = 0$	$u_\theta = u_\theta^P(r)$	
Pipe,	Γ_p	$u_x = 0$	$u_r = 0$	$u_\theta = 2Sr$	
Wall,	Γ_w	$u_x = 0$	$u_r = 0$	$u_\theta = 0$	
Axis,	Γ_a	$\partial_r u_x = 0$	$u_r = 0$	$u_\theta = 0$,	if $m = 0$
		$u_x = 0$	$\partial_r u_r = 0$	$\partial_r u_\theta = 0$,	if $\lvert m\rvert = 1$
		$u_x = 0$	$u_r = 0$	$u_\theta = 0$,	if $\lvert m\rvert \geq 2$
Open,	Γ_o	$\left(-\tilde{p}\boldsymbol{I} + Re^{-1}\boldsymbol{\nabla u}\right)\cdot\boldsymbol{n} - \frac{1}{2}\boldsymbol{u}\min(0, \boldsymbol{u}\cdot\boldsymbol{n}) = 0$			

Table 4.1: List of boundary conditions.

components such that $\boldsymbol{u} = 0$ on the *stationary* exit-plane walls Γ_w and $(u_x, u_r, u_\theta) = (0, 0, 2Sr)$ on the *rotating* inner and outer pipe walls Γ_p. A steady mass flux is prescribed through the annular pipe, which is imagined to be long enough for a region of fully developed flow to exist at some $x = -\ell$. Then, at $x = -\ell$, an inflow boundary Γ_i is introduced where Dirichlet conditions require the distribution of axial and azimuthal velocity to match the Poiseuille solution for a rotating annular pipe, i.e.

$$u_x^P(r) = \frac{2 - 8r^2 - 2\log(2r)(1-d^2)/\log(d)}{1 + d^2 + (1-d^2)/\log(d)}, \qquad \text{and} \qquad u_\theta^P(r) = 2Sr. \tag{4.2}$$

As in our previous work, a Neumann condition is enforced for the radial velocity component along Γ_i to promote the transparency of the inlet to upstream-propagating disturbances and more closely approximate a very long pipe [43, 20]. Next, three-dimensional symmetry conditions are enforced along the central axis Γ_a to ensure continuity of disturbances across the singularity at $r = 0$. These conditions are derived specifically for each azimuthal wavenumber m following a Fourier expansion in θ [44]. Finally, the unconfined flow in the reservoir is treated using the approach developed in Douglas et al. [20]. In brief, the semi-infinite reservoir is truncated to a finite characteristic radius R_∞ to yield a tractable system, where "modified directional outflow conditions" are enforced along Γ_o to model the open flow. The main results reported in this paper were obtained with $\ell = 4$ and $R_\infty = 40$, though redundant calculations with various ℓ and R_∞ values were considered throughout the analysis to ensure the results are independent of these parameters.

A key objective of this formulation was to use an inflow profile that remained consistent across the span of configurations. This is accomplished using a rotating pipe, similar to the circular jet experiments of Billant et al. [45] and Liang and Maxworthy [46], and a long inlet to ensure a fully developed flow profile. Note that this approach for introducing swirl is distinct from more common means, which typically introduce swirl using a stationary apparatus such as an array of angled guide vanes [e.g. 12]. However, adopting such strategies links the azimuthal velocity to other flow parameters and other aspects of the configuration, leading to variations in the jet's velocity profiles as the parameters are varied. The approach taken here offers a configuration that is both feasible to replicate experimentally and that is described by a completely independent set of flow parameters. This issue of parameter independence is also the reason why the swirl amplitude reported in our study is quantified by the kinematic "swirl ratio" S and not by the momentum flux ratio in the "swirl number" of Beér and Chigier [47], which depends on both S and d, as well as the resulting pressure field [48].

Finally, it should be pointed out that (4.2) is well-defined for $0 < d < 1$ but becomes singular at the extreme values of $d = 0$ and $d = 1$. In the case of $d = 0$, the singularity distinguishes the annular configuration from the distinct case of a circular jet studied in Douglas et al. [20]. Physically, the presence of an inner no-slip wall for any arbitrarily small $d > 0$ always implies the existence of a stagnation point along the axis. Likewise, the singularity at $d = 1$ is physically associated with a complete blockage of the inlet pipe, resulting in a trivial configuration with no incoming flow. Both of these singular situations are excluded from this study by limiting the considered range of centrebody diameters to the well-defined interval.

4.2.2 Discretisation

In order to solve (4.1), the strong statement outlined above is reformulated as a variational problem. Thus, as in Douglas et al. [20], we seek in the appropriate spaces $\boldsymbol{q} = (\boldsymbol{u}, p, p_o)^{\mathrm{T}}$ such that for all

DISTRIBUTION A: Distribution approved for public release.

test functions $\check{\boldsymbol{q}} = (\check{\boldsymbol{u}}, \check{p}, \check{p}_o)^{\mathrm{T}}$:

$$\left\langle r\check{\boldsymbol{u}}, \frac{\partial \boldsymbol{u}}{\partial t} + \boldsymbol{u}\cdot\boldsymbol{\nabla}\boldsymbol{u} \right\rangle_{\Omega} + \left\langle \boldsymbol{\nabla}(r\check{\boldsymbol{u}}), -p\boldsymbol{I} + \frac{1}{Re}\boldsymbol{\nabla}\boldsymbol{u} \right\rangle_{\Omega} + \langle \check{p}, \boldsymbol{\nabla}\cdot\boldsymbol{u}\rangle_{\Omega} + \left\langle r\check{\boldsymbol{u}}, p_o\boldsymbol{n} - \frac{1}{2}\boldsymbol{u}\min(0, \boldsymbol{u}\cdot\boldsymbol{n}) \right\rangle_{\Gamma_o} + \left\langle \check{p}_o, \boldsymbol{\nabla}p_o\cdot\boldsymbol{t} - \frac{u_\theta^2}{r} \right\rangle_{\Gamma_o} = 0, \tag{4.3}$$

where $\langle \bullet, \bullet\rangle_{\Omega}$ is the standard spatial inner product. Superficially, (4.3) is indistinguishable from the weak form in Douglas et al. [20]. However, the present work introduces one crucial but subtle distinction related to the discretisation that was necessary to ensure continuous dependence of the problem on the parameter d.

The primary spatial discretisation consists of a Delaunay triangulation of the meridional plane constructed using GMSH [49] and a Fourier decomposition along the azimuthal direction. Instead of using many different meshes characterised by different values of d, in this paper, we define generic, d-independent meshes over the meridional plane in terms of x and a new computational coordinate η related to r through d. This coordinate is defined such that $\eta = 1/2$ at $r = d/2$ and $\eta = 1$ at $r = 1/2$, yielding

$$r = \begin{cases} d\eta, & \eta < \frac{1}{2}, \\ (1-d)\,\eta + d - \frac{1}{2}, & \frac{1}{2} \le \eta \le 1, \\ \eta - \frac{1}{2}, & \eta > 1, \end{cases} \tag{4.4}$$

Consequently, the incorporation of (4.4) into (4.3) imbues the system with a continuous dependence on d through the conversion between computational η and physical r coordinates. The main triangulation for Ω in these coordinates features 134 270 elements and is defined with $\ell = 4$ and $R_\infty = 40$. Key calculations were also repeated on other meshes to ensure grid convergence with respect to the mesh density and the chosen values of ℓ and R_∞. Finally, the weak formulation of (4.3) is projected onto the basis of Taylor-Hood ($\mathbb{P}_2 \times \mathbb{P}_1$) finite elements associated with the mesh using FreeFEM [50], resulting in discrete flow states with 945 999 total degrees of freedom per Fourier component for the primary mesh. In addition, some calculations were performed on tetrahedral meshes with approximately one million elements to determine the stability of the three-dimensional steady states in Section 4.3.2 using the implementation of Moulin et al. [51].

4.2.3 Solution methodology

The numerical methods leveraged in this work are nearly identical to those of Douglas et al. [20], which are briefly recalled here for completeness. Adopting the state-space form of (4.1), the system is rewritten as,

$$\mathcal{M}(d)\,\frac{\partial \boldsymbol{q}}{\partial t} + \mathcal{R}(\boldsymbol{q}; Re, S, d) = 0, \tag{4.5}$$

where $\mathcal{M}$ and $\mathcal{R}$ are the respective mass matrix and residual operators and Re, S, and d are parameters. Following a parallel discretisation and abstraction in FreeFEM [50], the linear algebra associated with (4.5) is handled in a distributed manner using PETSc [52] or SLEPc [53], with factorisations from MUMPS [54].

Within this framework, axisymmetric equilibrium solutions represent steady states $\boldsymbol{q}_0$ that satisfy

$$\mathcal{R}_0\left(\boldsymbol{q}_0; Re, S, d\right) = 0, \tag{4.6}$$

where the 0-subscript indicates the restriction of a three-dimensional quantity to its axisymmetric Fourier component. To identify simple fixed points, a straightforward Newton scheme is sufficient to solve (4.6) for fixed parameter values. However, the configuration examined in this paper features multivaluedness for a significant range of parameters, making this elementary approach ill-suited for parameter continuation. Instead, the adaptive predictor-corrector scheme from Douglas et al. [20], which consists of a tangent predictor with a variable step length and an iterative Moore-Penrose corrector, is used to efficiently and robustly trace solution branches to (4.6) along a parameter.

The stability of the axisymmetric steady states defined by (4.6) is determined based on the time-asymptotic evolution of infinitesimal disturbances $\acute{\boldsymbol{q}}_m$ to the equilibrium. Such disturbances can be expanded as a superposition of normal modes $\hat{\boldsymbol{q}}_m$ associated with azimuthal wavenumber m, growth rate σ, and frequency f according to,

$$\acute{\boldsymbol{q}}(x, r, \theta, t) \propto \hat{\boldsymbol{q}}_m(x, r)\, e^{\mathrm{i}m\theta + (\sigma + \mathrm{i}2\pi f)t} + \hat{\boldsymbol{q}}_m^*(x, r)\, e^{-\mathrm{i}m\theta + (\sigma - \mathrm{i}2\pi f)t}, \tag{4.7}$$

DISTRIBUTION A: Distribution approved for public release.

where $(\bullet)^*$ denotes complex conjugation. Thus, the time-asymptotic linear stability characteristics of any $\boldsymbol{q}_0$ can be deduced from the spectrum of the generalised eigenvalue problem,

$$\lambda \mathcal{M} \hat{\boldsymbol{q}}_m + \mathcal{J}_m \left(\boldsymbol{q}_0 \right) \hat{\boldsymbol{q}}_m = 0, \tag{4.8}$$

where $\lambda = \sigma + \mathrm{i}2\pi f$ is the eigenvalue and $\mathcal{J}_m$ is the Jacobian operator defined in Douglas et al. [20]. Hence, bifurcation points are identified as those states that satisfy both (4.6) and (4.8) with $\sigma = 0$. These bifurcation points can then be traced along their corresponding neutral curves using the two-parameter predictor-corrector schemes for bifurcations detailed in Douglas et al. [20].

Finally, the periodic solutions which emerge from Hopf bifurcations identified by stability analysis can be traced along their solution branches using the harmonic balance method. This method expands the periodic solutions as N-th order temporal–azimuthal Fourier series, yielding,

$$\boldsymbol{q}\left(x, r, \theta, t\right) = \bar{\boldsymbol{q}}_0\left(x, r\right) + \sum_{j=1}^{N} \left[\hat{\boldsymbol{q}}_{jm}\left(x, r\right) e^{\mathrm{i}jm\theta + \mathrm{i}2j\pi ft} + \hat{\boldsymbol{q}}^*_{jm}\left(x, r\right) e^{-\mathrm{i}jm\theta - \mathrm{i}2j\pi ft} \right], \tag{4.9}$$

where $\bar{\boldsymbol{q}}_0$ represents the time–azimuth mean flow and the $\hat{\boldsymbol{q}}_{jm}$ represent the various harmonic components. Hence, these periodic solutions represent equilibrium solutions when $f = 0$ and limit cycles when $f \neq 0$. Substituting (4.9) into (4.5) and expanding the result in Fourier space yields the following system of coupled nonlinear equations describing each component of the Fourier expansion,

$$\mathcal{R}_0\left(\bar{\boldsymbol{q}}_0\right) + \sum_{j=1}^{N} \mathcal{H}_0\left(\hat{\boldsymbol{q}}^*_{jm}\right) \hat{\boldsymbol{q}}_{jm} = 0, \tag{4.10a}$$

$$\frac{1}{2} \sum_{j=1}^{k-1} \mathcal{H}_{km}\left(\hat{\boldsymbol{q}}_{(k-j)m}\right) \hat{\boldsymbol{q}}_{jm} + \mathcal{L}_{km}\left(\bar{\boldsymbol{q}}_0, kf\right) \hat{\boldsymbol{q}}_{km} + \sum_{j=k+1}^{N} \mathcal{H}_{km}\left(\hat{\boldsymbol{q}}^*_{(j-k)m}\right) \hat{\boldsymbol{q}}_{jm} = 0, \tag{4.10b}$$

$$\sum_{j=1}^{N} j \left(\hat{\boldsymbol{q}}^{\mathrm{H}}_{jm} \mathcal{M} \hat{\boldsymbol{q}}^*_{jm} - \hat{\boldsymbol{q}}^{\mathrm{T}}_{jm} \mathcal{M} \hat{\boldsymbol{q}}_{jm} \right) = 0. \tag{4.10c}$$

where $\mathcal{H}_m$ and $\mathcal{L}_m$ are, respectively, the Hessian and linearised Navier Stokes operators defined in our prior work, and (4.10c) is the integral phase condition used to uniquely define the frequency [55]. The solution processes for (4.10) are analogous to those used for (4.5); further numerical details are available in Douglas et al. [20].

4.3 Results and discussion

4.3.1 Overview of the steady flow topologies

As discussed in the introduction, the various physical processes involved in swirling jet mechanics tend to manifest an intricate state space underlying a wide range of distinct flow topologies. Therefore, before delving into the particular details of each of flow regime in the following sections, this section briefly presents the basic flow topologies of annular swirling jets. To this end, we consider a case where $d = 0.5$ and $Re = 100$ via numerical continuation along S. This particular value of d was selected to enable direct comparisons with the results of Sheen et al. [12], and the value of the Reynolds number was chosen as it is sufficiently low such that no unsteady solutions are identified for any S, yet sufficiently high that an interesting sequence of distinct axisymmetric steady states exists. A qualitatively similar evolution with S of the steady flow topology occurs at other Re and d values. The results of this analysis are presented in the bifurcation diagrams and flow visualisations of Figure 4.2. There, $\min u_x(x, 0)$ denotes the minimum axial velocity along the central axis. This quantity is extracted from each steady state, allowing any solutions exhibiting central recirculation features to be easily identified as those satisfying $\min u_x(x, 0) < 0$.

Based on Figure 4.2, we classify the annular jet flow at $d = 0.5$ and $Re = 100$ into three main flow regimes, which typically also occur at other Re and d values. First is the wake regime, which occurs at relatively low S values. In the wake regime, the primary flow feature is a small central recirculation vortex immediately beyond the expansion (see Figure 4.2(c) panels 1 and 2) caused by the momentum deficit behind the centrebody. As the rotation rate increases in the wake regime, the extent of this recirculation zone decreases (Figure 4.2(c) panel 3) until a small counter-rotating vortex forms along the centrebody wall. Eventually, this secondary vortex penetrates the main

DISTRIBUTION A: Distribution approved for public release.

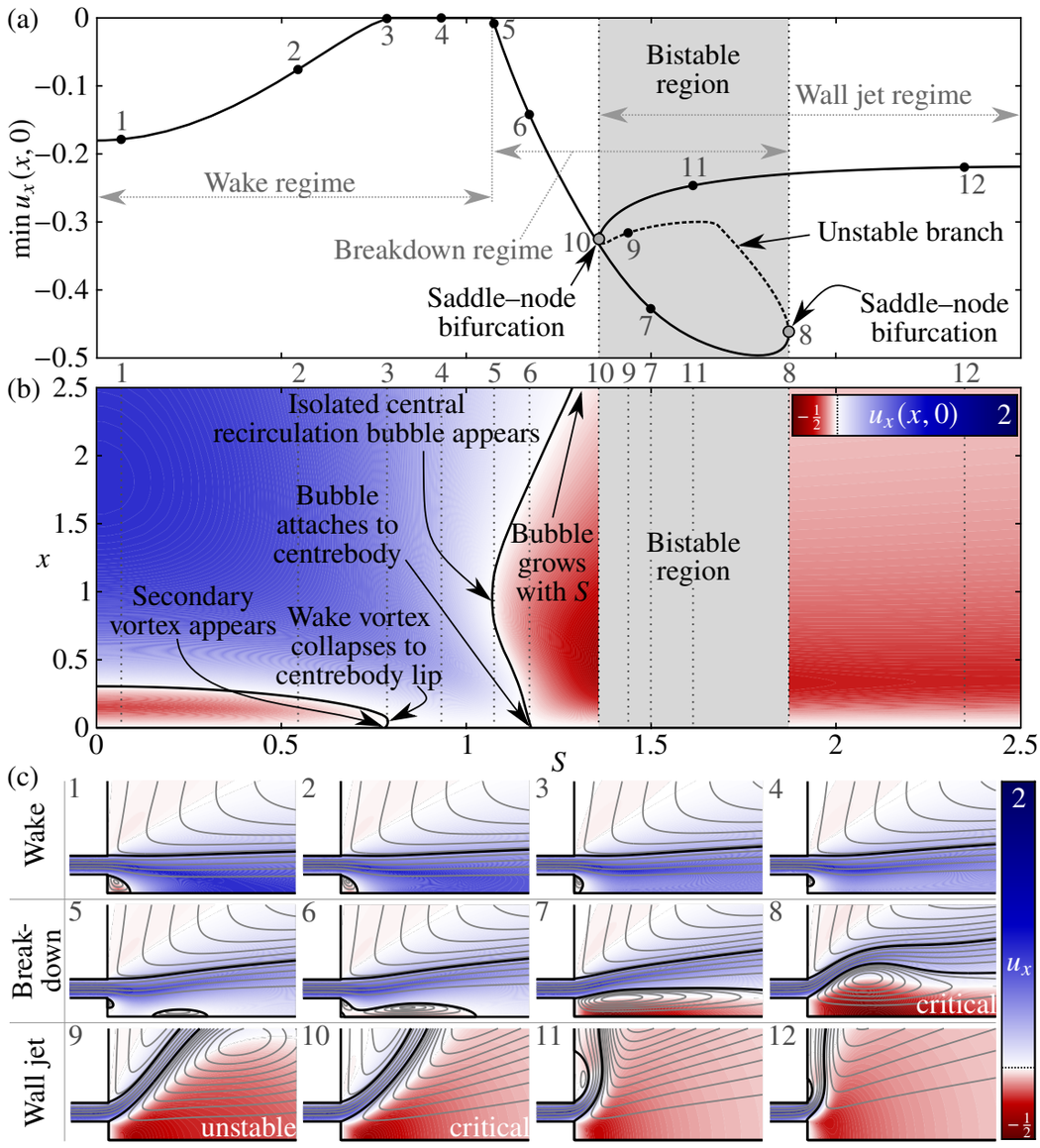

Figure 4.2: Dynamics of the swirling annular jet at $Re = 100$ and $d = 0.5$. (a) S–$\min u_x(x,0)$ bifurcation diagram. Solid curves indicate stable nodes, while the dashed curve indicates an unstable saddle. (b) Contour plot showing the evolution of $u_x(x,0)$ as a function of S. Here, the black curves indicate on-axis stagnation points. (c) Flow visualisations from points indicated on (a) and (b) illustrating how the steady flow topology evolves under varying S. The flow visualisations show coloured contours of the axial velocity and axisymmetric streamline projections over $(x,r) \in [-0.5, 2.5] \times [0, 1.5]$. Black curves are used to indicate stagnation streamlines.

DISTRIBUTION A: Distribution approved for public release.

wake vortex, causing the recirculation zone to recede to a narrow toroid along the centrebody lip such that the axial flow along the centreline is non-negative (Figure 4.2(c) panel 4). The mechanics of this collapse are consistent with the description by Sheen et al. [12] reviewed in the introduction which they referred to as the 'penetration' of the 'inverted triangle region'.

Further increase in swirl leads to the formation of a new momentum deficit downstream of the expansion due to the vortex breakdown phenomenon. The beginning of the second regime, termed the breakdown regime, is demarcated by the point where this momentum deficit is sufficient to trigger a flow reversal along the centerline (Figure 4.2(c) panel 5). Once vortex breakdown occurs, the new isolated central recirculation zone rapidly enlarges with increasing swirl until it collides and merges with the lip vortex (Figure 4.2(c) panel 6). The newly merged recirculation zone continues to grow in size as swirl increases (Figure 4.2(c) panel 7) until it eventually reaches a crisis (Figure 4.2(c) panel 8) where the recirculation bubble can no longer grow continuously with increasing S. At this point, the solution manifold experiences a saddle–node bifurcation beyond which the bubble grows tremendously with *decreasing* S along an unstable solution branch (Figure 4.2(c) panel 9). The mechanism behind this dynamics is identical to that in swirling circular jets [20]. It is driven by a nonlinear exchange of dominance between the central low pressure region associated with the vortex breakdown recirculation zone and the outer low pressure region associated with restricted entrainment of the ambient fluid near the wall as the bubble expands (i.e. the Coandă effect). It should be noted that this dynamics is affected strongly by the particular geometry of our configuration and, in particular, the presence of the flush wall along $x = 0$ [21].

Once another saddle–node bifurcation signals that this nonlinear transition is complete (Figure 4.2(c) panel 10), the flow enters the third regime. Here, a Coandă-type attachment of the jet occurs along the outer wall, resulting in a wall jet configuration similar to that observed by Ogus et al. [9]. As S increases further from this point, the strength of the outer separation vortex intensifies, reducing the size of the separation zone and causing the flow to cling ever more closely to the outer wall (Figure 4.2(c) panels 11 and 12). No additional flow states were identified within the range of rotation rates investigated (up to $S = 6$).

In closing this section, it is important to emphasise that the specific S values associated with the various transitions in steady state flow topology are strongly dependent on the other parameters. This will be further discussed in Section 4.3.4. It should also be noted that the interval of bistability for the circular jet ($2.05 \leq S \leq 2.10$) given by Douglas et al. [20] does not approximate the corresponding bistable interval for the annular jet even at small d (investigated here down to $d = 10^{-4}$). This is attributed to the aforementioned singularity at $d = 0$ associated with the incongruity of a no-slip surface along a one-dimensional centrebody. The effects of the centrebody diameter and Reynolds number are summarised in the regime diagrams of Figure 4.3. Most of the observed trends can be understood quite well based on physical intuition. For example, conservation of angular momentum ensures that jets with large centrebodies are endowed with more azimuthal momentum at a given rotation rate than jets with a lower value of d, which tends to shift the various transitions to lower S values at higher d. Similarly, higher Reynolds numbers result in less viscous entrainment of ambient fluid into the jet, causing the swirl to dissipate more gradually as the jet evolves axially. This reduced entrainment at higher Re also stalls the transition to the wall jet regime to higher values of S. Finally, note the significant sensitivity of the jet's centerline stagnation behaviour with respect to S as the flow transitions between regimes (see Figure 4.2b). This sensitivity of the number and location of the stagnation points has significant implications on the potential flame shapes in combustor flow fields with annular swirling jets.

4.3.2 Symmetry breaking in the nonswirling jet

Our analysis proceeds with an investigation of the flow behaviour before the introduction of swirl. With $S = 0$, the governing system and boundary conditions are symmetric under rotation and/or reflection in both θ and t. Thus, for sufficiently low Reynolds numbers, linearity ensures that the velocity field inherits these symmetries for any value of d, resulting in steady states that are both 2D axisymmetric (2DA) and 3D plane symmetric (3DPS). For such flows, disturbances with positive and negative m are degenerate, leading to non-rotating interference patterns [56]. Because of this degeneracy, the sign of m and f are unimportant, and we will refer to $|m|$ and $|f|$ throughout Section 4.3.2.

Using the branch continuation and stability analysis techniques outlined in Section 4.2.3, the elementary 2DA/3DPS steady solutions that appear in the low-Re limit are traced along Re and d to explore how the system bifurcates into more complex flow patterns. A stability map, a bifurcation

DISTRIBUTION A: Distribution approved for public release.

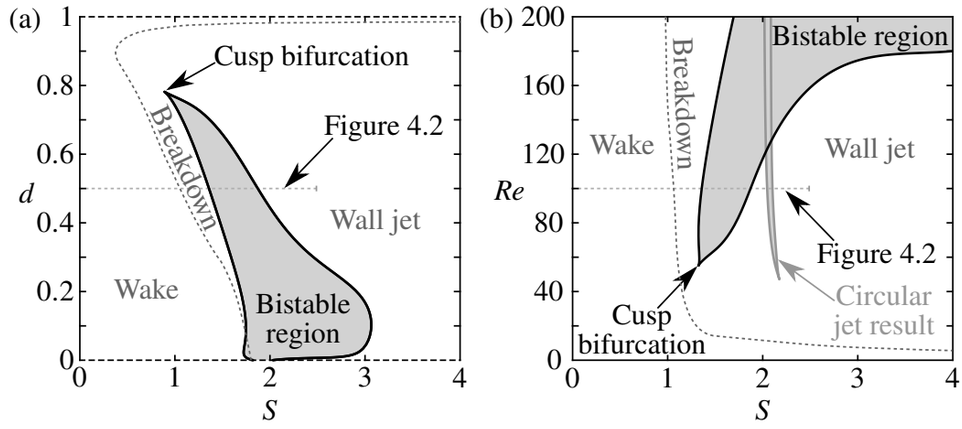

Figure 4.3: Regime diagrams for the swirling annular jet characterising the steady solutions present (a) in the *S*-*d* plane at $Re = 100$ and (b) in the *S*-*Re* plane at $d = 0.5$. In (b), the grey curve indicates the bistable region for a *circular* swirling jet [20]. Note that unsteady solutions are present within the range of *Re* shown, as discussed further below.

diagram, and flow visualisations that characterise the nonswirling annular jet's incipient dynamics are presented in Figure 4.4. In the bifurcation diagram, the evolution of the velocity fields is monitored through the maximum of the transverse velocity across the centerline, $\max |u_r(x, 0)|$, since $|u_r(x, 0)| > 0$ for any x indicates a violation of axisymmetry.

The results of Figure 4.4 indicate that the steady 2DA/3DPS nonswirling annular jet bifurcates to non-axisymmetric, 3DPS steady states beyond a certain critical Reynolds number that depends on d. This breaking of axisymmetry is triggered by a non-oscillatory ($|f| = 0$) $|m| = 1$ Hopf bifurcation (i.e. a pitchfork bifurcation with continuous rotational symmetry) that is either sub- or supercritical in nature, for lower and higher values of d, respectively. The interface between the sub- and supercritical bifurcations occurs where the steady 3DPS saddle–node curve intersects the steady $|m| = 1$ Hopf curve at a codimension-2 fold–Hopf bifurcation point, as indicated in Figure 4.4(b). Hence, the region between this 3DPS saddle–node curve and the steady axisymmetry breaking Hopf bifurcation curve for $d \lesssim 0.84$ yields an interval of bistability between the stable 2DA/3DPS and 3DPS steady states, allowing hysteresis. Visualisations of the steady 2DA/3DPS flow and the steady 3DPS flow are shown in Figure 4.4(c)1-2 at the point $(Re, d) = (420, 0.7)$.

As mentioned in the introduction, the loss of axisymmetry in nonswirling annular jet flows is a known phenomenon [7, 8, 57]. Nonetheless, the detailed dynamics revealed by our bifurcation analysis lead to new insights. First, the identified subcritical bifurcation behaviour in this flow for $d < 0.84$ is a new result. This dynamics indicates a strong sensitivity of the flow to initial conditions and parameter fluctuations in the bistable region. Second, in comparison to the observations of Del Taglia et al. [8], the neutral curve associated with the loss of axisymmetry in our results is located over a nearly identical range of Reynolds numbers but across a wider span of centrebody diameters. We expect that this discrepancy may be attributed primarily to the lack of an inlet pipe in their configuration, which prevented their jet from developing any non-axisymmetry upstream of the dump plane.

At *Re* values immediately beyond the axisymmetry breaking bifurcation, the 3DPS steady solution manifold is linearly stable. However, the steady 3DPS solution manifold loses its stability at higher *Re* values through oscillatory Hopf bifurcations as the degree of non-axisymmetry grows. As shown in Figure 4.4(a,b), three neutral curves exist on this steady manifold that each give rise to instability modes with distinct frequencies and spatial structures. Two of these bifurcations are associated with 3DPS structures, corresponding to unsteady Bénard–von Kármán-type vortex shedding behaviours. The main distinction between these 3DPS modes is their frequency. The slower oscillation has Strouhal numbers of $0.1 \lesssim |f| \lesssim 0.2$, while the faster mode reaches $0.4 \lesssim |f| \lesssim 0.5$. The slower mode is visualised in Figure 4.4(c)3 and movie 1 at the point $(Re, d) = (344, 0.7)$, and the faster mode is shown in Figure 4.4(c)4 and movie 2 at $(Re, d) = (483, 0.6)$. The remaining instability is associated with 3D plane-asymmetric (3DPA) streamwise streak structures that correspond to a gentle side-to-side "wobbling" of the wake asymmetry. This mode is nearly static, with a Strouhal number of $|f| \sim 0.001$. It is visualised in Figure 4.4(c)5 and movie 3 at $(Re, d) = (475, 0.87)$. Note that each of these bifurcations correspond to a primary instability of the steady 3DPS flow for some part of the parameter space.

The instabilities described in the previous paragraph provide new insight into several earlier

DISTRIBUTION A: Distribution approved for public release.

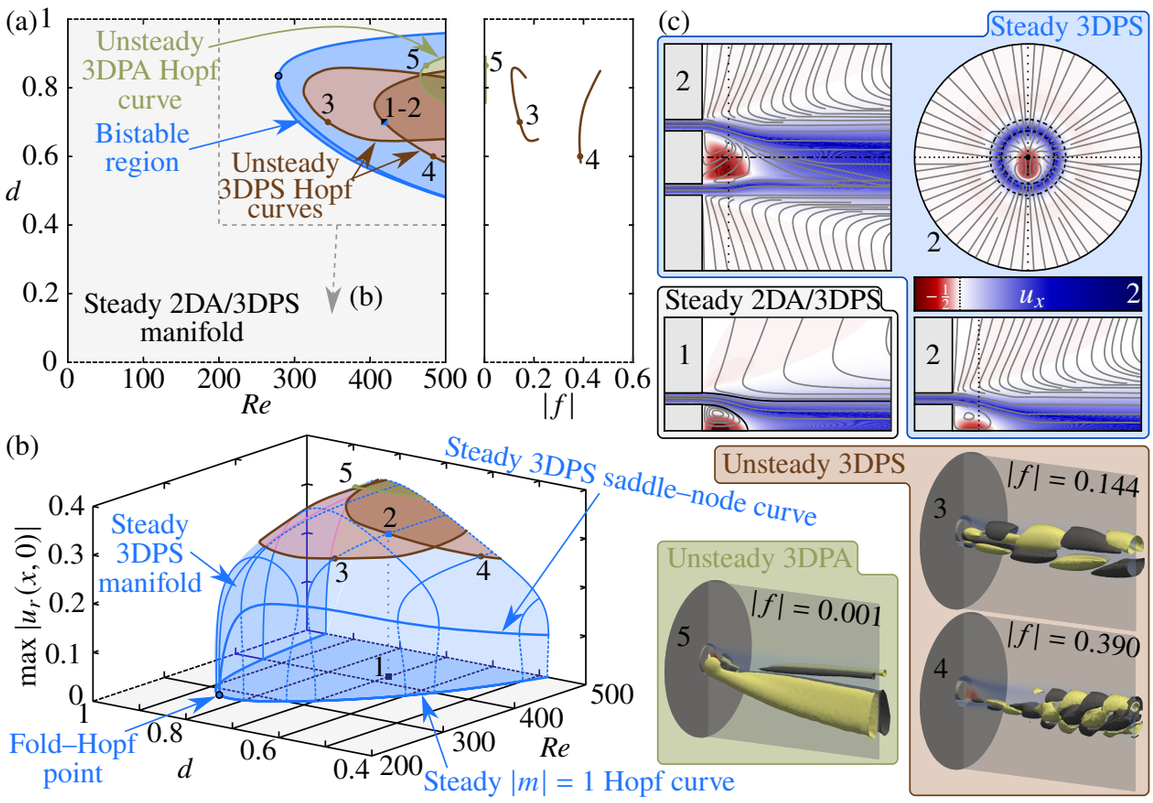

Figure 4.4: (a) Stability map in the *Re*-*d* plane and plot of critical frequency along the leading Hopf curves, (b) max $|u_r(x,0)|$ bifurcation diagram, and (c) flow visualisations from the indicated points illustrating the dynamics of the nonswirling annular jet. Planar visualisations show contours of axial velocity and streamline projections for the unstable 2DA steady state in the meridional plane and for the unstable 3DPS steady state within and orthogonal to the plane of symmetry as well as in an axial plane at $x = 0.35$. The 3D visualisations show yellow and black axial velocity isocontours from each branch of oscillatory Hopf bifurcations at a single instance of phase overlaid upon the symmetry plane from the 3DPS steady state.

DISTRIBUTION A: Distribution approved for public release.

results. First, the structure and frequency of the slower 3DPS instability characterised in our results matches closely with the $|f| = 0.187$ vortex shedding mode found in the laminar $d = 0.65$ jet studied by Ogus et al. [9]. Our results indicate that this particular instability is not universally dominant in non-swirling annular jets, and only appears as the primary instability over a range of centrebody diameters from $0.65 \lesssim d \lesssim 0.85$ for $Re \leq 500$. Below $d \sim 0.65$, the primary instability is the higher frequency 3DPS vortex shedding mode, while for $d \geq 0.85$, the primary instability is the 3DPA wobble mode. It should be emphasised here, however, that these neutral curves overlap at high Re values and are not mutually exclusive. It is likely that combinations of these basic instability modes and others will promote more complex interactions and time-aperiodic temporal dynamics as Re increases. As an example of this, we consider the strong similarities between the instability modes identified in our laminar study and the coherent turbulent structures observed by Vanierschot et al. [11]. Using a proper orthogonal decomposition (POD) of their time-resolved experimental data, those authors identified three dominant coherent oscillations that closely mirror the space-time behaviour of each instability mode identified in our study. This suggests that the dominant coherent dynamics are driven by the same physical mechanisms across a broad range of Reynolds numbers and motivates further studies in the transitional regime.

Second, it is interesting to speculate to possible connections between the elongated streak structures associated with the self-excited 3DPA instability in annular jets and the streak structures that are known to be temporally stable but strongly spatially amplified in round jets [58, 59, 60]. It seems plausible that the recirculation zone in the centrebody wake could provide an avenue for intrinsic feedback within the lift-up mechanism that could destabilise such structures. Nevertheless, more work would certainly be necessary to evaluate this hypothesis.

Finally, it should be remarked that all of the bifurcations described in this section are strongly influenced by the physics of the centrebody wake and have no analogues in circular jets [20]. They do, however, possess clear similarities to the bifurcations of axisymmetric wake flows [61, 62, 63, 64]. The onset of unsteadiness in both cases involves an initial steady break of axisymmetry followed by subsequent instabilities of a steady 3D solution manifold. Hence, oscillatory linear instability arises from a 3D state rather than an axisymmetric one. To better illustrate this point, we have performed stability calculations on the axisymmetric manifold beyond the leading neutral curve associated with the steady loss of axisymmetry. For the unstable steady axisymmetric flow, the minimum Reynolds number associated with an oscillatory instability is $Re = 574$, where an $|m| = 1$ Hopf bifurcation associated with vortex shedding at $|f| = 0.325$ occurs at $d = 0.68$. Nonetheless, this instability is of limited physical significance as neither it's critical parameter values nor its frequency are representative of the actual instabilities stemming from the 3DPS state. This has important implications toward modelling and controlling nonswirling annular jet flows, as the instability characteristics of the axisymmetric steady state do not reflect those of the true 3D flow.

4.3.3 Effect of low rotation rates on wake asymmetry

Though the system and boundary conditions remain 2DA with $S \neq 0$ at low Re, introducing any finite amount of rotation to the pipe immediately destroys the system's 3DPS property. Hence, for $S \neq 0$, disturbances with positive and negative m are no longer degenerate, leading to 3D structures that generally rotate in time.[1] In this work, as in Douglas et al. [20], we have restricted our analysis to $S \geq 0$ and $m \leq 0$ without loss of generality such that the sign of f determines whether a non-axisymmetric disturbance co-rotates ($f > 0$) or counter-rotates ($f < 0$) along θ. All results will nevertheless be reported in terms of $|m|$ to avoid confusion with other studies which sometimes use the sign of m to distinguish among disturbances with different rotation directions.

The stability map of Figure 4.5(a) illustrates the effect of weak swirl for a range of d and $S \leq 0.3$ with the Reynolds number fixed at $Re = 400$. It also shows that the subcritical and bistable behaviour described above for the nonswirling jet at certain d values persists for nonzero S. Taking the case of $d = 0.8$ as a representative example, Figure 4.5(b) demonstrates how the steady 3DPS solution from the nonswirling case inherits $f > 0$ for any $S > 0$, manifesting a co-rotating $|m| = 1$ limit cycle manifold. Flow visualisations provided in Figure 4.5(c)1 and movie 4 further reveal how the spatial structure of these limit cycle oscillations follows from a swirl-induced twisting of the steady 3DPS structure from the nonswirling case. The end result is a co-rotating $|m| = 1$ spiral structure that winds about the central axis in the direction opposing the pipe's rotation as

[1] Note that in systems not exhibiting such exact temporal–azimuthal symmetries as ours, it is possible for robust non-axisymmetric steady or time-averaged solutions to arise at nonzero swirl [65].

DISTRIBUTION A: Distribution approved for public release.

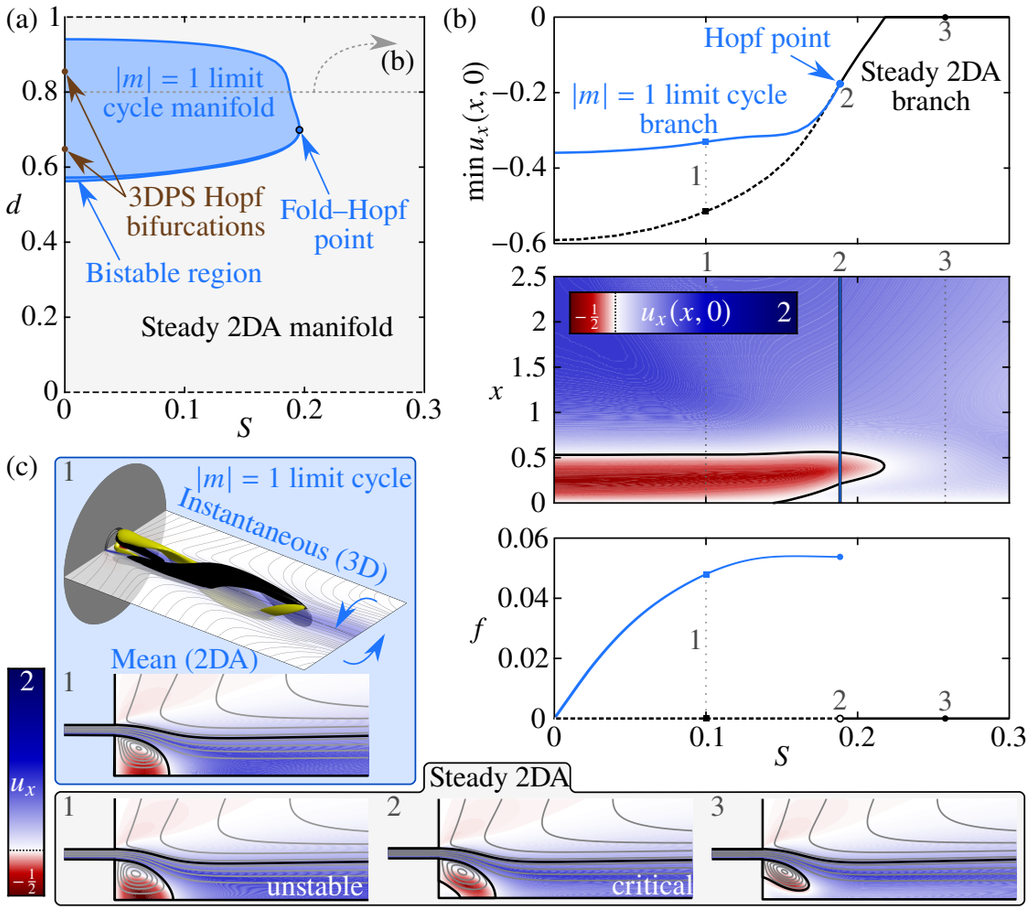

Figure 4.5: Characterisation of the weakly swirling jet at $Re = 400$. (a) Stability map in the S-d plane. (b) Results for the case of $d = 0.8$ with varying S showing a bifurcation diagram for $\min u_x(x, 0)$, a contour plot for $u_x(x, 0)$ of the steady and periodic solutions, and a bifurcation diagram for f. (c) Flow visualisations at $d = 0.8$ and three points in S showing meridional axial velocity contours and streamline projections for $(x, r) \in [-0.5, 2.5] \times [0, 1]$ of the 2DA states derived from the mean component of the $|m| = 1$ limit cycle and the steady 2DA solutions. A 3D visualisation of the instantaneous flow on the $|m| = 1$ limit cycle at $S = 0.1$ is also shown using a meridional slice plane and yellow and black isocontours of $\acute{u}_x = \pm 0.1$ for $(x, r, \theta) \in [-1, 9] \times [0, 2.5] \times [0, 2\pi]$.

the jet proceeds axially. Nonetheless, the amplitude of this limit cycle decays with increasing S as the structure of the wake recirculation region changes. The upward trend of $\min u_x(x, 0)$ in Figure 4.5(b) indicates that the reversed axial flow in the centrebody wake region diminishes with increasing swirl. As this wake recirculation weakens, the amplitude of the $|m| = 1$ limit cycle decays until the flow eventually becomes unable to sustain the wake asymmetry. At this point, depicted in Figure 4.5(c)2, the system bifurcates to a stable 2DA steady state. With further increase in S, the secondary 'inverted triangle zone' vortex apparent in Figure 4.5(c)2 'penetrates' through the primary wake vortex to yield the topology shown in Figure 4.5(c)3. This evolution of the time-mean and steady flowfields with increasing S occurs in a manner consistent with the description in 4.3.1 and earlier reports [12, 9].

It is interesting to note that the behaviour of the co-rotating, counter-winding $|m| = 1$ limit cycle described above and in Figure 4.5 bears a striking resemblance to the observations of Vanierschot et al. [57] in turbulent jets. This similarity suggests that the breaking of planar symmetry caused by nonzero swirl and the subsequent weakening of the wake recirculation zone with increasing swirl are both significant dynamical effects that control the jet's coherent structures even at much higher Reynolds numbers. Hence, it is plausible that low swirl could be used to manipulate the dominant frequencies present in annular jet applications.

Here, we should point out that the techniques used in our study only explicitly characterise steady and time-periodic solutions. Nonetheless, our results can be straightforwardly extended to more complex dynamics and bifurcations using the continuous parameter dependence and symmetry of (4.3). For example, the Hopf bifurcations of the 3DPS steady state associated with 3DPS vortex shedding at $S = 0$ (indicated on Figure 4.5 and detailed in Figure 4.4) must correspond to Neimark–Sacker bifurcations of the co-rotating $|m| = 1$ limit cycle state for $S > 0$ due to the destruction of

DISTRIBUTION A: Distribution approved for public release.

the 3DPS symmetry under finite S. Such dynamics indicate the existence of quasiperiodic solution manifolds (i.e. limit tori) within the weakly-swirling annular jet state space composed of 'fast' vortex shedding and 'slow' wake precession motions, consistent with the observations of Ogus et al. [9]. Furthermore, at (Re, d)-values where at least two modes are unstable for $S = 0$, the slow precession that appears for $S > 0$ may manifest a strange attractor with chaotic dynamics via a Ruelle–Takens–Newhouse scenario [66].

It will be shown in the next section that sufficiently strong rotation promotes flow instability. Yet, based on the above results, weaker rotation levels may be viewed to have a stabilising effect from the perspective of the annular jet's intrinsic dynamics. It is worth mentioning, however, that a nonmodal perspective toward flow instability may lead to a very different conclusion. Indeed, we did find 'arc branches' of slightly damped eigenvalues [67, 68] throughout the wake regime, and weakly swirling jets are well known to transiently amplify very small extrinsic perturbations through pseudo-resonance in a manner that is not directly captured by the normal modes approach used in this study [69]. For example, Montagnani and Auteri [70] considered weakly swirling co-axial jets (which do not have a centrebody wake) with underdeveloped velocity profiles at Reynolds numbers similar to those studied here, and showed that the optimal degree of nonmodal amplification grows monotonically with swirl under the conditions they investigated. They also showed that tremendous algebraic growth of small, transient perturbations can give rise to nonlinear interactions that are sufficient to sustain oscillations and/or turbulence. Nonetheless, as their transition was triggered by extrinsic forcing, such dynamics may not be accessible to the purely self-excited system considered in our investigation. The least stable subcritical eigenvalue branches in our study suggest a preference of the steady flow toward nonmodal amplification of counter-rotating $|m| = 1$ and $|m| = 2$ disturbances, with lower S conditions favouring $|m| = 1$ growth. However, nonmodal analysis would be necessary to confirm this.

4.3.4 Influence of centrebody size on vortex breakdown and precession

As the rate of rotation increases beyond the relatively small values considered above, vortex breakdown and flow instability eventually begin to play prominent roles in the jet's dynamics. The basic mechanics of this process for the steady solutions has already been discussed in Section 4.3.1. However, at higher Reynolds numbers, those steady dynamics are complicated by the emergence of unsteady behaviours which will be the main focus of this section. The present discussion will highlight the effects of varying d and S at a fixed Reynolds number of $Re = 400$. A stability map and flow regime diagram that summarise the topology (shading) and stability limits (lines) of the 2DA steady flow at $Re = 400$ are shown in Figure 4.6.

We begin with a brief discussion of the 2DA steady flow topologies, and their evolution with varying S and d. Figure 4.6(a) shows that the evolution of the flow topology with S described by Sheen et al. [12] and detailed in Figure 4.2 is typical of other centrebody sizes and higher Reynolds numbers. As the rotation rate and/or the centrebody diameter change, the flow progresses through this sequence of states in a manner that can be precisely distinguished by the number of stagnation points identified on the flow centreline. As noted earlier, unlike the circular jet, the presence of the centrebody in the annular jet ensures that at least one stagnation point is always present on the centreline. Nonetheless, the presence of the centrebody wake (regime A, e.g. Figure 4.2(c)1), the formation of the 'inverted triangle region' (regime B, e.g. Figure 4.5(c)2), the 'penetration' of the inverted triangle region (regime C, e.g. Figure 4.5(c)3), and the formation and attachment of the vortex breakdown recirculation zone (regimes D and E, e.g. figures 4.2(c)5 and (c)7, respectively) all introduce or eliminate stagnation points, as reflected in Figure 4.6(a). With the exception of the bistability between the merged vortex breakdown state and the wall jet state (regime F, e.g. figures 4.2(c)7 and 4.2(c)11, respectively), the steady 2DA solution manifold for the swirling annular jet is single-valued, and there is no parameter overlap among these distinct steady states. Furthermore, aside from the change between regimes E and F, the transitions among these steady flow patterns are not associated with bifurcations. It will be shown below that this single-valuedness does not carry over into the unsteady regime, and that some of the steady states do experience multivaluedness with unsteady solutions.

As was mentioned in Section 4.2.1, the presence of the centrebody introduces a no–slip condition that distinguishes the annular jet from a circular jet even at very small values of d. Such configurations are practically realised in applications where the centrebody gradually tapers to a point [as in 71, for example]. Nonetheless, when the centrebody is sufficiently small, viscous effects quickly dissipate the central momentum deficit, and the centrebody wake plays very little role in the jet's instability behaviour. As a result, we find that the jet's unsteady dynamics are dominated by

DISTRIBUTION A: Distribution approved for public release.

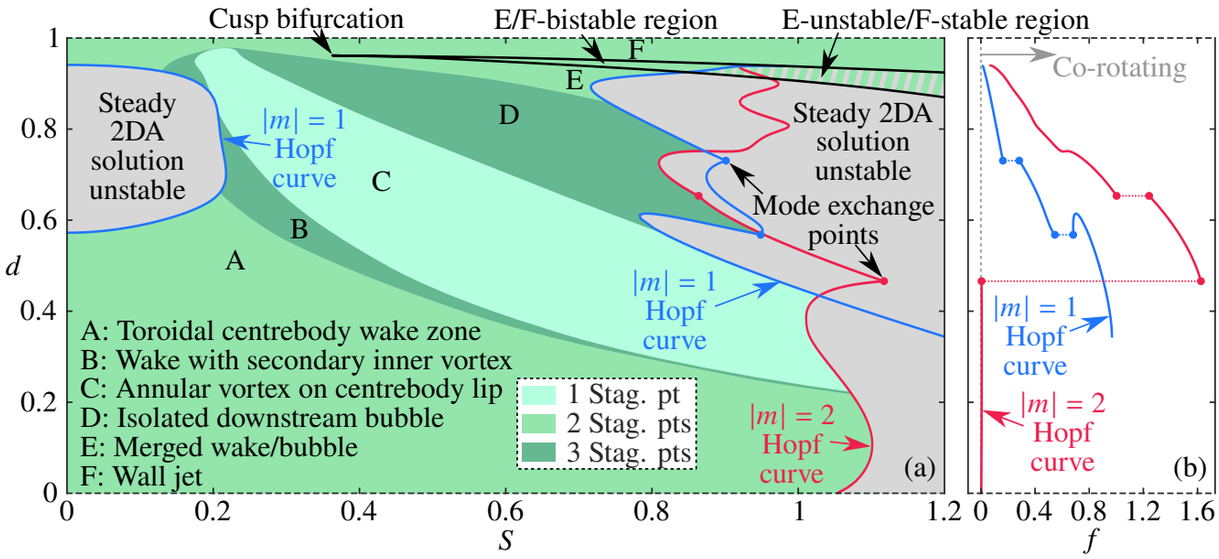

Figure 4.6: Summary of the dynamics of the steady annular swirling jet at $Re = 400$. (a) Stability map and flow regime diagram and (b) plot of critical frequency along the primary $|m| = 1$ and $|m| = 2$ Hopf curves shown in (a). In (a), the bistable region associated with the transition between breakdown and wall jet solutions is demarcated by the black curve. The neutral curves corresponding to Hopf bifurcations associated with $|m| = 2$ or $|m| = 1$ structures are indicated by the solid red and blue curves. The regions where a 2DA solution is linearly unstable are shaded gray, while the green regions indicate stable 2DA solutions. The shading of these green regions denotes the number of stagnation points present along the centreline, which is used to classify the steady flow topology into six categories.

instabilities of the outer shear layer that behave very similarly to the case of a circular jet for a range of d dependent on the Reynolds number and the nature of the instability. Thus, for annular jets at $Re = 400$ where the centrebody diameter lies within the range $0 < d \lesssim 0.4$, the primary instability occurs in the wake regime via a slowly co-rotating $|m| = 2$ mode as shown in Figure 4.6. The resulting periodic orbit emerges via a subcritical Hopf bifurcation to a limit cycle associated with a slowly co-rotating $|m| = 2$ spiral structure that also appears in the quasicolumnar regime of circular swirling jets [45, 20] and is driven by azimuthal shear along the outer shear layer [6]. Apart from this leading $|m| = 2$ instability, the steady jet also experiences instability toward a counter-rotating $|m| = 1$ mode, co-rotating $|m| = 3$ modes, and other $|m| = 2$ modes at S values beyond the range shown here, in a manner consistent with the description in our earlier paper. These instabilities generally exhibit large spatial amplification over an extended axial span, and structural sensitivity analysis shows that they are not strongly influenced by the flow structure in the interior of the jet. Thus, for small d, the annular swirling jet becomes unsteady and non-axisymmetric at S values before any central momentum deficit forms and therefore does not experience vortex breakdown via a steady or axisymmetric process. Instead, the transition to vortex breakdown likely involves several competing solution manifolds (which need not be steady or periodic), with the selection of any particular attractor being dependent on the specific initial conditions. Because of the similarity of the unsteady dynamics between the small d annular jet in the wake regime and the circular jet in the quasicolumnar regime, we will move on to situations where the effect of the centrebody–driven inner shear layer is more prominent. The reader is referred to Douglas et al. [20] for further details of these outer shear layer dynamics, though we must again emphasise the fundamental difference between a small-d annular jet and a circular jet.

At intermediate d values, Figure 4.6 indicates that a neutral curve associated with an $|m| = 1$ instability crosses over the critical $|m| = 2$ curve at $d \sim 0.45$ to become the primary instability mode. The diagram reveals that just prior to criticality, the steady flow exists in the wake regime with a steady flow topology analogous to that of Figure 4.5(c)3. Thus, the emergence of the $|m| = 1$ instability appears prior to the emergence of the vortex breakdown recirculation bubble for $0.45 \lesssim d \lesssim 0.6$. This indicates that the annular swirling jet at $Re = 400$ follows an unsteady, non–axisymmetric route to vortex breakdown for this range of centrebody diameters, and similar results were found for lower Reynolds numbers. An example of the resulting dynamics at $d = 0.5$ are considered in the bifurcation diagrams and flow visualisations of Figure 4.7 and in movie 5. Among the bifurcation diagrams, Figure 4.7 shows the amplitude of the limit cycle solutions as measured using the unsteady energy norm, $\|\acute{\boldsymbol{u}}\| = \|\boldsymbol{u} - \bar{\boldsymbol{u}}\|$. This spatially-integrated quantity

DISTRIBUTION A: Distribution approved for public release.

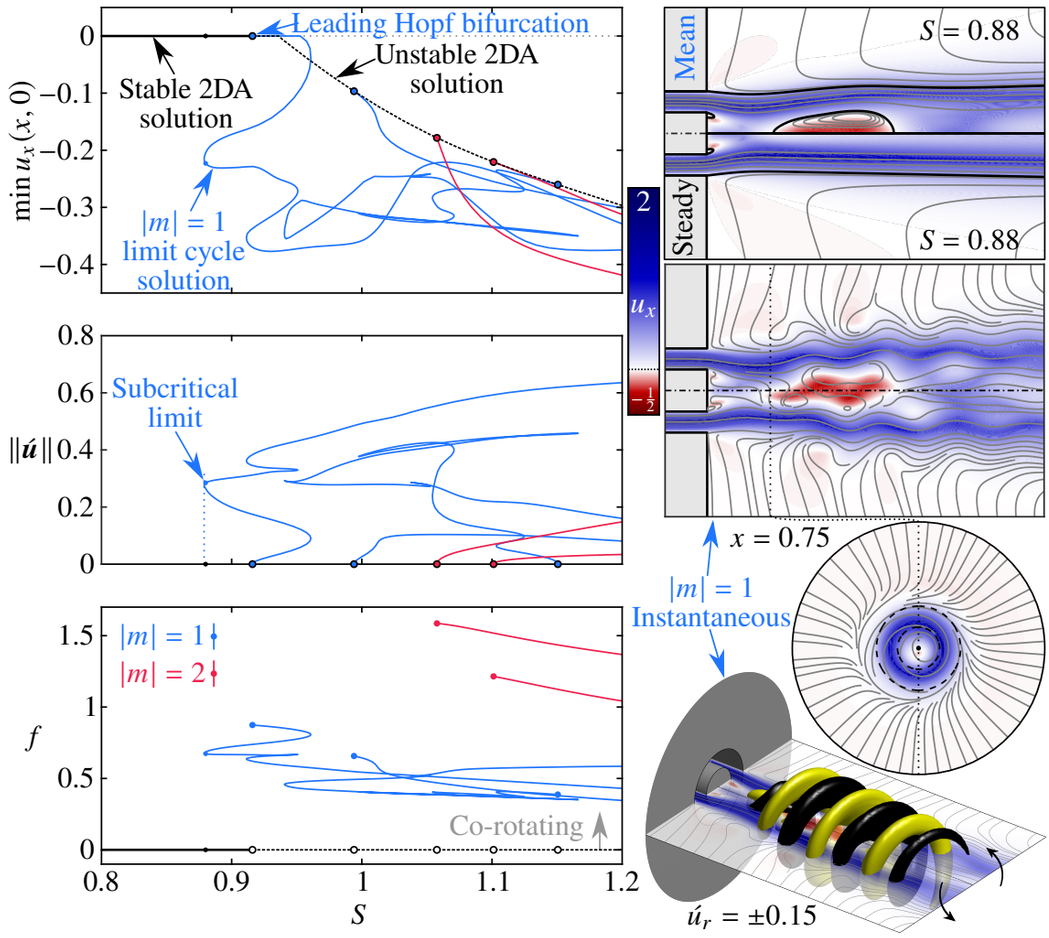

Figure 4.7: Bifurcation diagrams (left) illustrating the dynamics of the vortex breakdown process at $(Re, d) = (400, 0.5)$ and flow visualisations (right) of the $|m| = 1$ PVC solution at the indicated point ($S = 0.88$). The bifurcation diagrams show the minimum velocity along centreline, the limit cycle amplitude, and the oscillation frequency against S. Visualisations consist of a comparison of the axisymmetric steady and mean flowfields in the meridional plane, as well as a snapshot of the instantaneous flow from the $|m| = 1$ limit cycle via planar and 3D representations. Planar graphics shows contours of the axial velocity and with projected streamlines, while the 3D graphic includes an yellow/black isocontour representation of the radial velocity fluctuations at $\acute{u}_r = \pm 0.15$, respectively. The black dotted line shows the intersection of the axial and meridional planes.

includes all contributions from the oscillation's fundamental and harmonic tones over all space.

For the case of $Re = 400$ and $d = 0.5$, Figure 4.7 shows that the base flow becomes unstable with respect to several distinct $|m| = 1$ and $|m| = 2$ disturbances as S increases. These dynamics are led by the emergence of an $|m| = 1$ limit cycle, which bifurcates from the steady 2DA flow before the steady 2DA flow begins to express a central vortex breakdown recirculation zone. As this limit cycle's amplitude increases, nonlinear interactions between its mean and fluctuating components eventually begin to aid the deficit of momentum along the centreline more than a corresponding increase in S, leading to subcritical behaviour. The resulting oscillation consists of a co-rotating, counter-winding $|m| = 1$ PVC structure that exhibits a significant interval of multivaluedness between itself and the steady 2DA solution. This therefore represents a marked departure from an interpretation common to many existing studies of swirling flows. Such studies have typically adopted a linear framework for analysing flow oscillations and have mostly focused on simple swirling flow models like the Grabowski–Berger vortex. In such works, the formation of the vortex breakdown recirculation zone via an axisymmetric, steady or quasi-steady process is typically regarded as a prerequisite for unsteady vortex breakdown [72, 73, 74, 25]. Instead, our results demonstrate that the nonlinear Reynolds stresses induced by finite-amplitude oscillations can yield a time-averaged breakdown zone and instantaneous PVC at parameter values where vortex breakdown does not occur for the steady flow. This indicates an alternative subcritical route to unsteady vortex breakdown that exists in addition to the supercritical route associated with a simultaneous emergence of the central recirculation zone and PVC oscillations [38].

At higher d values along the boundary of regions C and D in Figure 4.6(a), the vortex breakdown recirculation zone forms in a steady manner as an isolated, axisymmetric bubble downstream of

DISTRIBUTION A: Distribution approved for public release.

the centrebody. It is only after the rotation increases well beyond the point where the internal stagnation point initially forms that self-excited flow instabilities become relevant to the overall dynamics. The primary unsteady dynamics subsequent to vortex breakdown include co-rotating, counter-winding structures with $|m| = 1$ or $|m| = 2$ spatial patterns depending on the specific d and Re values. Much like the intermediate-d case considered just above, the limit cycle solutions that emerge from these Hopf bifurcations may arise in either a sub- or supercritical manner depending on the specific flow circumstances at the considered parameter values. Lastly, it is interesting to note from Figure 4.6(b) that the frequencies associated with the unsteady $|m| = 1$ and $|m| = 2$ solutions in this regime tend to decrease with increasing d along the critical curves, with relatively little effect from the variations in S.

It is interesting to compare the results described above with existing works in the annular swirling jet literature which have considered the influence of the centrebody diameter. For example, in the turbulent regime, Mukherjee et al. [36] and Gupta et al. [75] have both suggested that PVC oscillation amplitudes may be diminished by increasing the centrebody diameter in order to merge the bubble and wake recirculation zones. This is akin to shifting the operating regime from a D to E-type solution in Figure 4.7. As pointed out by a referee, however, our results suggest the opposite effect, as increasing d near $S = 0.8$ is associated with the destabilisation of an $|m| = 1$ structure near the D/E transition. Even so, there are several plausible explanations for this potential discrepancy between our laminar results and the turbulent results cited above. These include effects related to configurational differences such as the swirl generation mechanism (rotating walls versus static vanes), jet profile (parabolic versus top-hat), or nozzle injection angle (perpendicular versus angled inward). It is also possible that higher Reynolds numbers and turbulence are sufficient to explain these different trends without such configurational influences. Further work will be necessary to systematically evaluate these various sensitivities and definitively relate these laminar and turbulent results.

4.3.5 Wall interactions and attachment

This section specifically focuses on the wall jet regime, which occurs at high levels of rotation. As shown in Figure 4.3, the transition to a wall jet solution occurs via a sequence of two saddle–node bifurcations of the steady 2DA flow whereby the vortex breakdown recirculation zone expands dramatically due to the realisation of a favourable pressure gradient along the dump plane wall related to the Coandă effect. A detailed account of the flow topology and flow physics in the wall jet regime and its hysteretic relationship with quasicolumnar-type solutions have been discussed in other works [9, 20, 21]. The main purpose of this section is to briefly note the extensive interval of bistability that forms in the annular swirling jet at moderate Reynolds numbers and to mention the implications of these physics in practical situations.

As suggested above, compared to a circular swirling jet, the annular swirling jet exhibits a very large interval of bistability in S. For $Re \geq 100$, Douglas et al. [20] showed that fully developed jets without a centrebody and with flush injection typically exhibit a hysteresis interval of width $\Delta S \sim O(0.1)$. However, for annular swirling jets, Figure 4.3 shows that $\Delta S \sim O(1)$ for $d \lesssim 0.5$ at $Re = 100$ and indicates that this range grows dramatically as the Reynolds number increases. For instance, at $Re = 250$, $\Delta S \sim O(10)$ for the same range of d, and this hysteresis interval continues to widen for higher Re. This stark broadening of the hysteresis region indicates that a transition to or from the wall jet regime is unlikely to occur spontaneously due to fluctuations in the incoming flow rate and swirl levels pushing a given state beyond the saddle–node bifurcation at S_b. Instead, such a transition would likely require external excitation or special initial conditions that cause the flow to spontaneously 'jump' between the breakdown and wall jet solution manifolds. Some experimental evidence for this scenario has been found previously in the forced turbulent study of O'Connor and Lieuwen [18], where a switch from a breakdown state to a wall jet state was reported under sufficiently strong external acoustic forcing.

The possibility of such an extreme shift in the bulk flow topology at high swirl conditions due to noise or other factors is a significant concern for engineering systems featuring swirling annular jets. The flat dump plane wall considered in our study offers a simple example of the possible dynamics associated with wall attachment at high swirl. However, more complex nozzle geometries and confinement situations could lead to hysteresis at more moderate swirl conditions [21]. For example, Ogus et al. [9] have provided numerical and experimental evidence of wall jet—central jet transitions in their recessed and tapered nozzle design, which seems to have shifted the interval of hysteresis to lower swirl levels than those seen in our study. Similar findings were also reported in the turbulent regime by Vanierschot and Van den Bulck [16, 17].

DISTRIBUTION A: Distribution approved for public release.

4.4 Concluding remarks

This work explores the dynamics underlying the complex flow behaviours seen in laminar annular swirling jets using nonlinear branch continuation and bifurcation analysis. It demonstrates how variations in the Reynolds number *Re*, the swirl ratio *S*, and the centrebody diameter *d* produce a clear sequence of distinct flow topologies and unsteady behaviours. Beginning at low *Re* values in the steady regime, we show how the axisymmetric flow evolves from a small centrebody wake at low *S* values to a large vortex breakdown recirculation zone at higher *S* through a sequence of intermediate states that agrees with earlier experiments by Sheen et al. [12]. Additionally, we detail a wall jet regime similar to that found by Vanierschot and Van den Bulck [16], which is bistable with respect to the breakdown solution over a significant parameter range. This wall jet solution shows clear parallels with other high *Re* experiments [18], and reinforces recent evidence that wall effects are not negligible in swirling jets [20, 21].

Moving on to higher *Re* values, results are presented for each of the three main flow regimes identified: wake, breakdown, and wall jet. Our investigation of the wake regime begins with the case of $S = 0$, where we identify a stationary $|m| = 1$ Hopf bifurcation that gives rise to a 3D plane symmetric steady solution resulting in a skewed wake structure behind the centrebody [61, 8]. We further demonstrate that this non-axisymmetric steady solution exhibits a small interval of bistability for $d \lesssim 0.8$ just before the critical *Re* and *d* values. With further increase in *Re*, the nonswirling, plane-symmetric steady wake solution experiences instability to infinitesimal 3D disturbances. These include plane-symmetric Bénard–von Kármán-type vortex shedding patterns and a very slow plane-asymmetric wobble pattern associated with quasi-static streak structures. These behaviours are strikingly similar to the dominant coherent structures that appear in the turbulent regime [11]. Introducing weak swirl to the flow causes the steady non-axisymmetry found in the $S = 0$ case to twist into a spiral shape that slowly precesses periodically in time about the centreline in the direction of swirl. Similar dynamics have been reported for weakly-swirling turbulent annular jets [57], suggesting that $S > 0$ plays the same symmetry-breaking role even at much higher *Re* values. In addition, we explain the link between the linear instabilities of the non-axisymmetric steady flow at $S = 0$ and the emergence of quasiperiodic and chaotic solution manifolds for $S > 0$. Our arguments clarify the origins of the quasiperiodicity at low *S* reported by Ogus et al. [9]. Nonetheless, a Floquet analysis or time-domain study delving further into such dynamics and exploring the system's route to chaos may be an interesting direction for future work.

At more moderate rotation levels but low *d*, the centrebody wake is small and weak and the inner shear layer apparently does not play an important role in the flow's instability behaviour. In such situations, the annular swirling jet behaves similarly to a circular swirling jet, expressing a form of the $|m| = 2$ instability first identified by Billant et al. [45], which occurs via a subcritical bifurcation as described in Douglas et al. [20] at *S*-values well before vortex breakdown. At intermediate *d*, where instability occurs near the threshold *S*-value for vortex breakdown, interactions between fluctuations and the mean flow open possibilities for hysteresis between a stagnation point–free steady 2DA solution and a co-rotating $|m| = 1$ PVC limit cycle solution. At higher *d*, multiple $|m| = 1$ and $|m| = 2$ modes do become unstable, but were only found to bifurcate from a steady 2DA flow that already exhibited a well–developed breakdown recirculation zone. Thus, it is shown that the vortex breakdown stagnation zone may develop either in an unsteady manner, where the flow experiences nonlinear instability before the formation of a steady central stagnation point, or in a steady manner, where the stagnation point emerges within the steady, axisymmetric flow. This finding presents a different understanding of the vortex breakdown and instability process than many previous modelling studies, which often insist that the central recirculation bubble is always a precursor to instability, rather than a possible product of it. It would be interesting for future work to consider how different flow configurations (e.g. other nozzle geometries) and parameter conditions (e.g. turbulent Reynolds numbers) influence the structure and dynamics of these unsteady flow features.

DISTRIBUTION A: Distribution approved for public release.

Bibliography

[1] N. Syred and J.M. Beér. Combustion in swirling flows: A review. *Combustion and Flame*, 23(2):143–201, 1974. ISSN 0010-2180. doi: https://doi.org/10.1016/0010-2180(74)90057-1. URL https://www.sciencedirect.com/science/article/pii/0010218074900571.

[2] Tim C. Lieuwen. *Unsteady Combustor Physics*. Cambridge University Press, 2012.

[3] Sidney Leibovich. Vortex stability and breakdown - survey and extension. *AIAA Journal*, 22 (9):1192–1206, 1984. doi: 10.2514/3.8761. URL https://doi.org/10.2514/3.8761.

[4] Robert L. Ash and Mehdi R. Khorrami. *Vortex Stability*, pages 317–372. Springer Netherlands, Dordrecht, 1995. ISBN 978-94-011-0249-0. doi: 10.1007/978-94-011-0249-0_8. URL https://doi.org/10.1007/978-94-011-0249-0_8.

[5] Henk A. Dijkstra, Fred W. Wubs, Andrew K. Cliffe, Eusebius Doedel, Ioana F. Dragomirescu, Bruno Eckhardt, Alexander Yu. Gelfgat, Andrew L. Hazel, Valerio Lucarini, Andy G. Salinger, and et al. Numerical bifurcation methods and their application to fluid dynamics: Analysis beyond simulation. *Communications in Computational Physics*, 15(1):1–45, 2014. doi: 10.4208/cicp.240912.180613a.

[6] F. Gallaire and J.-M. Chomaz. Instability mechanisms in swirling flows. *Physics of Fluids*, 15(9):2622–2639, 2003. doi: 10.1063/1.1589011. URL https://doi.org/10.1063/1.1589011.

[7] Christian Del Taglia, Lars Blum, Jürg Gass, Yiannis Ventikos, and Dimos Poulikakos. Numerical and Experimental Investigation of an Annular Jet Flow With Large Blockage . *Journal of Fluids Engineering*, 126(3):375–384, 07 2004. ISSN 0098-2202. doi: 10.1115/1.1760533. URL https://doi.org/10.1115/1.1760533.

[8] C. Del Taglia, A. Moser, and L. Blum. Spontaneous break of symmetry in unconfined laminar annular jets. *Journal of Fluids Engineering*, 131(8):081202, 2009. doi: https://doi.org/10.1115/1.3176960.

[9] G. Ogus, M. Baelmans, and M. Vanierschot. On the flow structures and hysteresis of laminar swirling jets. *Physics of Fluids*, 28(12):123604, 2016. doi: 10.1063/1.4972227. URL https://doi.org/10.1063/1.4972227.

[10] Karol Wawrzak, Andrzej Boguslawski, Artur Tyliszczak, and Michal Saczek. LES study of global instability in annular jets. *International Journal of Heat and Fluid Flow*, 79:108460, 2019. ISSN 0142-727X. doi: https://doi.org/10.1016/j.ijheatfluidflow.2019.108460. URL https://www.sciencedirect.com/science/article/pii/S0142727X19303935.

[11] Maarten Vanierschot, Mustafa Percin, and Bas W van Oudheusden. Asymmetric vortex shedding in the wake of an abruptly expanding annular jet. *Experiments in Fluids*, 62(4): 1–12, 2021.

[12] H. J. Sheen, W. J. Chen, and S. Y. Jeng. Recirculation zones of unconfined and confined annular swirling jets. *AIAA Journal*, 34(3):572–579, 1996. doi: 10.2514/3.13106. URL https://doi.org/10.2514/3.13106.

[13] M. Vanierschot and E. Van den Bulck. Influence of swirl on the initial merging zone of a turbulent annular jet. *Physics of Fluids*, 20(10):105104, 2008. doi: 10.1063/1.2992191. URL https://doi.org/10.1063/1.2992191.

DISTRIBUTION A: Distribution approved for public release.

[14] Manuel García-Villalba and Jochen Fröhlich. LES of a free annular swirling jet – Dependence of coherent structures on a pilot jet and the level of swirl. *International Journal of Heat and Fluid Flow*, 27(5):911–923, 2006. ISSN 0142-727X. doi: https://doi.org/10.1016/j.ijheatfluidflow.2006.03.015. URL https://www.sciencedirect.com/science/article/pii/S0142727X06000865. Special issue of the 6th International Symposium on Engineering Turbulence Modelling and Measurements – ETMM6.

[15] Shanwu Wang, Shih-Yang Hsieh, and Vigor Yang. Unsteady flow evolution in swirl injector with radial entry. i. stationary conditions. *Physics of Fluids*, 17(4):045106, 2005. doi: 10.1063/1.1874892. URL https://doi.org/10.1063/1.1874892.

[16] M. Vanierschot and E. Van den Bulck. Numerical study of hysteresis in annular swirling jets with a stepped-conical nozzle. *International Journal for Numerical Methods in Fluids*, 54 (3):313–324, 2007. doi: https://doi.org/10.1002/fld.1400. URL https://onlinelibrary.wiley.com/doi/abs/10.1002/fld.1400.

[17] M. Vanierschot and E. Van den Bulck. Hysteresis in flow patterns in annular swirling jets. *Experimental Thermal and Fluid Science*, 31(6):513–524, 2007. ISSN 0894-1777. doi: https://doi.org/10.1016/j.expthermflusci.2006.06.001. URL https://www.sciencedirect.com/science/article/pii/S0894177706000884.

[18] Jacqueline O'Connor and Tim Lieuwen. Recirculation zone dynamics of a transversely excited swirl flow and flame. *Physics of Fluids*, 24(7):075107, 2012. doi: 10.1063/1.4731300. URL https://doi.org/10.1063/1.4731300.

[19] Mario Falese, Laurent Y.M. Gicquel, and Thierry Poinsot. LES of bifurcation and hysteresis in confined annular swirling flows. *Computers & Fluids*, 89:167–178, 2014. ISSN 0045-7930. doi: https://doi.org/10.1016/j.compfluid.2013.10.033. URL https://www.sciencedirect.com/science/article/pii/S0045793013004167.

[20] Christopher M. Douglas, Benjamin L. Emerson, and Timothy C. Lieuwen. Nonlinear dynamics of fully developed swirling jets. *Journal of Fluid Mechanics*, 924:A14, 2021. doi: 10.1017/jfm.2021.615.

[21] Christopher M. Douglas and Lutz Lesshafft. Confinement effects in laminar swirling jets. *Journal of Fluid Mechanics (under review)*, 2022.

[22] I. Chterev, C. W. Foley, D. Foti, S. Kostka, A. W. Caswell, N. Jiang, A. Lynch, D. R. Noble, S. Menon, J. M. Seitzman, and T. C. Lieuwen. Flame and flow topologies in an annular swirling flow. *Combustion Science and Technology*, 186(8):1041–1074, 2014. doi: 10.1080/00102202.2014.882916. URL https://doi.org/10.1080/00102202.2014.882916.

[23] Qingguo Zhang, Santosh J. Shanbhogue, Shreekrishna, Tim Lieuwen, and Jacqueline O'Connor. Strain characteristics near the flame attachment point in a swirling flow. *Combustion Science and Technology*, 183(7):665–685, 2011. doi: 10.1080/00102202.2010.537288. URL https://doi.org/10.1080/00102202.2010.537288.

[24] Anindya Datta, Saarthak Gupta, Ianko Chterev, Isaac Boxx, and Santosh Hemchandra. Impact of Hydrogen Addition on the Thermoacoustic Instability and Precessing Vortex Core Dynamics in a CH4/H2/Air Technically Premixed Combustor. *Journal of Engineering for Gas Turbines and Power*, 144(2), 11 2021. ISSN 0742-4795. doi: 10.1115/1.4052202. URL https://doi.org/10.1115/1.4052202. 021013.

[25] Philippe Meliga, François Gallaire, and Jean-Marc Chomaz. A weakly nonlinear mechanism for mode selection in swirling jets. *Journal of Fluid Mechanics*, 699:216–262, 2012. doi: 10.1017/jfm.2012.93.

[26] S. Pasche, F. Avellan, and F. Gallaire. Onset of chaos in helical vortex breakdown at low reynolds number. *Phys. Rev. Fluids*, 3:064701, Jun 2018. doi: 10.1103/PhysRevFluids.3.064701. URL https://link.aps.org/doi/10.1103/PhysRevFluids.3.064701.

[27] Philippe Meliga and François Gallaire. Control of axisymmetric vortex breakdown in a constricted pipe: Nonlinear steady states and weakly nonlinear asymptotic expansions. *Physics of Fluids*, 23(8):084102, 2011. doi: 10.1063/1.3610380. URL https://doi.org/10.1063/1.3610380.

DISTRIBUTION A: Distribution approved for public release.

[28] Pradeep Moise and Joseph Mathew. Bubble and conical forms of vortex breakdown in swirling jets. *Journal of Fluid Mechanics*, 873:322–357, 2019. doi: 10.1017/jfm.2019.401.

[29] Davide Montagnani. *Stability and control of jet flows: a numerical study*. PhD thesis, Department of Aerospace Science and Technology, Politecnico di Milano, 1 2018.

[30] T. Loiseleux, J. M. Chomaz, and P. Huerre. The effect of swirl on jets and wakes: Linear instability of the Rankine vortex with axial flow. *Physics of Fluids*, 10(5):1120–1134, 1998. doi: 10.1063/1.869637. URL https://doi.org/10.1063/1.869637.

[31] Thomas Loiseleux, Ivan Delbende, and Patrick Huerre. Absolute and convective instabilities of a swirling jet/wake shear layer. *Physics of Fluids*, 12(2):375–380, 2000. doi: 10.1063/1.870315. URL https://doi.org/10.1063/1.870315.

[32] K. Oberleithner, M. Sieber, C. N. Nayeri, C. O. Paschereit, C. Petz, H.-C. Hege, B. R. Noack, and I. Wygnanski. Three-dimensional coherent structures in a swirling jet undergoing vortex breakdown: stability analysis and empirical mode construction. *Journal of Fluid Mechanics*, 679:383–414, 2011. doi: 10.1017/jfm.2011.141.

[33] Lothar Rukes, Christian Oliver Paschereit, and Kilian Oberleithner. An assessment of turbulence models for linear hydrodynamic stability analysis of strongly swirling jets. *European Journal of Mechanics - B/Fluids*, 59:205 – 218, 2016. ISSN 0997-7546. doi: https://doi.org/10.1016/j.euromechflu.2016.05.004. URL http://www.sciencedirect.com/science/article/pii/S0997754615303320.

[34] Maarten Vanierschot, Jens S. Müller, Moritz Sieber, Mustafa Percin, Bas W. van Oudheusden, and Kilian Oberleithner. Single- and double-helix vortex breakdown as two dominant global modes in turbulent swirling jet flow. *Journal of Fluid Mechanics*, 883:A31, 2020. doi: 10.1017/jfm.2019.872.

[35] O. Tammisola and M. P. Juniper. Coherent structures in a swirl injector at Re=4800 by nonlinear simulations and linear global modes. *Journal of Fluid Mechanics*, 792:620–657, 2016. doi: 10.1017/jfm.2016.86.

[36] Arnab Mukherjee, Nishanth Muthichur, Chaitali More, Saarthak Gupta, and Santosh Hemchandra. The role of the centerbody wake on the precessing vortex core dynamics of a swirl nozzle. *Journal of Engineering for Gas Turbines and Power*, 143(5), 03 2021. ISSN 0742-4795. doi: 10.1115/1.4050155. URL https://doi.org/10.1115/1.4050155.

[37] Christopher M. Douglas, Benjamin L. Emerson, Santosh Hemchandra, and Timothy C. Lieuwen. Forced flow response analysis of a turbulent swirling annular jet flame. *Physics of Fluids*, 33(8):085124, 2021. doi: 10.1063/5.0061053. URL https://doi.org/10.1063/5.0061053.

[38] Kiran Manoharan, Mark Frederick, Sean Clees, Jacqueline O'Connor, and Santosh Hemchandra. A weakly nonlinear analysis of the precessing vortex core oscillation in a variable swirl turbulent round jet. *Journal of Fluid Mechanics*, 884:A29, 2020. doi: 10.1017/jfm.2019.903.

[39] Igor Mezić. Analysis of fluid flows via spectral properties of the koopman operator. *Annual Review of Fluid Mechanics*, 45:357–378, 2013.

[40] Denis Sipp and Anton Lebedev. Global stability of base and mean flows: a general approach and its applications to cylinder and open cavity flows. *Journal of Fluid Mechanics*, 593: 333–358, 2007. doi: 10.1017/S0022112007008907.

[41] Sam E. Turton, Laurette S. Tuckerman, and Dwight Barkley. Prediction of frequencies in thermosolutal convection from mean flows. *Phys. Rev. E*, 91:043009, Apr 2015. doi: 10.1103/PhysRevE.91.043009. URL https://link.aps.org/doi/10.1103/PhysRevE.91.043009.

[42] Samir Beneddine, Denis Sipp, Anthony Arnault, Julien Dandois, and Lutz Lesshafft. Conditions for validity of mean flow stability analysis. *Journal of Fluid Mechanics*, 798:485–504, 2016. doi: 10.1017/jfm.2016.331.

DISTRIBUTION A: Distribution approved for public release.

[43] Z. Rusak. The interaction of near-critical swirling flows in a pipe with inlet azimuthal vorticity perturbations. *Physics of Fluids*, 10(7):1672–1684, 1998. doi: 10.1063/1.869685. URL https://doi.org/10.1063/1.869685.

[44] J.P. Boyd. *Chebyshev and Fourier Spectral Methods: Second Revised Edition*. Dover Books on Mathematics. Dover Publications, 2013. ISBN 9780486141923.

[45] Paul Billant, Jean-Marc Chomaz, and Patrick Huerre. Experimental study of vortex breakdown in swirling jets. *Journal of Fluid Mechanics*, 376:183–219, 1998. doi: 10.1017/S0022112098002870.

[46] Hanzhuang Liang and T. Maxworthy. An experimental investigation of swirling jets. *Journal of Fluid Mechanics*, 525:115–159, 2005. doi: 10.1017/S0022112004002629.

[47] J. M. Beér and N. A. Chigier. *Combustion aerodynamics*. Halsted Press Division, Wiley, New York, 1972.

[48] Guillaume Vignat, Daniel Durox, and Sébastien Candel. The suitability of different swirl number definitions for describing swirl flows: Accurate, common and (over-) simplified formulations. *Progress in Energy and Combustion Science*, 89:100969, 2022. ISSN 0360-1285. doi: https://doi.org/10.1016/j.pecs.2021.100969. URL https://www.sciencedirect.com/science/article/pii/S0360128521000678.

[49] Christophe Geuzaine and Jean-François Remacle. Gmsh: A 3-D finite element mesh generator with built-in pre- and post-processing facilities. *International Journal for Numerical Methods in Engineering*, 79(11):1309–1331, 2009. doi: 10.1002/nme.2579. URL https://onlinelibrary.wiley.com/doi/abs/10.1002/nme.2579.

[50] F. Hecht. New development in FreeFem++. *J. Numer. Math.*, 20(3-4):251–265, 2012. ISSN 1570-2820. URL https://freefem.org/.

[51] Johann Moulin, Pierre Jolivet, and Olivier Marquet. Augmented Lagrangian preconditioner for large-scale hydrodynamic stability analysis. *Computer Methods in Applied Mechanics and Engineering*, 351:718 – 743, 2019. ISSN 0045-7825. doi: https://doi.org/10.1016/j.cma.2019.03.052. URL http://www.sciencedirect.com/science/article/pii/S0045782519301914.

[52] Satish Balay, Shrirang Abhyankar, Mark F. Adams, Steven Benson, Jed Brown, Peter Brune, Kris Buschelman, Emil Constantinescu, Lisandro Dalcin, Alp Dener, Victor Eijkhout, William D. Gropp, Václav Hapla, Tobin Isaac, Pierre Jolivet, Dmitry Karpeev, Dinesh Kaushik, Matthew G. Knepley, Fande Kong, Scott Kruger, Dave A. May, Lois Curfman McInnes, Richard Tran Mills, Lawrence Mitchell, Todd Munson, Jose E. Roman, Karl Rupp, Patrick Sanan, Jason Sarich, Barry F. Smith, Stefano Zampini, Hong Zhang, Hong Zhang, and Junchao Zhang. PETSc/TAO users manual. Technical Report ANL-21/39 - Revision 3.16, Argonne National Laboratory, 2021.

[53] Vicente Hernandez, Jose E. Roman, and Vicente Vidal. SLEPc: A scalable and flexible toolkit for the solution of eigenvalue problems. *ACM Trans. Math. Software*, 31(3):351–362, 2005.

[54] P.R. Amestoy, I. S. Duff, J. Koster, and J.-Y. L'Excellent. A fully asynchronous multifrontal solver using distributed dynamic scheduling. *SIAM Journal on Matrix Analysis and Applications*, 23(1):15–41, 2001.

[55] Yuri A. Kuznetsov. *Elements of Applied Bifurcation Theory (2nd Ed.)*. Springer-Verlag, Berlin, Heidelberg, 1998. ISBN 0387983821.

[56] T. A. Long and R. A. Petersen. Controlled interactions in a forced axisymmetric jet. Part 1. The distortion of the mean flow. *Journal of Fluid Mechanics*, 235:37–55, 1992. doi: 10.1017/S0022112092001010.

[57] M. Vanierschot, K. Van Dyck, P. Sas, and E. Van den Bulck. Symmetry breaking and vortex precession in low-swirling annular jets. *Physics of Fluids*, 26(10):105110, 2014. doi: 10.1063/1.4898347.

DISTRIBUTION A: Distribution approved for public release.

[58] Petrônio A. S. Nogueira, André V. G. Cavalieri, Peter Jordan, and Vincent Jaunet. Large-scale streaky structures in turbulent jets. *Journal of Fluid Mechanics*, 873:211–237, 2019. doi: 10.1017/jfm.2019.365.

[59] Ethan Pickering, Georgios Rigas, Petrônio A. S. Nogueira, André V. G. Cavalieri, Oliver T. Schmidt, and Tim Colonius. Lift-up, Kelvin—Helmholtz and Orr mechanisms in turbulent jets. *Journal of Fluid Mechanics*, 896:A2, 2020. doi: 10.1017/jfm.2020.301.

[60] Chuhan Wang, Lutz Lesshafft, André V. G. Cavalieri, and Peter Jordan. The effect of streaks on the instability of jets. *Journal of Fluid Mechanics*, 910:A14, 2021. doi: 10.1017/jfm.2020.963.

[61] Ananias G. Tomboulides and Steven A. Orszag. Numerical investigation of transitional and weak turbulent flow past a sphere. *Journal of Fluid Mechanics*, 416:45–73, 2000. doi: 10.1017/S0022112000008880.

[62] David Fabre, Franck Auguste, and Jacques Magnaudet. Bifurcations and symmetry breaking in the wake of axisymmetric bodies. *Physics of Fluids*, 20(5):051702, 2008. doi: 10.1063/1.2909609.

[63] P. Bohorquez, E. Sanmiguel-Rojas, A. Sevilla, J. I. Jiménez-González, and C. Martínez-Bazán. Stability and dynamics of the laminar wake past a slender blunt-based axisymmetric body. *Journal of Fluid Mechanics*, 676:110–144, 2011. doi: 10.1017/jfm.2011.35.

[64] G Rigas, L Esclapez, and L. Magri. Symmetry breaking in a 3D bluff-body wake. In *Proceedings of the Summer Program*. Stanford University Center for Turbulence Research, 2016.

[65] J. R. Pacheco, J. M. Lopez, and F. Marques. Pinning of rotating waves to defects in finite taylor–couette flow. *Journal of Fluid Mechanics*, 666:254–272, 2011. doi: 10.1017/S0022112010004131.

[66] J. P. Eckmann. Roads to turbulence in dissipative dynamical systems. *Rev. Mod. Phys.*, 53: 643–654, Oct 1981. doi: 10.1103/RevModPhys.53.643. URL https://link.aps.org/doi/10.1103/RevModPhys.53.643.

[67] X. Garnaud, L. Lesshafft, P. J. Schmid, and P. Huerre. Modal and transient dynamics of jet flows. *Physics of Fluids*, 25(4):044103, 2013. doi: 10.1063/1.4801751. URL https://doi.org/10.1063/1.4801751.

[68] W. Coenen, L. Lesshafft, X. Garnaud, and A. Sevilla. Global instability of low-density jets. *Journal of Fluid Mechanics*, 820:187–207, 2017. doi: 10.1017/jfm.2017.203.

[69] Peter J. Schmid. Nonmodal stability theory. *Annual Review of Fluid Mechanics*, 39(1): 129–162, 2007. doi: 10.1146/annurev.fluid.38.050304.092139. URL https://doi.org/10.1146/annurev.fluid.38.050304.092139.

[70] D. Montagnani and F. Auteri. Non-modal analysis of coaxial jets. *Journal of Fluid Mechanics*, 872:665–696, 2019. doi: 10.1017/jfm.2019.356.

[71] N. W. M. Ko and W. T. Chan. The inner regions of annular jets. *Journal of Fluid Mechanics*, 93(3):549–584, 1979. doi: 10.1017/S0022112079002652.

[72] M. P. Escudier, J. Bornstein, and T. Maxworthy. The dynamics of confined vortices. *Proceedings of the Royal Society of London. Series A, Mathematical and Physical Sciences*, 382 (1783):335–360, 1982. ISSN 00804630. URL http://www.jstor.org/stable/2397398.

[73] M. R. Ruith, P. Chen, E. Meiburg, and T. Maxworthy. Three-dimensional vortex breakdown in swirling jets and wakes: direct numerical simulation. *Journal of Fluid Mechanics*, 486: 331–378, 2003. doi: 10.1017/S0022112003004749.

[74] M. A. Herrada and R. Fernandez-Feria. On the development of three-dimensional vortex breakdown in cylindrical regions. *Physics of Fluids*, 18(8):084105, 2006. doi: 10.1063/1.2338065. URL https://doi.org/10.1063/1.2338065.

DISTRIBUTION A: Distribution approved for public release.

[75] Saarthak Gupta, Santosh Shanbhogue, Masayasu Shimura, Ahmed Ghoniem, and Santosh Hemchandra. Impact of a Centerbody on the Unsteady Flow Dynamics of a Swirl Nozzle: Intermittency of Precessing Vortex Core Oscillations. *Journal of Engineering for Gas Turbines and Power*, 144(2), 11 2021. ISSN 0742-4795. doi: 10.1115/1.4052144. URL https://doi.org/10.1115/1.4052144. 021014.

DISTRIBUTION A: Distribution approved for public release.

Chapter 5

Permuted Proper Orthogonal Decomposition for Analysis of Advecting Structures

5.1 Introduction

High Reynolds number flows are characterised by complex spatio-temporal dynamics resulting from the superposition and interactions of flow features spanning a wide range of spatial and temporal scales. We often seek low-dimensional descriptions in the form of an optimal set of basis functions which capture the dominant flow dynamics, physically controlling features, and coherent patterns embedded in noise. The distinct vortex shedding pattern due to the Bénard/von Kármán instability [1], and shear layer vortices due to the Kelvin-Helmholtz instability [2] are examples of dynamically important coherent structures in turbulent shear flows. Low-dimensional structures such as these can be identified and extracted from high-dimensional data using a range of different methods. These include both physics-based methods, such as hydrodynamic stability analysis, and data-driven techniques, such as POD, dynamic mode decomposition (DMD), or traditional Fourier-mode decomposition. This work is based on POD [3, 4], which has been extensively used for dimensionality reduction, feature extraction, reduced-order modelling, and data reconstruction/visualisation [5, 6, 7].

Fluid flows are commonly described by space-time data, here denoted $\boldsymbol{q}(\boldsymbol{x}, t)$, where $\boldsymbol{q}$ represents a measured or calculated quantity, $\boldsymbol{x}$ represents a general spatial coordinate system, and t denotes time. The most commonly used form of POD, which provides a space-time separated representation of this data, is referred to as space-only POD in this work, following the naming convention used by Towne et al. [8]. This form of POD decomposes the mean subtracted flow, $\boldsymbol{q}'(\boldsymbol{x}, t) = \boldsymbol{q}(\boldsymbol{x}, t) - \bar{\boldsymbol{q}}(\boldsymbol{x})$, according to:

$$\boldsymbol{q}'(\boldsymbol{x}, t) = \sum_j a_j(t)\, \boldsymbol{\phi}_j(\boldsymbol{x}), \tag{5.1}$$

where $a_j(t)$ are the scalar time-dependent coefficients and $\boldsymbol{\phi}_j(\boldsymbol{x})$ are the spatially orthogonal modes. These modes are defined as the uncorrelated directions which maximise the projected variance (or equivalently, minimise the mean squared error) of the input data [9, 10, 7]. POD provides an optimal decomposition of a given flow, as the ordering of the modes ensures that the POD basis captures as much of the variance in the given data with as few modes as possible. Hence, the POD basis can be used to reconstruct a truncated approximation, $\boldsymbol{q}_r(\boldsymbol{x}, t)$, defined as:

$$\boldsymbol{q}_r(\boldsymbol{x}, t) = \bar{\boldsymbol{q}}(\boldsymbol{x}) + \sum_{j=1}^{r} a_j(t)\, \boldsymbol{\phi}_j(\boldsymbol{x}), \tag{5.2}$$

which provides an optimal linear representation of the flow for any order r. Equation (5.2) provides the smallest mean squared error approximation of the given flow: no other basis can reconstruct the flow with a smaller error. When the input data are in the form of constant-density turbulent velocity fields, the projected variance is proportional to the average turbulent kinetic energy in each mode [7, 6, 5]. Therefore, space-only POD is commonly used to extract high energy spatial structures from a given flow. Note, however, that there is no restriction on the properties of the time coefficients, and hence, a single mode can contain a superposition of flow structures with very different time scales. Further properties of space-only POD relevant to this work are discussed in section 5.2.1.

DISTRIBUTION A: Distribution approved for public release.

Spectral POD (SPOD) is an alternative decomposition approach for statistically stationary flows, which formulates POD in frequency space [4, 8]. The input data are transformed into Fourier space along the temporal dimension and POD is performed at each discrete frequency. This results in a set of time-harmonic, spatially orthogonal modes ranked according to their energy at each of these frequencies. Thus, SPOD targets flow structures which evolve coherently in space and time. As shown by Towne et al. [8], there is no localised relationship between space-only POD and SPOD modes. For example, a single space-only POD mode can potentially contain information from every single SPOD mode across all frequencies, and vice versa.

This work is motivated by the desire to analyse spatio-temporal data from advection-dominated turbulent flows. Advection is a prominent feature of fluid mechanics problems, as evidenced by the substantial derivatives appearing in the governing equations. However, different decomposition techniques capture advection differently. As discussed by Holmes et al. [7], Brunton and Kutz [11], space-only POD represents advecting features (i.e. features with coupled space-time dependencies via their translational character) by a superposition of modes. For example, the simplest case of a single frequency travelling wave, when cast in the form of equation (5.1), can be written as:

$$A \sin\left[\omega\left(t - \frac{x}{u_c}\right)\right] = A \sin\left(\omega t\right) \cos\left(\frac{\omega x}{u_c}\right) - A \cos\left(\omega t\right) \sin\left(\frac{\omega x}{u_c}\right), \tag{5.3}$$

where x refers to a one-dimensional spatial coordinate, A is the amplitude, ω is the angular frequency, and u_c is the convection velocity of the travelling wave. Thus, a combination of at least two standing waves is required to represent a travelling wave. In practice, travelling structures in real, high Reynolds number flows are spread across many space-only POD modes. Often, manual inspection is used to interpret which modes collectively represent a travelling disturbance (e.g., see figure 5.7), although techniques have been developed which automate this process, such as identifying "linked modes" via a DMD on the time coefficients from POD [12]. In contrast, the "translation" property of the Fourier transform enables SPOD to capture space-time correlated information, such as travelling waves [8]. For example, SPOD decomposes equation (5.3) as a single complex mode, whose mode shape is given by $\exp\left(\mathrm{i}\omega x/u_c\right)$, while decomposing a more general, non-dispersive travelling wave, $f\left(t - x/u_c\right)$, as a single mode with a spectrum given by $F\left(\omega\right) \exp\left(\mathrm{i}\omega x/u_c\right)$. However, in the event that a single physical flow feature contains multi-frequency content, SPOD splits this information across different SPOD modes. For highly turbulent flows, where coherent structures can occur intermittently and often display variable-frequency characteristics due to phase jitter or frequency modulations, a single physical feature is therefore likely to be represented by multiple SPOD modes.

Many alternative POD methods have been suggested to provide additional insights and complimentary perspectives to the ones offered by space-only POD and SPOD. Often, the goal of these methods is to capture space-time correlated flow features with an easy-to-interpret, more compact set of basis functions, as the performance of space-only POD depends on the coordinate system in which the data are represented. As discussed by Brunton and Kutz [11], the increased rank of the space-only POD basis due to translation is not intrinsic to the method itself but, rather, reflects the "geometric dependence" of the singular value decomposition (SVD). Using a spatial transformation, translational symmetries can be removed from the data before extracting the modes, as expressed by:

$$\boldsymbol{q}'_{\mathrm{sh}}\left(\boldsymbol{x}, t\right) = \sum_j a_j\left(t\right) \boldsymbol{\phi}_j\left(\boldsymbol{x} + c_j\left(\boldsymbol{x}, t\right)\right), \tag{5.4}$$

where $c_j\left(\boldsymbol{x}, t\right)$ denotes a specified shift velocity such that the decomposition is performed in the reference frame of a travelling structure. Commonly, a single shift velocity is assumed, which is determined using centring or template fitting. Centring refers to the procedure of identifying the centre point of a wave and then shifting the data such that the centre in each snapshot is at the same point [13]. Template fitting shifts the data at each time such that it aligns with (i.e. is maximally correlated to) a preselected template [14, 15, 16, 17]. Furthermore, Fedele et al. [18] reduced translational symmetry in turbulent pipe flow measurements using a Fourier-based method, while Reiss et al. [19] developed an iterative procedure which handles structures advecting at different velocities. This iterative procedure separates the modes into different reference frames using a spatial shift determined by the different advection velocities. Common to all these studies is that determining the shift velocity and calculating the (shifted) POD modes are independent, potentially iterative steps.

Extending the idea of a spatial transformation, Sesterhenn and Shahirpour [20] introduced a spatio-temporal transformation whereby the modal decomposition (space-only POD or DMD) is

DISTRIBUTION A: Distribution approved for public release.

carried out along a direction characteristic to the travelling structure. This direction is identified as the rotation of the data in space and time which produces the largest reduction in the singular values when performing an SVD. Physically, this direction coincides with the group velocity of the travelling structure. A new time coordinate is aligned with the direction of the characteristic and the decomposition (demonstrated using DMD) is performed on planes (snapshots) normal to it. Hence, each new, transformed snapshot contains spatial information about the travelling structure across a range of physical time steps, enhancing the method's ability to capture coherent space-time structures with fewer modes.

In a different vein, Sieber et al. [12] introduced a method which applies a filtering operation on the POD covariance matrix, resulting in a decomposition which mitigates the superposition of features with different time scales within a given spatial POD mode. Since coherent structures are generally associated with a relatively narrow range of time scales (but not necessarily a distinct frequency), this filtering operation allows for a single mode to provide a more comprehensive representation of a given flow structure. Furthermore, Schmidt and Schmid [21] proposed a conditional space-time POD formulation targeting the statistics of rare or intermittent events via their space-time coherence during finite time intervals. By construction, this method provides spatio-temporal POD modes which are orthogonal in a space-time inner product over a finite time interval.

A key motivator for this work is the re-orientation of the space-time coordinates noted by Schmid [22], who demonstrated that DMD can be applied either spatially or temporally. The temporal DMD analysis decomposes the data into spatial modes that temporally evolve as $\exp(\mathrm{i}\omega_r t)\exp(\omega_i t)$. In this way, the modes are analogous to the linear modes from global hydrodynamic stability analysis. However, Schmid also noted that the method could be applied equally well for a spatial analysis of the data by re-orienting the space-time axes. In this case, the DMD modes are transverse space-time modes that spatially evolve as $\exp(\mathrm{i}k_r x)\exp(k_i x)$ in a similar manner to spatial stability modes from local hydrodynamic stability analysis

This work utilises Schmid's (2010) approach of re-orienting the space-time coordinates in the context of POD, while noting that the multi-dimensional POD theory is independent of an *a priori* distinction between the space and time variables [7]. The re-orientation can be accomplished by simply permuting the input data to obtain a snapshot sequence in space rather than time. This permutation applied to POD, an approach referred to as *permuted* POD (PPOD), is the focus of this paper [23]. In PPOD, the space-time variables are permuted such that the PPOD modes are orthogonal in time and the spatial coordinate s, defined along the bulk advection direction, while the coefficients provide the profiles along the mutually-orthogonal directions $\boldsymbol{n} = (n_1, n_2)$ which are taken to be normal to the advection direction. PPOD is noted to have several interesting properties. First, PPOD targets correlations in s, t space and naturally captures advecting structures. As such, it is not necessary to do an *a priori* determination of disturbance advection speeds. Rather, such speeds are a natural output of the analysis and can vary in an arbitrary and dispersive manner along the s coordinate. Second, the modes can have an arbitrary time dependence, and need not be composed of a single fundamental frequency, so a broadband or multi-frequency disturbance can be described by a single mode. This can be an attractive property, as high Reynolds number flows generally have coherent advecting structures with a combination of narrowband fundamental and harmonic spectral features, as well as more spectrally distributed features. This arbitrary time dependence also allows PPOD to be applied to transient flow phenomena, since the method does not require the flow to be statistically stationary. Finally, the two-dimensional Fourier transform of the PPOD modes presents amplitudes in the $k - \omega$ plane, which provides a useful alternative way to summarise modal characteristics. For example, in cases where the PPOD mode is dominated by a structure with a narrowband spectral signature, the wavenumber-frequency spectrum can be compared with the dispersion relation from local linear hydrodynamic stability analysis and the transverse coefficients, $a_j(\boldsymbol{n})$, can be compared to the stability mode shapes. Thus, while space-only POD modes can be compared to the modes from a global linear stability analysis [24], a local linear stability analysis naturally lends itself to comparison with PPOD modes.

The objective of this paper is to further evaluate the PPOD technique and compare its results to space-only POD, emphasising the complementary and distinctive perspectives that the two approaches provide. In addition to basic characterisation of PPOD, key questions we wish to address include:

1. What are the dominant energetic structures in PPOD and how do they compare with space-only POD?

2. In cases where these dominant structures appear the same, how do the energy convergence

DISTRIBUTION A: Distribution approved for public release.

rates compare?

3. Due to nonlinearity, coherent structures generally consist of many disturbance frequencies with spatially-evolving spectral content and higher harmonics. How does PPOD decompose such multi-frequency content?

4. A given flow may consist of distinct structures which advect dispersively and at different phase speeds (e.g., the inner and outer shear layers of a co-axial or annular jet). How does PPOD decompose such different disturbances across modes?

This work consists of two major sections. First, section 5.2 presents the basic mathematical features of PPOD and highlights key differences compared to space-only POD. Then, section 5.3 presents three case studies, using data from high Reynolds number, advection-dominated flows including a reacting wake, a reacting swirling annular jet, and a non-reacting jet in cross flow.

5.2 Overview of Space-Only POD and PPOD Properties

5.2.1 Space-Only POD Properties

The implementation of space-only POD has been detailed by many authors [e.g. 5, 6, 7, 25], and this section briefly summarises key details in order to compare them to PPOD. The flow data, $\boldsymbol{q}(\boldsymbol{x}, t)$, are acquired at a number of discrete time instants over a set of discrete points in one, two, or three spatial dimensions. Here, we will assume for convenience that the data are obtained on a uniformly-spaced grid in a Cartesian coordinate system; more general situations will be addressed in 5.2.3. The mean-subtracted data at each time instant t_j are arranged as a column vector denoted $\boldsymbol{q}_j \in \mathbb{R}^{N_{\boldsymbol{x}}}$ which is then stacked alongside column vectors from other time instants to form the data matrix $\boldsymbol{Q} \in \mathbb{R}^{N_{\boldsymbol{x}} \times N_t}$. Here, $N_{\boldsymbol{x}}$ refers to the dimensionality of each observation which equals the number of spatial grid points multiplied by the number of variables considered at each grid point, and N_t is the number of temporal observations. The space-only POD modes are the eigenvectors of the spatial covariance matrix $\boldsymbol{C}_{\boldsymbol{x}} = \boldsymbol{Q}\boldsymbol{Q}^{\mathrm{T}} \in \mathbb{R}^{N_{\boldsymbol{x}} \times N_{\boldsymbol{x}}}$ (excluding the factor $1/N_t$ in the covariance definition). When the spatial dimensionality of an observation is much larger than the number of temporal observations (i.e. $N_{\boldsymbol{x}} \gg N_t$), it is computationally less expensive to obtain the space-only POD modes from a method commonly referred to as snapshot POD. Snapshot POD was introduced by Sirovich [26] and utilises the temporal covariance matrix $\boldsymbol{C}_t = \boldsymbol{Q}^{\mathrm{T}}\boldsymbol{Q} \in \mathbb{R}^{N_t \times N_t}$. Assuming a linearly independent set of observations, the rank of the space-only POD problem is governed by $\min(N_{\boldsymbol{x}}, N_t)$. The reader is referred to Taira et al. [5] and Holmes et al. [7] for more information on the spatial versus temporal eigenvalue problems and their connection to the SVD.

This work utilises an economy sized SVD of the data matrix $\boldsymbol{Q}$, computed using a direct algorithm, which provides M spatially orthogonal modes, where M is equal to the number of temporal snapshots (N_t) used for the decomposition (equivalent to snapshot POD). Associated with each space-only POD mode $\boldsymbol{\phi}_j(\boldsymbol{x})$ is an eigenvalue λ_j (related to the singular values σ_j from the SVD via $\lambda_j = \sigma_j^2$) and a time coefficient $a_j(t) = \boldsymbol{Q}^{\mathrm{T}}\boldsymbol{\phi}_j(\boldsymbol{x})$. The modes are ordered according to their eigenvalues via $\lambda_1 \geq \lambda_2 \geq \ldots \geq \lambda_M \geq 0$, where each eigenvalue λ_j is equal to the projected variance of the input data onto mode $\boldsymbol{\phi}_j(\boldsymbol{x})$. The projection operation is defined according to the standard inner product, which constitutes a sum over the spatial domain. This provides the energy-based ranking referred to in section 5.1, where it was remarked that the projected variance λ_j is proportional to the average turbulent kinetic energy in mode $\boldsymbol{\phi}_j(\boldsymbol{x})$ when the input data consists of mean-subtracted, constant-density velocity fields. This work utilises cumulative percent energy, $E_c(m)$, which is the sum of the energy of modes 1 through m as a fraction of the energy summed over all modes M, as a measure of convergence for the POD basis:

$$E_c(m) = 100 \times \left(\frac{\sum_{j=1}^{m} \lambda_j}{\sum_{j=1}^{M} \lambda_j} \right) \tag{5.5}$$

5.2.2 PPOD Properties

With this background, we next consider PPOD in more detail. PPOD is formulated by describing space in terms of $\boldsymbol{x} = (s, \boldsymbol{n})$ coordinates, where the s coordinate is taken along the bulk advection

DISTRIBUTION A: Distribution approved for public release.

direction in curvilinear space, and $\boldsymbol{n} = (n_1, n_2)$ are defined along mutually-orthogonal directions normal to it. This provides a decomposition of $\boldsymbol{q}'(\boldsymbol{x}, t)$ according to:

$$\boldsymbol{q}'(\boldsymbol{x}, t) = \sum_j a_j(\boldsymbol{n})\, \boldsymbol{\phi}_j(s, t)\,, \tag{5.6}$$

where $a_j(\boldsymbol{n})$ are the transverse coefficients and $\boldsymbol{\phi}_j(s, t)$ are the orthogonal modes. Utilising the discrete space-time form of the data $\boldsymbol{q}(\boldsymbol{x}, t)$ centred by the temporal mean, the s, t data at each normal location n_j is formed into a column vector $\boldsymbol{p}_j \in \mathbb{R}^{(N_s \times N_t) \times 1}$ and stacked side by side to form the data matrix $\boldsymbol{P} \in \mathbb{R}^{(N_s \times N_t) \times N_{\boldsymbol{n}}}$, where N_s is the dimensionality in the s coordinate (the number of grid points times the number of variables considered at each grid point) and $N_{\boldsymbol{n}}$ refers to the number of total grid points in $\boldsymbol{n}$. Hence, the data matrix $\boldsymbol{P}$ is constructed from a "snapshot" sequence in the spatial directions $\boldsymbol{n}$. In the case where the data are derived from a uniform Cartesian grid and where s is aligned with one of the coordinate directions, $\boldsymbol{P}$ can easily be obtained from a simple permutation of $\boldsymbol{Q}$. The PPOD eigenvalue problem is derived using a variational argument (similar to the derivations detailed by Bishop [9] and Holmes et al. [7]), where the variance of the input data is maximised as it is projected onto subsequent orthogonal directions, in this case in the s, t space. This provides a set of orthogonal modes, $\boldsymbol{\phi}_j(s, t)$, which are the eigenvectors of the s, t covariance matrix, $\boldsymbol{C}_{s,t} = \boldsymbol{P}\boldsymbol{P}^{\mathrm{T}} \in \mathbb{R}^{(N_s \times N_t) \times (N_s \times N_t)}$. When $N_s \times N_t \gg N_{\boldsymbol{n}}$, which is often the case for experimental data, it is computationally less expensive to obtain the PPOD modes from the $\boldsymbol{n}$ covariance matrix $\boldsymbol{C}_{\boldsymbol{n}} = \boldsymbol{P}^{\mathrm{T}}\boldsymbol{P} \in \mathbb{R}^{N_{\boldsymbol{n}} \times N_{\boldsymbol{n}}}$, i.e. the PPOD equivalent of snapshot POD. Assuming the "snapshots" in $\boldsymbol{n}$ are linearly independent, the rank of the PPOD problem is governed by $\min(N_s \times N_t, N_{\boldsymbol{n}})$.

The PPOD modes in this work are calculated using an economy sized SVD of the data matrix $\boldsymbol{P}$, the same direct method as for space-only POD, which provides M' orthogonal modes, where M' is equal to the number of normal locations ($N_{\boldsymbol{n}}$) used for the decomposition. Associated with each PPOD mode $\boldsymbol{\phi}_j(s, t)$ is a corresponding eigenvalue λ_j and normal coefficient $a_j(\boldsymbol{n}) = \boldsymbol{P}^{\mathrm{T}}\boldsymbol{\phi}_j(s, t)$. PPOD provides an optimal description of the input data, where the PPOD modes are ordered according to their eigenvalues, $\lambda_1 \geq \lambda_2 \geq \ldots \geq \lambda_{M'} \geq 0$, and the eigenvalue λ_j is equal to the projected variance of the input data onto mode $\boldsymbol{\phi}_j(s, t)$. The standard inner product for the PPOD projection operation constitutes a sum over the s, t domain, rather than a sum over the spatial domain as for space-only POD. In the case of mean-subtracted velocity data, the PPOD eigenvalues are proportional to the turbulent kinetic energy density (an intrinsic property) summed over s and t. The implications due to the different inner products, and hence, the different energy-based rankings associated with PPOD and space-only POD are discussed further in the context of a simple model problem in section 5.2.4 as well as in the high Reynolds number data sets in section 5.3. The convergence behaviour of PPOD is evaluated in a similar manner to equation (5.5), where the sum of the first m eigenvalues is divided by the sum of all the eigenvalues, 1 through M'. We will refer to the convergence behaviour and the ordering of both PPOD and space-only POD modes as being based on the flow "energy", keeping in mind that the "energy" metrics for PPOD and space-only POD are different and that a physical energy ranking based on the turbulent kinetic energy only applies to space-only POD performed on mean-subtracted, constant-density velocity data.

5.2.3 Coordinate Transformations

Since PPOD is formulated in a curvilinear orthogonal coordinate system where s is defined along the bulk advection direction, a coordinate transformation is often required before performing the decomposition. For example, when the bulk advection direction does not coincide with one of the coordinates in which the data are acquired, a transformation to curvilinear coordinates is necessary for optimal PPOD convergence characteristics, as demonstrated in section 5.2.4. To enable back-to-back comparison of PPOD and space-only POD results in the curvilinear orthogonal coordinate system (as utilised for Case 3, section 5.3.3), the space-only POD calculation must be appropriately weighted. Since we choose to formulate space-only POD in a uniformly-spaced Cartesian coordinate system (motivated by the physical energy interpretation of its spatial inner product), but perform the calculation in the $s, \boldsymbol{n}$ coordinate system, the spatial inner product must be weighted by the Jacobian determinant of the coordinate transformation to preserve the physical turbulent kinetic energy ranking of the space-only POD basis. In contrast, PPOD is defined based on the s, t inner product, which does not require any weighting for interpretation in uniformly-sampled $s, \boldsymbol{n}, t$ spaces. In the rest of this paper, we will consider data from planar measurements such that only two-dimensional (i.e. $\boldsymbol{x} = (s, n)$) coordinates are necessary. Furthermore, planar

DISTRIBUTION A: Distribution approved for public release.

three-component velocity data in curvilinear orthogonal form are denoted u_s, u_n, u_z, where u_z is the out-of-plane component.

A second set of coordinate transformation considerations arise when considering planar data through systems with other symmetries. For example, consider the transverse velocity component associated with planar data acquired through the centre of a round jet [as in, e.g. 27]. In a cylindrical coordinate system, radial velocity components directed away from the centreline are positive. These radial velocity components will have the same/opposite sign as the corresponding transverse velocity in a Cartesian coordinate system above/below the centreline, respectively. The same is true for the out-of-plane velocity component, which corresponds to an azimuthal velocity in cylindrical coordinates. This is important, as PPOD will decompose a velocity disturbance with azimuthal symmetry given by $\exp(\mathrm{i}m_\theta\theta)$ differently in these two coordinate systems. In the cylindrical coordinate system, the three velocity components (u_x, u_r, u_θ) have consistent symmetries across the centreline (i.e. at $\theta = 0$ or $\theta = \pi$). More specifically, the cylindrical velocity components all have even symmetry for even m_θ, and odd symmetry for odd m_θ. In contrast, in Cartesian form, the different velocity components have different symmetries. Thus, if a helical disturbance were considered in Cartesian coordinates, its disparate symmetries would necessarily be split between different PPOD modes despite representing a single disturbance.

Appropriate symmetries are achieved by simply reversing the sign of the transverse and out-of-plane velocity components below the jet centreline. The sign convention is consistent with that of a cylindrical coordinate system, but the velocity components are not scaled by a change in volume since the measurement plane, and hence the cell size associated with the measurement resolution, is constant. This coordinate system is therefore referred to as "locally cylindrical" in the rest of the paper.

It should also be noted that the locally cylindrical coordinate transformation can provide appropriate symmetries for non-axisymmetric flows. As in the JICF case study in section 5.3.3, where velocity data acquired in a plane through the jet and aligned in the direction of the crossflow are analysed, a sign convention corresponding to a cylindrical coordinate system provides consistent symmetries for capturing windward and leeward shear layer structures. If these structures appear in a symmetric (asymmetric) configuration across the jet centreline, the three velocity components associated with the shear layer rollup will all be symmetric (respectively, asymmetric) in locally cylindrical form, while the velocity components in a Cartesian coordinate system will have mixed symmetries (the axial component will have the opposite symmetry across the jet centreline compared to the transverse and out-of-plane components). Hence, all vector data are subject to the locally cylindrical transformation, and the velocity components do not carry the above noted subscripts (x, r, θ) when also transformed into curvilinear orthogonal form (applicable to the JICF velocity data in section 5.3.3).

5.2.4 Model Problem with Advecting Structures

This section compares the convergence characteristics of PPOD and space-only POD for a synthetic data set with advecting structures. To clearly illustrate key features of PPOD, consider a time series of linearly independent scalar data sampled uniformly in the two-dimensional plane s, n, which corresponds to a Cartesian plane where $N_{\boldsymbol{x}} = N_s \times N_n = 25 \times 25$. The number of temporal snapshots is chosen such that it equals the number of spatial points in n, i.e. $N_t = N_n = 25$, which governs the rank of the space-only POD and PPOD eigenvalue problems via $N_t < N_{\boldsymbol{x}}$ and $N_n < N_s \times N_t$, respectively. Hence, both methods provide the same number of modes ($M = M' = 25$), making comparisons of the convergence characteristics straightforward. The mean-subtracted scalar fields consist of a train of high intensity 5×5 pixel squares with a wavelength of $\lambda_s = 10$ pixels advecting across the domain at an angle α with respect to the s-axis. To emulate turbulent flow data and prevent rank deficiencies, these advecting structures are superimposed onto a background of low intensity noise sampled from a uniform distribution with ±20% relative amplitude. Additionally, the centre locations of the high intensity squares are randomly perturbed in order to simulate "phase jitter" effects [28]. These perturbations correspond to spatial shifts of ±1.75 pixels in both s and n. To illustrate, three consecutive temporal snapshots of the disturbance scalar fields are displayed in figure 5.1, where the advecting structures travel along the nominal trajectory indicated by the red dotted line oriented at an angle α with respect to the s coordinate axis. The black dotted outlines surrounding the advecting structures indicate their maximum allowable spatial variation due to phase noise.

It should be emphasised that this model problem is constructed such that two temporal snapshots exactly capture one period of advection, i.e. the sampling frequency is two times the frequency

DISTRIBUTION A: Distribution approved for public release.

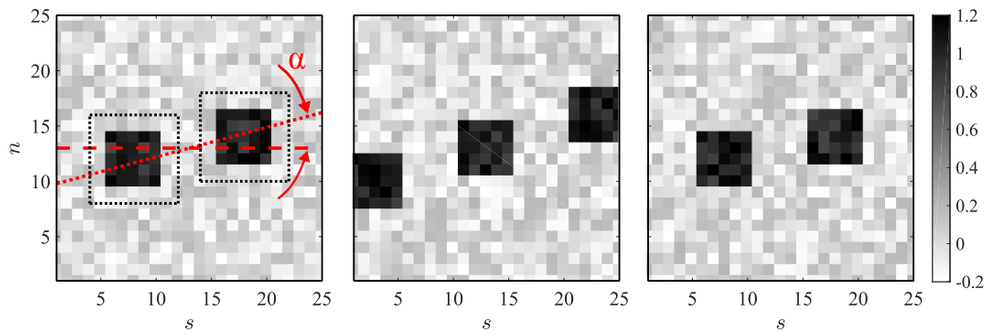

Figure 5.1: Three consecutive temporal snapshots of mean-subtracted scalar fields containing advecting, high-intensity squares, superimposed onto a noisy background. The advecting structures travel along the nominal trajectory indicated by the red dotted line, oriented at an angle α with respect to the red dashed line parallel to s. The black dotted outlines surrounding the advecting structures indicate their maximum allowable spatial variation due to phase noise.

of these structures, and the s-domain fits 2.5 structures ($s/\lambda_s = 2.5$). In the case of no phase noise, this means that the data is sampled/generated such that the advecting structures are captured in only two distinct spatial configurations as they travel through the domain, and the time series consists of repetitions of these two configurations. Intuitively, space-only POD captures the train of advecting structures with two high energy modes, while the random background noise is relegated to the remaining 23 low energy modes. This rank-2 representation of the advecting structures demonstrates that space-only POD can capture certain translations very efficiently (similar to the example of a harmonic travelling wave discussed in the introduction (e.g. equation (5.3)), which is also described by two space-only modes).

However, translating structures generally are not captured by such a small set of modes, as noted previously. For example, if the data are sampled/generated such that the square structures are captured at many different streamwise locations as they travel through the domain (e.g. if the sampling frequency is increased), the rank of the space-only POD representation of these structures will increase. This can be considered an artificial rank inflation which is strictly due to the translation since critical features no longer appear in the same spatial location from time to time. This decreases the correlation and the variance is redistributed from a few leading, high energy modes to many lower energy modes. Whether space-only POD provides a low or high rank representation of advecting structures depends on the underlying functional form of the data (i.e. sinusoidal, square, Gaussian, etc.), and the sampling frequency relative to the frequency of the advecting structures. PPOD, on the other hand, captures the advecting structures in these cases with a single high energy mode (assuming that the structure(s) travel along s). The objective of the data permutation associated with PPOD is to align critical features, whether periodic or non-periodic, such that they occur at constant n. As long as the critical features appear in the same s, t locations across "normal" snapshots, PPOD provides a rank-1 representation of the advecting structures. This is similar to the ability of space-only POD to provide a rank-1 representation of a spatially stationary structure [11].

The following paragraphs demonstrate the effects of phase noise and alignment of the nominal advection trajectory with the s-axis, which can be explained using intuition from the previous discussion. Calculations are performed on data sets with ten different values of α, from 0° to 45°. To ensure a statistical representation of the convergence behaviour at each angle, 100 data sets with 25 temporal snapshots each, are generated with randomly assigned phase and background noise, as specified above. Space-only POD and PPOD are performed on each of these 100 model data sets, and the results (i.e. the eigenvalues) at each α are averaged. The averaged cumulative percent energy as a function of mode number is shown in figure 5.2(a). Consider first the case where the nominal advection trajectory is perfectly aligned with s (i.e. $\alpha = 0°$). As expected from our previous discussion, PPOD displays a significantly higher convergence rate than space-only POD, since the advecting structures are mostly (apart from the random displacement caused by the normal phase noise) aligned in n. The first PPOD mode captures $\sim 70\%$ of the energy, while four space-only POD modes are required to capture the same amount. For a complete representation of the advecting structures, $E_c \sim 90\%$ is required, which is captured by the first four PPOD modes and the first 12 space-only POD modes. This can be compared to the one PPOD mode and two space-only POD modes required to capture these structures in the case of no phase noise and $\alpha = 0°$.

DISTRIBUTION A: Distribution approved for public release.

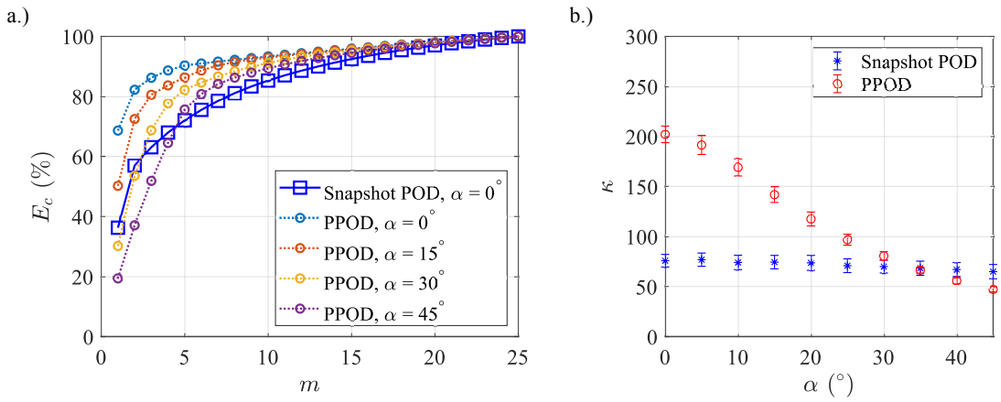

Figure 5.2: Dependence of (a) cumulative percent energy, E_c, as a function of the number of modes, m, and (b) condition number, κ, as a function of the angle, α, between the nominal advection trajectory and s. The error bars in (b) represent the variability in κ due to the random background noise and phase jitter displaying one standard deviation

Hence, the phase noise causes a 4× versus 6× increase in the number of modes required to capture the advecting information for PPOD and space-only POD, respectively. This demonstrates that the convergence behaviour of PPOD is less sensitive to phase noise than space-only POD, since the convergence of PPOD is only affected by the phase noise in the normal direction, while space-only POD is sensitive to the phase noise in both the normal and streamwise directions, consistent with the discussion in the previous paragraph.

Next, consider the effect of α. The convergence characteristics of PPOD are a strong function of the alignment of the advecting structures with respect to s. This is demonstrated in figure 5.2(a), where the energy of the leading mode decreases as α increases, and a larger number of modes is required to capture the advecting structures (i.e. reach 90% E_c). This increase in rank for increasing α occurs since the advecting structures are no longer perfectly aligned between "normal" snapshots, consistent with previous discussions. The convergence characteristics of space-only POD, on the other hand, are independent of α since the advecting structures appear in two distinct spatial configurations through time for each α.

To clearly visualise each method's convergence rate as a function of α, we use the condition number κ, defined as the ratio of the largest to the smallest eigenvalue. As mentioned previously, economy sized SVD's of the data matrices $\boldsymbol{Q}$ and $\boldsymbol{P}$ (which correspond to the eigenvalue problems of the temporal covariance matrix $\boldsymbol{C}_t$ and the normal covariance matrix $\boldsymbol{C}_n$) are used to compute all eigenvalues for space-only POD and PPOD, respectively. Since $N_t = N_s = N_n = 25$ for this model problem, $N_t < N_{\boldsymbol{x}}$ and $N_n < N_s \times N_t$, and the economy sized SVD's provide nonzero eigenvalues for both methods. Under such conditions, κ can be used as a measure of each decomposition's convergence rate, where a large κ indicates fast convergence. The averaged κ as a function of α is shown in figure 5.2(b), where the error bars indicate one standard deviation over the 100 data sets used for the calculation at each α. Figure 5.2(b) quantifies the slower convergence of PPOD as α increases and shows that the convergence rate of PPOD is higher than that of space-only POD below a certain α. For the specified phase noise, PPOD has a faster convergence rate when $\alpha \lesssim 30°$.

To summarise, this model problem demonstrates that PPOD achieves the highest possible convergence rates when it is performed in a coordinate system aligned with the bulk direction of advecting disturbances, i.e. $\alpha = 0°$. It also shows that PPOD achieves favorable convergence rates compared to space-only POD as long as α is sufficiently small. Realistic examples with small α, where the data are acquired in coordinate systems which are closely aligned with the direction of the advecting structures, are considered in sections 5.3.1 and 5.3.2. On the other hand, if α is large due to a misalignment between the measurement plane and the s, n coordinates, a spatial transformation can be performed to improve the PPOD convergence rate. Such a transformation is implemented in section 5.3.3.

5.3 Case Studies

This section contains three case studies, using scalar and velocity data from three different turbulent, shear flow experiments. Case 1 uses chemiluminescence data from a forced reacting wake flow with advecting shear layer structures with symmetric and asymmetric features. These data sets

DISTRIBUTION A: Distribution approved for public release.

Case	U_{lip} (m/s)	$\rho_{\text{u}}/\rho_{\text{b}}$
1A	26	7
1B	32	2.5
1C	39	1.7

Table 5.1: Test conditions for the bluff body cases.

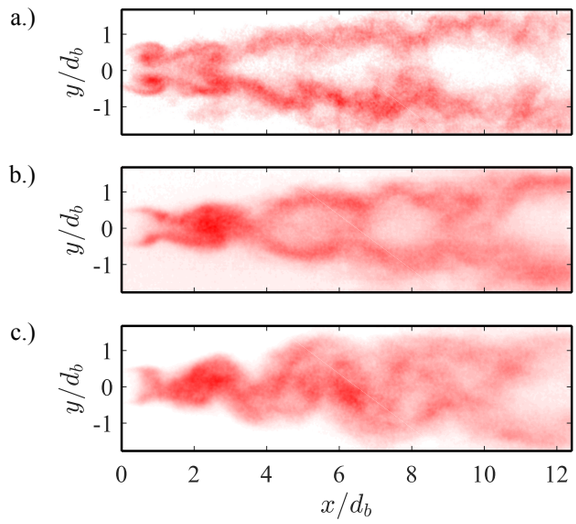

Figure 5.3: Instantaneous flame images of normalised CH* chemiluminescence for three different density ratios: case 1A, $\rho_{\text{u}}/\rho_{\text{b}} = 7$ (a), case 1B, $\rho_{\text{u}}/\rho_{\text{b}} = 2.5$ (b), and case 1C, $\rho_{\text{u}}/\rho_{\text{b}} = 1.7$ (c)

were used as they contain different transverse flow symmetries, as well as sharp spatial variation in the flame luminosity, and so require multiple wavenumbers in spectral space to decompose these spatial patterns. In addition, periodic disturbances manifest themselves as a number of spectrally concentrated temporal harmonics in flame luminosity at a given point. As such, this case illustrates how PPOD decomposes a single structure with many constituent frequencies. Case 2 uses planar, three-component velocity data from a reacting, swirl-stabilised flow. High Reynolds number swirl flows have significant amounts of strong helical disturbances and phase jitter (i.e., phase noise) in the space-time characteristics of their coherent structures. A common feature of Cases 1 and 2 are that the leading snapshot POD and PPOD modes capture similar information. In these cases, our analysis primarily considers the differences in their convergence rates, as well as fidelity in reconstructing spatial and temporal features. Case 3 is a JICF and the high energy snapshot POD and PPOD modes capture qualitatively different information, providing additional insights into the differences between the two approaches.

5.3.1 Case 1 – Scalar Imaging of a Forced, Reacting Wake Flow

This case study utilises CH* chemiluminescence data from a $Re_d \sim 10,000$, rectangular test section housing a flame stabilised by a nominally two-dimensional bluff body of width d_b, previously detailed by Emerson et al. [29] and Emerson and Lieuwen [30]. The data sets were acquired at a sampling frequency of 5 kHz, while subjected to axial acoustic forcing at a forcing frequency of $f_f = 515$ Hz. The bluff body lip velocity, U_{lip}, and the ratio of unburned to burned gas density, $\rho_{\text{u}}/\rho_{\text{b}}$, for each case are summarised in Table 5.1.

Combustion induced density stratification strongly affects the global stability characteristics, and associated mode shapes, of reacting wake flows. At high density ratios, represented by case 1A ($\rho_{\text{u}}/\rho_{\text{b}} = 7$), the flow is globally stable, but the axial forcing excites symmetric rollup of the convectively unstable shear layers, resulting in the symmetric flame wrinkling in figure 5.3(a). As the density ratio is decreased, the global wake mode is destabilised. Case 1B ($\rho_{\text{u}}/\rho_{\text{b}} = 2.5$) is an intermittent case; while the flow is still globally stable but convectively unstable, the flame wrinkling is intermittently symmetric and asymmetric due to the superposition of varicose forcing upon a sinuous global mode as seen in figure 5.3(b). At the density ratio of $\rho_{\text{u}}/\rho_{\text{b}} = 1.7$, case 1C, the flow is globally unstable and the flame shape displays the strong sinuous character of the underlying flow disturbances, see figure 5.3(c).

This case study is used to demonstrate PPOD on data sets dominated by coherent advecting

DISTRIBUTION A: Distribution approved for public release.

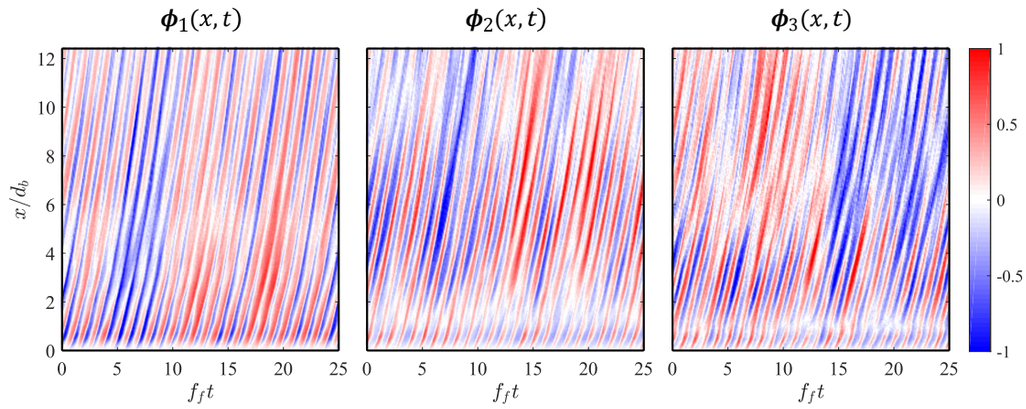

Figure 5.4: Space-time dependence of the first three PPOD modes, $\boldsymbol{\phi}_j\,(x,t)$, for case 1A.

structures with different symmetries. The primary focus of this section is the analysis of the high density ratio case (1A), while the lower density ratio cases (1B and 1C) will be used to highlight the different transverse symmetries of the flow.

Decompositions are performed on 1500 chemiluminescence snapshots from each of the three cases in Table 5.1. For these wake flows, the bulk advection direction above and below the bluff body centreline is defined along the trajectory of the maximum time-averaged intensity. The angle between each trajectory and the x-axis is small (approximately 5°), and PPOD is therefore performed on the data in Cartesian form (i.e. $(x, y) = (s, n)$), where the number of spatial grid points in x and y are 696 and 194, respectively. Since only one variable is considered at each grid point, $N_x = N_s = 696$, $N_y = N_n = 194$, and $N_{\boldsymbol{x}} = N_x \times N_y = 696 \times 194$. Snapshot POD produces $M = 1500$ modes (equal to the number of temporal snapshots, N_t) while PPOD produces $M' = 194$ modes (equal to the number of transverse locations, $N_y = N_n$).

First, the basic features of the PPOD modes, $\boldsymbol{\phi}_j\,(x,t)$, are considered. The first three most energetic modes for case 1A, corresponding to 65% of the energy, are presented in figure 5.4. The dominant features of these modes in x-t space form a roughly diagonal pattern, indicative of advecting flow structures propagating in the streamwise direction. Advection properties such as phase speed, wavenumber, and temporal frequency can be readily obtained from these modes. For example, it is apparent that the phase speed, which corresponds to the slope of the diagonal structures, increases as a function of streamwise distance, especially noticeable in the small x/d_b regions close to the bluff body. This is a gas expansion effect, reflecting the acceleration of the flow in the confined channel.

The PPOD coefficients, $a_j\,(y)$, describe the transverse structure of each mode. The profiles associated with the first three modes for case 1A are displayed in figure 5.5(a), from which it is apparent that the three dominant modes are all symmetric about the centreline. This is consistent with the strong varicose flame shape observed in figure 5.3, as symmetric vortex structures dominate the unsteady flow field. The transverse profiles associated with modes 1-3 for the lower density ratio cases, 1B and 1C, are shown in figure 5.5(b) and (c), respectively. For case 1C, where the flame exhibits a strong sinuous character, the transverse profiles corresponding to the first three modes are all asymmetric. For case 1B, the intermittent case, which exhibits a superposition of varicose and sinuous disturbance features, the profiles corresponding to the first two modes are symmetric, while the profile of the third mode is asymmetric. Although not plotted, the first two symmetric modes of case 1B contain 45% and 15% of the total energy, respectively, and the third asymmetric mode contains 10%.

Alternative visualisations of the PPOD modes can be obtained by considering the spatial evolution of the temporal Fourier transform or the spatio-temporal Fourier transform, denoted as $\hat{\boldsymbol{\phi}}_j\,(x,f)$ and $\hat{\boldsymbol{\phi}}_j\,(k,f)$, respectively. Here, we use f instead of $\omega = 2\pi f$ such that the frequency represents a Strouhal number. First, consider the temporal Fourier transform of the spatio-temporal mode, $\hat{\boldsymbol{\phi}}_j\,(x,f)$, shown in figure 5.6(a) for case 1A. This plot shows that the first mode is dominated by spectral content at the forcing frequency, but also clear spectral content at the first three harmonics. In other words, these lower amplitude, higher frequency harmonics are all superimposed into this first mode, rather than being divided out into other modes. As shown later, the snapshot POD analysis separates these higher order temporal harmonics into lower energy modes.

Performing an additional Fourier transform in the streamwise direction renders the modal structure as a function of frequency and axial wavenumber, k, which is shown in figure 6(b). The

DISTRIBUTION A: Distribution approved for public release.

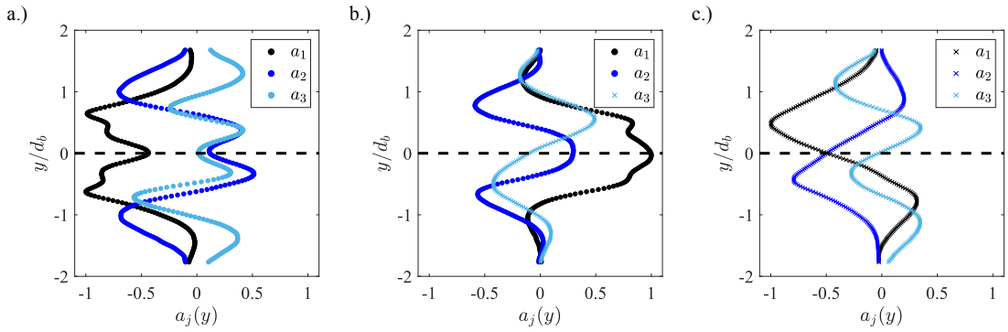

Figure 5.5: Transverse profiles, $a_j(y)$, corresponding to the first three PPOD modes for case 1A (a), case 1B (b), and case 1C (c). Circles indicate symmetric profiles and crosses indicate asymmetric profiles.

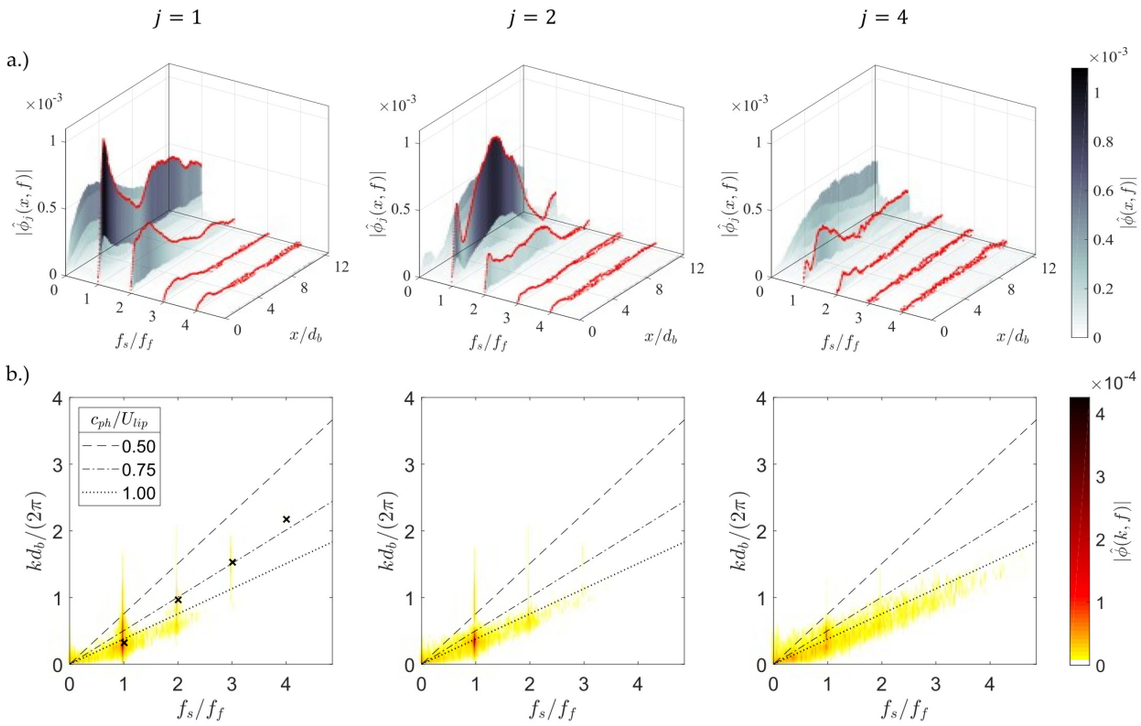

Figure 5.6: Fourier reductions of PPOD modes 1, 2, and 4 for case 1A; (a) shows amplitude of $\hat{\boldsymbol{\phi}}_j(x,f)$ as a function of frequency and streamwise position, where the red profiles represent the streamwise dependence of the amplitude at the forcing frequency and the harmonics, and (b) shows the amplitude of $\hat{\boldsymbol{\phi}}_j(k,f)$ as a function of frequency and streamwise wavenumber. The black lines indicate constant phase speed, while the black x's (mode 1) indicate the maximum amplitude at the forcing frequency and its harmonics.

DISTRIBUTION A: Distribution approved for public release.

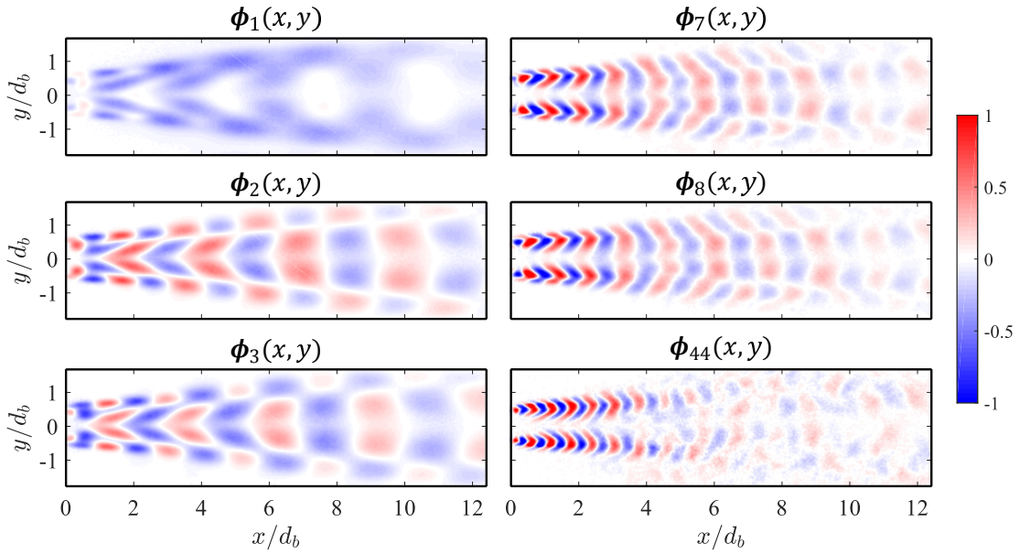

Figure 5.7: Snapshot POD modes, $\phi_j\,(x,y)$, for case 1A, where the colours represent regions of high (red) and low (blue) chemiluminescence.

black lines of constant slope correspond to lines of constant phase velocity, c_{ph}. It is apparent that the energy of the first mode is concentrated in a structure that is oscillating at the forcing frequency and advecting at a speed just above the lip velocity. It is noteworthy that the external excitation forces oscillations at the forcing frequency and its harmonics, which exhibit weakly dispersive behaviour. This is particularly apparent for mode 1 (and 5), where the peak amplitude at the fundamental frequency and its harmonics are indicated by black x's for clarity. For lower energy modes, which contain more information on higher degree of freedom turbulent motions than coherent advecting disturbances, spectral information is spread more broadly across the constant-speed line rather than clustered at the forcing frequency and harmonics, as demonstrated by mode 4.

We next provide a comparative analysis of the snapshot POD results for case 1A. Figure 5.7 presents the spatial modes, $\boldsymbol{\phi}_j\,(x,y)$, and the Fourier transform of the associated time coefficients, $\hat{a}_j\,(f)$, are shown in figure 5.8(a). Mode 1 seems to describe the inherent spatial phase variation in the disturbance characteristics at $f_s/f_f = 1$; i.e., spatial variability in the flame wrinkling at the same phase in subsequent cycles. Modes 2 and 3, which together contain approximately 33% of the energy, display the same spatial pattern shifted axially by a quarter-wave relative to one another, and their temporal frequency spectra both display a distinct peak at the forcing frequency, $f_s/f_f = 1$, indicating the same temporal evolution of these two modes. Modes 2 and 3 constitute the first advecting mode pair. Similarly, modes 7 and 8, which together contain approximately 2.7% of the energy, form a second advecting mode pair associated with a first harmonic frequency as indicated by the distinct peak at $f_s/f_f = 2$. Consistent with equation (5.3), the mode pairs (2,3) and (7,8) independently represent standing wave structures but superimpose in space and time to represent an advecting structure. The clear correlation between these modes is illustrated by the phase portrait in figure 5.8(b), which plots the relationship between the time coefficients of modes 2, 3 and 7. The (2,3) superposition captures the symmetric flame wrinkling throughout the domain, from the rollup immediately after the bluff body followed by the growth of these spatial features as they advect downstream. The (7,8) mode pair captures shorter length-scale advecting information, which provides the finer details of the flame rollup close to the bluff body (primarily in the region $x/d_b < 4$). Furthermore, second and third harmonics can also be identified; mode 44 (containing 0.2% of the energy) and mode 142 (with 0.048% of the energy) correspond to the peak amplitude at $f_s/f_f = 3$ and $f_s/f_f = 4$, respectively. As the order of the harmonic increases, the length scale associated with the coherent flame structures decreases, while the region in which they are coherent shifts closer to the bluff body. In comparison, note that spectral information at the forcing frequency and the harmonics were contained in the first PPOD mode (see figure 5.6). However, the information captured by this PPOD mode is not identical to the information captured by the combination of space-only POD modes in figure 5.7. Rather, they capture similar physical flow features, and should be considered approximate qualitative comparisons.

The snapshot POD results for the lower density ratio cases (1B and 1C) are similar to the ones just discussed. Both cases have a high energy advecting mode pair associated with the fundamental frequency, followed by a second advecting mode pair associated with the first harmonic. The primary difference between the three data sets are the spatial patterns associated with the advecting

DISTRIBUTION A: Distribution approved for public release.

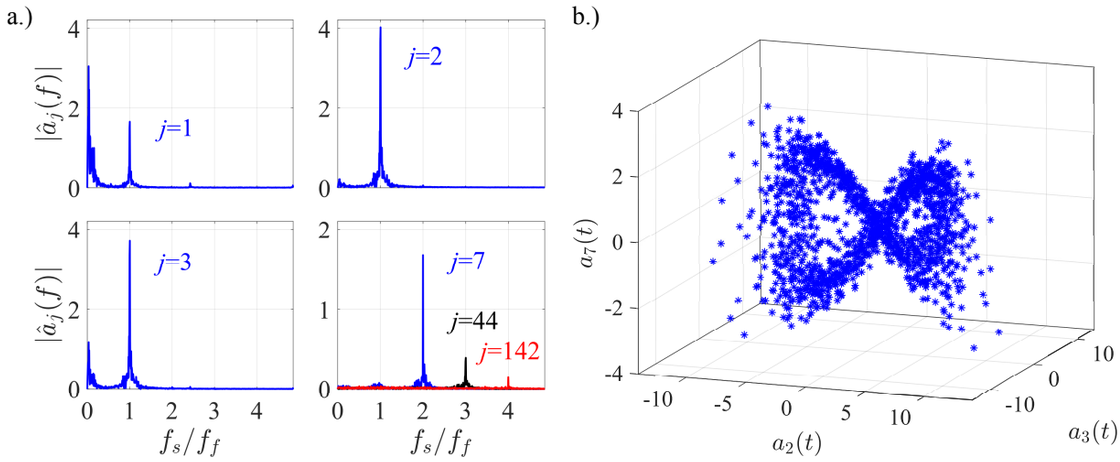

Figure 5.8: Fourier transform representation of the time coefficients, $\hat{a}_j\,(f)$, from snapshot POD for case 1A (a), where the spectra for mode 8 is very similar to the one corresponding to mode 7. Additionally, (b) contains the phase portrait of the time coefficients corresponding to modes 2, 3 and 7.

mode pairs, which reflect the different symmetries (as discussed previously in the context of figure 5.3) due to the difference in density ratio, and hence, stability characteristics.

We next compare the convergence characteristics, as well as the nature of the space-time reconstructions for snapshot POD and PPOD. Recall that the convergence according to equation (5.5) is a measure of the cumulative percent energy, or variance, in the data, and the low-order reconstructions according to equation (5.2) provide maximum variance/minimum mean squared error approximations of the given flow. Of course, it should be emphasised that these are not true comparisons, as the energy metrics of space-only POD and PPOD are different. However, as long as this caveat is kept in mind, it is still interesting to consider the convergence rates of each method and to plot them together to compare the number of modes required to capture a certain fraction of each one's energy metric. When evaluating the convergence rates, note that experimental flow data commonly consists of many temporal snapshots, N_t, while the spatial resolution is coarser (i.e. small N_y). Under such conditions, when $N_y \ll N_t$ the number of PPOD modes, M', is much smaller than the number of snapshot POD modes, M, i.e. $M' \ll M$. With this in mind, consider figure 5.9, which shows cumulative percent energy, E_c, as a function of the number of modes, m, for snapshot POD and PPOD. Using all the temporal snapshots for the comparison (i.e., $N_t = 1500$), it is clear that fewer PPOD modes are required to capture a specific percentage of the energy as compared to snapshot POD. This is especially apparent among the high energy modes. However, the total number of PPOD modes is much smaller as compared to the total number of snapshot POD modes due to $N_y \ll N_t$.

To gain more insight, consider the difference in rank between the two methods. For the reacting wake data sets, $N_t < N_x \times N_y$ and $N_y < N_x \times N_t$. Hence, N_t and N_y govern the rank of the snapshot POD and PPOD problems, respectively, and additionally $N_y < N_x$. Therefore, if the number of temporal snapshots used for the decompositions is reduced, the rank of the snapshot POD problem (N_t) will decrease, while the rank of the PPOD problem (N_y) is unaffected. To demonstrate, we have recomputed the results shown in figure 5.9 as the number of temporal snapshots is reduced from 1500 to 194, such that $N_y = N_t$ and $M' = M$. Here, the large reduction in temporal snapshots noticeably alters the snapshot POD convergence behaviour due to the change in rank (notice the deviation near $m \sim 10$), and since $N_t = 194$ is no longer a sufficient number of temporal snapshots for a statistical representation of this particular flow. The convergence behaviour of PPOD, on the other hand, is not affected by the reduction in the number of temporal snapshots, since the rank of the PPOD eigenvalue problem is unaffected and its convergence behavior is tied to the resolution and number of snapshots in the normal direction, rather then in time. Additionally, it should be noted that a change in rank does not necessarily impact convergence. For example, the effect of adding or removing snapshots is negligible if such changes only affect the near-zero eigenvalues, as would be the case for a converged statistically stationary flow.

A more direct way to compare the leading snapshot POD and PPOD modes is to evaluate their truncated space-time reconstructions calculated according to equation (5.2). Figure 5.10 shows three instantaneous chemiluminescence fields from the original time series (case 1A) (a), and the corresponding reconstructed ones based on modes 1-3 for snapshot POD (b) and PPOD (c), which accounts for $\sim$ 52% and 62% of the energy, respectively. The three instantaneous snapshots in

DISTRIBUTION A: Distribution approved for public release.

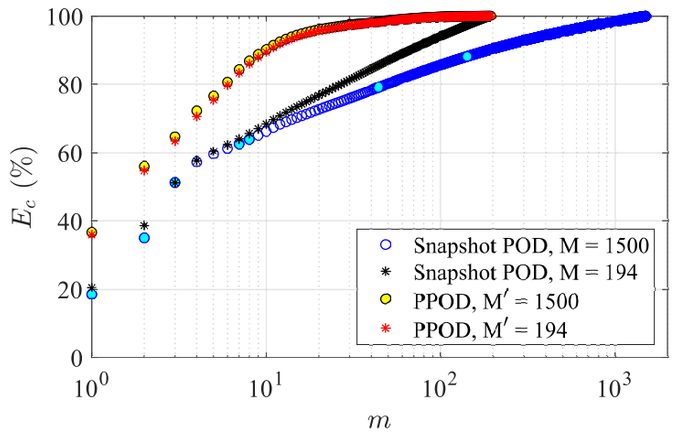

Figure 5.9: Cumulative percent energy, E_c, as a function of the number of modes, m, for snapshot POD and PPOD for case 1A. The light blue filled circles for snapshot POD ($M = 1500$) correspond to modes 1-3, 7, 8, 44 and 142 associated with the train of advecting flame wrinkles.

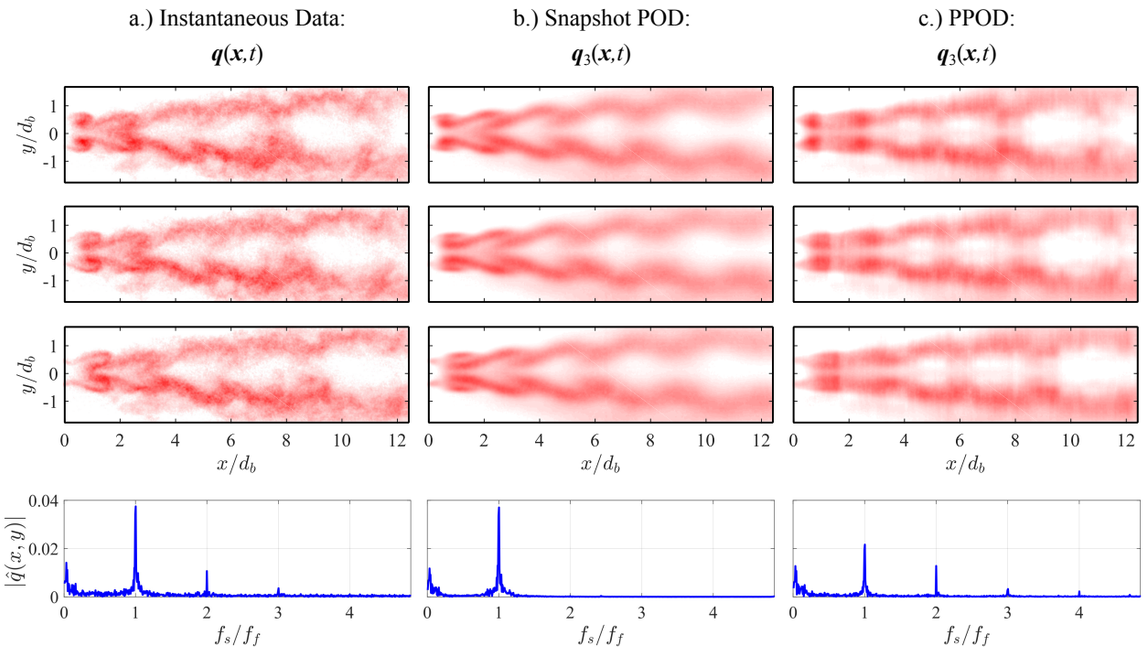

Figure 5.10: Three instantaneous chemiluminescence images (a) and the corresponding reconstructed fields based on modes 1-3 for snapshot POD (b), and PPOD (c), together with the frequency spectra for each time series.

figure 5.10 provide a typical representation of the instantaneous flow, and a visual comparison between these snapshots and the reconstructions can be used to qualitatively evaluate the types of flow structures that space-only POD and PPOD capture in their respective high energy modes. Additionally, the frequency spectra for each time series is included, calculated in the shear layer at $(x/d_b, y/d_b) = (2, 0.5)$. While the reconstructions from both snapshot POD and PPOD provide reasonable overall representations of the flame rollup, including both accurate symmetry and dominant length scale information, the primary difference between these results are observed in the fine scale spatial patterns and frequency spectra. While the spectrum of the reconstructed snapshot POD data displays a single, distinct peak at the forcing frequency, the PPOD spectrum contains information at the first four harmonics. In contrast, the fine scale spatial features, particularly near the first flame rollup region, are much better resolved in snapshot POD. These different results arise from the two different inner products used for maximising the variance as discussed in section 5.2 and provide insights into the differences in the two approaches for reduced-basis descriptions of the data.

5.3.2 Case 2 – Velocity Fields from a Reacting Swirling Annular Jet

This section considers three-component velocity data acquired in the centre plane of a high Reynolds number swirling flow. Notable features in the flow include vortex breakdown, shear layer structures,

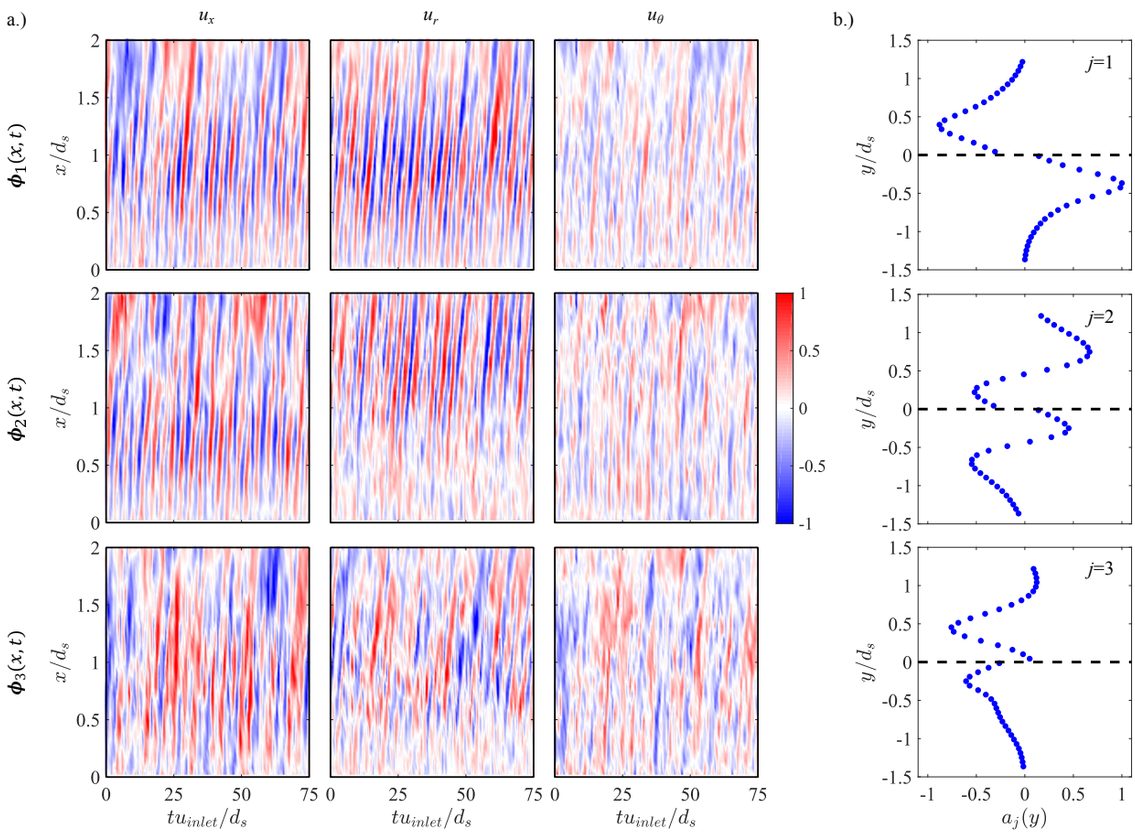

Figure 5.11: Space-time dependence of the first three PPOD modes, $\boldsymbol{\phi}_j\,(x,t)$, for case 2 (a), together with the corresponding transverse coefficient, $a_j\,(y)$, for each mode (b).

much more rapid spatial de-correlation of these structures, and significant levels of phase noise. Full details of the facility, optical setup, and particle image velocimetry (PIV) data processing approaches are presented in Rock et al. [31] and Chterev et al. [32]. The data set in this section was acquired at a combustor pressure of 3.6 bar, a preheat temperature of 445 K, an equivalence ratio of 0.36, and an air inlet velocity of 65 m/s using a liquid fuel (C5 [33, 31]) injected using a generic pressure atomizer. The nozzle exit diameter is denoted as d_s. Stereo-PIV measurements were acquired at 5 kHz in the region immediately downstream of the swirler exit.

A total of 3750 mean-subtracted velocity fields were used as input for the POD calculations, including all three velocity components. In this case, the bulk advection direction in each half plane is defined along the trajectory of the maximum time-averaged velocity magnitude. Near the nozzle exit, each trajectory form an angle of approximately 13° to the x-axis, a relatively small angle considering the effects of α on the PPOD convergence rate explored in section 5.2.4. Additionally, previous work on similar data has shown that a coordinate transformation which aligns the apparently traveling shear layer structures in the axial direction only marginally effects the results [23]. Hence, the coordinate transformation is not a critical step for the PPOD analysis on the annular swirling jet data. In this work, PPOD is therefore performed on data in its original spatial coordinates (i.e. $(x, y) = (s, n)$), where the number of spatial grid points in x and y are 35 and 45, respectively. Since three variables are considered at each grid point, $N_x = N_s = 3 \times 35$, $N_y = N_n = 45$, and $N_{\boldsymbol{x}} = N_x \times N_y = 3 \times 35 \times 45$. Additionally, the velocity data are converted to locally cylindrical form (for reasons discussed in section 5.2.3).

Figure 5.11(a) shows the first three PPOD modes (a), together with their associated transverse coefficient indicating the symmetry of each mode in figure 5.11(b). Based on the clear diagonal pattern in the axial and radial velocity components together with the asymmetric transverse profile, mode 1 describes an asymmetric inner shear layer structure appearing as a staggered pattern of vortices advecting downstream in the combustor centre plane. These vortices are the footprint of a three-dimensional spiral structure with an odd azimuthal-periodicity rotating about the flow centreline. Modes 2 and 3 also display diagonal patterns, indicating advecting disturbances in the measurement plane, but are accompanied by different transverse profiles compared to mode 1.

Figure 5.12(a) displays the Fourier transforms, plotting the amplitude of $\hat{\boldsymbol{\phi}}_1\,(x, f)$ as a function of frequency and axial position in the form of a waterfall plot for the three velocity components of mode 1, where the red profiles indicate the growth and decay along the peak frequency. Moving from the nozzle exit in the downstream direction, the amplitude initially grows, representing the

DISTRIBUTION A: Distribution approved for public release.

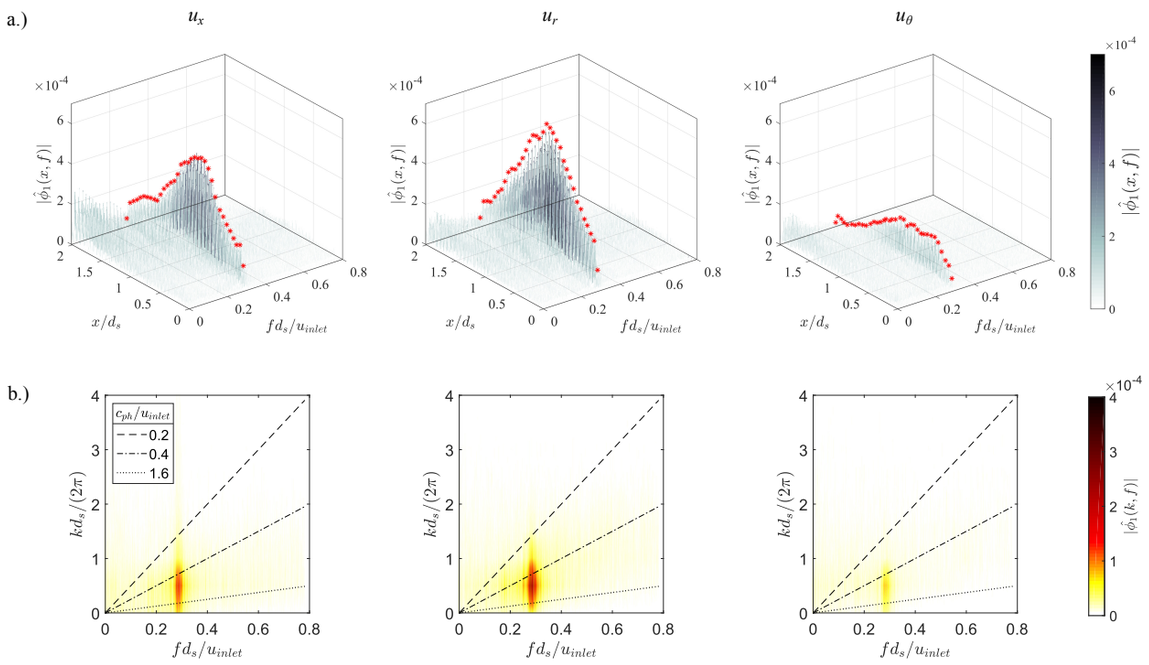

Figure 5.12: Fourier reductions of the three velocity components for the first PPOD mode; (a) shows the amplitude of $\hat{\boldsymbol{\phi}}_1\,(x,f)$ as a function of frequency and streamwise position, where the red profiles represent the streamwise dependence at the peak frequency, and (b) shows the amplitude of $\hat{\boldsymbol{\phi}}_1\,(k,f)$ as a function of frequency and streamwise wavenumber. The black lines indicate constant phase speed.

spatial amplification of the advecting structure. The amplitude then reaches a peak, followed by decay, which likely reflects the breakup of the helical structure into a more complex and less coherent pattern [34, 35]. Figure 5.12(b) plots the amplitude of $\hat{\boldsymbol{\phi}}_1\,(k,f)$ as a function of frequency and axial wavenumber. This latter representation displays how the information contained in the high energy modes can be reduced to a relatively concentrated $k-f$ region.

We next present the snapshot POD results. The three most energetic snapshot POD modes are shown in figure 5.13, together with their respective frequency spectra. It is apparent that modes 1 and 2 display similar spatial structures, phase-shifted 90 degrees in the streamwise direction, with the same temporal frequency. Although not plotted, these modes are a phase-correlated pair with a phase portrait similar to modes 2 and 3 in figure 5.8. In the measurement plane, these disturbances correspond to a train of advecting inner shear layer vortices, which physically correspond to a rotating three-dimensional structure, as mentioned in the discussion of the leading PPOD modes.

We next compare the convergence characteristic of snapshot POD and PPOD, keeping in mind the caveat noted earlier of their different energy metrics, and the difference between their eigenvalue problems and rank. As for case 1, E_c is evaluated for two different number of temporal snapshots: $N_t = 3750$, consistent with previous results, and $N_t = 45$, which is equal to the number of transverse locations ($N_y = N_n$) and, hence, the number of PPOD modes (M'). The results are displayed in figure 5.14, and observations similar to the ones for the wake flow can be seen here. Again $N_t < N_{\boldsymbol{x}}$ and $N_y < N_x \times N_t$, and hence, N_t and N_y govern the rank of the snapshot POD and PPOD problems, respectively. A reduction in the number of temporal snapshots will therefore have an effect similar to what is observed in section 5.3.2, where the rank of the snapshot POD problem is reduced, noting that $N_t = 45$ is not sufficient for a statistical representation of the flow. For PPOD, on the other hand, the rank is unaffected.

Next, the leading, high energy modes are reconstructed and compared for the two methods. Figure 5.15 shows three consecutive instantaneous velocity fields ordered from top to bottom (a), together with the corresponding reconstructions for snapshot POD modes 1 and 2 (b) and PPOD mode 1 (c). Both these snapshot POD and PPOD reconstructions capture a majority of the large-scale inner shear layer structures, providing strikingly similar results.

Although not displayed here, PPOD modes 2 and 3 also contribute to the advecting structures, and we can conclude that the dominant high energy PPOD modes contain primarily advecting information. In the case of snapshot POD, the inclusion of additional modes (for example modes 3-6) does not significantly alter the vortex shedding pattern as compared to the reconstruction of modes 1 and 2. Rather, modes even further down in the snapshot POD energy ranking must be identified and included in the reconstruction if a more accurate description of the vortex dynamics is

DISTRIBUTION A: Distribution approved for public release.

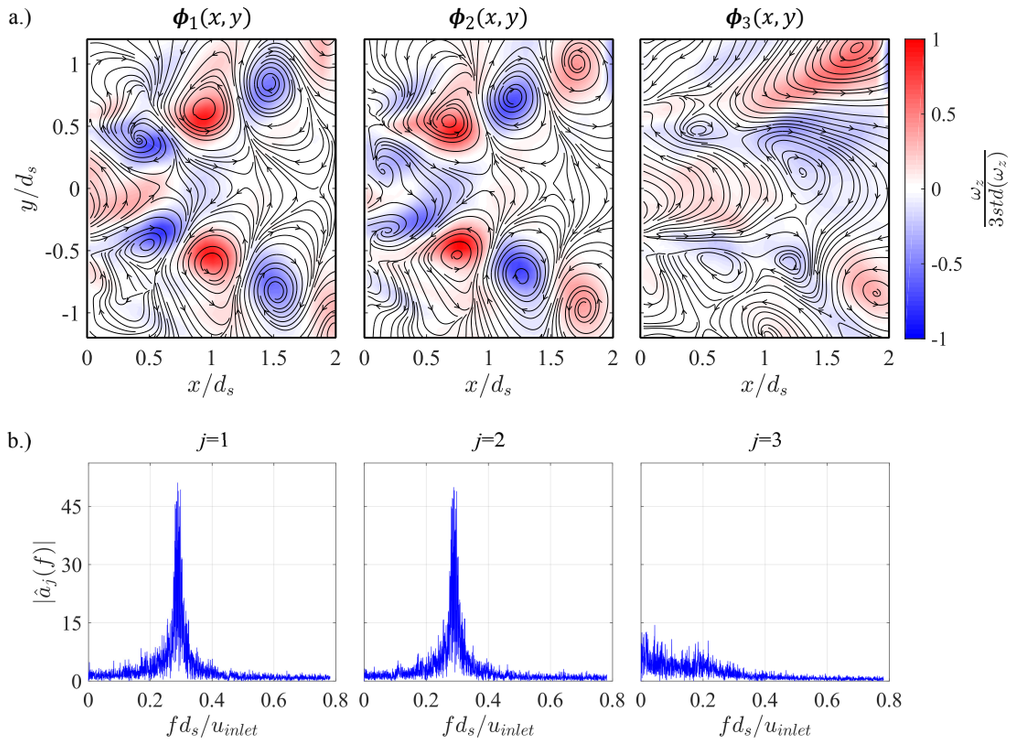

Figure 5.13: The first three snapshot POD modes, $\boldsymbol{\phi}_j\,(x,y)$, for case 2, where the flow is going from left to right, $(x/d_s, y/d_s) = (0,0)$ is the nozzle exit centerline, the in-plane velocity components are visualised as streamlines, and the background colour is the out-of-plane vorticity (a). Below each mode is the corresponding frequency spectrum, $\hat{a}_j\,(f)$, (b).

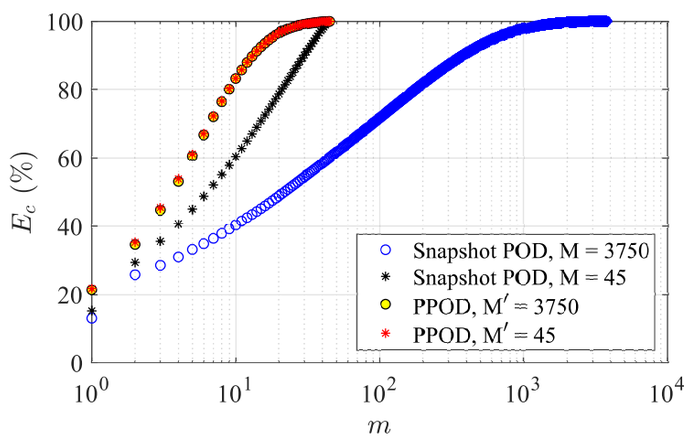

Figure 5.14: Cumulative percent energy, E_c, as a function of the number of modes, m, for snapshot POD and PPOD for case 2.

DISTRIBUTION A: Distribution approved for public release.

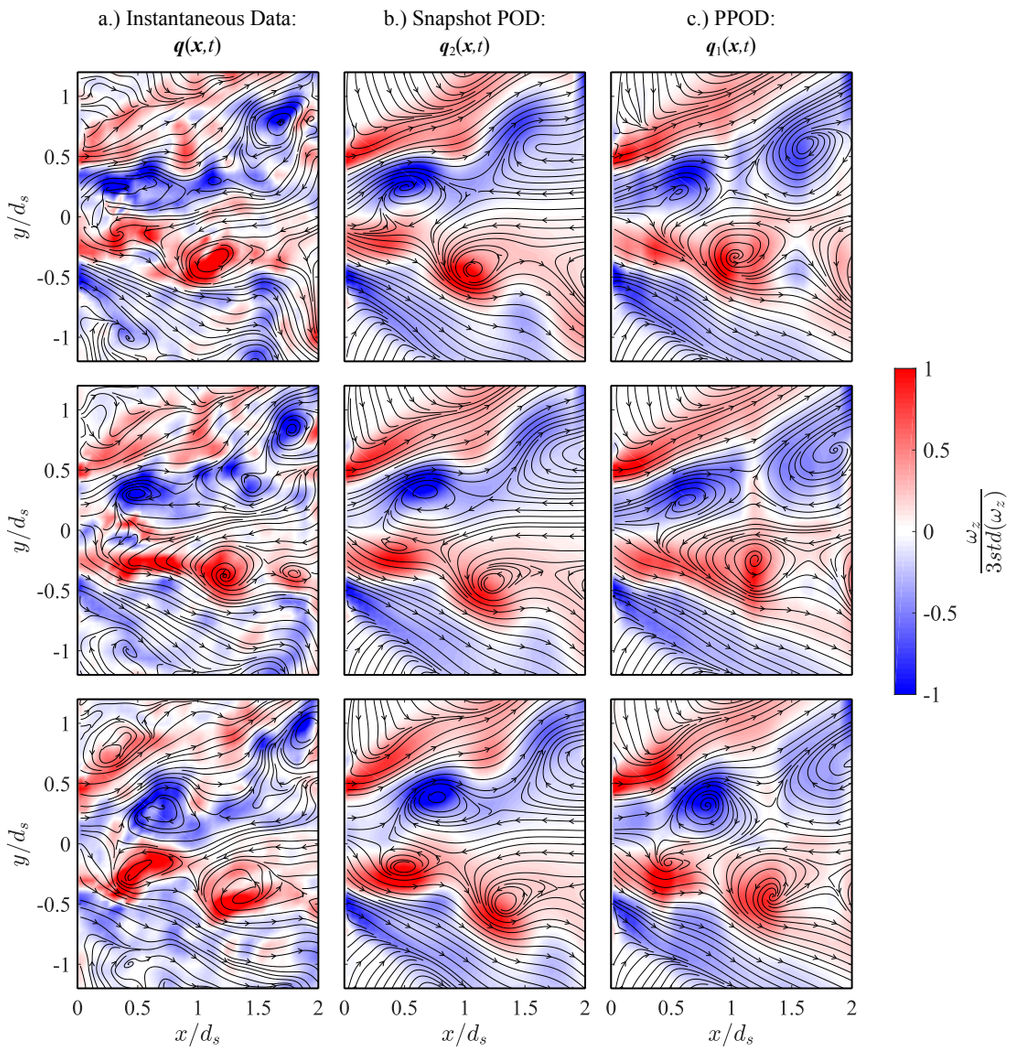

Figure 5.15: Three consecutive instantaneous flow fields (a), together with the corresponding reconstructed flow fields including mode 1 and 2 from snapshot POD (b), and mode 1 from PPOD (c). Note that the reconstructions include the time-averaged flow.

DISTRIBUTION A: Distribution approved for public release.

Case	u_j (m/s)	Re_j	S	Y_{N_2}/Y_{He}	N_s	N_n	N_x
3A	38	2900	1.75	0.79/0.21	3×68	34	$3 \times 68 \times 34$
3B	53	2200	1.0	0.452/0.548	3×68	30	$3 \times 68 \times 30$

Table 5.2: Test conditions and data properties for the two JICF cases; $J = 12$ for both cases.

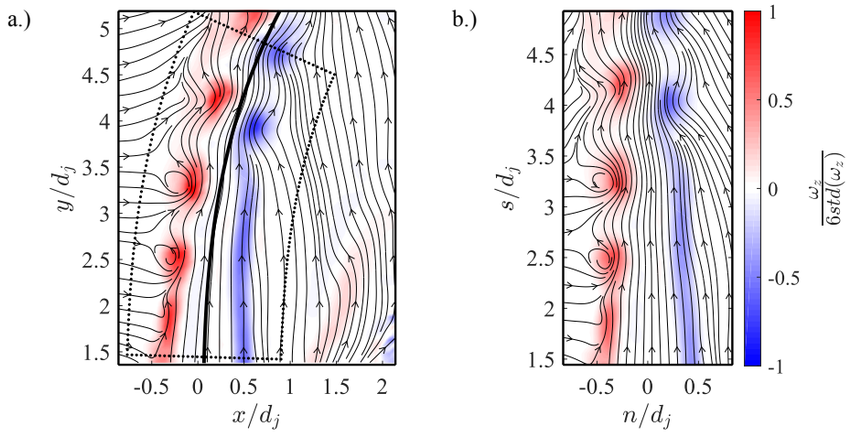

Figure 5.16: Representative instantaneous velocity field from case 3A in the original Cartesian coordinate system (a), where the streamlines provide the in-plane velocity information, the colour indicates the out-of-plane vorticity, the black solid line is the time-averaged jet centreline, and the black dotted outline represents the section of data used for the POD analysis in the curvilinear orthogonal coordinate system shown in (b).

desirable. We will come back to this for the JICF case study, where it becomes even more apparent that PPOD and snapshot POD target different types of flow structures, with PPOD focusing on advecting structures and shifting them up in the energy ranking.

5.3.3 Case 3 – Velocity Fields from a Non-Reacting Jet in Vitiated Crossflow

This section presents three-component velocity data acquired in the centre plane of a non-reacting JICF, detailed in Nair et al. [36], using the same jet nozzle profile as Megerian et al. [37]. The main flow entering the test section has a velocity of $u_\infty = 14.5$ m/s and a temperature of $T_\infty = 1250$ K corresponding to a bulk Reynolds number of $Re_\infty = 11,000$ based on the cross channel height. The jet temperature was fixed ($T_j = 300$ K) and the composition adjusted based on the required density ratio, $S = \rho_j/\rho_\infty$ for the two different cases in Table 5.2. The bulk averaged velocity, u_j, was set based on the momentum flux ratio, $J = \rho_j u_j^2/\rho_\infty u_\infty^2$ and S. The two test conditions correspond to convectively (case 3A) and globally (case 3B) unstable conditions [38, 37].

Stereo-PIV was used to obtain the velocity information in the near-field of the jet. Raw Mie-scattering image pairs were acquired at a rate of 40 kHz. A representative instantaneous velocity field is presented in figure 5.16(a), where the in-plane velocity components are displayed as streamlines and the background colour corresponds to the out-of-plane vorticity. The cross flow enters the measurement region from the left, while the jet is entering from the bottom. The point $(x/d_j, y/d_j) = (0, 0)$ corresponds to the jet exit centreline and the black solid trajectory represents the time-averaged jet centreline defined as the midpoint between the maximum and minimum vorticity. The dotted outline represents the subset of data displayed in figure 5.16(b), which have been mapped onto the s, n coordinate system, where s is the coordinate along the time-averaged jet centerline and n is the coordinate normal to it. Shear layer vortex (SLV) structures are evident in both the representations shown in figure 5.16. The measurement region slices these three-dimensional ring structures through the centre plane, resulting in a distinct windward and leeward shear layer, which appears as a staggered, asymmetric pattern, caused due to tilting of the vortex rings [39, 40], across the jet centreline. While not evident from a single instantaneous image, there is also a clear, lower frequency bulk jet flapping motion.

Similar to the previous case studies, the mean-subtracted velocity fields were analysed using PPOD and snapshot POD. A total of $N_t = 3750$ snapshots were used for the analysis including all three velocity components. Both the PPOD and snapshot POD analysis are conducted in the curvilinear orthogonal coordinate system, as motivated by the angle between the jet centreline and y-axis, which is negligible close to the jet exit, but increases up to 24° and 39° in the downstream

DISTRIBUTION A: Distribution approved for public release.

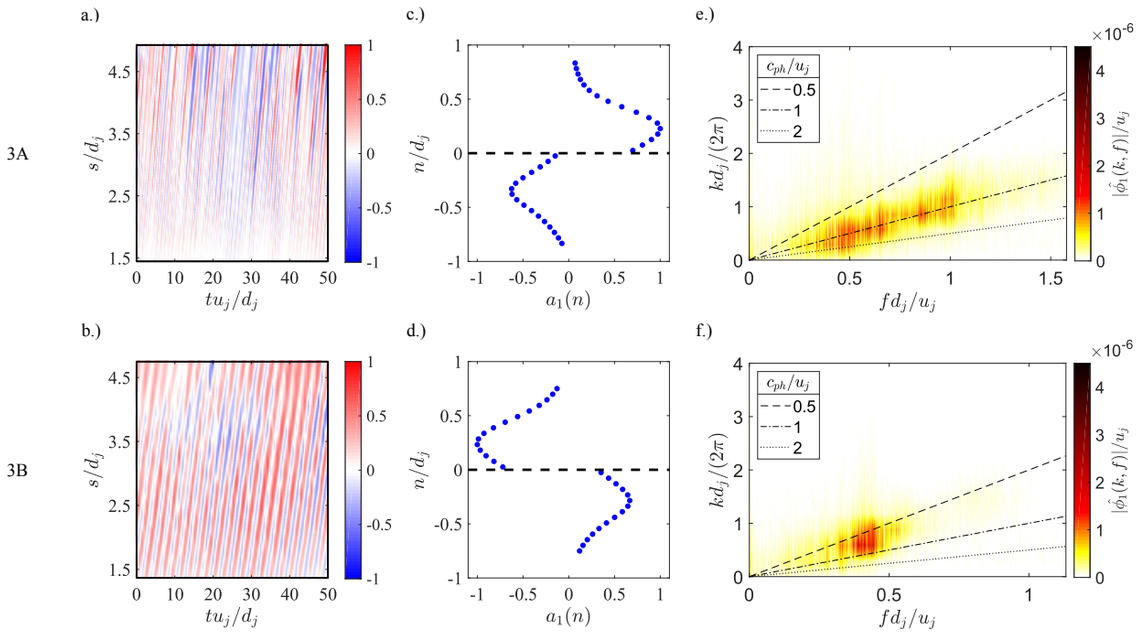

Figure 5.17: Space-time dependence of the first PPOD mode, $\boldsymbol{\phi}_1(s,t)$, (a,b), the corresponding transverse coefficient, $a_1(n)$, (c,d), and the amplitude of the two-dimensional Fourier reduction, $\hat{\boldsymbol{\phi}}_1(k,f)$, together with lines of constant phase speed, c_{ph}/u_j, (e,f) for the normal velocity component, u_n, for case 3A (top) and 3B (bottom).

region for case 3A and 3B, respectively. Additionally, the velocity components were converted to locally cylindrical form to enforce consistent symmetries across the jet centreline for the three velocity components associated with the SLV structures, as discussed in section 5.2.3. Even though the flow is not axisymmetric, the sign convention of the velocity components in locally cylindrical form prevents splitting of the physical structure across PPOD modes due to disparate symmetries. The following results are normalised by the frequency scale u_j/d_j, when applicable.

The normal velocity component, u_n, of the most energetic PPOD mode, $\boldsymbol{\phi}_1(s,t)$, and the associated transverse coefficient, $a_1(n)$, are presented in figure 5.17(a,c) and (b,d) for case 3A and 3B, respectively. Mode 1 is the primary contributor to the high frequency SLV dynamics in both cases. The Fourier transformed representations of these PPOD modes are shown in figure 5.17(e,f). Case 3A displays a high-amplitude band extending diagonally in k-f space, approximately along a constant phase speed line. Case 3B, on the other hand, has most of its high-amplitude information clustered in much narrower frequency and wavenumber bands. These observations are consistent with the convective and global stability characteristics for the two cases [37].

Next, a comparative analysis is performed based on the snapshot POD results for case 3A. As observed in previous work on reacting [41] and non-reacting jets [42], the leading, high energy modes represent jet flapping normal to the jet centreline. Modes 1 and 2, which together capture 28% of the energy, both represent flapping. Mode 1 is displayed in figure 5.18(a) as an example of such a mode, while modes 3, 4, 6, and 7 all contribute to the SLV dynamics, representing advecting motion aligned with the jet centreline. Modes 3 and 4, which together accounts for 9.5% of the energy, form the first advecting mode pair, primarily capturing large-scale vortex structures starting at $\sim s/d_j = 2.5$ and extending downstream. Modes 6 and 7, which together account for 5.5% of the energy, form a second vortex shedding pair, capturing closely spaced vortex structures closer to the jet exit, and their development downstream. Frequency spectra of modes 1, 3, and 6 are displayed in figure 5.18(b), where the relatively broadband nature of the peaks for spectra 3 and 6 are characteristic of a convectively unstable JICF. The frequency and length scales of the two mode pairs indicate that these modes correspond to the fundamental and subharmonic shear layer instability mode [37].

These results clearly demonstrate that the leading order PPOD and snapshot POD modes capture different features of the jet dynamics – the advecting SLV structures in the case of PPOD and the flapping jet motion for snapshot POD. These points can also be seen by reconstructing the high energy modes from the two methods. Figure 5.19(a) shows three consecutive instantaneous flow fields (top to bottom) for case 3A. The corresponding reconstructed flow fields based on snapshot POD modes 1-4 ($\sim$ 37% of the energy) and 1-7 ($\sim$ 47% of the energy) are displayed in figure 5.19(b) and (c), respectively. The reconstruction of modes 1-4 is dominated by the contribution from the jet flapping modes 1,2 (as confirmed by reconstructing these modes separately), while the contribution

DISTRIBUTION A: Distribution approved for public release.

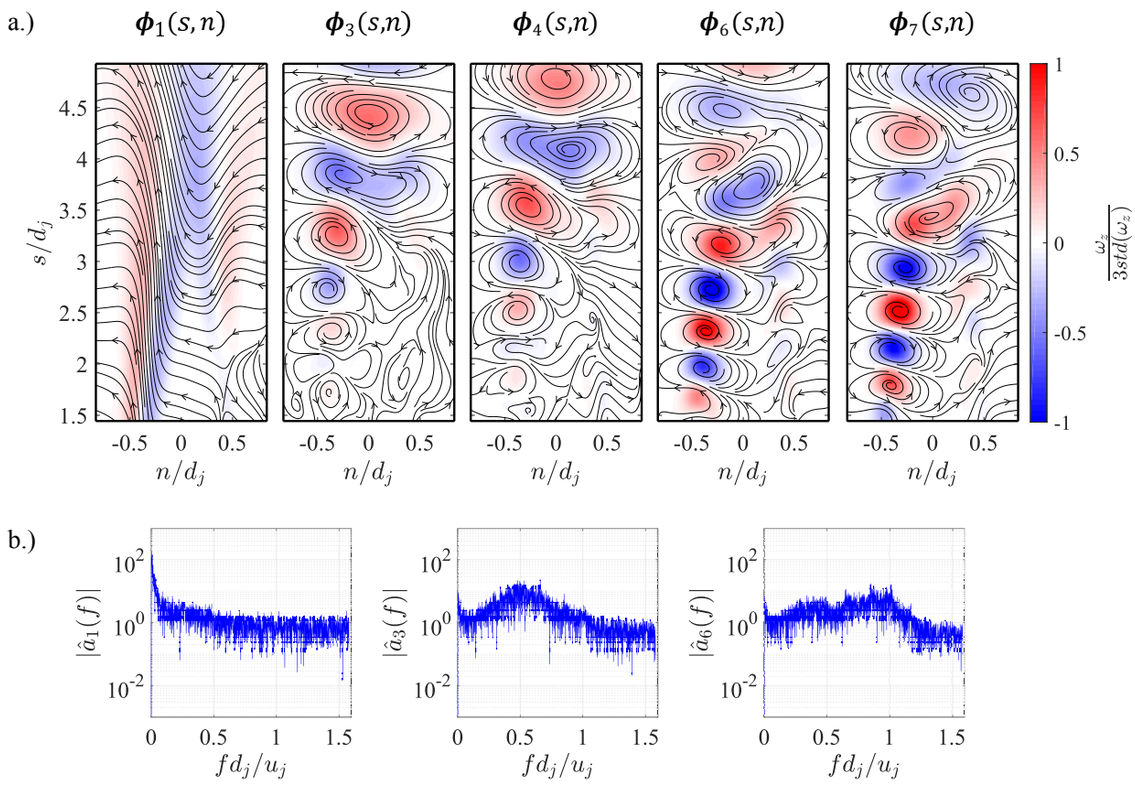

Figure 5.18: High energy snapshot POD modes, $\boldsymbol{\phi}_j\,(s,n)$, for case 3A, where the in-plane velocity components are displayed as streamlines and the out-of-plane vorticity is displayed as the background colour (a). Frequency spectra from the time coefficients, $\hat{a}_j\,(f)$), corresponding to modes 1, 3, and 6 are displayed in (b), where the spectra for modes 4 and 7 are similar to those of modes 3 and 6, respectively

from the vortex shedding modes 3,4 add only a subtle wave-like pattern in the downstream region. A minimum of the first seven snapshot POD modes must be included in the reconstruction for it to capture the SLV structures along the entire shear layer region, including the smaller but yet distinct features closer to the jet exit. For PPOD, on the other hand, the reconstruction of only mode 1 ($\sim$ 39% of the energy), as displayed in figure 5.19(d), captures the staggered SLV pattern, including the location of both windward and leeward structures throughout the entire domain. In this manner, extraction of the SLV dynamics in a JICF lends itself to analysis in a PPOD frame of reference, since the s,t inner product of PPOD allows us to directly target coherent structures advecting along a fixed direction.

5.4 Concluding Remarks

The PPOD formulation inherently targets s,t correlations by decomposing a given flow field as $\boldsymbol{q'}\,(\boldsymbol{x},t) = \sum_j a_j\,(\boldsymbol{n})\,\boldsymbol{\phi}_j\,(s,t)$, where s is along the bulk advection direction. This decomposition is optimal in the s,t inner product and therefore targets high energy advecting structures, while the commonly used space-only POD method is based on a spatial inner product and therefore targets high energy spatial structures. PPOD exhibits several useful properties for analysis of advection-dominated flows as showcased in this work. First, PPOD modes are not restricted to have any particular time dependence. Hence, a single mode can capture a physical disturbance characterised by multiple frequencies, while the coefficient provides insight about its normal profile. Furthermore, the two-dimensional Fourier transform of a given PPOD mode provides an amplitude map in the $k-\omega$ space, which provides a compact visualisation of disturbance advection velocity or dispersion, and in certain cases can be compared to results from local linear hydrodynamic stability analysis. Note also that the phase speed information in the wavenumber-frequency representation, which can display frequency and space dependencies when applicable, is an output of the decomposition rather than a quantity to be determined *a priori*.

These properties were considered through the analysis of three case studies using experimental data from high Reynolds number canonical flows. Scalar image data from a reacting wake, which is characterised by a broad range of spectral and wavenumber content, showed that the most energetic PPOD and snapshot POD modes appear to be focusing on similar features (also true for the swirling

DISTRIBUTION A: Distribution approved for public release.

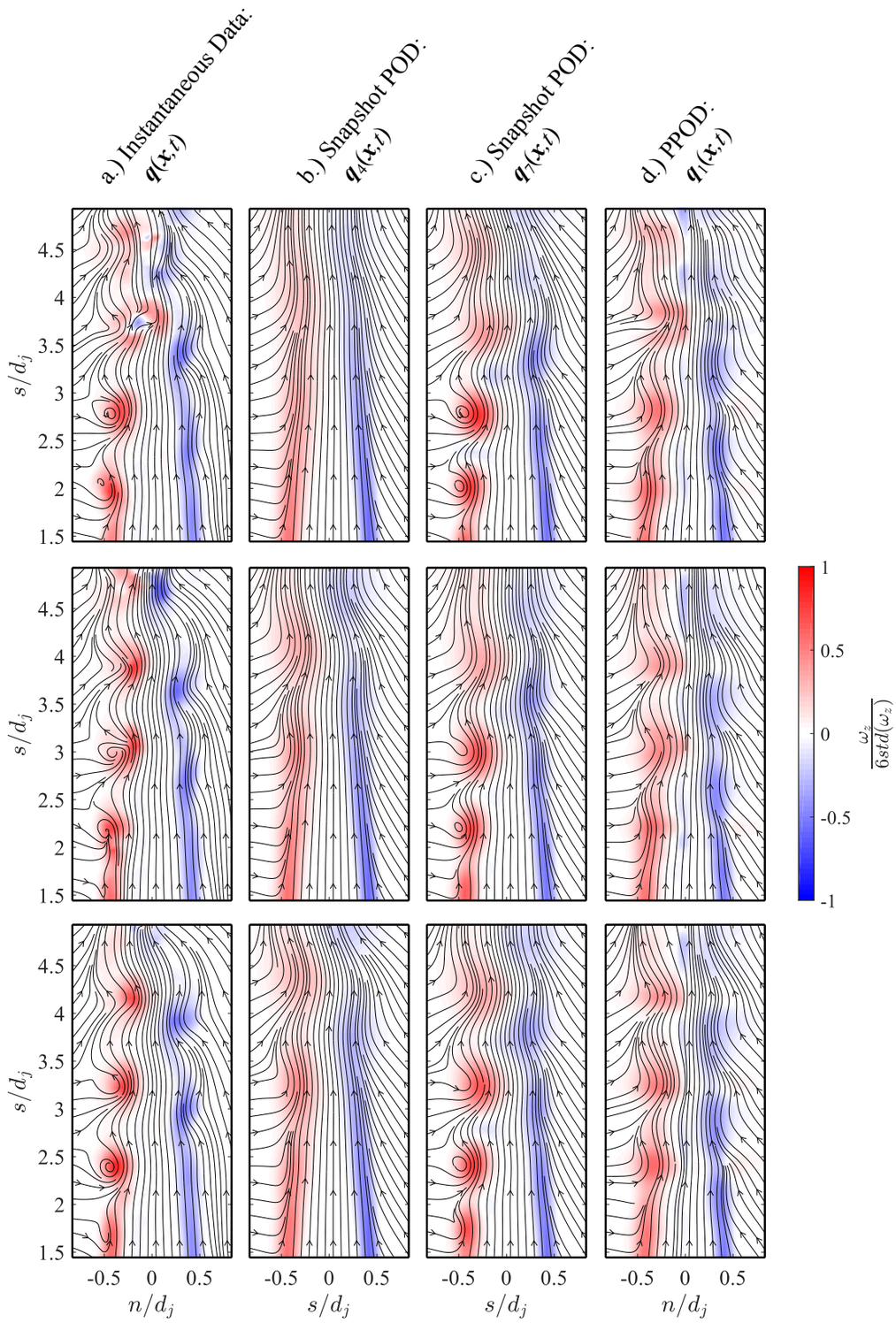

Figure 5.19: Three consecutive instantaneous flow fields (a), together with the corresponding reconstructed flow fields for snapshot POD modes 1-4 (b), 1-7 (c) and PPOD mode 1 (d) for case 3A. The reconstructions include the time-averaged flow.

DISTRIBUTION A: Distribution approved for public release.

annular jet). However, considering the low-rank approximations of the wake flow, there are in this case clear differences in the methods' fidelity in capturing spatial and temporal information: space-only POD clearly provides higher-fidelity spatial reconstructions with a smaller number of modes, while PPOD provides more higher-order temporal-spectra content (e.g. the inclusion of the first four harmonics seen in figure 5.10(c)). In contrast, the high energy PPOD and snapshot POD modes for the JICF cases capture completely different types of flow structures. The most energetic snapshot POD modes capture side to side flapping of the jet column (standing wave), while the leading PPOD mode(s) captures advecting shear layer structures. This example, in particular, shows that the different energy metrics of PPOD and space-only POD, tied to their different inner products (the s, t inner product and the spatial inner product, respectively), clearly target different features in flows consisting of both advecting and stationary disturbances.

Taken together, these results demonstrate that there is no "best" method for decomposing these complex, high degree of freedom turbulent flows. Rather, these different approaches provide fascinating insights and "lenses" into different features of the flow that, taken together, provide a deeper understanding of the system dynamics.

DISTRIBUTION A: Distribution approved for public release.

Bibliography

[1] AE Perry, MS Chong, and TT Lim. The vortex-shedding process behind two-dimensional bluff bodies. *Journal of Fluid Mechanics*, 116:77–90, 1982. ISSN 1469-7645.

[2] Anil Prasad and Charles HK Williamson. The instability of the shear layer separating from a bluff body. *Journal of fluid mechanics*, 333:375–402, 1997. ISSN 1469-7645.

[3] John Leask Lumley. The structure of inhomogeneous turbulent flows. *Atmospheric turbulence and radio wave propagation*, 1967.

[4] John L Lumley. *Stochastic tools in turbulence*. Academic Press, 1970.

[5] Kunihiko Taira, Steven L Brunton, Scott TM Dawson, Clarence W Rowley, Tim Colonius, Beverley J McKeon, Oliver T Schmidt, Stanislav Gordeyev, Vassilios Theofilis, and Lawrence S Ukeiley. Modal analysis of fluid flows: An overview. *Aiaa Journal*, pages 4013–4041, 2017. ISSN 0001-1452.

[6] Clarence W Rowley and Scott TM Dawson. Model reduction for flow analysis and control. *Annual Review of Fluid Mechanics*, 49:387–417, 2017. ISSN 0066-4189.

[7] Philip Holmes, John L Lumley, Gahl Berkooz, and Clarence W Rowley. *Turbulence, coherent structures, dynamical systems and symmetry*. Cambridge university press, 2012. ISBN 1107008255.

[8] Aaron Towne, Oliver T Schmidt, and Tim Colonius. Spectral proper orthogonal decomposition and its relationship to dynamic mode decomposition and resolvent analysis. *Journal of Fluid Mechanics*, 847:821–867, 2018. ISSN 0022-1120.

[9] Christopher M. Bishop. *Pattern Recognition and Machine Learning*. Springer, 2006. ISBN 1493938436.

[10] I. T. Jolliffe. *Principal Component Analysis*. Springer, 2 edition, 2002.

[11] Steven L Brunton and J Nathan Kutz. *Data-driven science and engineering: Machine learning, dynamical systems, and control*. Cambridge University Press, 2019. ISBN 110838658X.

[12] Moritz Sieber, C. Oliver Paschereit, and Kilian Oberleithner. Spectral proper orthogonal decomposition. *Journal of Fluid Mechanics*, 792:798–828, 2016.

[13] Sonja Glavaski, Jerrold E Marsden, and Richard M Murray. Model reduction, centering, and the karhunen-loeve expansion. In *Proceedings of the 37th IEEE Conference on Decision and Control (Cat. No. 98CH36171)*, volume 2, pages 2071–2076. IEEE, 1998. ISBN 0780343948.

[14] L Sirovich, M Kirby, and M Winter. An eigenfunction approach to large scale transitional structures in jet flow. *Physics of Fluids A: Fluid Dynamics*, 2(2):127–136, 1990. ISSN 0899-8213.

[15] Michael Kirby and Dieter Armbruster. Reconstructing phase space from pde simulations. *Zeitschrift für angewandte Mathematik und Physik ZAMP*, 43(6):999–1022, 1992. ISSN 0044-2275.

[16] Clarence W Rowley, Ioannis G Kevrekidis, Jerrold E Marsden, and Kurt Lust. Reduction and reconstruction for self-similar dynamical systems. *Nonlinearity*, 16(4):1257, 2003. ISSN 0951-7715.

DISTRIBUTION A: Distribution approved for public release.

[17] Clarence W Rowley and Jerrold E Marsden. Reconstruction equations and the karhunen–loève expansion for systems with symmetry. *Physica D: Nonlinear Phenomena*, 142(1-2):1–19, 2000. ISSN 0167-2789.

[18] Francesco Fedele, Ozeair Abessi, and Philip J Roberts. Symmetry reduction of turbulent pipe flows. *Journal of Fluid Mechanics*, 779:390–410, 2015. ISSN 0022-1120.

[19] Julius Reiss, Philipp Schulze, Jörn Sesterhenn, and Volker Mehrmann. The shifted proper orthogonal decomposition: A mode decomposition for multiple transport phenomena. *SIAM Journal on Scientific Computing*, 40(3):A1322–A1344, 2018. ISSN 1064-8275.

[20] Jörn Sesterhenn and Amir Shahirpour. A characteristic dynamic mode decomposition. *Theoretical and Computational Fluid Dynamics*, 33(3-4):281–305, 2019. ISSN 0935-4964.

[21] Oliver T. Schmidt and Peter J. Schmid. A conditional space–time pod formalism for intermittent and rare events: example of acoustic bursts in turbulent jets. *Journal of Fluid Mechanics*, 867:R2, 2019. doi: 10.1017/jfm.2019.200.

[22] Peter J Schmid. Dynamic mode decomposition of numerical and experimental data. *Journal of fluid mechanics*, 656:5–28, 2010. ISSN 1469-7645.

[23] H Ek, W Proscia, T Lieuwen, and B Emerson. Re-oriented pod for feature extraction from time resolved reacting flow datasets. In *Proceedings of ASME Turbo Expo*, 2019.

[24] Outi Tammisola and Matthew Pudan Juniper. Coherent structures in a swirl injector at re= 4800 by nonlinear simulations and linear global modes. *Journal of Fluid Mechanics*, 792: 620–657, 2016. ISSN 0022-1120.

[25] Gal Berkooz, Philip Holmes, and John L Lumley. The proper orthogonal decomposition in the analysis of turbulent flows. *Annual review of fluid mechanics*, 25(1):539–575, 1993. ISSN 0066-4189.

[26] Lawrence Sirovich. Turbulence and the dynamics of coherent structures. i. coherent structures. *Quarterly of applied mathematics*, 45(3):561–571, 1987. ISSN 0033-569X.

[27] Antoni I. Alomar, A. Nicole, D. Sipp, Valérie Rialland, and F. Vuillot. Reduced-order model of a reacting, turbulent supersonic jet based on proper orthogonal decomposition. *Theoretical and Computational Fluid Dynamics*, 34:49–77, 2020.

[28] Santosh J. Shanbhogue, Michael Seelhorst, and Tim Lieuwen. Vortex phase-jitter in acoustically excited bluff body flames. *International Journal of Spray and Combustion Dynamics*, 1 (3):365–387, 2009. doi: 10.1260/175682709789141528.

[29] Benjamin Emerson, Kelvin Murphy, and Tim Lieuwen. Flame density ratio effects on vortex dynamics of harmonically excited bluff body stabilized flames. In *ASME Turbo Expo 2013: Turbine Technical Conference and Exposition*. American Society of Mechanical Engineers Digital Collection, 2013.

[30] Benjamin Emerson and Tim Lieuwen. Dynamics of harmonically excited, reacting bluff body wakes near the global hydrodynamic stability boundary. *Journal of Fluid Mechanics*, 779: 716–750, 2015. ISSN 0022-1120.

[31] Nicholas Rock, Ianko Chterev, Benjamin Emerson, Sang Hee Won, Jerry Seitzman, and Tim Lieuwen. Liquid fuel property effects on lean blowout in an aircraft relevant combustor. *Journal of Engineering for Gas Turbines and Power*, 141(7):071005, 2019. ISSN 0742-4795.

[32] Ianko Chterev, Nicholas Rock, Hanna Ek, Benjamin Emerson, Jerry Seitzman, Naibo Jiang, Sukesh Roy, Tonghun Lee, James Gord, and Tim Lieuwen. Simultaneous imaging of fuel, oh, and three component velocity fields in high pressure, liquid fueled, swirl stabilized flames at 5 khz. *Combustion and Flame*, 186:150–165, 2017. ISSN 0010-2180.

[33] James T Edwards. Reference jet fuels for combustion testing. In *55th AIAA Aerospace Sciences Meeting*, page 0146, 2017.

[34] FF Grinstein and Christer Fureby. Les studies of the flow in a swirl gas combustor. *Proceedings of the Combustion Institute*, 30(2):1791–1798, 2005. ISSN 1540-7489.

DISTRIBUTION A: Distribution approved for public release.

[35] Ying Huang, Shanwu Wang, and Vigor Yang. Systematic analysis of lean-premixed swirl-stabilized combustion. *AIAA journal*, 44(4):724–740, 2006. ISSN 0001-1452.

[36] Vedanth Nair, Matthew D Sirignano, Sara Schmidheiser, Lane Dillon, Christopher A Fugger, Tongxun Yi, Naibo Jiang, Paul S Hsu, Mikhail N Slipchenko, and Sukesh Roy. Tomographic piv characterization of the near field topology of the reacting jet in crossflow. In *AIAA Scitech 2020 Forum*, page 1420, 2020.

[37] S Megerian, J Davitian, LS De B Alves, and AR Karagozian. Transverse-jet shear-layer instabilities. part 1. experimental studies. *Journal of fluid Mechanics*, 593:93, 2007. ISSN 0022-1120.

[38] DR Getsinger, L Gevorkyan, OI Smith, and AR Karagozian. Structural and stability characteristics of jets in crossflow. *Journal of Fluid Mechanics*, 760:342, 2014. ISSN 0022-1120.

[39] Richard Malcolm Kelso, TT Lim, and AE Perry. An experimental study of round jets in cross-flow. *Journal of fluid mechanics*, 306:111–144, 1996. ISSN 1469-7645.

[40] TF Fric and A Roshko. Vortical structure in the wake of a transverse jet. *Journal of Fluid Mechanics*, 279:1–47, 1994. ISSN 1469-7645.

[41] Vedanth Nair, Christopher Douglas, Benjamin Wilde, Benjamin Emerson, and Timothy Lieuwen. High-frequency imaging of a reacting jet in crossflow. *Bulletin of the American Physical Society*, 63, 2018.

[42] Knuderik E Meyer, Jakob M Pedersen, and Oktay Ozcan. A turbulent jet in crossflow analysed with proper orthogonal decomposition. *Journal of Fluid Mechanics*, 583(199-227):3.1, 2007.

DISTRIBUTION A: Distribution approved for public release.